Cardiovascular Health: From Cardiomyocyte Electrostimulation to miRNA Detection

Fionn Ó Maolmhuaidh, B.Sc

A thesis submitted at Dublin City University for the degree of
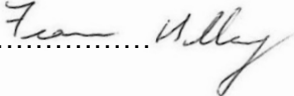
PhD

School of Chemical Sciences

Supervisor:

Prof. Robert J. Forster

September, 2023

I.   <u>**DECLARATION**</u>

I hereby certify that this material, which I now submit for assessment on the programme of study leading to the award of doctor of philosophy is entirely my own work, that I have exercised reasonable care to ensure that the work is original, and does not to the best of my knowledge breach any law of copyright, and has not been taken from the work of others save and to the extent that such work has been cited and acknowledged within the text of my work.

Signed:………………………………

ID no.:…13335646….

Date:…08/12/2022…

II. <u>DEDICATION</u>

I dedicate this to my brothers, to show them what is possible.

"*Ar scáth a chéile a mhaireann na daoine*" – Irish proverb

III. <u>ACKNOWLEDGEMENTS</u>

First, I must acknowledge my parents, whose nature and nurture combine to form my very essence. Without them I surely would not be where I am today or possess the skill nor the will to complete this thesis. They allowed me to be myself with gentle guidance, which in turn allowed me to foster my love of science. That love of science allowed me to pursue this opportunity for which I will forever be grateful. They have helped emotionally and financially such that I could focus solely on my selfish pursuits. I can never repay them what is owed, only take advantage of what they have given me to the fullest and spread the values they have instilled in me as far and wide as possible.

In truth my brothers Rían, Conall, and Brógan contributed very little, yet they must be acknowledged all the same. I will hence forth claim that this thesis is most certainly the spark of inspiration for anything noteworthy they do from here on out and as such I am directly responsible. I have no doubt that each of them will achieve a great deal as they forge their own paths in life.

Miren, mi amada, mo stór, is uniquely placed to experience with me what it truly means to write this document and persevere in this scientific community. Her undeniable Basque beauty inspires me every day to focus my mind and achieve everything I know I am capable of. Her kind words have helped me through any difficult patches and also spurred my on after exciting breakthroughs. Her love of science and of me are, and forever will be, an inspiration. Go raibh maith agat, eskerrik asko, gracias for all that you continue to do for me and with me.

I would like to thank Robert for all the wisdom guidance and patience he has shown me through-out my time under his supervision. He told me when I started that he would rather teach a biologist chemistry than a chemist biology and I hope this still holds true. He is an incredible scientist, and it has been an honour to have worked with him.

Thank you also to Paul and his group for giving me access to their lab for work. It became an oasis of biology in a sea of electrochemistry when sometimes some familiarity is needed to recuperate. All the friendly faces, kind words, and valuable insight were greatly appreciated.

I would like to acknowledge all those who worked with me in Robert's group over the years particularly those I worked closest with; Loanda, Eadaoin, Sara, Amanda, Angelo,

Ahmed, Ellie, the aforementioned Miren, and most recently Estefania. A diverse group who made working in the group wonderfully entertaining, whether intentionally or not.

I would finally like to acknowledge my friends Danielle, Darren, John, Kate, Maddy, and Roisin (listed alphabetically, relax). They provide a captive audience for me which has allowed me to grow as a person from when I first met them. They are all essentially the same however, which suggests the benefit was somewhat one way.

IV.   <u>TABLE OF CONTENTS</u>

V. <u>LIST OF ABBREVIATIONS</u>

Acronyms	Explanation
ADSS1	Adenylosuccinate synthetase 1
AI	Artificial Intelligence
ANSA	Ammonium 8-anilino-1-naphthalenesulfonate
ATP	Adenosine triphosphate
ATR	Attenuated Total Reflection
BNP	B-type natriuretic peptides
BPE	Bipolar Electrode
BEC	Bipolar Electrochemical Cell
BPM	Beats per minute
BSA	Bovine Serum Albumin
cDNA	Complementary DNA
COVID-19	Coronavirus disease
CRP	C reactive protein
cTnI	cardicac troponin I
cTnT	cardicac troponinT
CV	Cyclic Voltammetry
CVD	Cardiovascular disease
CX45	connexin 45
DAPI	4′,6-diamidino-2-phenylindole
DKD	Diabetic kidney disease
DPBS	Dulbecco's Phosphate Buffer Saline
DS	Dextran Sulphate

ECG	Electrocardiogram
ECM	Extracellular matrix
EDTA	Ethylenediaminetetraacetic acid
EF	Electric Field
EIS	Electrochemical Impedance Spectroscopy
FBS	Foetal Bovine Serum
Fib	Fibronectin
FITC	Fluorescein isothiocyanate
FTIR	Fourier-transform infrared spectroscopy
FTO	Fluorine-doped Tin Oxide
Hz	Hertz
G2-PS	1,4-diaminobutane core
GRK2	G protein-coupled receptor kinase 2
ICC	Immunocytochemistry
IMS	Industrial Methylated Spirits
ITO	Indium Tin Oxide
MCH	6-Mercapto-1-hexanol
MGB	Minor Groove Binder
miRNA	microRNA
MUA	11-Mercaptoundecanoic Acid
MyBP-C	Myosin Binding Protein C
NPC	Neural Progenitor Cells
NT-proBNP	N-terminal proBNP
PAMAM	poly(amidoamine)
PBS	Phosphate Buffer Saline
PBST	Phosphate Buffer Saline Tween

PCR	Polymerase Chain Reaction
PPy	Polypyrrole
PVDF	Polyvinylidene Fluoride
qPCR	quantitative Polymerase Chain Reaction
RISCs	RNA Induced Silencing Complexes
RNAi	interference RNA
RSD	Relative standard deviation
RT	Reverse Transcriptase
RT-qPCR	Reverse Transcriptase qPCR
SAM	Self-assembled monolayer
SEM	Scanning Electron Microscopy
SFE	Surface Free Energy
SPE	Screen-Printed Electrode
TE buffer	Tris EDTA buffer
TMP	Transmembrane Potential
TRPA1	transient receptor potential ankyrin 1
UV-Vis	Ultraviolet Visible
α-SMA	α-Smooth Muscle Actin

VI. <u>LIST OF SYMBOLS</u>

Symbols	Explanation	Units
ΔE_{elec}	Interfacial potential of the bipolar electrode	V
E_{tot}	Total electrical potential applied by the driving electrodes across the channel	V
l_{elec}	Relative length the bipolar electrode	cm
$l_{channel}$	Length of the channel	cm
ν	Scan rate	V s^{-1}
Vpp	Peak-to-peak potential	V
$\Delta G°$	Gibbs free energy	J$\cdot$ K^{-1} $\cdot$mol^{-1}
R	Gas constant	J$\cdot$mol$^{-1}\cdot$K^{-1}
T	Temperature	K
K_{eq}	Equilibrium constant	Unitless
r_p	Particle radius	nm
r_{pp}	Interparticle distance	cm
D	Diffusion coefficient	cm^2 s^{-1}
t	Time	s

VII. LIST OF FIGURES

VIII. <u>LIST OF TABLES</u>

IX. **RESEARCH OUTPUTS**

Publications

1. Qin, Chunyan, Zhilian Yue, Yunfeng Chao, Robert J. Forster, Fionn Ó. Maolmhuaidh, Xu-Feng Huang, Stephen Beirne, Gordon G. Wallace, and Jun Chen. "Data on the bipolar electroactive conducting polymers for wireless cell stimulation." Data in Brief 33 (2020): 106406.

2. Qin, Chunyan, Zhilian Yue, Yunfeng Chao, Robert J. Forster, Fionn Ó. Maolmhuaidh, Xu-Feng Huang, Stephen Beirne, Gordon G. Wallace, and Jun Chen. "Bipolar electroactive conducting polymers for wireless cell stimulation." Applied Materials Today 21 (2020): 100804.

3. Gaur, Manish, Charu Misra, Awadh Bihari Yadav, Shiv Swaroop, Fionn Ó. Maolmhuaidh, Mikhael Bechelany, and Ahmed Barhoum. "Biomedical applications of carbon nanomaterials: fullerenes, quantum dots, nanotubes, nanofibers, and graphene." Materials 14, no. 20 (2021): 5978.

Oral presentations

1. Biological Research Society 11th annual research day 2019 – An overview of assay design for the ultrasensitive detection of miRNA associated with heart disease.
2. 4th Annual DCU Chemical Research Symposium 2019 – Investigation into the biocompatibility of screen-printed electrode and their effects on cell viability
3. ECME conference 2020 – The electrochemical and biological characterisation of electrodeposited Polypyrrole films and their co-doping with Dextran Sulphate and varying levels of Fibronectin for use in bipolar electrostimulation.
4. BRS Research Day 2021 – Characterisation of the distribution and biological activity of fibronectin in PPy films.
5. 6th Annual DCU Chemical Research Symposium 2021 – Design, testing and application of a wireless bipolar electrostimulation of HL-1 cardiomyocytes in vitro conditions.

6. 1st international symposium on Molecular Biosensing: From Theory to Practice 2021 - miRNA biomarker detection in the fight against Cardiovascular Disease

Poster presentations

1. XXV International Symposium on Bioelectrochemistry and Bioenergetics, Limerick, 26-30 May 2019. Author of a poster on "Biocompatible Screen-Printed Electrodes: Cell Viability Investigations".

X. <u>ABSTRACT</u>

Cardiac Health: From Electrostimulation of Cardiomyocytes to miRNA Detection

Fionn Ó Maolmhuaidh

Current methods of cell culture where electrical stimulation is applied during culture require a wired connection to a power supply to generate an electric field with which to stimulate the cells. This method is intrusive in a lab setting and does not conveniently allow for traditional cell culture techniques during stimulation, hence it is frequently omitted from cell culture protocols. The aim of this work is to demonstrate a novel method of electrical stimulation of cardiomyocytes using wireless bipolar electrochemical techniques. The work describes the design and characterisation of a wireless bipolar electrode and wireless bipolar electrochemical cell to facilitate wireless bipolar electrostimulation. By using a wireless connection more versatile experiments can be conducted on cells in culture while mitigating the contamination risk of a traditional wired stimulation platform.

Using a polypyrrole based conducting film doped with fibronectin molecules to facilitate the adherence and growth of cardiomyocytes on the bipolar electrode surface. Cell culture on a conductive film opens the possibility of future applications in electroceuticals by providing a wireless platform to deliver and electric field to cells in culture.

Demonstrating cell culture on conductive polymer with the application of electric fields allows for the study of healthy and disease cell populations in the presence of electrical stimuli. Biomarker monitoring during this work is important to characterise and understand the impact of stimuli on the cells in culture. As such, an electrochemical miRNA biosensor was also explored in this work. The assay was based on the detection of miRNA through hydrogen peroxide degradation. The assay was built of screen-printed electrodes as a method to characterise cell cultures. The ability to monitor biomarkers both in vitro and in vivo is important in generating an understanding of disease models and in the development of point-of-care testing capabilities.

Chapter 1
Literature Review

From Cardiomyocyte Electrostimulation to miRNA Detection

1. Introduction to Cardiovascular Biology

1.1. Cardiovascular disease: Definition

Cardiovascular disease (CVD) is the leading cause of death globally. Approximately 17.9 million deaths per year are attributed to cardiovascular disease according to the World Health Organisation [1]. One major contributor to this is the fact that cardiovascular disease is an umbrella term encompassing several disease pathologies [2]. Diseases covered by the definition of cardiovascular disease include coronary heart disease, cerebrovascular disease, peripheral arterial disease, rheumatic heart disease, congenital heart disease, deep vein thrombosis and pulmonary embolism. The most common manifestations include strokes, heart attacks (myocardial infarctions), and heart disease [3]. Strokes occur through the occlusion in the vasculature of the brain, known as an ischemic stroke, or through the rupture of a blood vessel, known as a haemorrhagic stroke [4–8]. These are acute incidents in the cerebrovascular system which cause damage to brain tissue due to a lack of oxygen. The tissue death can have a varied impact depending on the location of the stroke and the role of the affected tissue area of the brain [9–11], which can cause chronic impairments to its function. Similarly, myocardial infarctions are also characterised as an acute event which can have a serious acute and chronic impact on the heart [12,13]. Myocardial infarctions are part of a wider disease group known as ischemic heart disease, which is also known as coronary artery disease occurs when blood flow to the cardiac muscle cells is obstructed, resulting cell death. All of these contributing diseases carry both immediate, acute risks to patient life but also create long term chronic issues with regards to cardiac function and volume. This can have a dramatic impact in the patient's overall quality of life as well as a shortened lifespan [14–17].

1.2. CVD global impact

The global impact and burden of cardiovascular disease is constantly being assessed both globally and more locally at the national level. Naturally, this is driven by the global impact on mortality as discussed in section 1.1, however cardiovascular disease was again brought to the forefront of the national interest with the recent COVID-19 pandemic. Detailed research into the impact of COVID-19 on those already suffering from cardiovascular disease was conducted in a variety of countries. Both the possibility of COVID-19 contribution to the development of cardiovascular disease and the impact of contracting COVID-19 with an underlying cardiovascular disease were assessed [18].

Studies of laboratory analysis showed that patients who had contracted COVID-19 had an approximately 10% incidence rate of elevated cardiac troponins [19–21]. The troponin family of proteins is associated with actin in healthy cardiac muscle. They assist in the regulation of muscle contraction and relaxation of muscle cells through the regulation of calcium. Elevated cardiac troponins are associated with multiple cardiovascular diseases as they are released into the bloodstream upon cell death, indicating cardiac muscle trauma [22,23]. The impact of cardiovascular disease comorbidity is well understood and similar trends are seen with patients who present with COVID-19 and cardiovascular disease comorbidities showing much poor patient outcomes than those with this comorbidity [24,25]. As we struggle to wrestle control of the increasing cardiovascular disease epidemic and the risks of future concurrent pandemics the importance of cardiovascular disease research is even more boldened and underlined [26–28].

1.3. Cardiomyocyte biology

The heart is the central organ of the cardiovascular system and is a muscular pump used to distribute blood throughout the body. In the human heart there are two atria and two ventricles with blood flowing into and out of these chambers regulated by the tricuspid, pulmonary, aortic, and mitral valves. The predominant tissue type found in the heart is the muscle cells found sandwiched between the endocardium and the epicardium [29]. This muscular layer of cells is known as the myocardium and the muscles cells of which it is comprised of are known as cardiomyocytes [30].
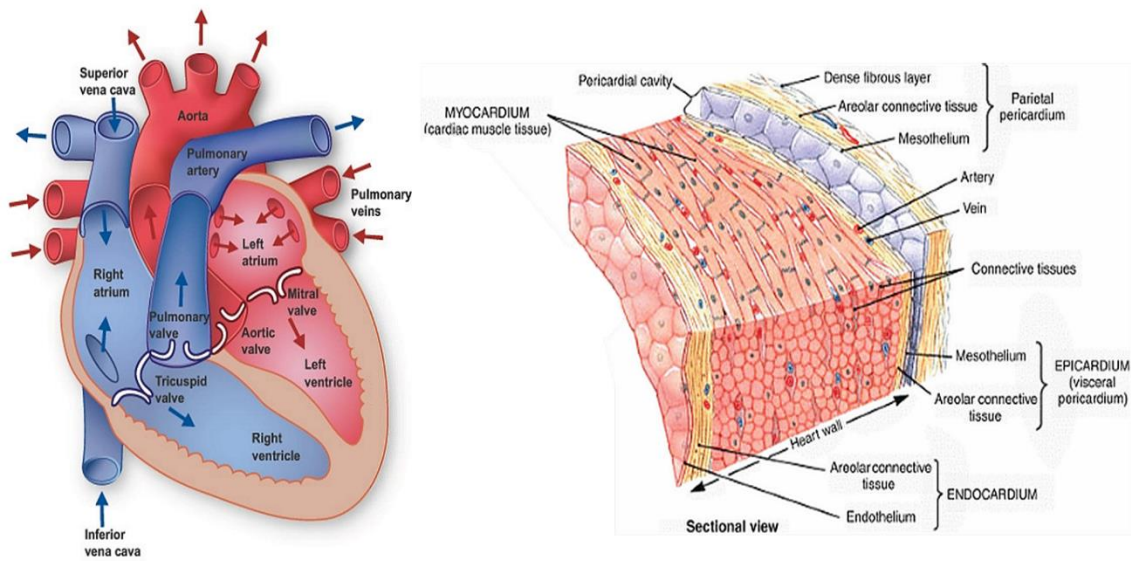
Figure 1. Illustration of heart anatomy (left) and heart wall (right). Adapted from The Texas Heart Institute [31] and Anatomy of the Human Heart. In Handbook of Cardiac Anatomy, Physiology, and Devices, Third Edition [32].

1.3.1. Morphology

Cardiomyocytes are muscles cells specific to the heart that are characterised by their contractile phenotype and key protein expression profiles. Characterisation of the cardiomyocyte is essential as both internal and external morphology, which can vary depending on the age of the cell. During the cells maturation process key proteins in the cells are expressed at different intervals affecting both the cells phenotypic appearance and ability to contract. Immature cells do not have the same contraction capabilities as those of fully mature cardiomyocytes [33,34]. Electrical stimulation has been shown to be essential for physiologically comparable contraction force. Contraction force is a useful metric for estimating the *in vitro* cells maturity relative to *in vivo* cells as it is effected by the expression levels and organisation of key proteins, which will be discussed in further detail across the following two sections 1.3.2, and 1.3.3 [35,36]. Cell maturity can be broken down into two primary categories, the first being the immature cardiomyocyte which is known as the pre-natal phase, and the second being the mature cardiomyocyte which is also the post-natal phase. Therefore, it is important to highlight at which development phase the cardiomyocytes used in a given study. Frequently studies will use the qualitative difference between immature and mature cells to determine the effect of electrical stimulation.

Immature cardiomyocyte morphology is typically characterised as more rounded (height to width ratio of approximately 1 : 1) than mature cardiomyocyte which have a rod shape (height to width ratio between 1 : 1.5 and 1 : 7)[37,38]. Cell morphology is critical for the contractile role of the cells within the heart wall. For instance, a culture of highly conforming rod-shape cells helps to improve contractile strength, contraction direction, action potential propagation, and gap-junction based cell to cell communication. As such it is important to ensure the presence of these phenotypes during the maturation process and culture of cardiomyocytes regardless of lineage given the dramatic phenotypic differences between mature and immature cells. These changes can impact observed responses in cardiomyocyte cultures, which in turn could undermines conclusions of studies.
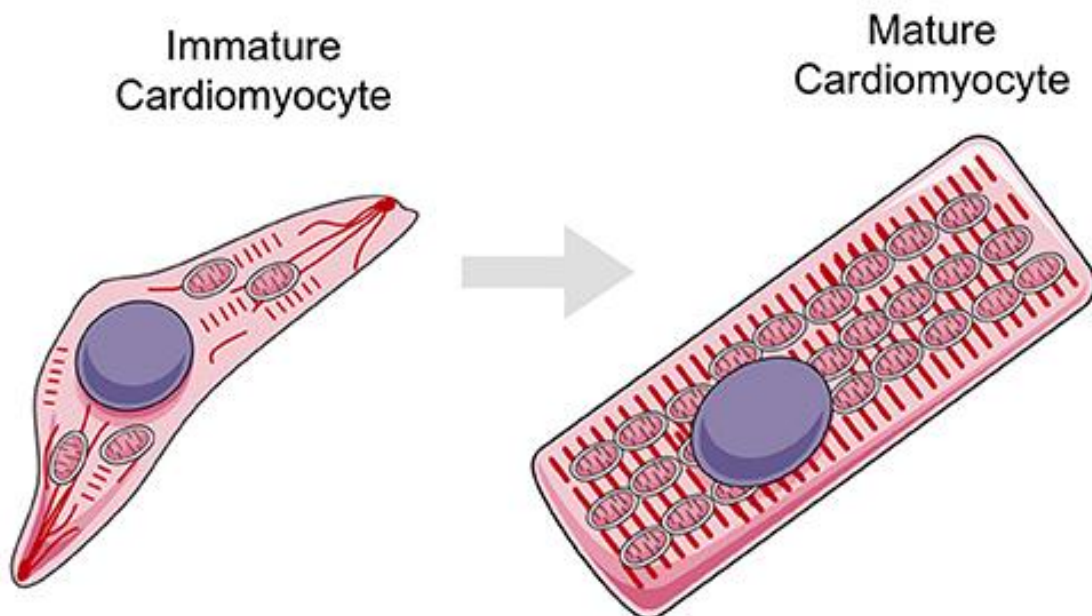
Figure 2. Schematic representation of morphological difference between an immature and mature cardiomyocyte highlighting shape and cytoskeletal differences. Image adapted from Liao *et al.* [39].

It should also be noted that there is interspecies morphological variability in cardiomyocytes. Murine, porcine, and human cardiomyocytes have different morphologies even at the post-natal mature phase. For instance individual mature porcine cardiomyocytes increase in size through hypertrophy which is accompanied by multinucleation of the cell [40,41]. By contrast, multinucleated murine cardiomyocytes are present in a lower percentage of total cardiomyocyte population, and human cardiomyocyte show the lowest percentage of multinucleated cardiomyocytes within the overall cardiomyocyte population of any commonly used mammalian animal model.

Human cardiomyocytes do however show the highest percentage of polyploidy cells within the cardiomyocyte population. Polyploidy, the presence of a greater number of genome copies than the typical diploid number of 2N within a single cell, is common in terminally differentiated, also known as mature cells, of many lineages [42,43]. It may occur through multiple diploid nuclei being present in the cell or through the duplication of the genome in a single nucleus. Therefore, phenotypic changes in cells during maturation should be taken in the context of the species of cell model used [44,45].

1.3.2. Contractions and role of ion channels

One key phenotype of the cardiomyocyte is the ability to contract. Contraction is a dynamic process where-by the cells undergo cytoskeletal rearrangement resulting in the shorting of the cells length. By orientating groups of cells in line with each other it is possible to multiply the contractile force through the tissue and generate a physiological response. In the case of the heart, the cardiomyocytes are orientated in the wall of the heart around the chambers of the heart such that when the contraction occurs the chambers are constricted and the blood within is pumped out [46,47].

The cardiomyocytes carefully control the intracellular and extracellular concentration of Na^+, Ca^{2+}, and K^+ maintaining a membrane potential of approximately -80 mV [48–51]. In the heart the pacemaker cells trigger the contraction of cardiomyocytes. Pacemaker cells are specialised cardiomyocytes who have lost the ability to contract and possess as special set of ion channels which trigger spontaneous depolarisation. The depolarisation triggers a switch in the membrane potential, known as an action potential through the influx of Ca^{2+} ion, this is represented in **Figure 3** [52,53]. This action potential is conducted by gap-junction proteins which allows the transfer of these Ca^{2+} ions from the pacemaker cell to the contractile cardiomyocytes [54,55]. This influx of Ca^{2+} triggers a positive increase in the membrane potential towards -70 mV. Upon reaching the -70 mV action potential threshold, fast pumping Na^+ ion pumps activate which triggers a rapid influx of Na^+ into the cell. As the action potential continues to move positively, Ca^{2+} ion pumps are triggered at -40 mV. These create an influx of Ca^{2+} ions into the cell however the rate of this influx is less than that of the Na^+ fast ion pumps. When the action potential reaches its peak, approximately +20 mV, the Na^+ channels close and K^+ channels open. The K^+ ion channels induce an efflux of K^+ ions from the cell. The Ca^{2+} influx and the K^+ efflux balance each other maintain the action potential briefly. Finally, the voltage gated Ca^{2+} close and the K^+ ion efflux continues until the resting membrane potential is once again reached. The remaining Ca^{2+} is taken up by the cardiomyocyte or pumped out of the cell.

Similarly, Na$^+$ / K$^+$ pumps continue to manage the other ions and maintain the resting membrane potential until the next action potential triggers a contraction [52,56,57].
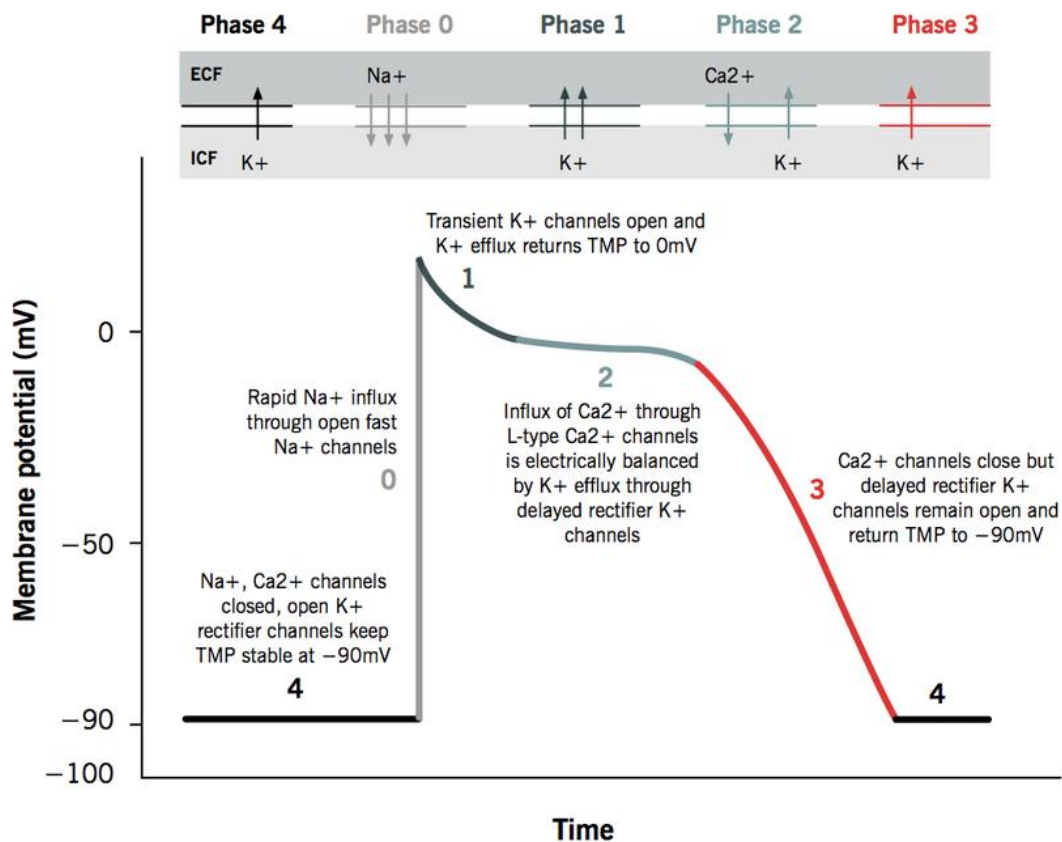
Figure 3. Graphical representation of the influx and efflux of relevant ions at across the cardiomyocyte cell membrane at each phase of the action potential propagation [58].

Of the three ions discussed above Ca^{2+} is the most important when it comes to cardiomyocyte contraction, as it is the only ion which actively participates in the contraction mechanism of the cell. The influx of Ca^{2+} is not a sufficiently high enough concentration to facilitate the necessary contractions, however the cardiomyocytes have a store of Ca^{2+} ions, which they hold in the sarcoplasmic reticulum, and the release of these ions is triggered by the influx of Ca^{2+} [59,60]. The contraction is performed using a collection of proteins bundled into myofibrils. These myofibril protein bundles run parallel to the length of the cardiomyocyte. The myofibrils are composed of four primary proteins known as actin, tropomyosin, troponin, and myosin which are laid out in a repeating pattern along the length of the myofibrils. Each individual unit is known as a sarcomere and are based on overlapping layers of actin and myosin with tropomyosin and troponin situated between each layer [61–63]. The orientation of these layers can be seen in **Figure 4** below. It is important to note at this point the myosin heads which bridge between the myosin and the actin upon which the contraction relies.
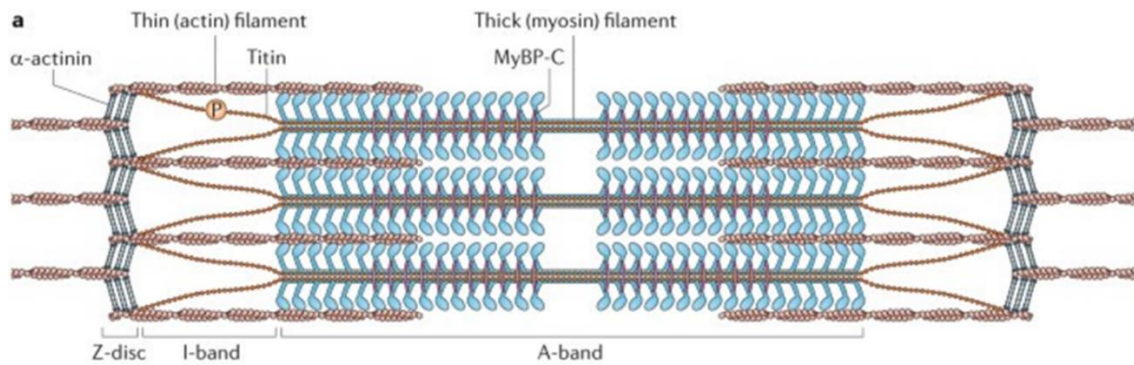
Figure 4. Schematic of sarcomere featuring the myosin filaments in blue and the actin filaments in pink. This single sarcomeric unit is repeated along the length of the myofibril. Adapted from Hwang and Sykes [64].

On the other hand, tropomyosin is wound around the actin which in the normal state blocks the myosin binding site preventing any contraction from occurring. The troponin protein is bound to the tropomyosin and is composed of three sub-units, troponin I, troponin T, and troponin C. Troponin I modulates the activity of the troponin complex through interaction with various signalling cascades in the cell, troponin T binds the troponin to the tropomyosin, and most importantly troponin C interacts with the intracellular Ca^{2+} ions [65–67]. Upon contact with the Ca^{2+} ions the troponin C triggers a conformational change in the troponin complex which triggers a subsequent conformational change in the tropomyosin, exposing the myosin binding site on actin. This available binding site leads to cross-bridging between the two filaments. Using energy provided by adenosine tri-phosphate (ATP) the myosin head switches its orientation and therefore increases the area of overlap between the myosin and actin, leading to an overall shortening in the length of the sarcomere [68–71]. As each sarcomere in the myofibril undergoes this shortening the overall effect of the cell is to contract. The myosin head releases the actin and binds to the next available binding site on the actin and uses another ATP molecule to continue the cycle. The cycling of the myosin head along the length of the actin continues to shorten the sarcomeres and hence continue to contract the cell. The cycling continues as long as the intracellular Ca^{2+} ion concentration remains high enough. The interaction of the Ca^{2+} ions provide the link between action potential and the observed contraction of the cell. As the cell undergoes the process of Ca^{2+} re-uptake and efflux the interaction between the Ca^{2+} and troponin C is no longer possible, and the troponin returns to its original state [72,73]. The tropomyosin in turn also returns to its original state, the myosin binding sites are again blocked, and the contractions cease. In summary, through a cascade of conformational changes Ca^{2+}

ions trigger myosin to pull on the actin filaments creating a contraction of the cell. This is by no means an exhaustive description of the mechanism of muscle contraction but is merely meant as a general overview of the more relevant aspects to muscle contraction with electrical stimulation in mind.

1.3.3. Primary markers

As described in section 1.3.2 there are many key proteins which are relied upon to facilitate cardiomyocyte contraction. As such cardiac troponin I and T (cTnI, cTnT) are natural markers for cardiomyocytes. The role of the cardiac troponin in an exclusively intracellular capacity makes the ideal candidates for cardiovascular cell trauma. Any evidence of these proteins in the bloodstream is a sign of cardiomyocyte damage as they are not part of any signalling mechanism within the cell and hold no extracellular role or function. This makes them ideal biomarkers for traumatic heart injuries related to cardiovascular disease such as myocardial infarctions [74–76]. Other protein biomarkers are also in clinical use for cardiovascular disease which include but is not limited to C-reactive protein (CRP), B-type natriuretic peptides (BNP), and D-dimer [77]. CRP protein is elevated in inflammatory disease such as atherosclerosis [78,79]. Typical healthy levels are considered to be 0.8 µg/ml and between 3 and 10 µg/ml are considered elevated and indicative of inflammation. CRP is strongly correlated to atherosclerosis but is not specific to the disease and may also be elevated in other inflammatory processes [80,81]. Like many biomarkers associated with heart disease, CRP is symptomatically expressed as a response to inflammation in the cardiovascular system, as opposed to being a cause of this inflammation [82,83]. BNP and its associated protein N-terminal proBNP (NT-proBNP) help to regulate blood pressure and plasma levels in order to modulate salt content and water retention [84]. Similarly to CRP it is released by cardiomyocytes undergoing hypertrophy [85,86]. Finally, D-dimer is associated with the degradation of fibrinogen. This fibrinogen breakdown is indicative of the initiation of clotting in the blood and is specifically linked to thrombus formation in cardiovascular disease. It is present in healthy blood because of the natural breakdown of these clotting factors, typically fibrin, in the bloodstream in order to prevent clots. High levels associated with cardiovascular disease are thought to be associated with large fibrin formations [87–89].

Table 1 – List of most relevant clinical protein biomarkers for cardiovascular disease.

Biomarker	Healthy	Disease
cTnI	1.8 pg/ml	> 3 pg/ml
cTnT	3.2 pg/ml	> 6.2 pg/ml
CRP	0.8 µg/ml	3 – 10 µg/ml
BNP	100 pg/ml	> 150 pg/ml
D-Dimer	< 110 ng/ml	>170 ng/ml

Proteins are the gold standard for clinical biomarkers and have been for several years. In the effort to develop more sensitive assays alternative biomarker types are being developed. One of the forerunners for the next generation of biomarkers are the microRNA sequences (miRNA). They are short sequences of single stranded non-coding RNA, typically 22 nucleotides long [90,91]. They provide a regulatory role in gene expression. Using RNA interference (RNAi) pathways miRNA supress the translation of complementary mRNA sequences in the cells cytoplasm in order to control protein expression levels in the cell [92,93]. They are attractive biomarkers targets as it has been established that miRNAs are excreted and can be detected in the bloodstream [94–96]. Studies have also correlated the concentrations of circulating miRNA to be clinically relevant in disease [97–101]. This makes them suitable biomarkers as they are clinically relevant and samples can be collected in traditional means i.e., blood drawing, meaning existing processes can be used for sample preparation on clinical miRNA assays which reach the production phase.

Due to their role in gene expression regulation miRNA are present in all cell types. Hence there is very unlikely to be a cell specific miRNA which can be a standalone marker for a given disease or symptom, such as cardiac troponin I for cardiomyocytes. However, this can be overcome using a panel-based approach, where the relative concentration of multiple miRNAs shows a stronger correlation to a specific disease rather than a single miRNA [102–104]. Modern approached such as next generation sequencing and microarray testing can facilitate the identification of such panels for further assessment as targets for clinical assays [105–108]. The diversity and distribution of miRNA sequence means there are many targets being assessed in the literature as future biomarkers for cardiovascular disease. There is no evidence to date of a commercial miRNA assay in use in a hospital setting as a point-of-care test or as a diagnostic platform for the directed treatment of patients.

To date some of the most cited miRNA sequences associated with cardiovascular disease include miR-1, miR133a, miR-208, miR-499 [109–111]. There are many more and it would be impractical to list them all in the scope of this review however several excellent reviews endeavour to compile miRNAs of interest in the cardiovascular research scene. High impact reviews such as Zhou *et al*, and Kaur *et al* provide a high-level overview and systematic review of miRNAs in cardiovascular disease research respectively and are excellent starting points for understanding the landscape as it currently stands [112,113]. Most of the current data on miRNA correlation to disease is gathered using PCR based platforms and as such much of the data is presented as relative fold change of a miRNA in a healthy *vs* disease sample. Consequently, it is difficult to find circulating miRNA concentrations using amplification-free methodology. Circulating concentration data is important for the development of direct detection, amplification-free clinical point-of-care diagnostic assays.

Table 2 – miRNA sequences related to cardiovascular disease.

miRNA	Sequence (5' – 3')	Reference
hsa-miR-1-3p	UGGAAUGUAAAGAAGUAUGUAU	Belevych *et al.* [111]
hsa-miR-133a-3p	UUUGGUCCCCUUCAACCAGCUG	Belevych *et al.* [111]
hsa-miR-208a-3p	AUAAGACGAGCAAAAAGCUUGU	Kondkar *et al.* [110]
hsa-miR-499-5p	UUAAGACUUGCAGUGAUGUUU	Kondkar *et al.* [110]

There are challenges when it comes to the use of miRNA as a biomarker. These are not always addressed in research papers intending to use and advance them as biomarkers. The primary concern is their overall stability in the environment. RNA is less stable than DNA and as such is more prone to degradation even in laboratory settings [114]. Even as synthetic RNA strands, RNA can be readily degraded by RNases and thus extreme care must be used to preserve the strands integrity [115]. Even in buffers there can be a significant challenge in preserving the RNA strand as it is more stable at a pH between 4 and 5 and is susceptible to hydrolysis in pHs greater than 6 [116]. This is further complicated by the fact that RNA does not exhibit good stability at room temperature, with a half-life of only about 30 minutes.

There are also problems with extracellular miRNA from biological sources, i.e. cell media, body fluids, cell lysis etc. Primarily the issue surrounds the chaperoning protein complex RNA-induced silencing complex (RISC) is ubiquitous with the miRNA strands within the cell. There is little understanding about the presence of RISC proteins circulating with extracellular miRNA however it is likely the association is maintained,

particularly in vesicle mediated extracellular miRNA. Hence, there is a significant challenged imposed by how these miRNAs are processed from the sample. The RISC complex significantly increase the steric hinderance involved in a miRNA target recognising a surface bound capture strand. Secondly, as was highlighted circulating miRNA are present in vesicles when present extracellularly. These lipid vesicles can vary in size and are typically denoted as extracellular vesicles which encompasses vesicles between 40 and 1000 nm in diameter, all of which have been shown to have miRNA present. This lipid vesicle vehicle poses a sample processing challenge for assays which aim to quantify miRNA from biological sources. Any method which aims to do so must balance the extraction of the miRNA for quantification with the strenuous stability concerns of unstabilised miRNAs [117,118].

2.   Cardiomyocyte research models

Developing a research model for cardiovascular disease can assist in the development of biomarker targets and drug therapies [119–121]. Outputs from these areas of research can be valuable in the clinical diagnostics and treatment, something that is invaluable for such a wide-reaching disease such as cardiovascular disease. To optimise research outputs with tangible impact on the patients suffering from cardiovascular disease a good agreement between the *in vitro* cell module and the *in vivo* cell population effected by the disease state. Hence, developing platforms which can improve the accuracy of *in vitro* cell models is very important [122–124]. A key stimulus which is essential for cardiomyocyte development, growth, and function is electrical stimulation. Below is discussed current platforms and methodologies frequently used to deliver electrical stimulation to *in vitro* cardiomyocyte culture (regardless of cell origin or animal model). Also discussed is the relative merit of the cutting-edge wireless bipolar methodology described in this thesis.

2.1. Cardiomyocytes used in research

In vitro culture of cardiomyocytes is typically conducted using one of three cell origins, however, the animal model can vary depending on the specific pathophysiology being examined i.e., murine, porcine, human, etc [125,126]. These three cell origins are primary cells, immortalised cells, and stem cells [127–129]. It is possible to obtain each of these three cell origins from any animal model required. In the case of primary cells, they are taken directly from the animal model. They are typically mature cells and have the most accurate genotype for *in vitro* cell modelling of disease. However, removing them from

their *in vivo* environment can cause genotypic and phenotypic changes which can be difficult to assess. Furthermore, they are also not suitable for passaging and continuous testing due to their mature phenotype [130]. On the contrary, immortalised cell lines are created by hybridising cell models of interest with cancer cell lines creating cells that can be passaged, however, the hybridisation process can impact the phenotype of the cells. Typically cells also present immature or foetal phenotypes which may not be appropriate for certain areas of study, particularly in those cases were the cell model is reproducing a mature phenotype *in vivo* [131,132]. Finally, stem cells can be taken from foetal stem cell populations or induced from other cell lineages. They are frequently used because of the control researchers can have in inducing disease models, specifically those with genetic components. They are also useful for elucidating the effect of development on pathophysiology or the effect of pathophysiology on development. The disadvantage of stem cell models is the immaturity of the cells can impact the genotype of the cell model such that it no longer represents the *in vivo* genotype. A strong understanding of the developmental pathway of the cell lineage required is necessary. Additionally, there is disagreement in the community about the accuracy of cells cultured *in vitro* in a 2D environment may not represent well *in vivo* native cells [133,134].

2.2. Electrical simulation

Electrical stimulation is the application of an electrical current to cells which can be applied *in vivo* or *in vitro,* however all methodologies described here in Section 2.2 will focus on *in vitro* application of electrical stimulation. The majority of *in vivo* electrical stimulation focuses on the electroceutical application of current to muscle grouping in the body, for example pace-makers in the heart [135–137]. Research which focuses on implementing electrical stimulation typically cite the current density, frequency, pulse duration, and total stimulation time when outlining the parameters used in electrical stimulation of *in vitro* cultures.

2.2.1. Methods

Before discussing the stimulation methodologies used for the electrical stimulation of cardiomyocytes, it must first be noted that the majority of experiments described in the literature, particularly in relation to tissue engineering, omit electrical stimulation from the experimental parameters altogether. A systematic review by Scott *et al.* [138] from June of 2022 is quoted as saying "stimulation has a key role in the growth, development,

maintenance, and even dysfunction of cardiac muscle — which is why the absence of electrical stimulation in the majority of cardiac [tissue engineering] cannot be overstated".

There are primarily three methods used for delivering a stimulating current to cardiomyocyte cultures *in vitro*. First is direct coupling whereby the cells, typically in an organelle, or the scaffold is directly coupled to a programable power supply to deliver the electrical stimulation to the cells. Currently direct coupling is most used in the biowire system [139]. Cardiomyocytes are cultured on a synthetic scaffold which is directly connected to a power supply using platinum wire. This method is very successful as culturing cardiomyocytes which have been mechanically induced orientation and a more 3D culture environment when compared to traditional 2D culture methods. While direct coupling is often described as the most effective method of electrical stimulation it is not frequently used in the literature likely because developing the direct coupling interface between either scaffold or cells in more difficult.

The second method of electrical stimulation of cardiomyocytes in culture is capacitive coupling, whereby the conductive properties of the media is used to apply a current to cells being cultured in the media using a pair of driving electrodes. Much of the work using capacitive electrical stimulation is dominated by research in hydrogel. Hydrogels are a crosslinked polymer matrix capable of holding a large volume of water making them suitable as a cell culture scaffold [140,141]. The hydrogels are used to support cell organoids, a recent advance in cell culture, whereby stem cells are grown into a co-culture tissue, which mimics the environment of an organ in a 3D environment [142]. Hydrogels can also be used to culture spheroids or microtissues which are 3D cell cultures similar to an organoid, but often focusing on a subset of cell types or a specific organ phenotype. The hydrogel acts as a scaffold to support the cells and its physical properties can be tuned for specific parameters such as stiffness or conductivity by varying the hydrogels constituents. Work by Li *et al.* [143] describes the successful stimulation of heart organoids using a hydrogel containing polydopamine and reduced graphene-oxide as the polymer material. The properties of the material allowed the organoids to be stimulated and the contractions recorded. However, the stimulation parameters of the system are limited with respect to the effect of stimulation of the cell culture. There is a limited attempt to fully elucidate the effect of the stimulation and interaction of the cells with the electrical stimulation. Only the frequency is varied, and most of the discussion focuses solely on the impact of the polydopamine and reduced graphene oxide concentrations. The work does offer exceptional images and video of the culture's contractions. The characterisation of the cells is detailed with respect to the variation of polydopamine and reduced graphene oxide concentration. Zhang *et al.* [144]

also conducted research into the electrical stimulation of rat neonatal cardiomyocytes for the purposes of maturation using a gelatin-based hydrogel. Once again in this work the only parameter varied in the electrical stimulation was the frequency. A 2 millisecond (ms) rectangular biphasic pulse was applied across all frequencies assessed. Elucidating the impact of the stimulation on the maturation of the cells in culture, however, is done in detail, and the genotypic assessment of expression changes in the cells in the stimulated vs unstimulated conditions is a useful guide for the application of electrical stimulation for maturation of cells in culture. Of those papers which apply capacitive electrical stimulation to the cells in culture, very few aim to characterise or understand the perceived potential of the cells I culture given they are not in contact with the electrodes. In other work by Zhang *et al.* [145] where they describe a heart-on-a-chip fabrication they devote significantly more attention to the potential field distribution of the platform. This is done through modelling of the field distribution for the stimulation of cardiomyocyte cells which are cultured in a microfluidic chip environment.

The final method for electrical stimulation of cardiomyocytes is inductively coupled electrical stimulation. This method is frequently cited by review articles as a means to introduce electrical stimulation to cells in culture, however, functionally it is rarely used in experimental work [146–149]. Be placing the cell culture into a coiled wire and using an alternating current in the wire to induce an electromagnetic potential field at the cells in culture. Like due to the extreme specialisation, unwieldy culture protocols, and limited applicability this technique is rarely seen and does not appear to have been used for the electrical stimulation of cardiomyocytes to date in the literature.

2.2.2. Electrical Stimulation Application

Electrical stimulation is applied to cells who typically require an electrical stimulation in vivo. These are cell lineages such as cardiomyocytes, smooth muscles cells, and neurons where electrical stimulation is important for cell maturation and function [38,150–154]. Cardiomyocytes require electrical stimulation for correct phenotypic growth and maturation [155–157]. Electrical stimulation is also used to induce myopathic pathologies in vitro [158]. Inducing hypertrophy in monocellular and pluricellular cultures allows the study of microenvironments and dysregulation within the cells as they would experience in vivo. Applications beyond cardiomyocytes include studying the reaction of skeletal muscle cells to drugs from medical trials [159,160]. This involves characterising the contractile variances in the presence or absence of different drug molecules used to alleviate diseases such as muscular atrophy. Electrical stimulation of neurons is used to

study the growth and response of neuron to electric fields. This electrical stimulation could be used in future to induces cell growth in injured brain tissue [161,162].

Conventionally, cells are stimulated using direct stimulation. Direct electrical stimulation involves the driving electrodes being introduced directly to the cell culture. An electric field is induced between the driving electrodes. In the way the electric field is induced does not significantly differ from the driving electrodes in the bipolar electrochemical stimulation platform. However, the cells are not cultured on a conductive substrate, instead they are grown on traditional culture surfaces such as the bottom of a polystyrene cell plate or a microscope slide. The surface does not impact the stimulation and is typically limited by the application of the experimental protocol being used. The disadvantage of this direct electrostimulation is that there is a necessity of wires to be introduced to the cell culture media which brings with it an increased risk of contamination. The method is also further disadvantaged by the fact that traditional cell culture equipment such as Petri dishes and cell culture plates are not readily adaptable to accept driving electrodes and the accompanying wiring. Petri dishes provide a greater degree of space; however, they do not allow for high throughput culture. Alternatively, using cell culture plates allows for culturing of independent cell populations in parallel but the small size of the wells makes adding driving electrodes challenging.

The objective of this work is to address the issue of cell culture with independent cells using electrical stimulation in parallel. Using parallel cells within a single stimulation platform allows for simultaneous stimulation of cultures. Using bipolar electrochemistry also allows the cells to be cultured directly on an electrode surface in the presence of extracellular matrix protein. High throughput electrical stimulation using convenient layouts with no wires directly impacting the cells in culture would improve the integration of electrical stimulation in experimental protocols across cell lines such as skeletal muscle, neuronal, and cardiomyocytes.

2.2.3. Wireless Bipolar electrostimulation – overview and advantage

This work takes advantage of the electrochemical principle of bipolar electrochemistry. The technique has existed in the literature for decades and now has seen its applications spread to interdisciplinary fields which take advantage of its inherent bipolar characteristics and the wireless nature bipolar electrode at the centre of the technique [163,164]. When applied as described in the following working chapters the technique can offer the best of both direct coupling, and capacitive coupling electrical stimulation [165]. Allowing direct contact of the stimulating electrode to the cells, reducing the potential to

induce an action potential in the cells, while also maintaining the convenience and benefits of a wireless system, as the bipolar electrode does not require a direct connection to the driving electrode on the power supply to generate an electrical potential.
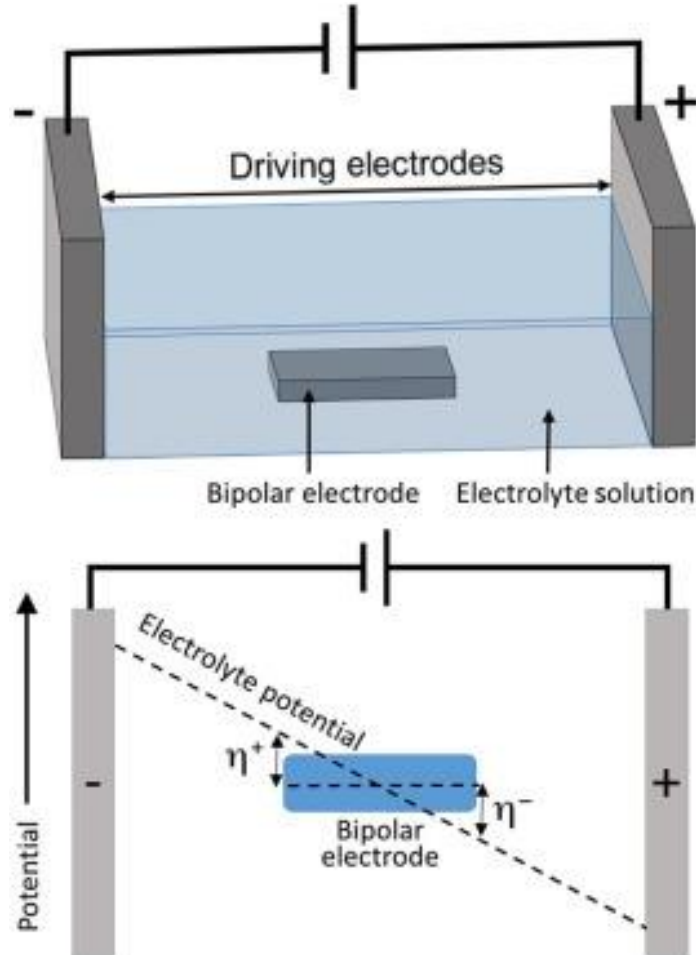
Figure 5. Schematic representation of (upper) the typical bipolar electrochemical configuration showing conductive material in the centre of the channel with anodic and cathodic driving electrode and the electrolyte filling the channel and (lower) potential field distribution in the channel between the driving electrodes. Note the interfacial overpotential at the poles of the bipolar electrode and the reversal of the pole charge compared to the driving electrode [166].

The general technique, regardless of applications, is as follows for the general wireless bipolar electrochemical principals. A conductive material is placed between two driving electrodes in a suitable electrolyte. The conductive material, electrolyte, and driving electrode material can vary depending on the applications of the technique. Cell culture media is a possible electrolyte for wireless bipolar electrochemistry. When a potential is applied to the driving electrodes, a linear potential field gradient is generated between the two driving electrodes. The conducting material maintains a single potential along its

length, this potential relative to the potential filed gradient creates an interfacial potential between the conductive material and the electrolyte and at this point is considered to be a bipolar electrode [164,166,167]. The interfacial potential at the bipolar electrodes surface is in a gradient with zero potential at the centre point of the electrode's length and the greatest interfacial potential at the farthest ends, known as poles. The closest to the cathodic driving electrode acts as an anodic pole and the pole closest to the anodic driving electrode acts as a cathodic pole. The relationship between the absolute interfacial potential at each pole is described by the following equation:

$$\Delta E_{elec} \ = \ E_{tot} \ \left(\frac{l_{elec}}{l_{channel}} \right) \tag{1}$$

Equation 1 shows that the interfacial potential of the bipolar electrode (ΔE_{elec}) is primarily dictated by the total electrical potential applied by the driving electrodes across the channel (E_{tot}) and is also dependent on the relative length of the bipolar electrode (l_{elec}) to the length of the channel ($l_{channel}$) [164,168,169]. This model does not account for potential lost at the diving electrode and electrolyte interface. When E_{tot} is sufficiently great, the interfacial potential at the pole of the bipolar electrode may become sufficient to reach the overpotential of a redox species in the electrolyte and a faradaic reaction can occur, dependent on kinetics of the species. To maintain the electroneutrality of the bipolar electrode the anodic and cathodic processes are coupled and the faradaic reaction of the can only occur when the overpotential of the reduction and oxidation is reached. By this coupled reaction a flow of electrons is present in the electrode material from the anodic to the cathodic pole of the bipolar electrode. This current flow is not considered in this work as a coupled faradaic reaction is not necessary for the purpose of electrical stimulation. It is the interfacial potential and its interaction with the cells on the wireless bipolar electrodes conductive surface which is necessary for the successful electrical stimulation of the cells [165]. It is important to note at this point that the exact mechanism or pathway by which an environmental potential field induces electrical stimulation is unclear and not well understood however, the benefits and impacts of the electrical stimulation are demonstrated in a variety of literature [170,171].

2.2.4. Implementation and assessment of cell stimulation

Perhaps the most used cell culture exposed to electrical stimulation during experimentation is the stem cells. Stem cells, also known as progenitor cells, are a class of undifferentiated cells which when provided the appropriate stimulus differentiate into a certain cell lineage. Typically, research focuses on the foetal stem cell, which

elucidates many of developmental function of cell pathways. However, adult progenitor stem cells which can be present in certain organelles. It can often be difficult to isolate and confirm the presence, function, and pathology of these stem cells in certain orans or tissues which makes their study difficult [172,173]. While the methods of obtaining cardiac stem cells are numerous and each method and lineage has their own merits and drawbacks, the focus here is on the use and feasibility of stimulation in those studies which apply them. There are excellent reviews on the subject, both succinct and exhaustive, such as those by Matsa *et al.* and Hou *et al* [174] which cover in detail the topic of cardiac stem cells and their use in various fields of research.

The use of electrical stimulation has been shown to promote the development of sarcomeres in the immature cells [175,176]. Much of this research is conducted twenty years ago and yet does not get incorporated into *in vitro* cells models of primary cells with any consistency. A large number of studies have been conducted in the past on neonatal cardiomyocytes as the need for maturation provides a greater differentiation between stimulated and unstimulated cultures [177,178]. These works have highlighted the importance of electrical stimulation beyond that of intracellular organisation but also in the genetic expression levels across key genes. The impact of electrical stimulation was seen in a variety of ways including mitochondrial activity, muscle specific proteins such as adenylosuccinate synthetase 1 (ADSS1), as well as connexin 45 (CX45), reduced action potential duration, and overall cell morphology (length to width ratio) were all significantly impacted by electrical stimulation [37,176,179,180].

The electrical stimulation of primary cell lines is also used in studies focused on identifying the impact of different factors on cardiomyocyte *in vitro*. These studies are less common than those looking to optimise the maturation of foetal cardiomyocytes however they illustrate the necessity for electrical stimulation in cardiomyocyte research regardless of research area. Studies, such as Hoebart *et al.* [181] examination into the role of transient receptor potential ankyrin 1 (TRPA1) in cardiomyocytes, require the use of electrical stimulation and reinforce the importance of the stimuli in order to evaluate the contributions of proteins of interest more accurately.

Wireless bipolar electrochemical techniques have recently been used for the electrical stimulation of cell cultures. The Gordon Wallace group showed the effective stimulation of PC12 neuronal cells by demonstrating the increased dendritic formation of the cells cultured on a wireless bipolar electrode. The cells who were grown on the electrode substrate and subjected to wireless bipolar electrical stimulation demonstrated

increased dendritic formations than those cells which did not receive the electrical stimulation [165].

2.3. Nucleic acid detection

Molecular genetics are an essential way to characterise cells. They are also essential to all pathways of protein production within a cell. Therefore, they are involved in many aspects of disease progression. Nucleic acid screening is an important research tool when it comes to elucidating the impact of a given stimulus on the biological system of interest [182–184]. Researchers can explore deviations in regulation using nucleic acid detection. Most frequently nucleic acid quantification in experimental studies and disease research as a whole is performed using polymerase chain reaction (PCR). This technique is widely used and is considered the gold standard for nucleic acid quantification [185,186]. Alternative methods involving electrochemical biosensors for nucleic acid detection are being developed which prioritise direct detection of the nucleic acid strands without the need of any amplification steps. Thus, the relative merits of both PCR and direct detection of nucleic acids will be discussed in the following section with a specific focus on miRNA.

2.3.1. PCR

PCR is a diverse nucleic acid detection method which has a wide range of application in molecular genetics. The technique uses the same building blocks as the cell to replicate a specific sequence of nucleic acid. Depending on the processing techniques, PCR can effectively amplify both DNA and RNA sequences [187]. A primer is used to select the miRNA sequence of interest. The most common primer design is a stem-loop design, where one end of the stem primer is complementary to the miRNA sequence [188,189]. Reverse transcription extends the stem-loop primer complementary to the miRNA overhang creating a complementary DNA (cDNA) sequence. Heat denaturing is used to split the strands and generate a linear nucleic acid sequence. The miRNA is released to begin the next cycle. A forward primer, complementary to the cDNA formed from the reverse transcription of the miRNA to ensure specificity, hybridises with the extended stem-loop probe. Polymerisation then occurs to generate a complementary cDNA copy of the stem-loop sequence. A second heat denaturing cycle is performed which releases the stem-loop primer to become involved in the next cycle. Finally, a reverse and probe primers hybridise with the cDNA and polymerisation takes place. This polymerisation

degrades the probe and the quencher and probe separate allowing the emission of the fluorescent probe [190–192]. The relative fluorescent unit emitted by the probes through each cycle is then correlated to a miRNA concentration, these steps are visualised in **Figure 6**. The short nucleotide length of miRNA makes primer design difficult especially considering primer fidelity and specificity dictate the overall sensitivity of the assay. Amplification techniques such as RT-qPCR and its variations make it difficult to correlate the fluorescent signal generated to an absolute concentration of miRNA, either in moles or copy number, as the amplification does not allow such a specific correlation [193]. This makes RT-qPCR a semi-quantitative assay with most experimental work using this technique citing the results as relative expression instead of concentration [194,195]. This is useful for analytical assays, in particular elucidating the effect of drug treatments, etc., however in a clinical setting where the differentiation of disease versus healthy sample miRNA concentrations may be small the ultra-sensitive direct detection of miRNAs is preferable. The use of PCR as the gold standard for miRNA quantification to date makes it difficult to determine accurate circulating concentrations of relevant miRNAs to establish optimal standard curves and limits of detection for the development of clinical assays using direct detection methodologies.
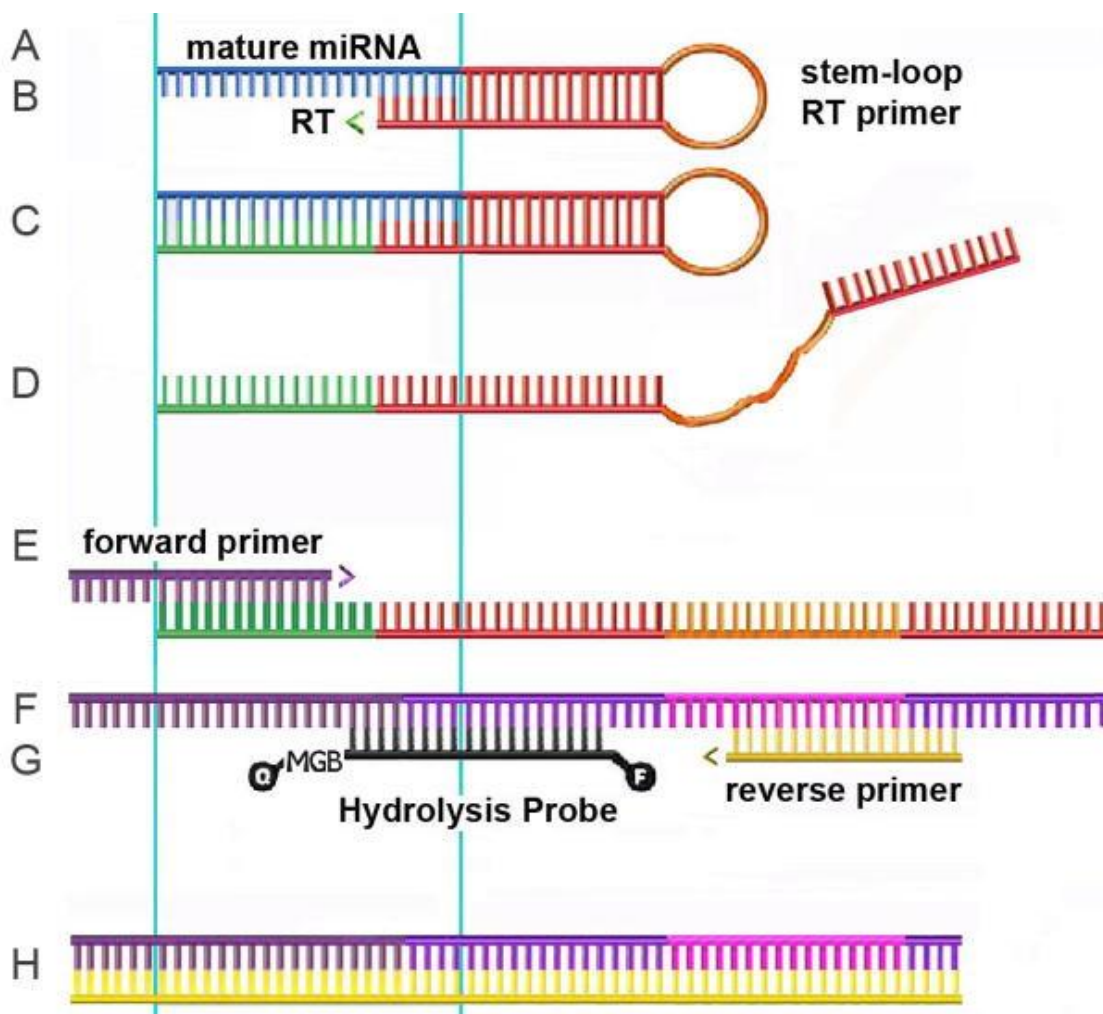
Figure 6. Stepwise approach to stem-loop RT-qPCR detailing A) miRNA hybridisation, B) reverse transcription of the primer, C) completion of the stem-loop, D) denaturing of the stem-loop with release of target miRNA to repeat the cycle, E) hybridisation of forward primer and polymerisation, F) followed by denaturing, G) hybridisation of reverse primer and probe which is followed by a polymerisation initiated by the reverse primer, and H) final PCR product [196].

2.3.2. Electrochemical biosensors - miRNA

There are a wide variety of miRNA sensor which use every detection method available in the literature to generate a signal. To discuss them all would fall beyond the scope of this review. Therefore, for the final section a review of miRNA assays which employ an electrochemical detection method will be discussed as these are the most relevant to the work detailed in this thesis.

Electrochemical miRNA biosensors typical focus on three areas to develop a specific and sensitive assay. The first is the electrode material surface on which the assay is constructed. The assay surface will dictate the immobilisation method used for the

capture element for the assay. Metallic electrodes offer multiple ways of immobilising capture elements to its surfaces. Thiol binding is useful as it will form a self-assembled monolayer which can orientate and disperse capture elements on the electrode surface [197–199]. Surface modification of electrodes also allows alternative electrode substrates to be used such as glassy carbon and thin film electrode; gold electrodes can also be modified [200–202]. Single-use and disposable electrodes are a useful substrate for assays with an eye to commercial diagnostic assays. Development of flexible, versatile, and disposable screen-printed electrode materials offer and attractive platform for electrochemical miRNA assays [203–206]. The second is the capture element itself. This is typically a nucleic acid sequence which contains a complementary sequence to the target miRNA, although the length of them capture sequence may vary in order to facilitate the chosen signalling pathway [207–209]. The final is the aforementioned signalling pathway. In the case of electrochemical biosensors this can be a variety of methods such as electrochemical impedance spectroscopy (EIS) where changes in resistance elements in the electrochemical circuit of the assay which are attributed to the target miRNAs presence or absence are used as the signal, chronoamperometry where the current from a faradaic reaction attributed to the probe element is measured at a single potential in order to generate a correlation to the concentration of the target miRNA, and voltammetry where probe generates a faradaic current which is measured by varying the potential and recording the current at each point [210–212]. Each of these three elements effect the selectivity of the assay and the sensitivity of the assay. As has been mentioned previously it is exceedingly difficult to determine an absolute concentration of circulating miRNA in whole blood, serum, or plasma to generate a biologically relevant range around which to design the assay [213,214]. Therefore, work conducted on electrochemical assays typically focus on describing novel platform designs and pushing the limit of detection as low as possible.

Screen-printed electrodes refer to the fabrication method of the electrode material. A template screen is used to outline the area for the ink to be extruded through the screen onto the supporting substrate [215,216]. Once the ink had been deposited on the substrate it is cured in the oven to dry and bind. By printing in a layered fashion, it is possible to design complex electrode configurations which include multiple electrode compositions. Using this layering method a complete electrode array including a working electrode, reference electrode, and a counter electrode can be produced. Increasing the number of templates on the screen facilitates the mass productions of electrodes. Tailoring the ink compositions and the screen templates allows electrochemical and physical characteristics of the electrodes to be tuned for the desired applications [217–219].

Electrochemical characteristics such as resistance/conductivity, electroactivity/inertness, and surface functionality call been tuned by ink altering the inks composition [220,221]. Physical characteristic such as electrode shape, working area, and multiplexing can be tuned by manipulating the screen template.

Screen-printed electrode-based sensors for miRNA have become popular because of the benefits outlined above. Ink composition is a key design feature when developing an electrochemical biosensor. The choice of ink composition dictates what further processing steps are required for capture element immobilisation. Carbon inks are the most common electrode substrate for screen-printed electrodes. The inks can be purchased commercially or be developed in-house for specific applications. Due to intellectual property rights the exact formulations, whether in-house or commercial, are rarely described. However, the general formulation includes carbon black for conductivity, graphene, or graphite, to modify the conductivity, and a binder to provide structure to the ink. The binder also controls viscosity which is important for printing. Solvents can be used to ensure even distribution of components throughout the ink and also to adjust the ink viscosity [222–224]. Smith *et al.* [225] modified the carbon electrode with ANSA in order to facilitate amine modified capture RNA modification. This work used reductive and oxidative chronocoulometry to determine the presence and absence of the miRNA target. The charge observed was lower when the target miRNA was hybridised with the capture and the peak charge could be correlated to miRNA concentration. This used a urine sample matrix for miR-21, a miRNA associated with diabetic kidney disease (DKD). While it describes a facile way of carbon surface modification using commercially available products it does require a lot of sample processing prior to analysis. The urine sample were treated using protein kinase K and a size exclusion filter, the sample was also heat treated to 50 °C. They also determined that the assay was sensitive to protein interference, specifically bovine serum albumin (BSA).

One of the most attractive methods of miRNA detection using screen-printed electrodes is EIS. It is most frequently conducted without the need for labelling of a probe. Congur and Erdem [226] recently published an impedance-based screen-printed electrode assay. They used a second-generation poly(amidoamine) (PAMAM) dendrimer with 1,4-diaminobutane core (G2-PS) adsorbed to the screen-printed electrode surface. The probe DNA was functionalised to the dendrimers of the cores. They used impedance spectroscopy to characterise the electrode surface during each modification step and as a means to detect the concentration dependent presence of the miRNA target. While the G2-PS represents a novel method of surface modification for screen-printed electrode the assay does encounter issues. While the paper cites good linearity of the assay (R^2

= 0.9903) the assay suffers from reproducibility with large standard deviations at each point.

Issues with standard deviation of standard curves plague miRNA electrochemical assays regardless of spectroscopy used for signal generation. Pothipor *et al.* [227] used square wave voltammetry and three individual redox probes; anthraquinone, methylene blue, and polydopamine. The screen-printed design featured a working electrode area for each of the three probes on a single printed platform. While each redox probe showed excellent separation on the square-wave voltammogram however the calibration curve for all three target redox probes did not show good reproducibility across the linear range.

Some assays have shown good reproducibility using electrochemical methods, such as Cardoso *et al.* [228]. They used both square-wave and EIS techniques to verify the sensitivity and selectivity of their assay. The variation in the observed current and electron transfer resistance, respectively, at low concentrations was greater than at the higher concentrations. While a strong correlation coefficient was strong for both assays the standard curve using the square-wave voltammetry method did show lower overall standard deviation than that of the EIS generated data. The issue remains that these assays are conducted over a broad concentration range which does not necessarily reflect biologically relevant circulating miRNA in diseased versus healthy cohorts. The good correlation over a broad concentration range does not inherently confer robustness over what is likely a much narrow relevant concentration range which would be necessary for diagnostic testing. This will continue to be an issue with amplification-free miRNA quantification techniques until robust and varied data is presented on circulating miRNA. This is essential as the relevant concentrations will likely change over based on the miRNA of interest and the disease used in the study.

To date there is no evidence of screen-printed electrodes being used for the electrochemical detection of miR-1. However, there have been screen-printed electrodes described to detect other miRNAs. These miRNAs include miRNA-34a, miRNA-15a, and miRNA-21 have all been documented as being detected using screen-printed electrodes [229–231]. There is no available literature as of this work which describes the use of a screen-printed electrode for the electrochemical detection of miRNAs which are specifically involved in cardiovascular disease. Instead reviews show that electrochemical assays based on screen-printed electrodes which target cardiac biomarkers overwhelming focus on protein targets and thus it remains an area for further research. Therefore, the objective of this work is to describe an electrochemical method using screen-printed electrodes for the detection of cardiac miRNAs. While the

fundamental methodologies of nucleic acid-based capture elements should be transferable to a wide variety of miRNA sequences, it is possible that variations in nucleic acid sequences such as guanine/cytosine contents which can affect the ΔG of the sequence and hence the binding affinity to its complementary sequence which would subsequently impact the assays sensitivity.

3.   Conclusion

As the pressure of cardiovascular disease increases on the global mortality rate, it is clear that research into diagnostic, prevention, and treatment will be essential for improving patient outcomes. To improve our understanding and development of reliable, reproducible, and accurate cell models are required to facilitate biologically relevant *in vitro* data. A key component in this will be the addition of electrical stimulation to cells *in vitro*, regardless of application or cell origin. This cell stimulation is often missing from contemporary cardiac research which, in the opinion of this author and others in the field, is a significant omission from the models currently in use. Electrical stimulation impacts crucial factors such as developmental phase, morphology, gene expression, and cell orientation among other aspects as thus its importance cannot be overlooked or overstated.

As discussed in the review above there are many existing methods of electrical stimulation each with advantages and disadvantages for the user. It is proposed here that the relative merits of bipolar electrochemistry have been outlined and defined such that it offers an attractive platform for future cardiovascular disease research. Wireless bipolar electrochemistry can be adapted to parallel existing laboratory procedures with regards to cardiovascular disease research. It can also be utilised in a simple manner such as in capacitive stimulation methodologies and should not require expensive equipment or expertise to operate. Sound fundamentals and understanding provided by decades of electrochemical research means that parameter variation can be applied maximising research impact and optimising experimental conditions.

As research methods advance and insights provided by *in vitro* models under electrical stimulation become more impactful, the scope of cell model research can be expanded significantly to novel methods for disease diagnosis. As with all disease finding, elucidating, and corroborating novel biomarkers is a key area for advancement which offers attractive benefits and may hold the key for significant improvement in patient outcomes. Since its discovery miRNAs have taken leaps and bounds to become an

attractive source of novel biomarkers. While their ubiquity across cell types poses an initial problem for disease correlation, this will most likely be overcome using multiplexing methodology and miRNA panels for disease diagnosis and prognosis. For this purpose, screen-printed electrodes offer a versatile substrate to facilitate multiplexing via multiple working electrode surfaces or through signal separation.

A concerted approach is required to provide the necessary data to increase the impact of cardiovascular disease research when focusing on miRNA. The publishing of circulating miRNA concentrations for key miRNAs involved in cardiovascular disease, such as miR-1, miR-133, and miR-499 as discussed in this review, to facilitate the development of impactful and applicable diagnostic assays. The ability to construct a diagnostic assay around statistically generated biologically relevant concentration ranges is paramount. Furthermore, when *in vitro* cell culture is required for research purposes, it is essential that electrical stimulation, with biologically relevant parameters, should be used for rigorous and robust data collection with meaningful correlation to *in vivo* conditions.

For the reasons outlined in review the following work is focused on the electrical stimulation of cardiomyocytes through wireless bipolar methodology and the subsequent electrochemical amplification-free ultrasensitive detections of miRNA related to CVD. It is hoped that the outcomes and results described within constitute an impactful contribution to the field of cardiovascular research.

Chapter 2

Electrochemical and Surface Characterisation of Electrochemically Polymerised Polypyrrole-Dextran Sulfate-Fibronectin Films on Fluorine-Doped Tin Oxide Glass

1.   Introduction

Electroceuticals are medical treatments for disease which work to by generating an electrical potential and/or current in order to treat or prevent illness [232,233]. They have seen a recent boom in research interest as the miniaturisation of electronic components alongside advances in biocompatible materials makes them a viable treatment for a variety of illnesses. In recent years technological advances in electronics miniaturisation and conductive materials have led to a steady increase in electroceutical application [234,235]. The next great hurdle to be faced is to limit the invasiveness of these treatments [236]. A useful and important aspect of this will be the application of wireless technologies [237]. This removes the need of wiring to be inserted subcutaneously into the body during the implantation. This must be achieved through development of a conductive electrode material which can simultaneously support and integrate into a biological system. This work aims to address this need and describe an electrode material which can meet all the electrochemical and physical requirements of a bipolar electrode suitable for biological systems.

The use of electrical devices implanted in the body is not a new one [238]. One thing they all currently have in common is the requirement for a wired circuit between the control system and potential generator and the electrode where the application is applied. This is the case with two of the most familiar electroceuticals in modern day medicine, the pacemaker, and the cochlear implant. Both the former and the latter consists of a generator and control system implanted in the patient. Electrical leads are threaded through the body. In the former through the venous system, and the latter through the ear canal. The end of the circuit involves the application of a potential through electrodes placed at the necessary site to stimulate a response. These electroceuticals target the cardiac smooth muscle cells of the heart and the auditory nerve of the ear respectively [239–243].

Development of electroceuticals capable of electrical stimulation of cells can also be applied to in vitro cell culture. The correct stimulation of cells in culture is essential for a variety of applications, including cell modelling of differentiated cells, and stem cell differentiation [244,245]. These are essential for good cell models for contractile cells such as muscle cells and cells which require an action potential for normal function such as neuronal cells [246]. Cells are known to change their genetic expression in the presence of electrical stimulation and that's why electrical stimulation is also an important tool for stem cell differentiation.

To remove the necessity for the culture of cells to be directly in the electrical circuit creates a more dynamic platform for cell stimulation. The ability to generate a potential at a conductive substrate using wireless electrochemistry has been understood for years [247,248]. Using a method known as bipolar electrochemistry it is possible to induce a potential in a conductive substrate **without direct connection to a power supply**. This wireless technology opens a range of applications in the field of cell stimulation. Bipolar electrochemistry is electrochemistry performed using an electrically conductive electrode substrate which is polarised in an electric field created by a potential difference between two or more driving electrode. The electrode is placed in an electrolyte between the driving electrodes and the potential difference between the electrolyte and the bipolar electrode induces potentials in the bipolar electrode. This potential is greatest at the poles of the bipolar electrode. Given a sufficiently high potential difference between the driving electrodes, it is possible to drive oxidation and reduction reactions at the bipolar electrode. Bipolar electrochemistry is considered wireless as no direct electrical connection to the bipolar electrode is required to drive the redox reactions. It has been available as an electrochemical technique for decades and has enjoyed a resurgence in recent years particularly in the field of biosensors [169]. The simultaneous anodic and cathodic poles provide an effective means for sensing and reporting with the use of multiple electrodes.
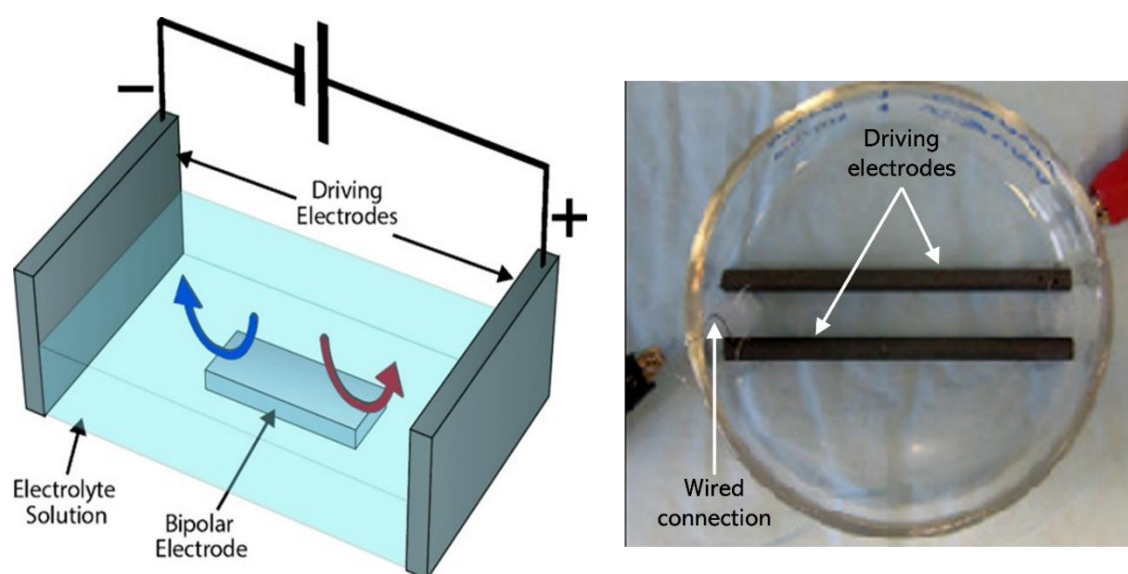
Figure 7. Graphical representation of the key differences between the proposed wireless bipolar set up (left) featuring a bipolar electrode surface where cells can be stimulated without a direct wired connection to the power supply, and a traditional wired electrical stimulation set up (right)

for a cardiomyocyte culture where wire form a direct connection between the power supply and the cull culture.

The most common method for wired systems for cell stimulation requires the introduction of two driving electrodes to the cell culture as shown in **Figure 7**. The cells are grown on their traditional cell surface with adhesion proteins present. These are typically glass coverslips and polystyrene culture materials, either flasks or well plates. The electrodes are typically made from glassy carbon or platinum [249,250]. Their shape can vary by application although they are typically rods or sheets as these are the most convenient. The driving electrodes are then connected, generally with platinum wire directly from the culture to the power supply. A potential difference is placed on the driving electrodes and the cells are stimulated in this manner. While a wired system of cell stimulation can be convenient at times for simple stimulation purposes, there can be significant drawbacks. The primary drawback of the wired set up is that the traditional wired connection for cell stimulation does not offer innovation towards the electroceutical applications of electrical stimulation of cells in vitro and is a restrictive pathway to protocol development [165]. It often requires complicated set up and relies on the medication of existing cell culture materials such as the flasks, petri dishes, and well plates. The wires must be carefully sterilised and cause inconvenience when working with cells. Cell culture requires constant monitoring and feeding of the cells in culture and a wired connection can make this difficult and cumbersome.

To improve the design and functionality of electrostimulation techniques with a focus on applications beyond in vitro work and into electroceuticals a bipolar electrode surface must be developed and characterised. To do this, a Polypyrrole film co-doped with dextran sulphate was chosen, a material which is known for its electrochemical properties and its suitability in a biological environment [165,251,252]. PPy films require co-doping and dextran sulphate was chosen as the anion to stabilise the film while avoiding introducing potentially toxic compounds which may impact the viability of cells in the presence of the film [253,254]. To optimise the electrode for future biological work, the PPy-DS film was also co-doped with fibronectin, the extracellular matrix protein required for cardiomyocyte adhesion to occur. The net positive charge of the PPy polymer allows for the incorporation of biological materials such as dextran sulphate (an anionic polysaccharide) and fibronectin (a polyampholytic polypeptide) to be incorporated during polymerisation process. This is shown to occur in the literature and the co-doped counterions are incorporated through adsorption and subsequent entrapment as the PPy film is formed [255–257]. In this case the aim is to incorporate these co-dopants to have dual functionality. The counterions also play an important role in the oxidation and reduction

53

of the PPy film. The role is typically provided by anions within the electrolyte solution. During deposition the polypyrrole backbone has a net positive charge and thus necessitates the incorporation of negatively charged anions. The oxidation of the polypyrrole film further necessitates the influx of anions to balance the charge. Upon reduction there is a reciprocal efflux of the anions to balance the charge once again. The oxidation and reduction of polypyrrole is shown below, where X^- are anions. In this use case the dextran sulphate and fibronectin provide the charge balancing negative charge during polymer oxidation.
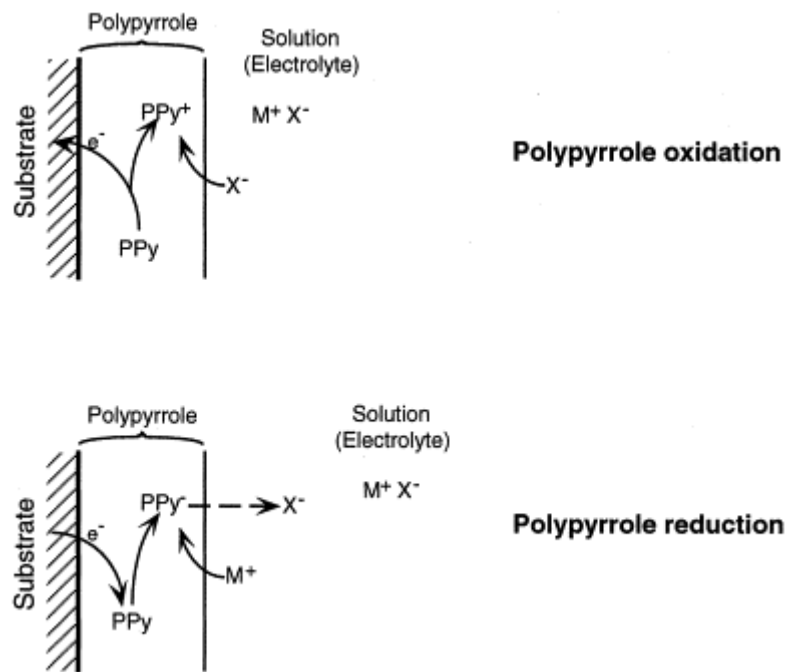
Figure 8. Schematic representation of ion charge compensation during oxidation and reduction of a polypyrrole film [258].

Fibronectin is a necessary component of the film's composition. Many cell lines require the presence of extra cellular matrix proteins to facilitate their adhesion to surfaces. It is common practice in the cell culture protocols to coat the surface of the culture vessels with the extracellular matrix proteins required for that given cell line. There is a variety of proteins which make up the ECM however cells are typically grown in the presence of one or two in in vitro culture. The ECM proteins used varies from cell type to cell based on literature for each cell lineage, development stage, and application. Cells bind to the ECM proteins at cell binding sites in the proteins tertiary structure. This binding is facilitated by integrins, which are trans-membrane proteins, and create adherence to the surface through this protein binding. Protein binding is essential for cells which require a fixed substrate to grow, these cells are known as adherent cell lines. Adherence to ECM molecules is essential because it provides orientation for the cell as it grows, this

is important in contractile cell lines such as smooth muscle cells as the contraction in a single plane is essential for function. It also triggers signalling pathways in the cell which are necessary for developing or maintain a certain phenotype. Again, smooth muscle cells are an example of this as the structure of the cytoskeleton and maturation of the sarcomeres is, in part, triggered be presence of the ECM. Without these proteins present the cell does not display required phenotypic traits which are essential for in vitro cell modelling and may not adhere or grow at all in their absence.

The counter ions are required in the PPy film to balance the charge and therefore stabilise the film as a whole, however it is possible to select the co-dopants to also maximise the films suitability for biological systems. The electrochemical performance of the film is necessary to accommodate the bipolar system. As mentioned above the bipolar electrode must be conductive to function in its role as a bipolar electrode. The development of a PPy-DS-Fib film for this purpose must deposit and arrange the PPy film to maintain these conductive properties [254,259,260]. Their presence as charged molecules also provides a useful secondary trait for facilitating cell adhesion. Their charged properties allow for a hydrophilic film surface which improves conditions for cell adhesion, a necessary quality for electroceutical applications [261–263].

The deposition potential, and therefore the deposition time is an important aspect when considering the optimal properties of the bipolar electrode. Additional to electrostimulation there are many characteristics which are favourable for biological experimental protocols. Typically, cell cultures are monitored using light microscopy to determine cell density, culture health, and confluency. A frequent method of data acquisition is also the use of fluorescent labelling using antibody staining protocols such as immunocytochemistry (ICC). As cells in the bipolar electrochemical stimulation protocol will be seeded and grown on the bipolar electrode surface it is preferable to maintain a good optical transmittance for cell analysis in situ. Film thickness can be tuned using a variety of deposition potential windows and fixing the scan rate of the cyclic voltammogram, effectively modulating the deposition time while maintain the pyrrole polymerisation overpotential. The effect of electrodeposition parameters on PPy polymer films co-doped with biomolecules is not well characterised in the literature. Preserving as much optical transmittance as possible in the visible spectrum of light, the range of most typical fluorescent dyes, while tuning the primary characteristics of the film (conductivity and hydrophilic surface free energy) is an important aspect of this work.

This work describes the development of an electrochemical deposition protocol of a PPy based bipolar electrode material which is co-doped with dextran sulphate and fibronectin

for the express purpose of integration into a wireless bipolar system supporting the electrostimulation of cells in culture. The work represents the electrochemical profile of the bipolar electrode to assess the suitability of the material for bipolar electrochemical processes, including assessing the potential window to ensure suitable potential range for the electrostimulation of a variety of cell cultures. The physical characteristics of the electrode was also assessed to determine and optimise the hydrophilic surface free energy, this assists in the cell adhesion in future cell culture experiments. Presented here is a viable bipolar electrode material showing a promising potential window for electrostimulation, hydrophilic surface characteristics for cell adhesion, and excellent light transmittance for use in traditional biological experiments such as light and fluorescent microscopy. The aim is to develop and characterise a wireless bipolar electrode using PPy-DS-Fibronectin with good optical transmission, a potential window at positive potentials, and a hydrophilic surface for use in cell culture in a wireless bipolar electrostimulation platform.

2. Materials and Methods

2.1. Fabrication

2.1.1. PPy-DS-Fibronectin BPE

Pyrrole (Sigma Aldrich, Ireland) was distilled under nitrogen and stored in a -20°C freezer prior to use. For the deposition of a doped pyrrole film on a conductive substrate, 50 ml of a 0.2 M aqueous solution of pyrrole was prepared. Dextran sulphate (Sigma Aldrich, Ireland) was added to the aqueous solution as a charge compensating anion for the pyrrole polymer at concentration of 250 µM. [264–269]. To facilitate cardiomyocyte adhesion to the bipolar electrode (BPE), 23 nM fibronectin (MW 450 kDa) was added to the solution.

Table 3 – Breakdown of the constituents in 50 ml of aqueous Pyrrole solution for electrodeposition onto FTO substrate

Constituent	Mass added per 50 ml	Molar concentration	Molar ratio
Pyrrole	0.6709 g	0.2 M	8.7×10^6
Dextran Sulphate	0.1 g	250 µM	1.09×10^4
Fibronectin	250 µg	23 nM	1

This concentration was chosen as it is the recommended fibronectin concentration for the gelatin / fibronectin gel on which cardiomyocytes are cultured in traditional cell culture techniques using HL-1 cardiomyocytes. Fluorine doped tin oxide was purchased in 100 mm x 100mm sheets with a sheet resistance of 8 Ω/sheet (Sigma Aldrich). The cutting of the FTO was performed by an external glass cutting professional in Dublin into strips approximately 50 mm x 10 mm for deposition and further processing for experimental procedure and characterisation as needed. The FTO strips were cleaned prior to deposition; the cleaning procedure consisted of initial sonication in milli-Q water for 10 minutes. Sonication was followed up with consecutive washes of ethanol and milli-Q water, this was repeated three times in total. To dry the cleaned FTO the strips were placed in an oven at 100 °C for 30 minutes. Once dried the strips were allowed to cool to room temperature. Electrochemical deposition of polypyrrole co-doped with dextran sulphate and fibronectin (PPy-DS-Fib) was performed on the same day as FTO cleaning. PPy-DS-Fib electropolymerisation on FTO was performed using a 3-electrode system in a single chamber cell using a CH instruments CHI760E potentiostat. FTO was used as the working electrode substrate (approximately 1 cm x 4 cm immersed in pyrrole solution, dimensions differed slightly as electrodes were hand cut from bulk FTO sheets) with a platinum wire acting as the counter and an 1M KCl Ag/AgCl reference electrode (all potentials cited are vs Ag/AgCl unless otherwise stated). 50 ml of aqueous pyrrole solution with co-dopants was placed in the electrochemical cell. The potential at the working electrode was cycled from 0.000 V to 0.650 V, 0.700 V, and 0.750 V respectively for a total of 20 cycles each to produce PPy-DS-Fib varying qualities. Following deposition, the BPEs were cleaned using consecutive washes of ethanol and milli-Q water to remove any remaining material from the electrode surface. The electrodes were dried overnight and stored in plastic petri dishes until they were required.

2.2. Characterisation

2.2.1. Cyclic voltammetry

Cyclic voltammetry was carried out using a 3-electrode cell with either pristine FTO or the PPy-DS-Fib BPE acting as the working electrode, a platinum wire as the counter electrode and an 1M KCl Ag/AgCl reference electrode. The supporting electrolyte for all the cyclic voltammetry experiments was Dulbecco Phosphate Buffer Solution (DPBS) as it is a complex electrolyte with known salt concentrations which closely mimics the complex biological medium that will act as the electrolyte in the cell stimulation experiments. First the potential window for the BPE was established and after the cyclic

voltammograms were then recorded in this potential range in both oxygenated and deoxygenated electrolyte. The BPEs were cycled once, and each CV was recorded in triplicate for each maximum oxidation potential. The electrolyte was deoxygenated by passing a nitrogen stream through it for 5 minutes prior to recording the cyclic voltammogram. The voltammograms were recorded on a CH Instruments CHI760E potentiostat at room temperature (22±2C).

2.2.2. UV-vis Spectroscopy

To determine the transmittance of the three PPy-DS-Fibronectin layers a PerkinElmer Lambda 900 UV-Vis spectrometer. Blank FTO was used as a reference material to calculate the transmittance percentage of each of the BPE films.

2.2.3. Surface free energy

To estimate the surface free energy of the PPy-DS-Fib films a FTÅ 200 contact angle instrument (First Ten Ångstroms) was used. A single drop of 20 µl de-ionised water was deposited on the BPE substrate and the contact angle was calculated using the software provided with the instrument. The baseline of the water drop was manually established, and the contact angle was automatically calculated by the software for each image. The surface free energy of the polymers was then extrapolated from the contact angle measurements and the known dispersion and polar tension of water in the surface energy software provided by FTÅ. Several measurements were taken along the length of each electrode to determine the change across the length of the electrode. The surface energy of FTO was also calculated in the same manner.

3.   Results

First, the electrochemical properties of the underlying FTO electrode were investigated to determine the available potential window and to identify any redox processes that might influence the bipolar experiments. At a minimum, the electrode must provide a stable platform which allows for the oxidation and electrodeposition of pyrrole, between 0.65 V and 0.75 V vs Ag/AgCl. As shown in **Figure 9**, Fluorine doped Tin Oxide (FTO) gives a featureless cyclic voltammogram between 1.07 V and -0.36 V in oxygenated Dulbecco Phosphate Buffer Solution (DPBS) containing 1.8 mM $CaCl_2$, 5 mM KCl, 44 mM $NaHCO_3$, and 110 mM NaCl. Oxidation processes and reduction processes occur beyond these potentials.
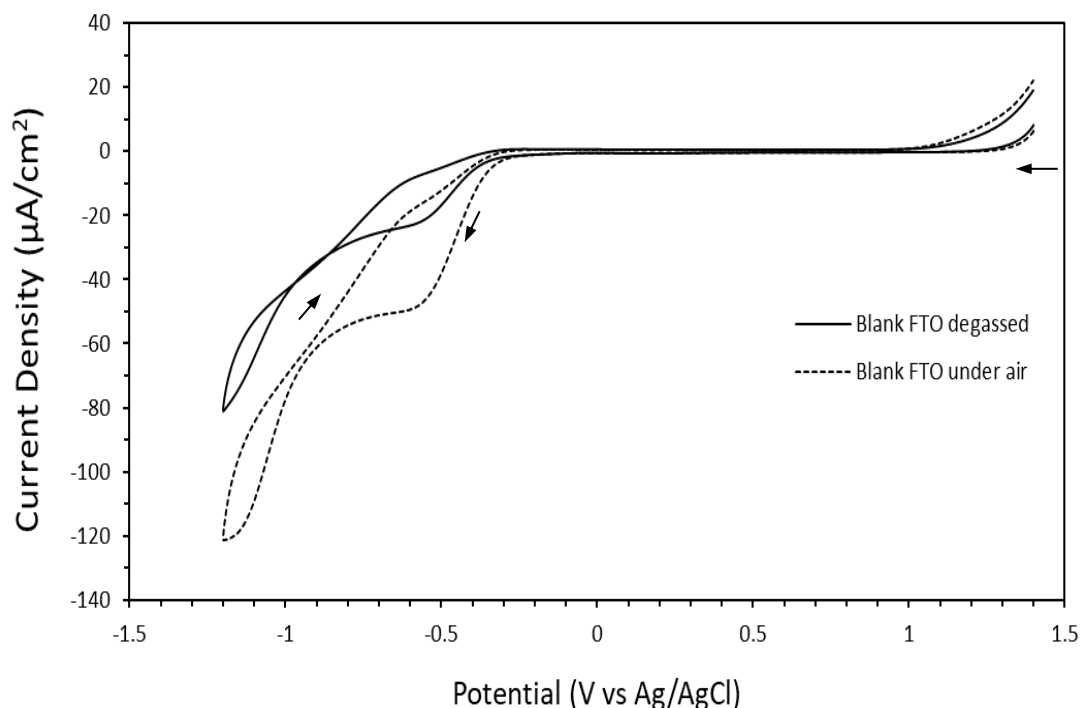
Figure 9. Comparison of blank FTO in Dulbecco Phosphate Buffer Solution (DPBS) containing 1.8 mM $CaCl_2$, 5 mM KCl, 44 mM $NaHCO_3$, and 110 mM NaCl before and after deoxygenating using nitrogen gas. CV were scanned in a negative direction first between 1.4 V and -1.2 V and then back in the positive direction. Potential was recoded vs 1M KCl Ag/AgCl reference electrode and using a platinum wire counter electrode, the scan rate used was 0.03 V s^{-1}. All CVs were performed independently in triplicate using fresh electrodes from the same batch.

When performed in *deoxygenated* DPBS the oxidation processes are pushed to 1.259 V in the anodic direction while the onset potential of the reduction is unaffected. A reduction peak is observed in the CV at approximately -0.5 V and is present in both the oxygenated and deoxygenated voltammograms. The is most likely oxygen reduction processes. The reduction in current density of the oxygen reduction reaction indicates that there remained oxygen within the system. FTO is known to facilitate oxygen reduction and this reduction has also been shown in phosphate buffers [270]. The subsequent reduction peak is mostly likely the hydrogen evolution reactions. Maintaining this featureless potential window in an oxygenated electrolyte makes FTO a suitable electrode material for the electrostimulation of cardiomyocytes as mammalian cells require oxygen to be present in the environment for healthy cell growth and long-term culture survival.
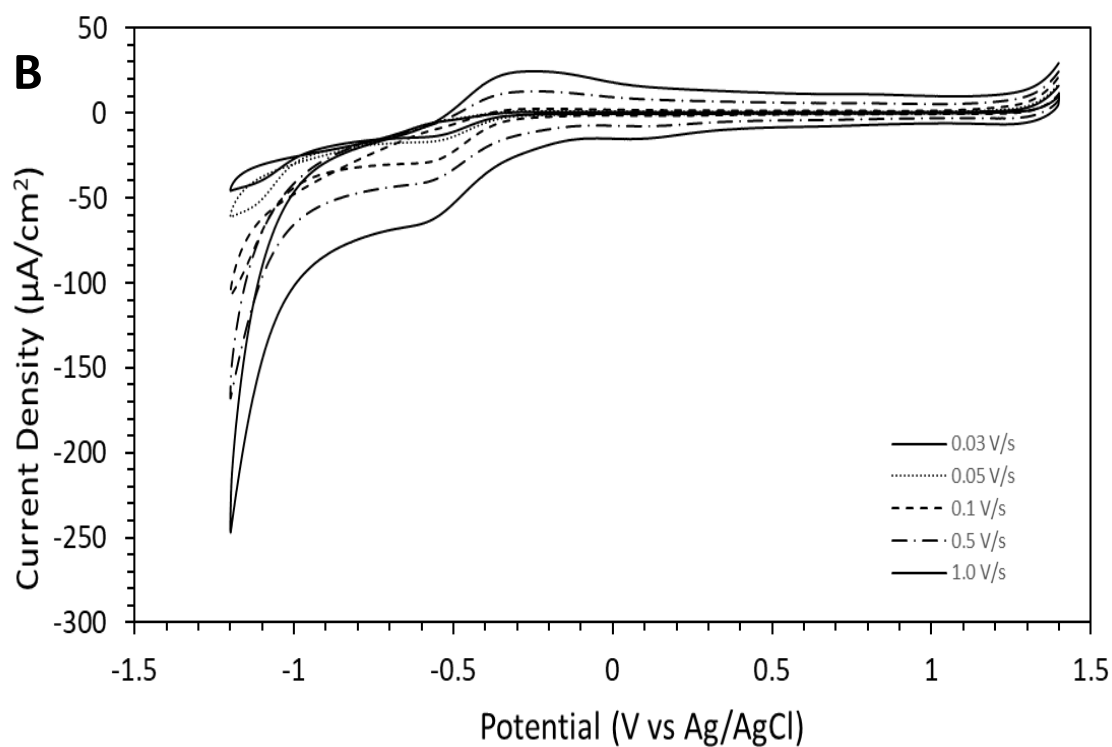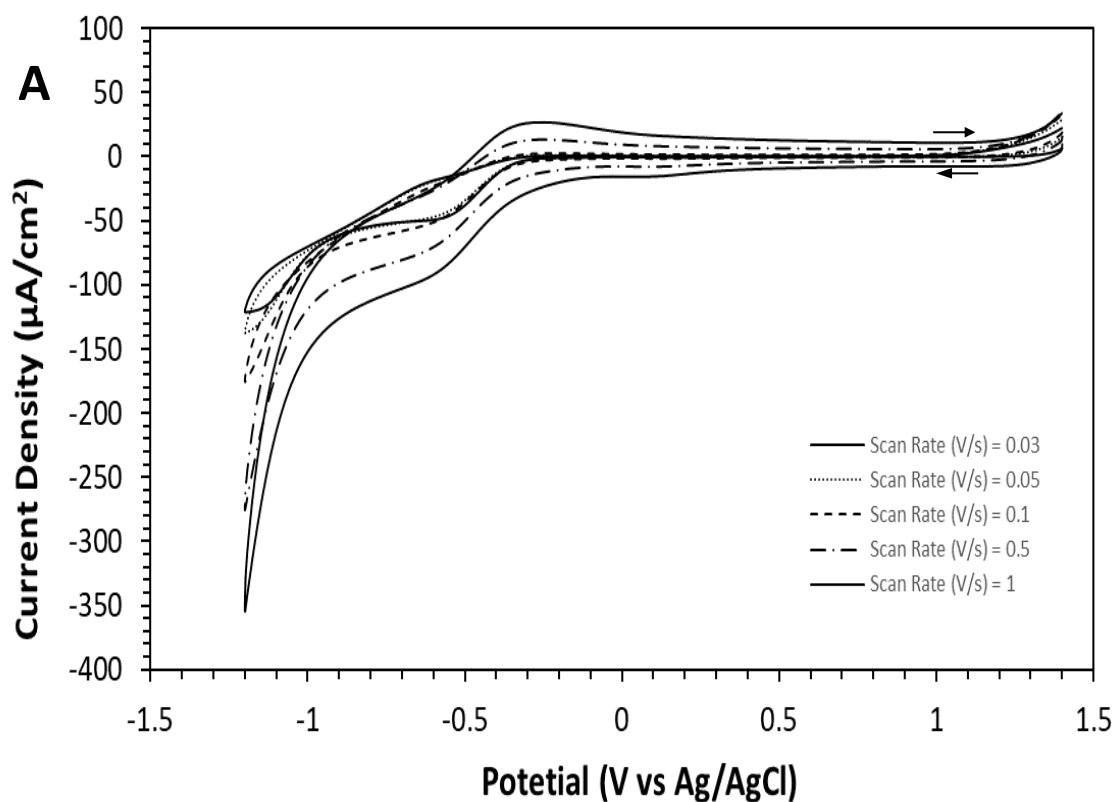
Figure 10. Progressive scans of blank FTO in DPBS of (A) oxygenated and (B) deoxygenated. The potential was cycled between 1.4 V and -1.2 V at a range of scan rates from 0.03 V s^{-1} to 1.0 V s^{-1}, inclusive. The voltammograms were recorded using an 1M KCl Ag/AgCl reference and a platinum wire counter electrode. Only CVs for the scan rates 0.03, 0.05, 0.1, 0.5, and 1.0 V s^{-1}

are graphed to represent the data. All CVs were performed independently in triplicate using electrodes from the same batch.

Cell stimulation has been reported using frequencies ranging between 1 and 5 Hz. The average resting heart rate is approximately 70 beats per minute, 1 Hz is equivalent 60 BPM making the average resting heart rate approximately 1.2 Hz. In order to determine the effect of rapid change in potentials applied to the electrode, a scan rate study of FTO in oxygenated DPBS was performed at scan rates between 0.03 V s^{-1} and 1 V s^{-1}, **Figure 10**. The potential window at scan rates between 0.03 V s^{-1} and 0.1 V s^{-1} it remains featureless between 0.65 V and 0.75 V, which allows for the oxidation of pyrrole at a range of scan rates. To determine if the potential window was affected by the presence of oxygen in the electrolyte while varying the scan rate the experiment was repeated using deoxygenated DPBS, **Figure 10**. The presence of oxygen in the electrolyte again showed an oxygen reduction reaction at approximately -0.5 V in both the oxygenated and deoxygenated electrolyte, indicating that the deoxygenation was incomplete. There was no redox peaks observed between 0.65 V and 0.75 V, regardless of the scan rate used, indicating that the FTO electrode substrate was suitable for polypyrrole electrodeposition at scan rates between 0.03 V s^{-1} and 1.0 V s^{-1} without the need to deoxygenate the solution.

A
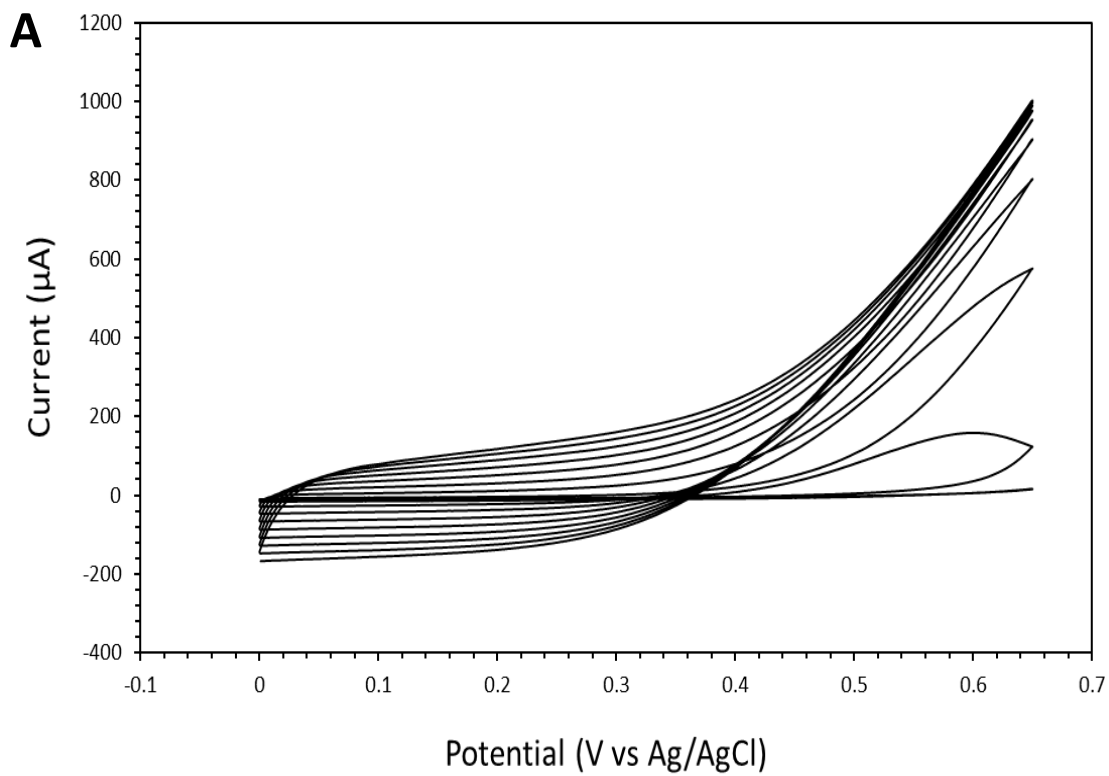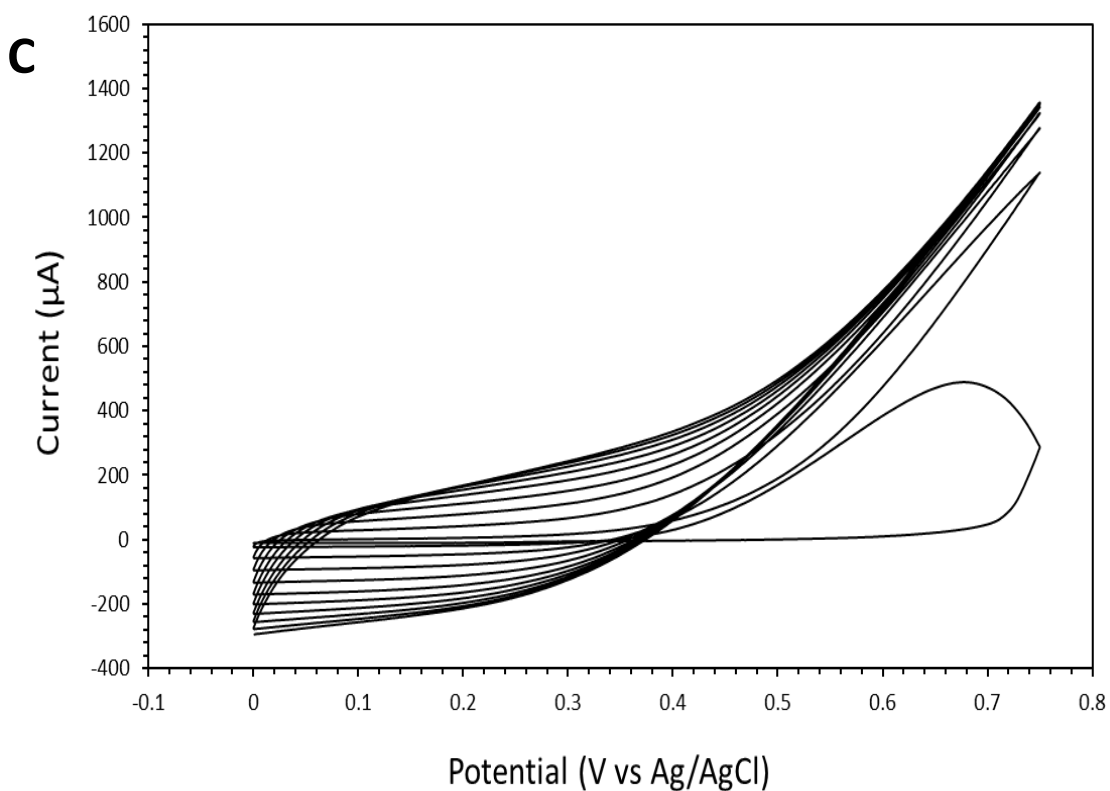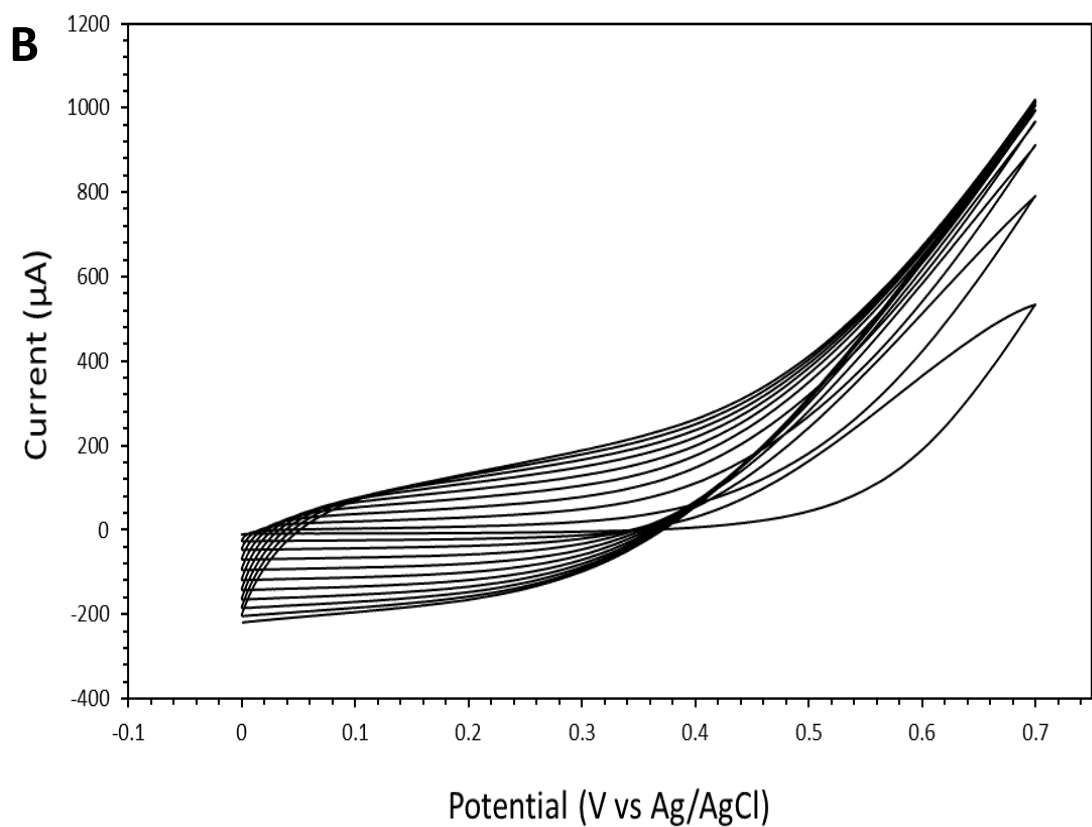
Figure 11. Electropolymerisation of 200 mM pyrrole in the presence of 2 mg/ml dextran sulphate and 5 µg/ml fibronectin in water to form PPy-DS-Fibronectin on an FTO substrate using cyclic

voltammetry swept between (**A**) 0 and 0.65 V (**B**) 0 and 0.7 V and (**C**) 0 and 0.75 V at 0.02 V s^{-1} using 1M KCl Ag/AgCl reference and platinum wire counter electrodes for a total of 10 cycles. The depositions were performed on multiple occasions using multiple batches of deposition solutions. The CVs shown here were performed independently in triplicate for the purposes of deposition thickness calculation.

Effective deposition of PPy-DS-Fibronectin relies on the oxidation of pyrrole to form a conductive polymer. Polypyrrole alone contains a net positive charge and requires the addition of co-doped anions for stability. Dextran sulphate is a polyanionic polysaccharide and fibronectin is a polyampholytic polypeptide whose negatively charged peptides at a neutral pH can also act as a polypyrrole stabilizer. These charged molecules are both incorporated into the film through adsorption and entrapment within the PPy backbone. A commonly used method for pyrrole polymerisation is cyclic voltammetry [271–273]. The literature describes methods using maximum potentials of between 0.6 V and 1 V for the oxidation and deposition of pyrrole. For this work, three maximum potentials within this range were selected to determine the optimum conditions for the deposition of a polymer layer. An ideal film would provide a stable potential window for electrostimulation of cardiomyocytes, a high surface energy to facilitate cell adhesion, and reasonable transmittance to allow for fluorescent microscopy for quantitative analysis of cell culture. FTO was used as the substrate having previously established that it maintained a stable potential window, across a range of scan rates and without the need for deoxygenation, which included the potentials at which pyrrole is oxidised. To determine which was the most effective maximum potential for the deposition of a conductive film formed from 200 mM pyrrole co-doped with 2 mg/ml (250 µM) dextran sulphate and 5 µg/ml (23 nM) fibronectin in water three maximum potentials, 0.6 V, 0.7 V, and 0.75V, were examined, **Figure 11**. Using the potentiodynamic method increases the time of deposition. These potentials are all above the oxidation potential for pyrrole. A scan rate of 0.02 V s^{-1} was used to allow the oxidised pyrrole time to polymerise and deposit on the surface of the FTO and to replenish the pyrrole layer at the electrode surface for the further oxidation events to occur with following sweeps. The first cycle of each deposition shows that PPy-DS-Fibronectin layer deposits consecutively on the FTO substrate. An initial deposition event can be observed followed by a consecutive increase in the measure current in the FTO as the deposition continues which is consistent with the nucleation events described in other methods for cyclic voltammetry-based deposition of polypyrrole in the literature [274,275]. The current density of the second cycle is on average 450% that of the first cycle. The current continues to increase with each subsequent cycle with average increases in measured current: 140%, 75%, 30% respectively for the following 3 cycles. The 5th cycle no longer

generates a significant increase in current from the previous cycle. Each of the final 5 cycles increase the measured current < 5% each on the previous cycle. The presence and stability of the faradaic current observed in both the initial deposition cycles and the final cycles indicates that the polymer being deposited on the surface of the FTO is conductive. The oxidation maximum potential used varies the deposition conditions of the PPy films. Maintaining a constant scan rate while increasing the potential window in the anodic direction means the time at which the electrode is above the oxidation potential for pyrrole (0.4 V) is increased and therefore the deposition time is increased. The time where the electrode is at rest (below the oxidation potential for pyrrole) is therefore maintained and allows the same time for diffusion of pyrrole, DS and Fibronectin from the bulk layer to the diffusion layer that the electrode surface.

The thickness of the film can be estimated using the following equation:

$$x = qM/pAzF$$

Where x is the film thickness, q is the charge passed, M is the molar mass of the polymer, p is the density, A is the area of the electrode, z is the number of electrons involved, and F is Faraday's constant. Assuming the molar mass of the polymer to be 67 g/mol, the density of polypyrrole films to be 1.5 g/cm^3, the area of the working electrode is 3 cm^2, and the number of electrons involved to be 2.25, then it is possible to estimate the thickness of each of the films at the given deposition potential to be 8 nm, 12 nm, and 15 nm for 0.65 V, 0.7 V, and 0.75 V respectively, which correlates well with the literature for PPy film thicknesses using this method.

The effect this has on the electrode with respect to the electrochemical performance as a bipolar electrode and the physical characteristics of the layers such as transmittance will be examined in following sections. The absence of any other oxidation peaks in the three potential ranges used shows that if the dextran sulphate and fibronectin are incorporated into the PPy layer they are not electroactive in the potential range used.

Based on the pI of Fibronectin of ~6 – 6.5 it should act as an anion in solution at pH 7, as in the electrodeposition solution. Therefore, it is possible for the fibronectin molecules to be incorporated as a counterion to balance the net positive charge of the polypyrrole polymer during deposition. This mechanism for macro biomolecules incorporation into polypyrrole films has been discussed in the literature [253,276,277]. There is no evidence within the CV that fibronectin has been incorporated however, the film remains conductive.
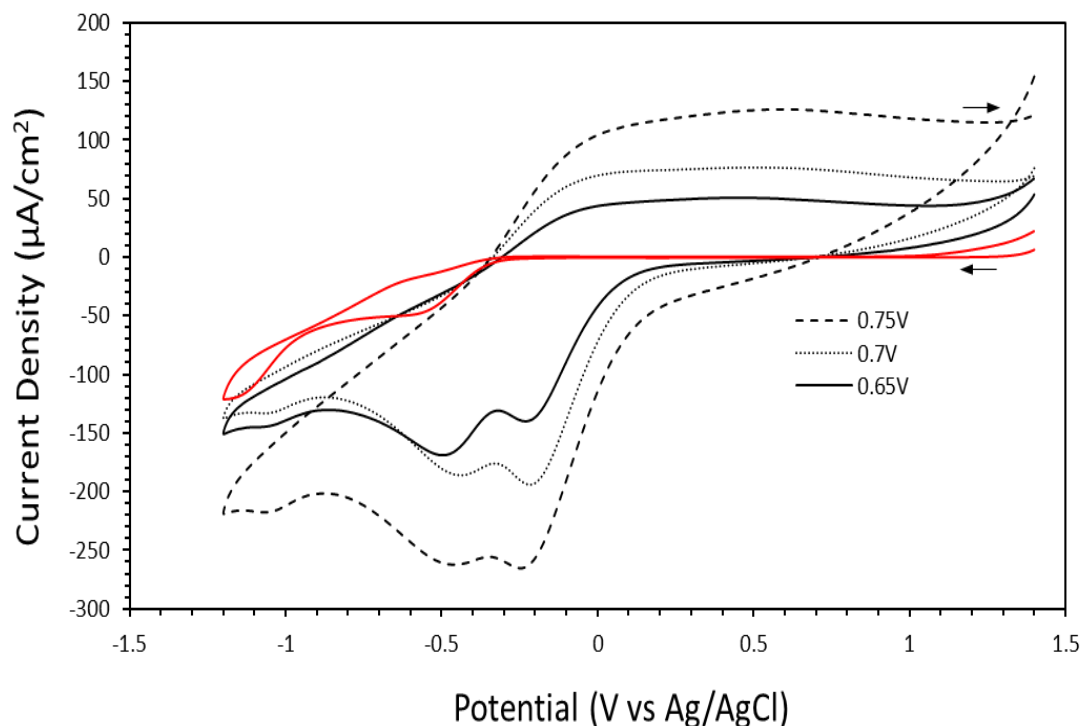
Figure 12. First sweep at 0.03 V s^{-1} in oxygenated DPBS of blank FTO (red) and FTO with PPy-DS-Fibronectin electropolymerised and deposited at a maximum potential of 0.65 V (Black), 0.7 V (dotted), and 0.75 V (dashed) deposited through cyclic voltammetry. CVs were independently recorded in triplicate with electrodes from the same batch.

The aim of electrodepositing the Polypyrrole film co-doped with DS and Fibronectin is to create a conductive electrode surface which is conducive to mammalian cell adhesion and facilitates long term cell culture. The electrochemical properties of the conductive polymers must be established to ensure a potential window that avoids oxidative and reductive process of compounds in the cell culture environments, such as cell culture medium ingredients, and does not create toxic by-products during stimulation which could interfere with cell viability. The potential window of all three maximum deposition potential is shown to be from 0.1 V to 1.2 V, **Figure 12**. The reduction peaks outside of the potential window indicate that a conductive film has been successfully deposited on the surface of the FTO substrate. The oxidation and reduction peaks increase in current density with the maximum potential used for deposition which suggests that using higher maximum potentials leads to an increased deposition of PPy-DS-Fibronectin. The reductive peak of oxygen reduction is present in the voltammogram of all four electrodes. This is consistent with the previous observations of a persistent oxygen reduction peak, especially for aerated Dulbecco PBS electrolyte. A second reduction peak is visible at potential -0.2 V. This reduction peak may be attributed to a reduction of the PPy, the

absence of the peak in the bare FTO CV indicted that the reduction is associated with the deposition of the PPy-DS-Fibronectin film [278]. Fibronectin does contain many sulphur containing amino acids which have redox potentials recorded within the potential window of the CVs however a high capacitance means there is no evidence of the oxidation peak at potentials commonly associated with the oxidation of amino acids. The increasing capacitance of the PPy-DS-Fibronectin films are likely due to the increased thickness of the layers as a consequence of the maximum deposition potential used [279].

 The characteristics of the conductive polymer layer can therefore be tuned depending on the maximum potential used for deposition. However, the maximum deposition potential used does not affect the available potential window of the modified electrode. Depositing the PPy-DS-Fibronectin does not significantly change the potential window compared to that seen for blank FTO. For cell stimulation to occur, a positive potential is required therefore the large potential window of PPy-DS-Fibronectin appears to be a viable candidate for the stimulation of cells. One concern is the evidence that during oxidation of polypyrrole films a significant interfacial pH can be generated, this can contribute to cell lysis at lower potentials than on traditional metal-based electrodes. One was this can be avoided is to minimise the applied potentials as the cardiomyocyte electrical stimulation does not typically require potentials greater than 500 mV [280–283].
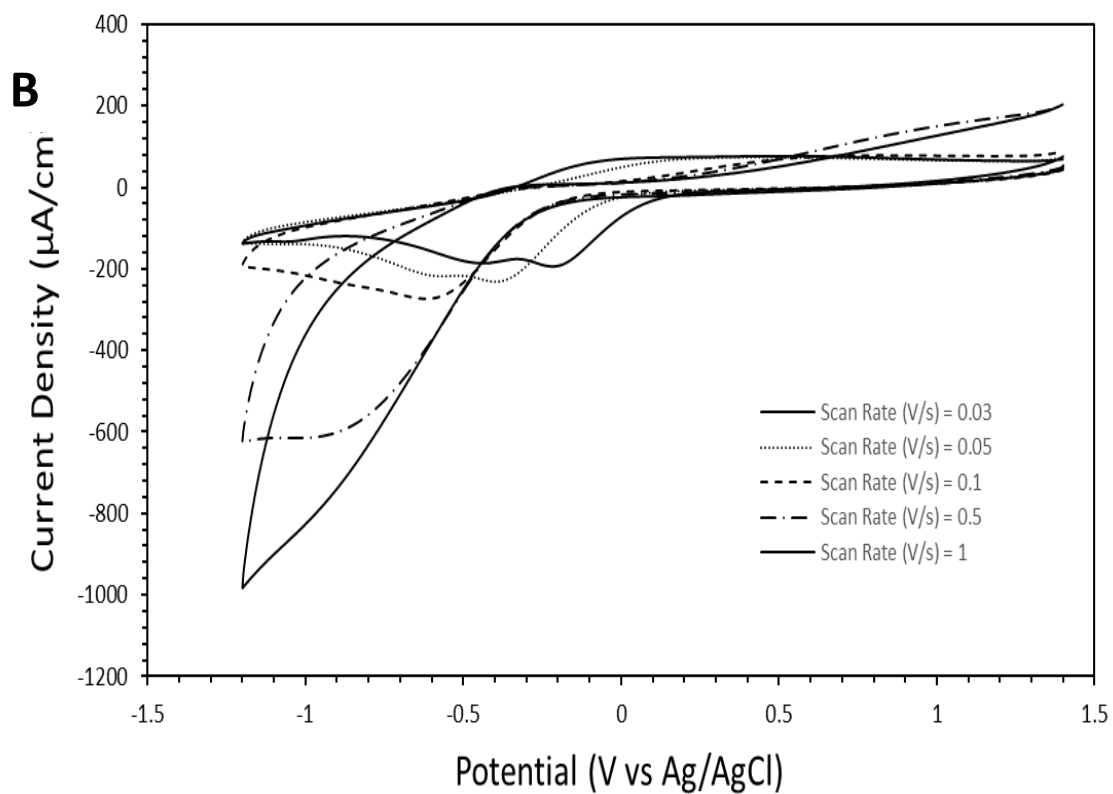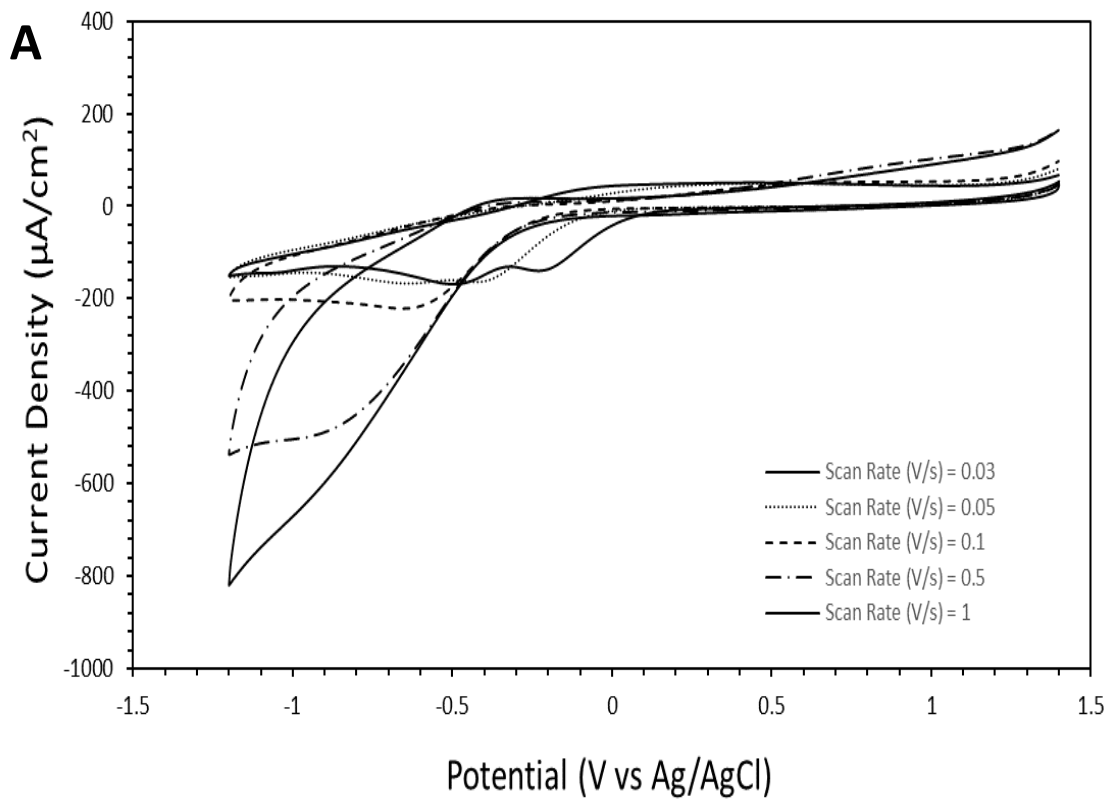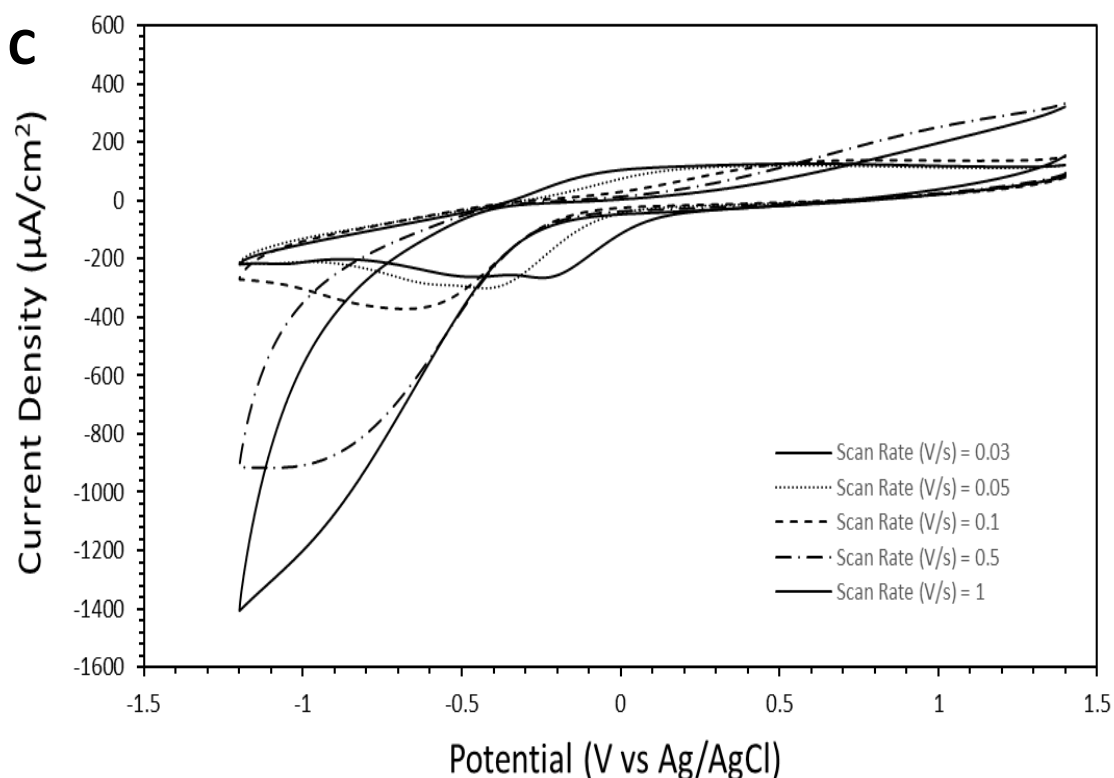
Figure 13. Progressive scans of PPy-DS-Fibronectin in DPBS of (**A**) deposited with a maximum potential of 0.65 V (**B**) deposited with a maximum potential of 0.7 V (**C**) deposited with a maximum potential of 0.75 V. The potential was cycled between 1.4 V and -1.2 V at a range of scan rates from 0.03 V s^{-1} to 1.0 V s^{-1} inclusive. The voltammograms were recorded using an 1M KCl Ag/AgCl reference and a platinum wire counter electrode. Only CVs for the scan rates 0.03, 0.05, 0.1, 0.5, and 1.0 V s^{-1} are graphed to represent the data. CVs were independently performed in triplicate with electrodes from the same batch.

The frequency of stimulation is an important parameter of cell stimulation. In order to determine the effects of the frequency over which the potential is changed on the response of the conductive PPy-DS-Fibronectin film, the scan rate of the was varied from 0.03 V s^{-1} to 1.0 V s^{-1} using cyclic voltammetry in oxygenated DPBS, **Figure 13**. At slow scan rates, i.e., up to 0.2 V s^{-1}, the behaviour of all three conductive films are indistinguishable. The current density increases linearly from 0.1 V to 1.4 V. As noted earlier in **Figure 12** reduction processes related to PPy can be observed. The scans were conducted consecutively on the same electrode, moving from slow to fast. The cyclic voltammetry was conducted on three electrodes of each deposition potential which were electrodeposited from the same deposition solution. The CV of each electrode was conducted independently using fresh electrolyte solution. This likely lead to an over-reduction of rhe polypyrrole film as the incorporated dextran sulphate and fibronectin cannot migrate into and out of the film for charge balancing as would be the case with

polypyrrole films using typical anions such as Cl- as counterions. The consistent and wide potential window in all three PPy-DS-Fibronectin films across a range of scan rates suggests that the polymer can be useful for the electrical/electrochemical stimulation of mammalian cells in culture.
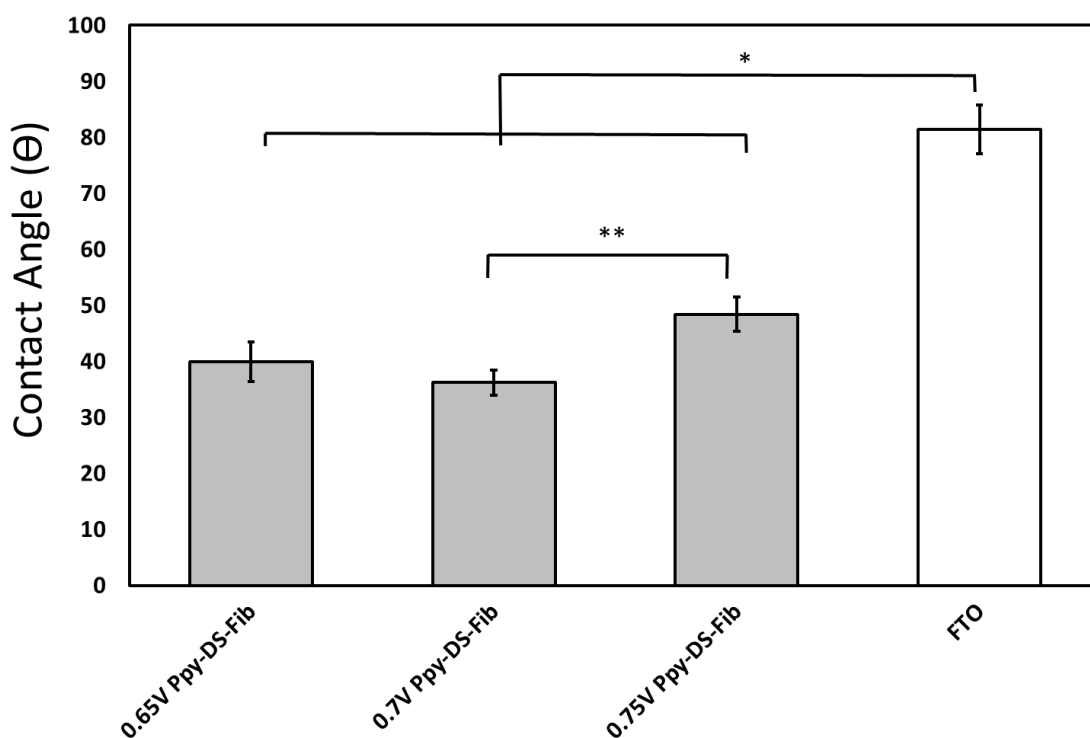
Figure 14. Contact angle measurements for the 3 PPy layers deposited on FTO and a bare FTO reference. All three PPy electrodes have significantly lower contact angles than the bare FTO indicating an increase in the hydrophilic properties. 0.7V PPy-DS-Fib had a significantly more hydrophilic surface than that of the 0.75V PPy-DS-Fib. Contact angle was performed independently in triplicate for each condition on electrodes from a single deposition batch.

The hydrophobic or hydrophilic properties of the BPE polymer must be controlled as it will have an impact of cell adhesion. Insights into the hydrophobicity of a surface can be obtained through the surface free energy (SFE). Material with a high surface energy is more hydrophilic as their surface energy is enough to break the surface tension of a liquid at the liquid / solid interface. Cells interact well to a hydrophilic surface and as such the BPE surface must be optimised to provide satisfactory conditions for cell adhesion and subsequent culture [284,285]. The contact angle for polymers is commonly estimated using the sessile drop method and deionised water as the reference liquid [286,287]. The relationship between the contact angle and the SFE can be described using the following equation:

$$\gamma^{sv} = \gamma^{sl} + \gamma^{lv} \cos \theta \qquad (2)$$

Were γ^{sv} is the solid surface free energy, γ^{sl} is the solid/liquid interfacial free energy, γ^{lv} is the liquid surface free energy, and θ is the contact angle. Hence, a contact angle of < 90° is considered to have a high surface energy. High surface energy is a feature of hydrophilic surfaces. **Figure 14** shows that the PPy-DS-Fib films are significantly more hydrophilic than bare FTO electrodes. Interestingly, there is a statistical difference in the contact angle of the polymer film deposited at a maximum deposition potential of 0.75 V when compared to 0.65 V and 0.7 V, however this is minor. There is no significant difference between the latter polymer layers (Figure 7). All three polymer films provide a more hydrophilic surface than bare FTO and offer a potentially more suitable environment for cell adhesion. To efficiently carry out future work the 0.7 V maximum deposition potential film was nominally chosen as it represents the most hydrophilic surface according to the data obtained.
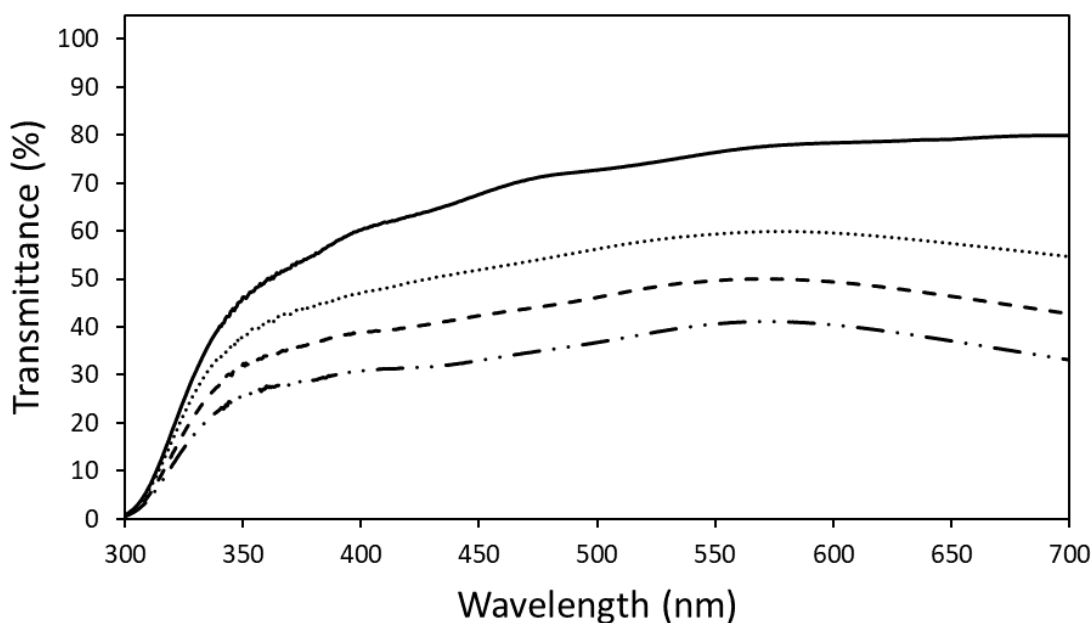
Figure 15. Transmittance of 300 nm - 700 nm wavelength light through FTO (solid), 0.65 V PPy-DS-Fib (dot), 0.7 V PPy-DS-Fib (dashed), and 0.75 V PPy-DS-Fib electrodes (dot and dash). Transmittance was recorded independently in triplicate on electrodes from the same batch.

Generating meaningful and insightful data from cell culture experiments frequently requires the use of microscopic techniques [288,289]. Microscopic techniques such as ICC provide valuable information such as the up- or down-regulation of protein expression in reaction to a stimulus or the localisation of those proteins intra- or extra-cellularly [290,291]. They can also provide important information on the morphological changes in the cells

which may indicate a reaction to a stimulus in the case of some cell lineages or, in the case of stem cell lines, indicate that there has been a differentiation of the cell line. However, more basic light microscopy is required for the maintenance of cell cultures during passaging or in experiments to monitor confluency. Here, the cell culture substrate must maintain a sufficient transmittance of visible light and emission wavelengths of traditional conjugates for antibody ICC.

Figure 15 illustrates the UV vis transmittance spectra of the bare FTO prepared using maximum oxidation potentials of PPy 0.65 V, 0.7 V, and 0.75 V, respectively. The initial substrate for the bipolar electrode, FTO, has an excellent optical transmittance of up to 80 % in the visible light region PPy generates a black film which naturally leads to a decrease in the transmission of the visible light. As expected, a decrease in transmittance is observed for all three films in comparison to the bare FTO. Specifically, there is a significant decrease of 20 % transmission from the 0.65 V PPy film, with each subsequent scan decreasing the transmission of the visible light. The decrease in the transmittance is expected given the increase in the deposition time meaning the 0.75 V PPy theoretically has the most PPy deposited on the electrode. Using the charge consumed during deposition, and assuming 100% faradaic efficiency, it is possible to estimate the surface coverage of the films using the three deposition potentials, these are 2.7×10^{-9} mol cm^{-2}, 9.0×10^{-9} mol cm^{-2}, and 2.3×10^{-8} mol cm^{-2} respectively for 0.65 V, 0.7 V, and 0.75 V deposition maximum potentials.
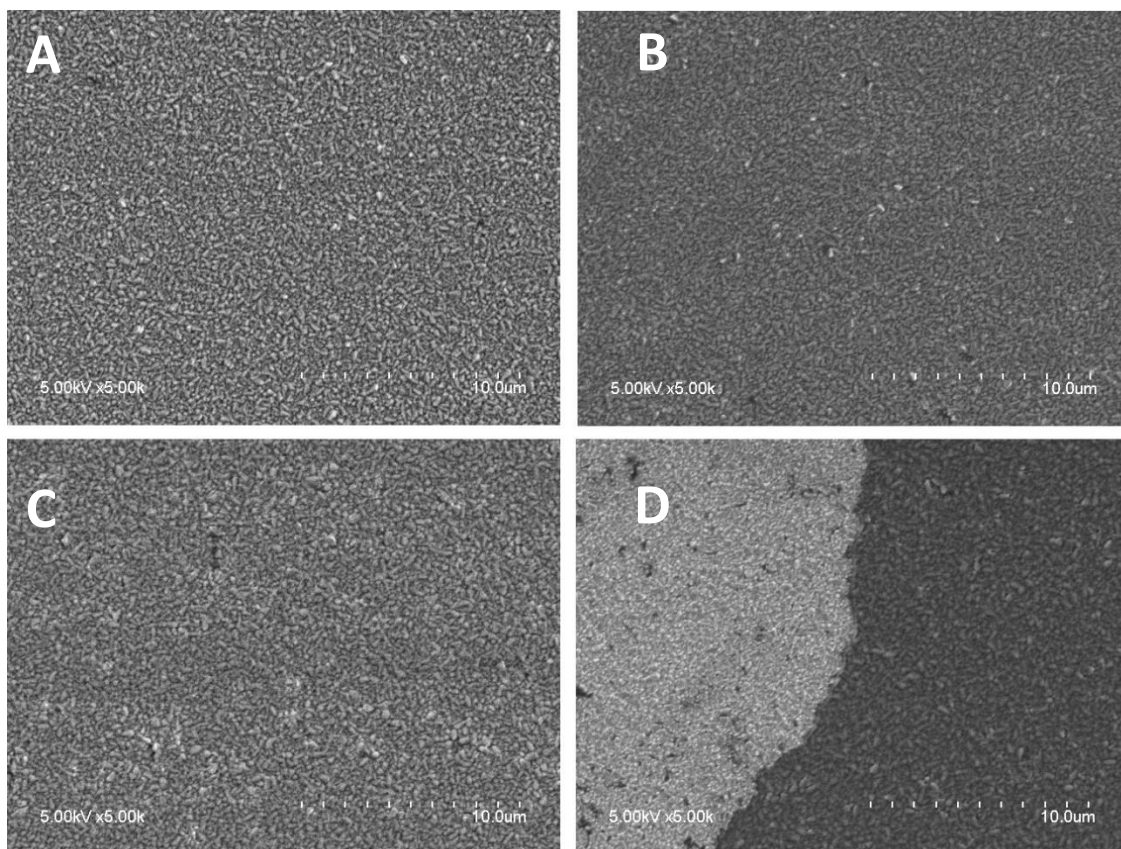
Figure 16. SEM image of the surface of the PPy-DS-Fibronectin deposited on FTO substrate. A) PPy-DS-Fibronectin layer deposited using potentiodynamic method. Potential was cycled between 0 V and 0.65 V for ten complete cycles. B) Potential was cycled between 0 V and 0.7 V for ten complete cycles. C) Potential was cycled between 0 V and 0.75 V for ten complete cycles. D) Border of the FTO substrate and deposited PPy-DS-Fibronectin deposited between 0 V and 0.75 V illustrating the change in surface morphology upon the deposition of the PPy layer. SEM images were taken of three independent electrodes in each condition.

Surface analysis using SEM imaging of the surface of the modified bipolar electrode (**Figure 16**) shows that the surface of the PPy film is relatively smooth. Small nodules are observed on the surface which are consistent with other PPy films observed formed under similar conditions using electrochemical techniques and formed from an aqueous solution [292,293]. As is illustrated in **Figure 16** the surface of the film is continuous, has a reasonably uniform thickness and shows significant surface roughness. At the sides of the electrode, it is possible to observe stratification due to the deposition of consecutive layers of PPy. At the resolution of the SEM, it is not possible to identify the presence of the fibronectin in the PPy film. Globular fibronectin is typically < 10nm which is not visible x6k magnification shown above. It should also be noticed that the relatively featureless surface makes focusing images at higher magnification very technically challenging. The

SEM images also show that the surface morphology of the PPy film is independent of the maximum oxidation potential used in the deposition of the layer.

4.   Conclusions

This work aimed to develop a conductive bipolar electrode for use in a biological stimulation platform. For this purpose, a conducting film with the ability to be modified for biological systems must be developed. The key characteristics required are good conductivity, materials suitable for biological systems and a hydrophilic surface to maximise cell adhesion to the electrode surface. Secondary characteristics required are a high percentage of light transmittance for microscopy experiments and a broad potential window to avoid electrochemical reactions occurring during stimulation protocols.

The work above describes the electrochemical deposition of a polypyrrole film co-doped with dextran sulphate and fibronectin. Cyclic voltammetry determined that all deposition parameters described provide a broad potential window in the positive potential region. A broad potential window is necessary for the electrical stimulation of cardiomyocytes using the interfacial potential in a wireless bipolar electrochemical cell. The CVs also showed evidence of oxygen reduction at negative potentials in the aqueous solutions even when de-aerated briefly. The reduction peak was present on bare FTO and the deposited films demonstrating that at negative potentials < -500 mV there is the possibility of oxygen reduction occurring during cell stimulation in a wireless bipolar electrochemical platform. Contact angle measurements demonstrated that the 0.7 V deposition potential displayed the optimal hydrophilic surface, which is advantageous to encourage cell adhesion. All electrochemically deposited PPy-DS-Fib films displayed improved hydrophilicity over bare FTO however, there was no functional difference in hydrophilicity between the three deposition parameters used. Ultimately 0.7 V was chosen for future work due to the marginally improved hydrophilicity in the data gathered. FTIR demonstrated that all three films maintained good optical transmittance in the visible light region which is important for both light and fluorescent microscopy techniques. These results suggest that PPy-DS-Fib can be used as a conductive, hydrophilic bipolar electrode material for cell culture. However, the electrochemical characterisation in the work has address only the performance of the electrode material in a traditional three electrode cell. The electrodes performance in relation to its ability

to generate a voltage in a potential field of a wireless bipolar platform must now be investigated.

This work here successfully describes the characterisation of the bipolar electrode electrochemical and elucidates many of the properties. The next step of the development process is to optimise these characteristics for use in a biological system, which will require confirmation of the presence of fibronectin integration during the electrochemical deposition of the PPy film. There is evidence to suggest the adsorption and entrapment of fibronectin will occur during electrochemical deposition of the PPy film in the literature. The availability if the fibronectin at the cell surface for the successful adherence of cells is also a critical component for the deposition of fibronectin into the film. Fibronectin's presence alone will not facilitate the adhesion of cell, the cell-binding domain must be available for the cell surface integrin proteins to bind too. Furthermore, the level of fibronectin doping required for cell adhesion must be adapted for cell adhesion optimisation. Tangentially, the effect of the fibronectin doping levels on the film deposition must also be determined.

Chapter 3

Design of Wireless Bipolar Electrochemical Platform and Characterisation of variable doping of Fibronectin concentration in PPy-DS-Fibronectin Bipolar Electrodes

1. Introduction

Developments in cell culture techniques are essential for the improvement of our understanding of biological processes [294–296]. Understanding cellular mechanisms, reactions, and gene expression changes in response to environmental stimuli before *in vivo* experimentation allows for more effective and cost-efficient studies of a variety of materials [297,298]. *In vitro* cell culture is a vital tool to study new and developing materials, drugs and drug delivery systems, tissue-engineering, single cell characterisation at a phenotypic and genotypic level, and stem cell research [299–302]. State of the art research in biomaterials, nanomaterials, electronics, and even electrochemistry can be used to improve and adapt current gold standard techniques.

This work aims to design and create a platform for the wireless electrostimulation of cells during culture with a focus on compatibility for current standard biological wet lab experimentation. This includes the use of light microscopes during culture to monitor cell morphology and confluency, medium changes, fluorescent microscopy of cell (post culture), live/dead cell analysis, etc. The suitability of the platform will be assessed through cell viability to determine the materials toxicity and optimise the delivery of the stimulation potential to the cell cultures. The bipolar electrode (BPE) will be assessed for both the fibronectin loading optimisation, through cell adhesion studies, and through the cell stimulation live/dead assays. The success of the platform will be judged by its ability to culture cells on the surface of the bipolar electrode with comparable cell densities and morphology to traditional cell cultures.

Historically, cell culture was carried out using 2D techniques where cells were grown either adhered to a polystyrene flask modified with attachment proteins for the cells (protein G or other extracellular matrix proteins) or in suspension using serum-based media to provide nutrients and growth factors [303,304]. This approach does not mimic *in vivo* cellular conditions very well and provides limited information about the impact of stimuli on the cells behaviour, gene expression or morphology which could be transferred to *in vivo* cells [305,306]. This work aims to provide a solution for *in vitro* culture of cells which require an electrical stimulus in order to correctly mimic *in vivo* conditions [307,308]. Typically, electrically sensitive cell types are those which encounter electrical stimulation either constantly or sporadically during their maturation cycle, e.g., neurons, skeletal and smooth muscle cells, and cardiac muscle cells. Electrical stimulation of cells has become of particular importance with the increase in stem cell cultures to differentiate and mature lineages from their stem cell precursors. Neurons carry

electrical signals through the body to and from the brain, when cultured *in vitro* they often lack the mature phenotypes observed *in vitro* [309–311]. Electrical stimulation applied to myocytes has a maturation effect which leads gene expression more closely matching *in vivo* myocytes [312–314]. In the case of cardiomyocytes, the physical properties of the cells are also more representative of *in vivo* cells with the addition of electrical stimulation [315,316].

Introducing electrical stimuli to cells could lead to improved mimicking of the genotypic and phenotypic achieved by the cells *in vivo* [317]. This is a well-accepted fact in cell culture techniques which study these electrically sensitive cell lines [318–320]. The literature describes many platform designs for the stimulation of cells during culture which are generally adapted for specific goals of the study and are not typically general protocols which can be easily adapted for various cell types. A common electrical cell stimulation platform is the ion Optix C-pace shown in **Figure 17**. The system consists of a power generator which is linked to carbon electrode plates extending from the top of a traditional cell culture 6 well plate. The carbon electrodes apply an electric field to a cell culture which is grown in a traditional manner on the bottom surface of each well, or on a microscope cover slip when necessary [321]. This system is useful as it maintains the sterile integrity of the cell plates and can be reused. The biggest downfall of this system is that it relies exclusively on a wired connection. This limits its applications outside of *in vitro* cell cultures and does not allow for the adaptation of these platforms into future electroceutical developments. By using bipolar, contactless, or wireless, electrostimulation this work aims to bridge the gap between *in vitro* and *in vivo* applications.
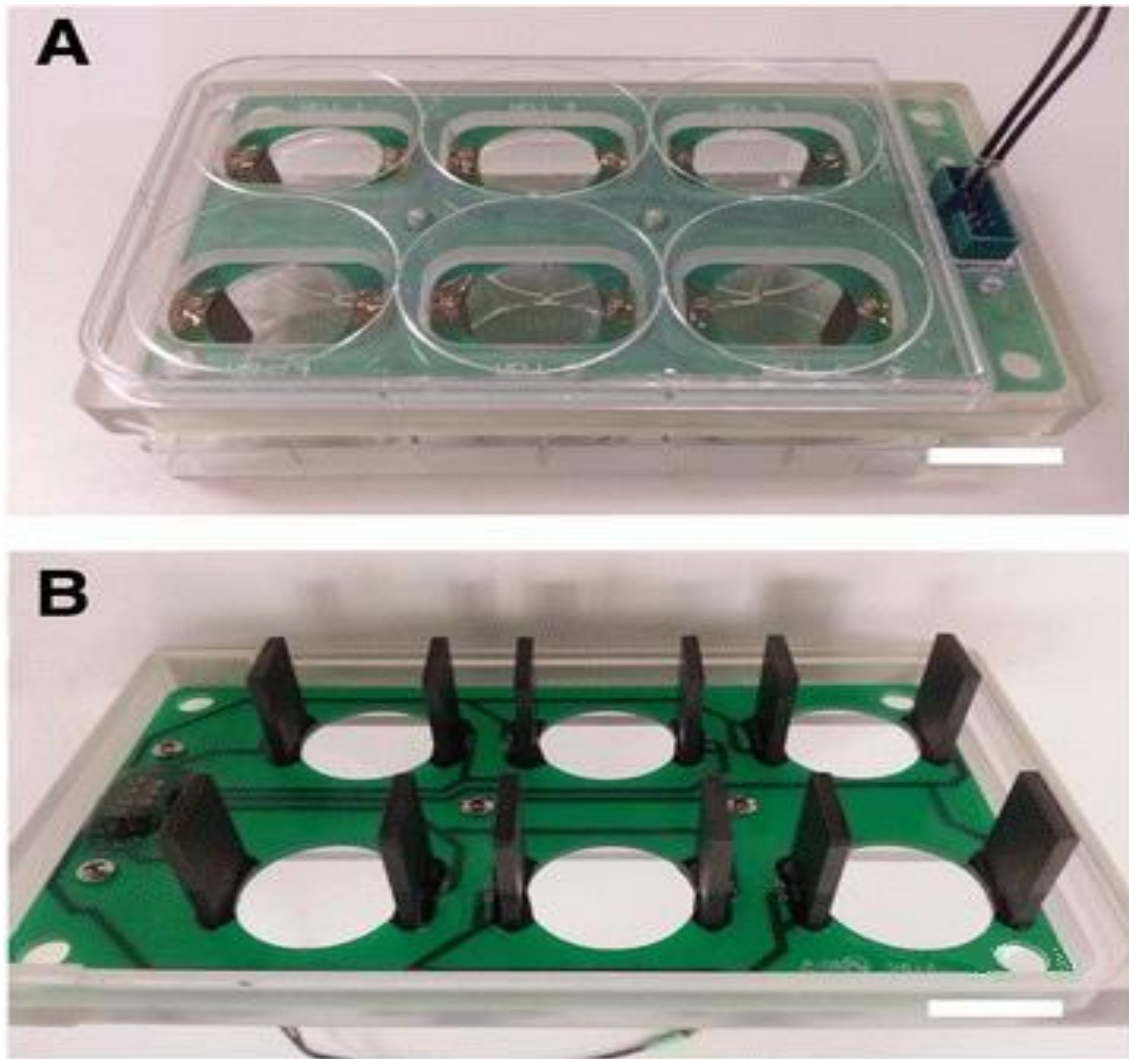
Figure 17. Typical experimental apparatus and experimental data collect from electrical stimulation and maturation experiments on cell lines. A) represents the apparatus set up in a cell culture procedure, B) highlights the electrode configuration for the application of an electric field to the cells during culture with "motherboard" style wired circuitry integrated into the lid section of the 6 well plate. Adapted from Chan et al "Electrical Stimulation Promotes Maturation of Cardiomyocytes Derived from Human Embryonic Stem Cells". J. Cardiovasc. Transl. Res. 2013 [322].

In contrast to the capacitive electrical stimulation applied to the cells in culture, whereby the cells are cultured in a potential field on traditional cell culture substrates, the cells are grown directly on the electrode surface of the bipolar electrode (BPE). In this case the cells are exposed to the interfacial potential of the bipolar electrode and the surface of the bipolar electrode itself. While capacitive stimulation is most commonly used cells stimulated in direct contact with the electrode is frequently used in microelectronic cell-on-a-chip style equipment [323,324]. These systems often allow for both electrical stimulation and electrophysiological recording of the cells in culture however their small

size can make it difficult to scale and reduces the applicability of the microfluidic with respect to in vitro studies.

The BPEs surface plays an important component when it is applied to a biological system. Cell adhesion is essential for culture as the majority of cell lines requiring electrical stimulation are adherent cell lines, this means a suitable surface for cell attachment is required for cell viability and normal cell growth.

This work describes the design optimisation for the wireless electrical stimulation of cells using wireless bipolar electrochemical techniques. The design parameters are assessed on the basis of cell culture health which is comparable to that of traditional unstimulated cell culture. The presence of a biologically relevant level of extracellular matrix present in the bipolar electrode surface is assessed by ICC and the observation of *in situ* cells in culture. Cells were observed following exposure to variable electrochemical field strengths and stimulation durations to assess the platform components stability. The ability of the electrochemical cell to deliver electrical stimulation to the cells on the electrode surface using these parameters was also assessed.

2. Materials and Methods

2.1. Cell culture

HL-1 murine cardiomyocytes were sourced from Sigma Aldrich (Ireland). Cells were passaged in a T75 culture flask coated with 0.02% Gelatin Fibronectin using supplemented Claycomb medium purchased from Sigma at 37°C with 5% CO_2. Claycomb medium was supplemented with 10% HL-1 screened Foetal Bovine Serum (FBS), 100 μg/ml Penicillin/Streptomycin, 0.1 mM Norepinephrine, and 2 mM L-Glutamine. Cells were cultured until they reached confluency then split using Trypsin/EDTA and soybean trypsin inhibitor, spun at 500 g for 5 minutes and seeded 1:3 in a precoated T75 flask. Claycomb medium is a custom mix of nutrients specifically designed for the culture of HL-1 cardiomyocytes designed by Claycomb *et al.* whom also first established the cell line for use in culture.

2.2. Bipolar electrochemical cell design 1

The bipolar electrochemical cells were formed from a 3D printed scaffold, printed from commercially available "Dental LT Clear" resin (Formlabs, USA), containing 12, 1 cm x 1 cm wells, mounted to a clear acrylic base using glass sealing adhesive (RTV silicone adhesive, Permatex, USA). Stainless steel (0.025mm pore size, The Mesh Company, United Kingdom) was used as the feeder electrodes and were located at the outside edge of the furthest most wells in each row of three wells. They were inserted bottom up and sealed in using the silicone adhesive. The feeder electrode ends were left free at the bottom of the scaffold to allow for the attachment of the power supply via crocodile clips. Between the two outside wells and the central well a 0.2 µm filter was placed to ensure cells did not adhere to the feeder electrode creating unwanted resistance. The centre wells were for the bipolar electrodes. The total length of the channel was 3 cm with each well volume approximately 1000 µL. An acrylic lid was used to maintain the sterility of the cell cultures during growth in the incubator. The assembly of these bipolar electrochemical cells was done in the laboratory.

2.3. Bipolar electrochemical cell design 2

For the second BPE cell design (BEC2), the major components of the platform, the 3D printed scaffold and clear acrylic base remained the same. Key component changes between BEC1 and BEC2 are highlighted in bold for clarity. The bipolar electrochemical cells were formed from a 3D printed scaffold containing 12, 1 cm x 1 cm wells, mounted to a clear acrylic base using **ARALDITE® RAPID RESIN,** instead of the silicone adhesive used in BEC1. The stainless-steel mesh feeder electrodes were replaced by **titanium foil (thickness 0.025 mm, 99.98% trace metals basis)**. The feeder electrodes were cut by hand using a stencil. The electrodes were **inserted top down** instead of sealed in from the bottom as in design 1 but maintained the tail for the attachment of the power supply via crocodile clips. The **filters** between the bipolar electrode chamber and the driving electrode chamber either side were **removed**. The centre wells were for the bipolar electrodes as in BEC1. A **single piece low density polyethylene lid** was fashioned to replace the two-piece acrylic lid used in BEC1 to prevent contamination due to incomplete sealing of the two pieces.

2.4. PPy-DS-Fibronectin doping of BPE

The optimal levels of fibronectin doping of PPy for cell adhesion and stimulation were investigated. The deposition method is the same as described in the previous chapter, were the FTO substrate is places in the PPy-DS-Fibronectin solutions and cyclic voltammetry was used between 0 and 0.7V. To determine the effect of fibronectin concentration in the deposition solution and its impact on the electrodeposited film the concentration of fibronectin was varied. A total volume of 50 ml was used for PPy-DS-Fibronectin deposition on the FTO substrate, the concentration of Pyrrole and Dextran Sulphate remained constant and the concentration of fibronectin was increased from 0 μg/ml to 20 μg/ml. The mole ratio of Fibronectin was increased in each deposition solution as outlined in the following table:

Table 4 – Composition of deposition solution for the electrochemical deposition of PPy-DS-Fib film on FTO substrate

Film PPy-DS-Fib	Pyrrole Mass (molar concentration)	Dextran Sulphate Mass (molar concentration)	Fibronectin Mass (molar concentration)	Molar ratio
5 μg/ml	0.6709 g (0.2 M)	0.1 g (250 μM)	250 μg (23 nM)	**1**: 1.2×10^{-3}: **1.15×10^{-7}**
10 μg/ml	0.6709 g (0.2 M)	0.1 g (250 μM)	500 μg (46 nM)	**1**: 1.2×10^{-3}: **2.3×10^{-7}**
15 μg/ml	0.6709 g (0.2 M)	0.1 g (250 μM)	750 μg (69 nM)	**1**: 1.2×10^{-3}: **3.45×10^{-7}**
20 μg/ml	0.6709 g (0.2 M)	0.1 g (250 μM)	1000 μg (92 nM)	**1**: 1.2×10^{-3}: **4.6×10^{-7}**
0 μg/ml	0.6709 g (0.2 M)	0.1 g (250 μM)	0 μg (0 nM)	**1**: 1.2×10^{-3}

The deposition CVs were conducted under constant conditions of room temperature and electrochemical cell setup, using a standard three electrode cell: FTO working electrode, a coiled platinum wire counter, and 1M KCl Ag/AgCl reference.

2.5. FTIR analysis PPy-DS-Fib

FTIR analysis was conducted on the deposited PPy-DS-Fibronectin films using a FTIR-ATR (Spectrum Two FTIR, Perkin Elmer). The film was analysed while deposited on an FTO substrate. The film was analysed face down in contact with the FTIR crystal, and the measurements were recorded at three distinct locations on each electrode and each location was assessed in triplicate across independent electrodes. The FTIR

spectroscopy was conducted using a single (n=1) electrode of each deposition formula i.e., 0, 5, 10, 15, and 20 μg/ml fibronectin.

2.6. Bipolar electrochemical cell sterilization and preparation for culture

To sterilise the electrochemical cell before culture, the cells were first rinsed in 70% IMS. Following drying from the 70% IMS solution the cell components (lid, Ti driving electrodes, and well chambers with the base) were exposed to UV radiation for at least 1 hour (30 Watt, maximum 1 meter from lamp) in the laminar flow hood.

To prepare and sterilise the PPy-DS-Fibronectin bipolar electrodes prior to HL-1 cardiomyocytes being cultured on their surface the electrodes were cut from the PPy-DS-Fibronectin deposited strips of FTO into 1 cm x 1 cm bipolar electrodes immediately before use, PPy-DS-Fibronectin electrodes were never reused during this work to avoid contamination. These electrodes were then placed in 70% IMS, left to dry, and then exposed to UV light prior to being inserted into the central chambers of the electrochemical cell (BEC2) [325–328]. Each platform could accommodate four bipolar electrodes to allow for high throughput culture. Post culture the entire platform along with the driving electrodes were sterilised using Diffex sterilisation solution in a sonicator for 15 minutes, after which it was rinsed with deionised water and allowed to airdry overnight and then stored until needed again.

2.7. Platform cell culture and stimulation

For culture using the bipolar electrochemical cell, the cells were removed from the T75 culture flask using Trypsin and soybean trypsin inhibitor as before and spun at 500 g for 5 minutes. The cell pellet was resuspended in 2 ml of wash medium (Claycomb medium with 10% FBS) and a sample was counted using a haemocytometer and Trypan Blue as an alive/dead stain for viable cell counting. Each well containing the bipolar electrode that was pre-coated with the gelatin fibronectin was seeded with 2000 cells/cm^2. For the control, the cells were seeded on the electrode and cultured unstimulated in the incubator at 37 °C with 5% CO_2. The medium was exchanged daily in all three wells of each row to ensure there was enough nutrients for the cells to grow. For the cells experiencing stimulation, the feeder electrodes were attached to a TENMA 72-13320

dual channel power supply which was computer controlled for potential. The stimulation protocols were applied as follows:

Table 5 – Details of stimulation protocol, a 1 V and 3 V stimulation protocol was administered over a 3-day and 7-day period.

Protocol	Potential	Duration of potential	Rest	Total stimulation time per day	Total experiment duration
1-1	1 V	10 minutes	5 minutes	1 hour	7 days
3-1	3 V	10 minutes	5 minutes	1 hour	7 days
1-8	1 V	10 minutes	5 minutes	8 hours	3 days
3-8	3 V	10 minutes	5 minutes	8 hours	3 days

During the stimulation process the medium was also changed in each well daily and the cell number, distribution and morphology was of the cultures was monitored using light microscopy.

2.8. Immunocytochemistry

Following culture of the cells on the bipolar electrodes, ICC was performed on the cultures using mouse anti-α smooth muscle actin monoclonal antibodies (1mg/ml, MA1-06110, ThermoFisher, Ireland) and mouse anti-cardiac Troponin T (0.5 mg/ml, MA5-12960, ThermoFisher, Ireland) and stained using goat anti-mouse IgG secondary antibodies conjugated with Alexa Fluor 488 dye. Once the experimental conditions had been completed, the cells were prepared for fixing by aspirating the cell culture media followed by washing gently with PBS 3 times with gentle agitation then fixed using 4% paraformaldehyde in PBS for 20 minutes at room temperature. The paraformaldehyde was then aspirated and washed again with PBS three times with gentle agitation. The surfaces were then blocked to prevent non-specific binding of primary and secondary antibodies using 500 µl of a blocking buffer of PBS with 5% Bovine Serum Albumin, 0.1%

Tween-20, and 0.3 M Glycine for an hour at room temperature. The blocking buffer was removed from all wells except for the negative control which was left in place. 500 µl of the primary antibody was added to each bipolar electrode, either α-SMA or cTnT was added to avoid non-specific binding of the secondary antibody cause by species immunoglobulin overlap. The antibody for both α-SMA and cTnT were diluted 1:200 with antibody dilution buffer (PBS with 1% BSA and 0.1% Tween-20). The primary antibodies were incubated overnight at 4°C. Following overnight incubation, the primary antibody solutions were removed by pipette, and the bipolar electrodes were again gently rinsed three times in PBS. Once washed, 500 µl of the secondary antibody, diluted 1:1000 with antibody dilution buffer, was added to each electrode and incubated for 1 hour at room temperature covered from the light. The secondary antibody was then decanted, and the electrodes were washed 3 times with PBS with Tween-20 using gentle agitation. For nuclear visualisation the cells were also stained with 10 µg/ml DAPI (D5942, Sigma Aldrich, Ireland) diluted in PBST by incubating the electrodes for 15 minutes at room temperature protected from light. Once the DAPI had been removed the electrodes were rinsed a final three times using PBST, they were then inverted onto a microscope slide and mounted using 15 µl of mounting media (P36970, ThermoFisher, Ireland). Once mounted the microscope slides were stored for at least 3 hours, preferably overnight, at 4°C while protected from light to allow mounting media to cure and then imaged using an Olympus fluorescent microscope.

2.9. Immunofluorescence Microscopy of Fibronectin

Primary anti-fibronectin monoclonal antibody (Invitrogen) was diluted 1:500 with antibody dilution buffer formulated from PBS without magnesium and calcium with 1% Bovine Serum Albumin (Sigma) and 0.1% Tween-20 (Sigma Aldrich, Ireland)). 100 µl of the primary antibody was then pipetted onto a strip of Parafilm and the bipolar electrodes were placed upside down into the deposited primary antibody, 100 µl per electrode was used (0.65 V, 0.7 V, 0.75 V, and blank FTO). As a control, cells cultured on bipolar electrodes were left in Bovine Serum Albumin and no primary antibody was used. All electrodes were then incubated overnight at 4°C, after which they were removed and washed x3 in room temperature PBS without calcium and magnesium (Sigma Aldrich, Ireland) for 5 mins with gentle agitation once or twice per wash. Once cleaned 1000 µl anti-mouse secondary antibody conjugated with Alexa Fluor 488 at a 1:1000 dilution was added to the bipolar electrode and was incubated at room temperature concealed from

light to protect the fluorescent probe for 1 hour. The secondary was then decanted, and the electrode was washed x3 in PBST (PBS with 1% Tween-20) at room temperature. 20 µl of mounting media was added to the electrodes and then the electrode was flipped onto a cover slip, taking care to avoid the capture of air bubbles between the electrode and the coverslip. The edges were then sealed with nail varnish to ensure the coverslips did not dry out. At least 8 – 10 images of the electrodes were then captured at magnifications of 10X, 20X, and 60X using a confocal microscope.

3. Results and Discussion

3.1. Bipolar electrochemical cell design 1
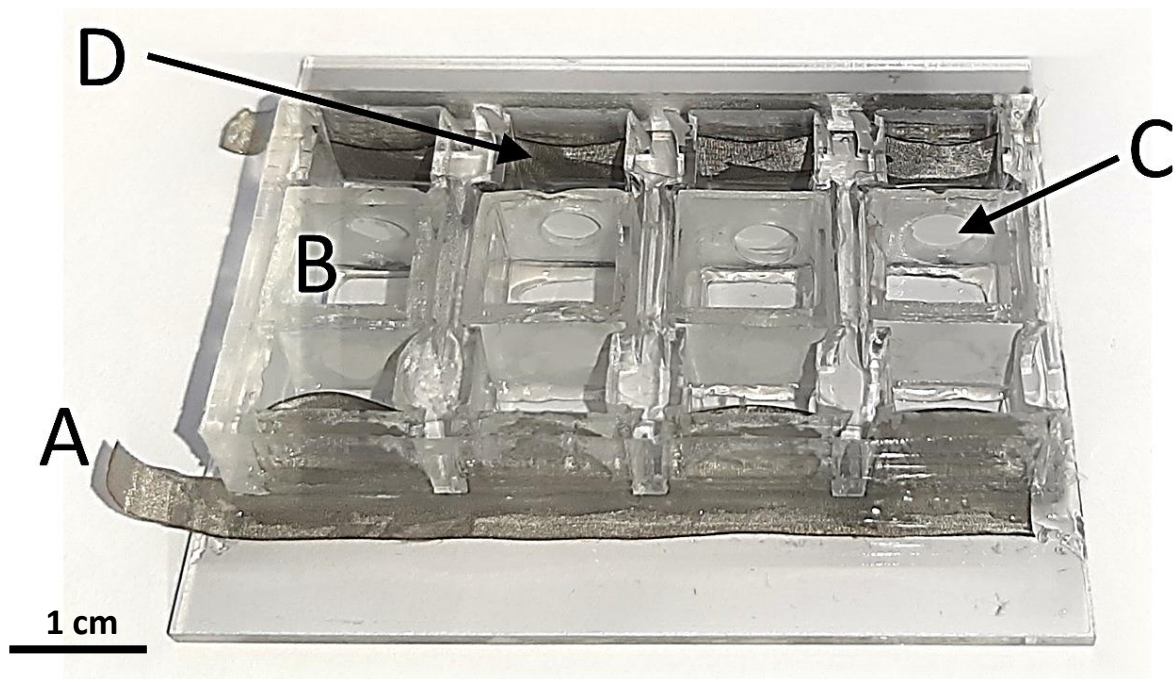
Figure 18. Cell used for culturing of HL1 cardiomyocytes while under electrical stimulation. A) Stainless-steel mesh driving electrodes which are connected via crocodile clip cable to a power source. B) the four central chambers for the PPy-DS-Fibronectin electrode on which the cardiomyocytes are cultured. C) Filter used to prevent cell adherence to the stainless-steel driving electrodes. D) Driving electrodes to complete the bipolar electrochemical circuit, this cell is filled with electrolyte or cell culture media during bipolar electrochemical experiments.

The device was generously donated by Professors Gordon Wallace and Jun Chen of the University of Wollongong, Australia. It came from a collaboration on a similar

electrochemical stimulation platform for use with PC-12 neuronal cells. These cells respond to electrochemical stimulation in culture which leads to an improved phenotypic cell growth more closely resembling primary *in vivo* cells, and I was a co-author on this work [165]. PC-12 cells were prepared in DCU in the same manner as the HL-1 cardiomyocytes. The Wallace group produced PPy-DS- Collagen type 1 wireless bipolar electrodes on an FTO electrode substrate. The film was deposited using a standard three electrode cell using an FTO working electrode, a 1M KCl Ag/AgCl reference electrode, and a platinum coil counter electrode and were produced in the University of Wollongong and transported to DCU. The cells were cultured on these electrodes and using the BEC1 wireless bipolar electrochemical cell. The cells were stimulated using a basic monophasic stimulation and cultured for 3 days. Following the third day the cells were removed from the BEC1 and the cells were stained for ICC to determine if dendrite formation had occurred. This work demonstrated that the platform shown above could successfully electrostimulate the PC-12 cell culture which led to an observable increase in dendritic growths from the cells in culture.

As discussed in the previous chapter the stimulation platform takes advantage of the electrochemical technique of bipolar electrochemistry. This method allows an interfacial potential to be induced when a conductive material, the bipolar electrode (BPE) is placed in an electric field driven by the connection of two driving electrodes.

The bulk of the design is formed using a 3D printed well design, closely resembling traditional culture platforms such as 6 well plates. The 3D printed cell consisted of four by three well pattern as can be seen in **Figure 18.** The 3D printed cell structure was then bonded to a transparent acrylic sheet to form the base of the platform. The upper and lower portions were sealed using silicon adhesive sealant.

To induce a bipolar electrochemical effect the driving electrodes must be connected to a power supply. To achieve this a stainless-steel wires mesh was employed for its conductive properties and its inertness. The mesh was cut in a long outer strip with four driving electrode "teeth" with are inserted into the outer wells on the upper portion of the platform. The outer strip is cut approximately 1 cm beyond the length of the 3D printed section. This is to facilitate the connection of the driving electrode to the power supply. This feature can be seen highlighted by **A** in **Figure 18.** This connection allows all four rows of the platform to be stimulated in parallel, increasing the number of cultures which can simultaneously stimulated.

Each well of the 3D printed upper consists of a 1 cm x 1 cm x 1 cm volume well, with three wells to a row. This makes the overall length of the channel 3 cm. The length of

the channel is a very important parameter for a bipolar electrochemical set up. The key equation for bipolar electrochemistry is the calculation for the maximum polar overpotential achievable at the BPE. This equation is a simple one and is represented by Equation 3:

$$\Delta E_{elec} = \frac{E_{tot}}{l_{channel}} l_{elec} \tag{3}$$

Therefore, the potential available for cell culture stimulation is proportional to the length of the BPE relative to the distance between the driving electrode i.e., the length of the channel.

The BPE is placed in the central well, represented by **B** in **Figure 18**, thus placing the BPE in the centre of the channel. The dimensions of the are 1cm x 1cm, hence the maximum ΔE_{elec} is a third of the total applied potential (1 cm / 3 cm). These distances are maintained by the wall structures of the 3D printed upper structure of the platform.

The BEC 1 the cells were seeded onto the BPE surface after it was placed in the BPE cell. The seeding procedure was similar to that of traditional culture with the cell concentration calculated to a given volume and diluted from the stock culture prior to seeding, typically at a seeding density of 5000 cells cm^{-1}. The cell medium mixture was then added to the central well and allowed to adhere overnight. After 15 hours, the medium was changed to remove any non-viable or unadhered cells. The custom cut Polyvinylidene Fluoride (PVDF) membrane was then placed between the outer and central wells, as denoted by **C** in **Figure 18** above. This permeable membrane allowed the medium, also acting as the electrolyte, to pass between wells but did not allow cells through during the seeding period. The potential at the driving electrode is three-fold higher than that experienced at the BPE and therefore any cells that may adhere to this surface would certainly be destroyed at high potentials. These destroyed cells can lead to the secretion of cytotoxic compounds triggering further cell death in the rest of the culture.

The final design feature to draw attention to are the driving electrodes at the ends of each row of wells, denoted by **D** in **Figure *18***. The driving electrodes are the protrusions from the single cut-out of the stainless-steel mesh. The driving electrodes are cut to extend the full width of the channel to ensure a potential gradient which can be applied to the full width of the BPE also, thus ensuring all areas of the cell culture are exposed to an interfacial potential when growing on the BPE. In this design the driving electrodes

are inserted between the 3D printed upper section and the acrylic lower section of the platform. The silicon sealant is applied on and around the driving electrodes under the 3D printed upper allowing it to be secured in place and also maintain the seal to prevent leakage. The driving electrodes are located in a slot in the upper section to hold them upright and fix their position, therefore also fixing the distance over which the voltage is dropped.

3.2. Cell Stimulation Experiments

Traditionally HL-1 cardiomyocytes are cultured on a 0.02% gelatin and 5 µg/ml fibronectin layer on the culture substrate. This layer aids the cell adhesion of this particular cell line. The initial experiments were conducted using the BEC1 supplied by the Wallace group of the University of Wollongong. The Wallace group also supplied PPy bipolar electrodes for the electrical stimulation. These electrodes originally had Collagen type 1 incorporated instead of fibronectin. To adapt these electrodes a gelatin/fibronectin coating was deposited on top of the electrodes to enable the adherence of HL-1 cardiomyocytes in culture. The aim of these initial experiments was to examine if the bipolar electrochemical cell could deliver significant stimulation to the cardiomyocytes to generate a quantifiable physiological response in the HL-1 cardiomyocyte cell type. The experiment was broken into three parameters, a control group of cells which were cultured unstimulated for the duration of the experiment to examine any potentially toxic effects of the PPy films which may influence the growth of cells in culture. The second group of cells were exposed to one hour per day of electrical stimulation at 1 V for a total of 7 days. The third group of cells were exposed to one hour per day of electrical stimulation at 3 V for a total of 7 days. The control group of cells did not experience an ill effect in terms of growth relating to the presence of the PPy, indicating that within this system the PPy film is compatible with cell culture. When examined under the light microscope the cells did not differ with respect to morphology, distribution, or confluency indicating a healthy culture was achieved within the bipolar electrochemical cell, due to instrument down-time it was not possible to quantify and compare viable cells. Both stimulated cell groups experienced one hour of electrical stimulation per day over the course of seven days with one group experiencing 1 V at the driving electrode (0.333 V cm^{-1}) and another experiencing 3 V at the driving electrode (1 V cm^{-1}). The primary goal of the experiment was to begin to optimise the stimulation voltage for the cells since a larger electric field leads to a higher potential at the bipolar electrode. However, upon application of the two potentials it became clear that the higher

potential would not be suitable for cell stimulation since the cell culture media becomes discoloured most likely due to oxidation of the stainless steel. Observations under the light microscope showed that the cells in culture had died and by the end of the seven days experiment and no cells were visible. At the end of the experiment, it was also observed that the stainless-steel feeder electrodes were deteriorating to the point where they had lost their physical integrity. It is unclear whether the potential was too high and lead to the oxidation of some constituents of the cell culture medium or if the discolouration was directly linked to deterioration of the feeder electrodes leading to a cytotoxic effect on the cells.

As the optimal potential for cell stimulation on the wireless bipolar electrodes may require a high voltage to be applied to the feeder electrodes, a secondary experiment was conducted adjusting the stimulation time frame to 8 hours per day for 3 days. This was done to examine if a shorter time frame could preserve the cells using a 3 V potential and mitigate the deterioration of the feeder electrodes. The shorter time frame did not yield an improved outcome. Once again, the feeder electrodes deteriorated significantly, and the cell culture medium progressively fouled leading to the loss of the cell culture. There was no appreciable difference in the performance of the bipolar electrochemical cell at either 1 hour per day over 7 days or 8 hours per day over three days at 3 V and it is clear that under with this set up, this potential is not viable for cell stimulation. If a higher potential (above 1 V) is required for the stimulation of the HL1 cardiomyocytes, then further investigations of composition of the feeder electrode material will be required, e.g., the use of titanium. Currently, a fine stainless-steel mesh is used as the feeder electrode in order to maximise the surface area; it may be possible to achieve better performance at a higher potential by using a higher gauge mesh, using a more corrosion resistant stainless steel, e.g., marine 361, or by switching to a platinum feeder electrode. With regards to the 1 V stimulation, the experimental set up showed satisfactory performance with no visible deterioration of the feeder electrodes and no discolouration of the growth medium. Examination of the culture under light microscopy showed that the distribution and morphology of the stimulated and control population of cells were similar.

3.3. Immunocytochemistry

Following the successful culture of the control group along with both stimulation protocols, a quantitative review of the three cultures was then carried out using ICC. The proteins chosen for the ICC were cardiac Troponin T (cTnT) and α-smooth muscle actin

(α-SMA). These proteins were chosen as they are not only cardiomyocyte specific proteins which serve to characterise the cells as cardiomyocytes, they are also structurally relevant within the cells. In the case of cTnT it has been shown to have altered expression level in cells exposed to different stimuli and it was possible that by staining for cTnT a differential expression or localisation of the protein could be observed between the stimulated and control groups. α-SMA is a structural protein expressed in smooth muscle cells and aids in the contraction of these cells. This protein was stained for to visualise internal structures of the cardiomyocytes and to identify any specific changes observed in the cell cultures following stimulation. The proteins were stained using traditional ICC protocols; primary anti-mouse cTnT and anti-mouse α-SMA were used followed by goat anti-mouse secondary antibody conjugated with Alexa Fluor 488.
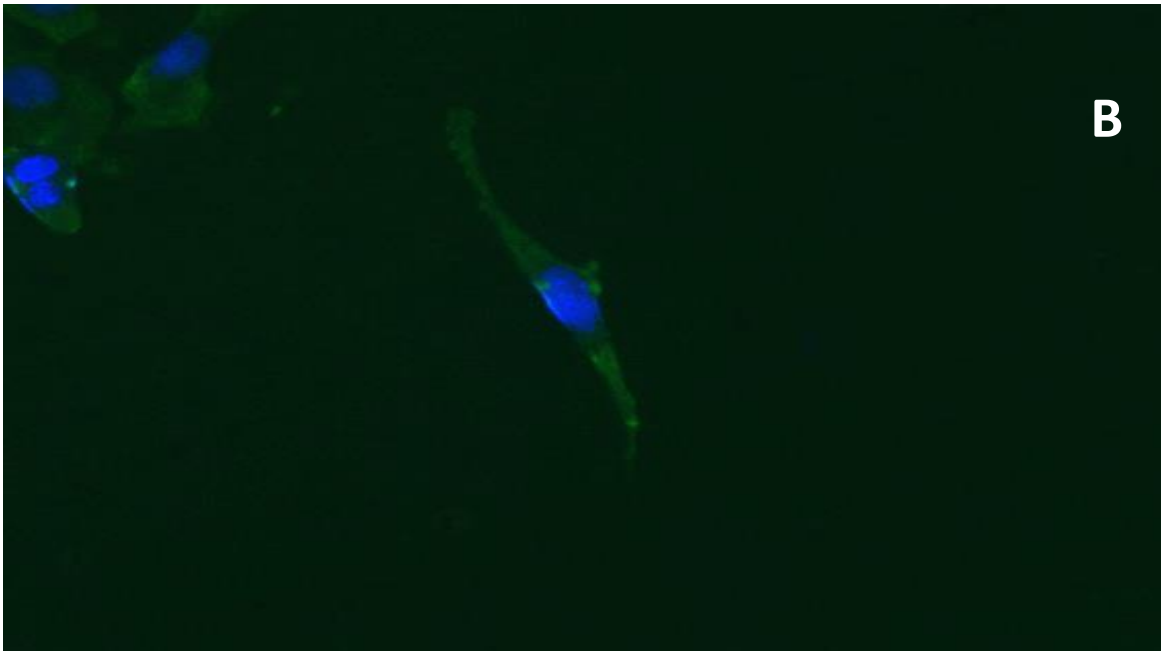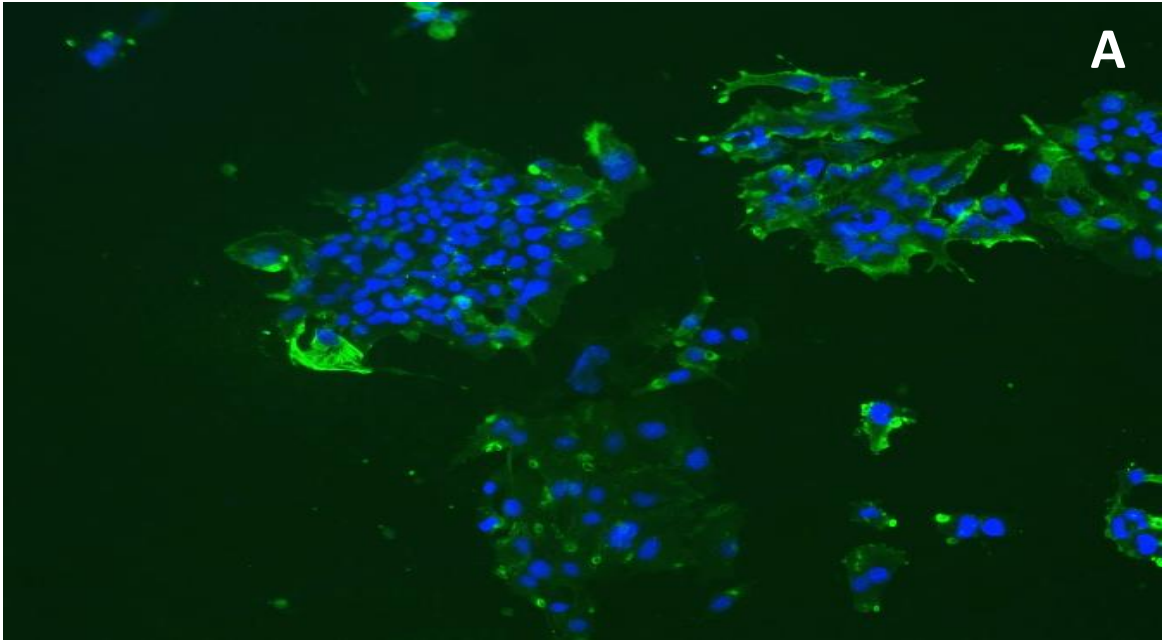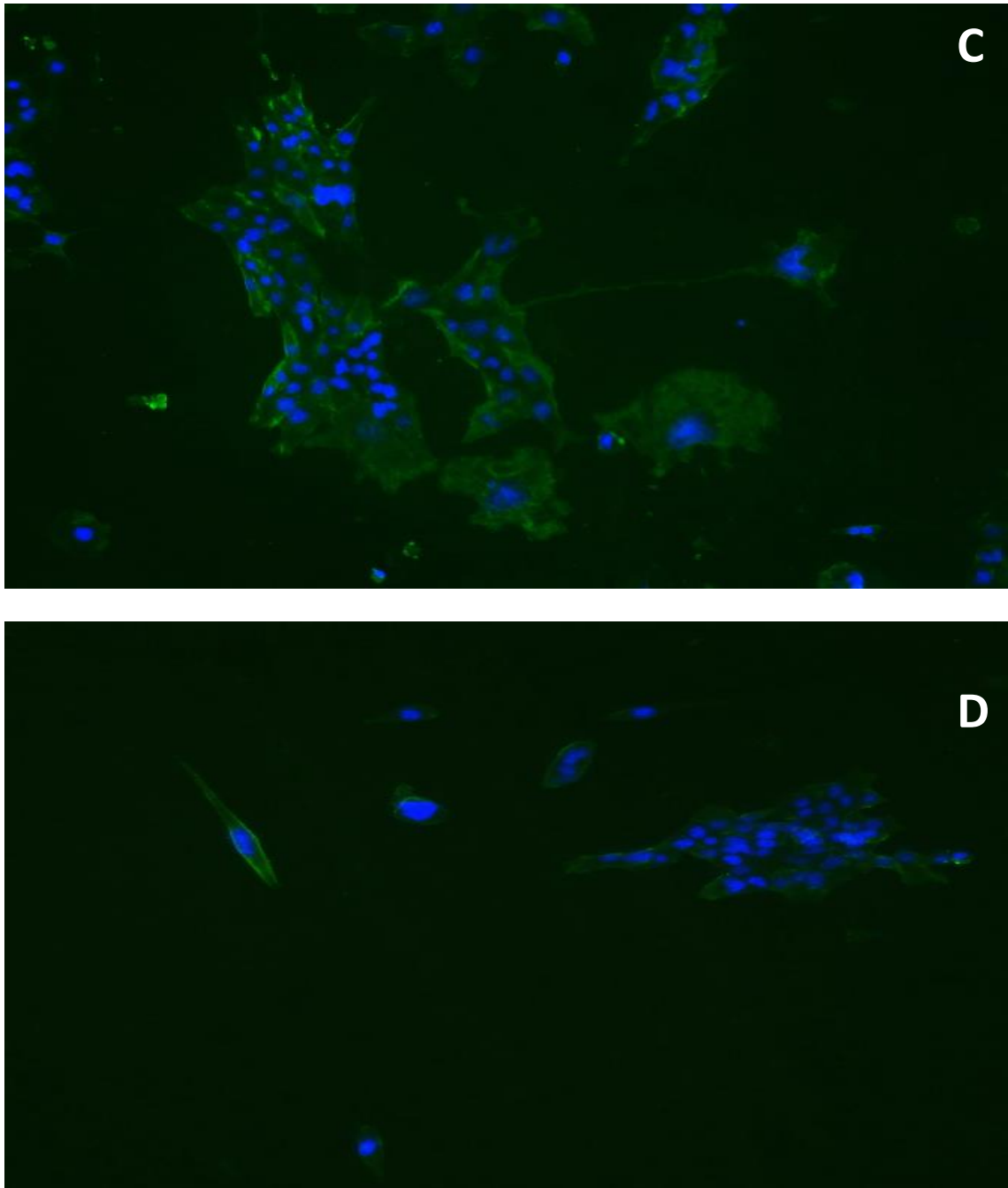
Figure 19. Fluorescent microscopy images of HL-1 cardiomyocytes stimulated using stimulation protocol A and B represent two images from independent electrodes stimulated at 1 V for 1 hour per day with 10 minutes of stimulation and 5 minutes rest for a total of 7 consecutive day,s and C and D represent two images from independent electrodes stimulated at 1 V for 8 hours per day with 10 minutes of stimulation and 5 minutes rest for a total of 3 consecutive days.. The cells were cultured on PPy-DS-Collagen I electrodes coated with 0.02% gelatin fibronectin. Images shown are nuclear stained using DAPI (Blue) and mouse anti-α SMA primary antibody with goat anti-mouse secondary conjugated with Alexa Fluor 488. Each condition was replicated a single time generating four independent cultures stimulated in parallel.

ICC images of the cells following stimulation at 1 V for 1 hour per day with 10 minutes of stimulation and 5 minutes rest for a total of 7 consecutive days (A, B) and 1 V for 8 hours per day with 10 minutes of stimulation and 5 minutes rest for a total of 3 consecutive days (C, D) are shown in **Figure 19**. All images shown above represent α-SMA in the cardiomyocyte cells. There were issues regarding the permeability of the cells and therefore it was difficult to fully resolve intracellular localisation of the primary antibodies. The stimulated ICC images illustrate the various cell morphologies of the culture following exposure to the electrical stimuli. Two observations can be made firstly, there are predominantly two morphologies observed in the culture. The first being the disordered confluent "islands" of cells which can be seen in images A and C above. These cell morphologies are consistent in their disordered irregular pattern and are the primary morphology observed in the stimulated cultures. These "islands" of confluent cells are consistent with unstimulated cell cultures grown using traditional methods at a high rate of confluency (> 75%) prior to full confluency where cell sheets are formed. The second morphology observed in the cultures can be seen in images C and D (which have been expanded to better highlight the morphology and are not same scale as images A and B). The morphology observed in these cells is that of an orientated mature cardiomyocyte and has been shown in literature to be optimised in this elongated shape for contractions [49–51]. This morphology of cell is also seen in unstimulated cultures at a lower confluency level between 10% and 60% where cells have adhered, but not yet come into contact with neighbouring cells to begin the formation of the aforementioned cells sheets of a fully confluent culture of HL-1 cardiomyocytes [52,53]. Previous work on the electrical stimulation of muscle cell including cardiomyocytes suggest that the cells, when cultured using electrical stimulation, align themselves in culture. In the case of this work there is no current conducted through the bipolar electrode in the absence of redox reactions, as such the potential experienced by the cells in this case does not have a direction and therefore the orientation of the cells should not be affected [54,55]. Observations of the cells under bright field and fluorescent microscopy are inconclusive as to the influence of the potential at the bipolar electrode on the cells in culture. While there was evidence of the matured rod shape cardiomyocytes observed in both culture 1-1 and 1-8 these cell morphologies were also observed in the control. There was no quantifiable difference between the control cell phenotype and those that experience the stimulation conditions. The most immediate reason for this being the case would be that the gelatin fibronectin layer did not provide a suitable substrate for the conduction of the applied potential to the bipolar electrode surface. It is also possible that the electrode did

transmit the potential, but the gelatin fibronectin layer significantly removed the cells from the surface or otherwise insulated them from the potential. If this is the case, we would expect to see a significant divergence from the control group when cells are applied directly to the PPy-DS-Fibronectin bipolar electrode which has been developed and characterised above and has shown to be electrochemically active. The results observed using the gelatin fibronectin film further reinforce the need to develop a bipolar electrode which incorporates extra cellular matrix proteins to allow direct cell adherence to the electrode.

The second observation is that there was no appreciable difference between the two stimulation protocols, the cells did not respond to a short stimulation protocol nor an extended stimulation protocol. It is important to note that the total duration of stimulation is different, i.e., 7 vs. 24 hours, however in unstimulated culture the cardiomyocytes will reach confluency in three days before passaging is required. While a direct comparison is not possible between the two protocols, it should be noted that neither provided more suitable conditions for stimulating the cells. The same cell morphology and distribution was observed in both cultures with both parameters yielding predominantly confluent islands with small individual cells showing a more mature phenotype and rod shape expected of a developed cardiomyocyte. Clearly the stimulation applied to both cultures did not cause a significant change in morphology. However, there was a significant difference in duration of both experiments with those cells under the 1-8 stimulation undergoing a shorter stimulation period (3 days vs 7 days). Given that the confluency of both the 1-1 and 1-8 was approximately the same, it is possible to conclude that simulation for 8 hours for a total of three days offers an advantage to the 1 hour per day for 7 days protocol as it does not inhibit the cell growth and provides a similar cell density and morphology in half the incubation time meaning follow up experiments can be conducted in a more time efficient manner with comparable results to a slower and more moderate stimulation protocol.

3.4. Bipolar electrochemical cell design II

To address the issues with the original BEC1 design, minor adjustments were made to improve functionality.

The main area of concern was the inability of the stainless-steel mesh driving electrodes to withstand driving potentials greater than 1 V, i.e.,   the stainless-steel disintegrated at a driving potential of 3 V, even for a relatively short stimulation times whereas cell culture

stimulations require several days. The time of stimulation, 10 minutes of potential and 5 minutes resting with no potential applied, is also well within normal stimulation experiment protocols seen in the literature. EF Stimulation protocols can vary in terms of the electric field strength applied. As the first-generation platform reduced the potential difference at the BPE to a third of the potential difference between the two feeder electrodes, the ability to apply relatively high potential at the driving electrodes is essential.

To address this issue the stainless-steel mech was replaced by a titanium sheet (99.98% Ti, 0.025 mm). The thickness of the Ti sheet allowed it to be cut using some scissors to the same dimensions as the stainless-steel mesh. It also meant that the sheet could be cut using the same outline as the mesh and could be placed in the platform in the same slot and hold its position. The orientation of the driving electrodes was also switched. Instead of being inserted from the bottom, as the stainless-steel mesh was, the driving electrodes were now placed from the top down. This made the electrodes removable which aided in their sterilisation. The structural integrity of the sheet over the mesh allowed for this new orientation as the driving electrodes could hold their shape better that the mesh alternative. The driving electrodes did not require fixing into position using an adhesive as a simple crease along the top of the electrode strip was enough to hold them securely in place while in use. Again, an extra length of sheet was left on the electrode strip as a connection point for the crocodile clip used to form the circuit with the power supply. The Ti sheet performed very well as an alternative driving electrode material capable of maintaining higher potentials for longer periods of time than the stainless-steel mesh used previously [329]. The Ti driving electrode performance was confirmed using deionised water and a universal indicator. The reduction and oxidation at the anode and cathodic driving electrodes using a driving potential used was 1 V cm^{-1} and the colour change indicates the presence of a potential field, **Figure 20**.
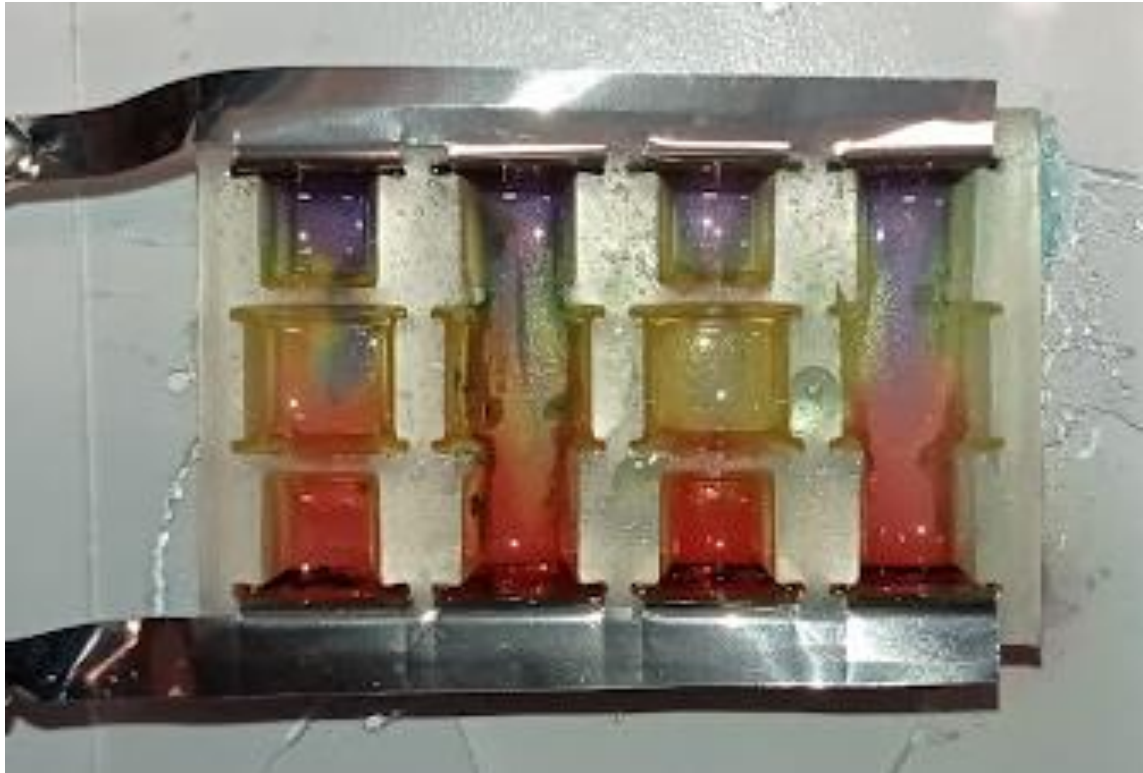
Figure 20. Universal indicator showing the potential at the Ti driving electrodes when a potential field of 1 V cm^{-1} is applied. The driving electrode triggers water splitting which in turn alters the pH at the driving electrodes, which is illustrated by the red and blue colour change observed in the Universal Indicator. Note the bipolar electrode is not present, this figure serves to illustrate the driving electrode potential. Experiment was performed with a duplicate using two independent bipolar electrostimulation platforms.

In line with the improved durability of the driving electrodes other durability features of the BEC was also improved. It was noted in previous experiments that the silicon adhesive used to bind the 3D printed upper and the acrylic lower was not suitable for extend use or re-usable following the completion of electrostimulation. While it did provide an excellent waterproof seal it could not be used more than once and, on the occasions where re-use was attempted, the two sections of the platform came away from each other rendering them useless. It is believed the continued exposure to 37 °C of the incubator combined with the high humidity and contact with moisture for extended periods of time effected the integrity of the seal. It is also possible that the use of solvents, such as ethanol and 70% IMS could also contribute to the deterioration of the seal. To compensate, a more robust method of adherence was required. To achieve this a two-part epoxy adhesive was used. Both parts of the adhesive are combined and applied to the bottom of the 3D printed upper section. The entire bottom of the upper

section was completely covered in adhesive to ensure a tight seal. All efforts were made to ensure no bubbles were included in the adhesive during applications in order to avoid leaks from the upper section out onto the base but also between the rows of the upper. Cross contamination between the rows of wells is essential to avoid cytotoxic components transferring between cultures in the event of any issues during stimulation. The seal between well rows and to the outside edges is also critical in the event of bacterial or fungal contamination; however, the presence of any microbiological contamination led to the termination of any experiment where it was detected. As mentioned above, the relocation of the driving electrode from between the upper and lower section to insertion from the top of the upper section also played a critical role in durability and leak-free construction of the BEC II platform.

3.5. Fibronectin incorporation into the film – ICC

The presence of fibronectin is an important component in the film in order to ensure good cell adhesion to the surface and provide suitable stimulus for representative phenotypic growth. The level of fibronectin doping was varied it to determine the optimal concentration of fibronectin in the film surface. The doping level was varied by adding the protein to the deposition solution using the same deposition method. Fibronectin was added to the pyrrole and dextran sulphate aqueous solution at concentrations of 0 µg/ml, 5 µg/ml, 10 µg/ml, 15 µg/ml, 20 µg/ml.

Electrochemical deposition of the PPy-DS-Fib was performed using a three-electrode cell, using FTO as the working electrode, an 1M KCl Ag/AgCl reference, and a coiled platinum wire counter electrode. The potential was cycled from 0 V to 0.7 V and the pyrrole is oxidised to form a polymer with the incorporation of stabilising counter ions. As discussed previously, the fibronectin is expected to incorporate into the PPy film to help balance the positive charge of the PPy. The most important function of the fibronectin in the film is to function as an extracellular matrix protein anchor point for cell adhesion. This anchoring of the cell using fibronectin also initiates a signal cascade in the cells expression profile which helps to ensure the correct phenotypic response in the cells in culture. To elucidate the presence of biologically relevant fibronectin, i.e., fibronectin on the surface of the film which the cell membrane can functionally adhere to, ICC was used. The adherence of the primary anti-fibronectin antibody is used as a proxy for the integrin receptor proteins of the cell membrane. Dye functionalised secondary antibodies highlight the regions of exposed fibronectin which cell membranes could also access.

0 ug/ml

100 µm

5 ug/ml

100 µm

10 ug/ml

100 µm

15 ug/ml

100 µm
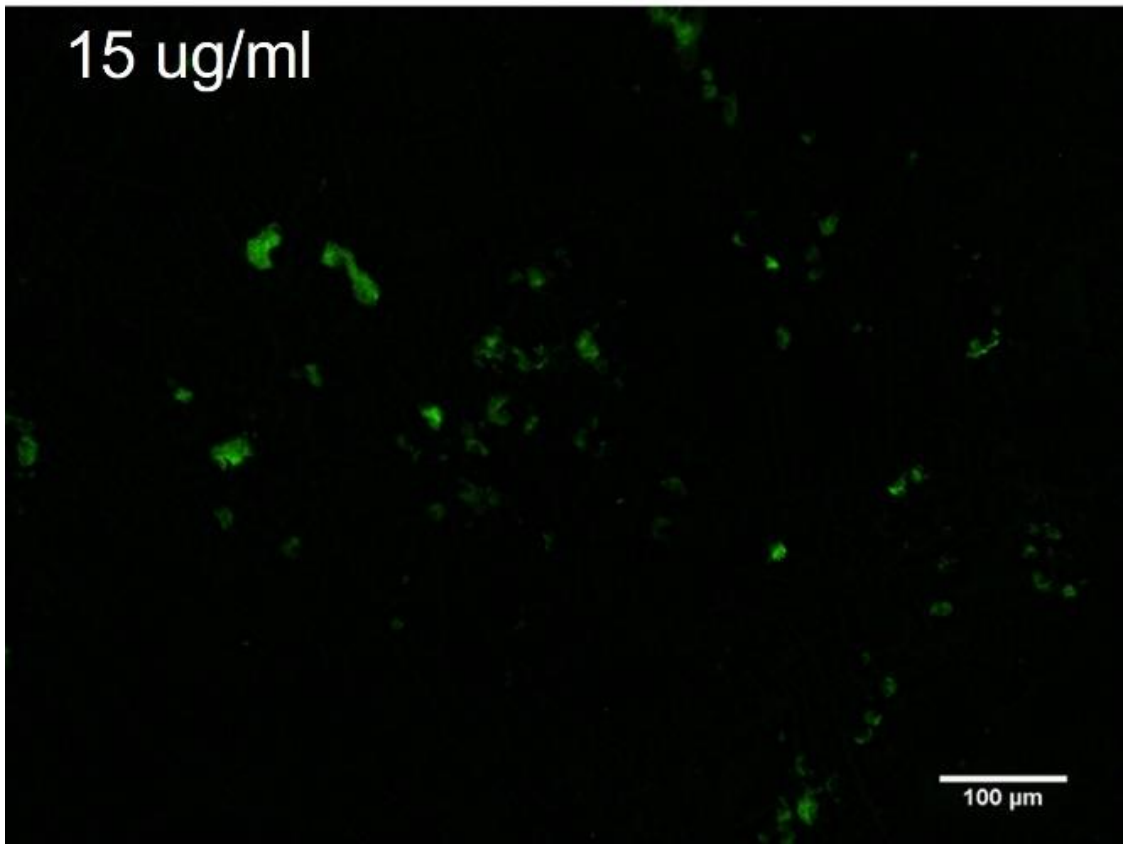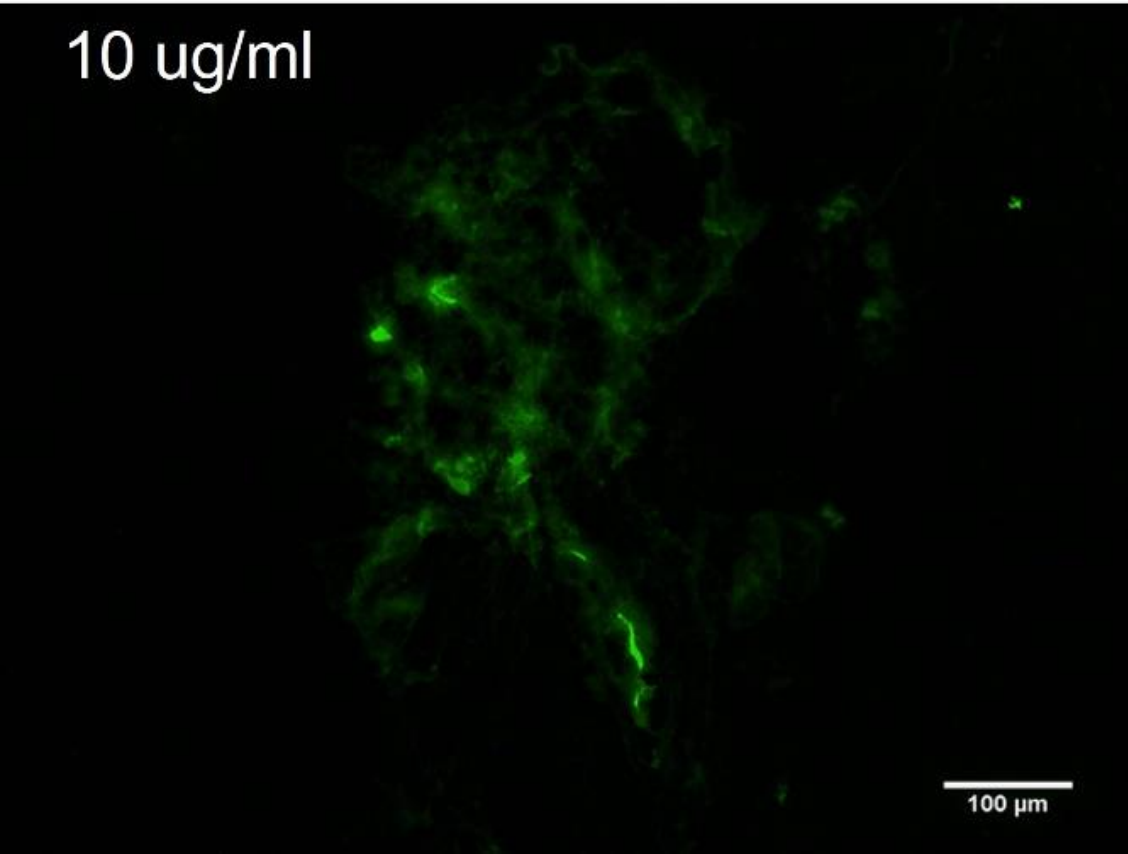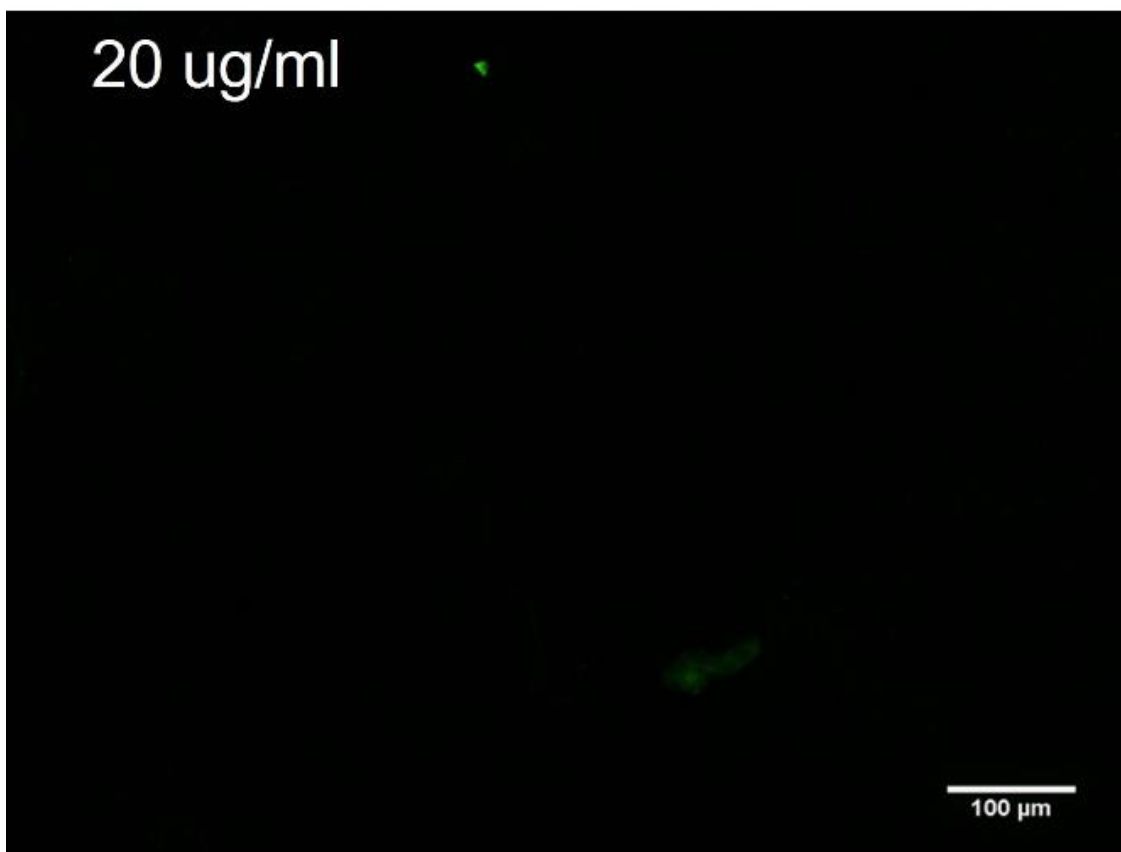
Figure 21. ICC of different PPy-DS-Fib film deposited from films using various loadings of fibronectin in the bulk solution during deposition. The films were stained using and anti-fibronectin (1:50) primary antibody and a FITC labelled secondary antibody. The loading level of each film is indicated above each image and ranged from 0 to 20 µg/ml. Staining was performed in triplicate on three electrodes from the same batch.

ICC of the PPy-Dextran sulphate film with no fibronectin present in the deposition solution did not show any evidence of antibody binding when examined under a fluorescent microscope. This is an expected result as the primary antibody was raised against the fibronectin protein, however, this result confirms the absence of any cross reactivity between the primary or secondary antibodies with the constituents of the film. Therefore, no measurable cross reactivity occurs with the dextran sulphate, pyrrole polymers, or the intrinsic surface topography of the film. Positive antibody staining was observed in the samples containing fibronectin in the deposition solution, confirming that fibronectins addition in the deposition bulk solution leads to the proteins inclusion in the films formed through electrodeposition.

The films deposited from containing the solutions containing 5 µg/ml and 10 µg/ml loadings of fibronectin showed the highest intensity responses for the positive presence of fibronectin along with the most wide-spread distribution through the film. The staining

of the fibronectin is not uniform throughout the film. As can be seen in Figure 21 the fibronectin deposits in the film appear in a fibrous and concentrated areas. These areas are distributed across the surface area of the film. The film deposited from the solution containing 15 µg/ml showed less concentrated areas of fibronectin deposits but showed less surface availability than the 5 and 10 µg/ml concentrations. The highest loading of fibronectin tested, 20 µg/ml, did show many positive areas of fibronectin.

It is unclear what is impacting the distribution pattern of the fibronectin from the results of the ICC imaging. Fibronectin deposited in the typical adsorption method for cell culture flasks provides a random homogenous and aggregation-free distribution pattern as opposed to the aggregated, island distributions observed with the PPy-DS-Fib films. Fibronectin proteins tend to aggregate in solution and do not solubilise well into solution. This physical characteristic on the proteins could help explain the fibrous depositions identified in the films. It would also explain the lower observed fibronectin in the highest loading concentration, suggesting that at 20 µg/ml the proteins do not mix well in the solution and therefore are not deposited with the film. Observations of the 20 µg/ml showed a concentrated film at the top of the bulk solution also indicating the lack of solubility at the highest fibronectin concentrations. This experiment shows that there is accessible surface level fibronectin available following deposition of PPy-DS-Fib bulk solution using cyclic voltammetry. Logistical issues with the thickness of the FTO substrate relative to the focal length of the fluorescent microscope meant a higher magnification could not be used. The dark nature of the PPy film coupled with the dark backlight of the fluorescent microscopy also adds to the difficulty in visualising the FITC labelled antibodies in the image. The absence of a strong colour coupled with the magnification limit makes it harder to visualise more diffuse fibronectin on the electrode surface which might provide quantitative analysis of the concentration of fibronectin present in each film in relation to the initial loading of the bulk solution; i.e., if the concentration of fibronectin in the bulk solution of 5 and 10 µg/ml translates to the film or if there is a relative two-fold increase in the level of fibronectin observed in each film.

3.6. Fibronectin incorporation into the film – FTIR

To elaborate further on the constitution of the film when the fibronectin loading is varied in the bulk deposition solution FTIR analysis was performed on the different film compositions. The aim was to determine a quantitative analysis of the fibronectin presence in the film. The presence of all three constituents can be determined for the FTIR spectra of the films, PPy, DS, and fibronectin, represented in **Figure 22**.
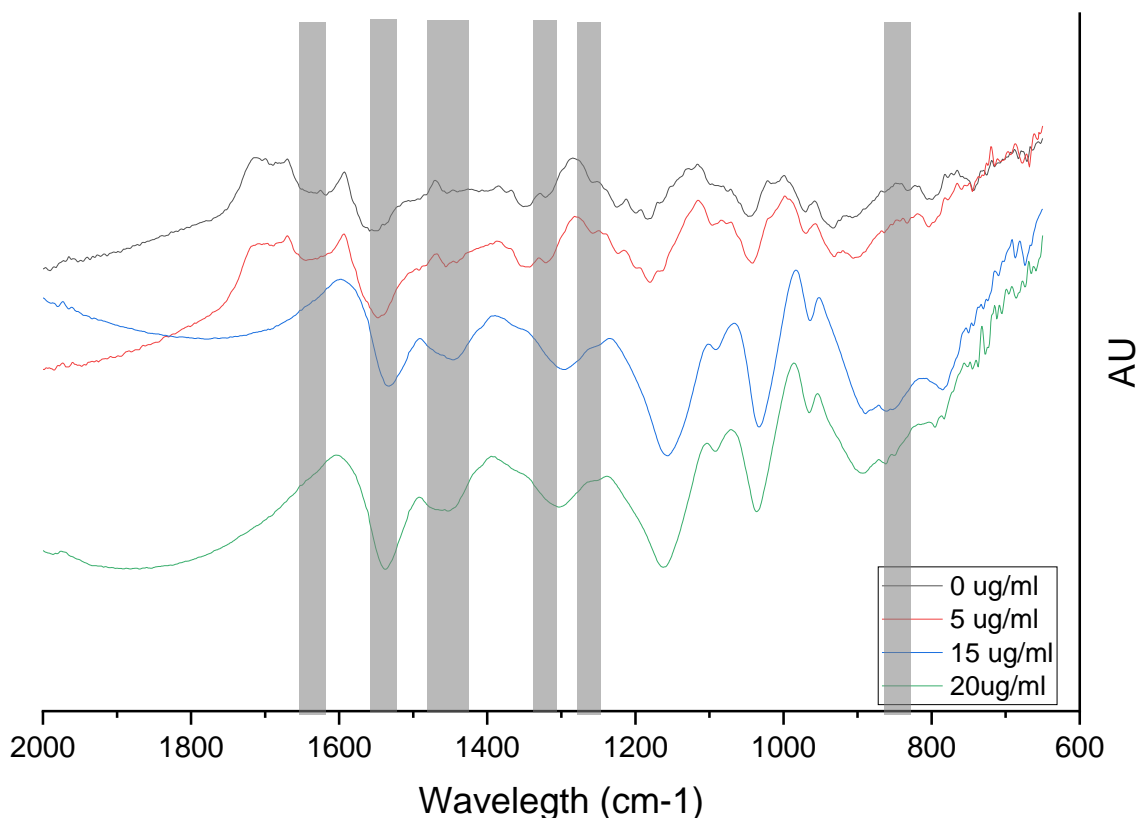
Figure 22. FTIR spectra of PPy-DS-Fib films containing 0 µg/ml, 5 µg/ml, 15 µg/ml, and 20 µg/ml fibronectin in the bulk deposition solution prior to electrochemical deposition. A single replicate of each spectrum was obtained.

Firstly, multiple peaks in all four spectra indicate that indeed the films consist of polypyrrole. The characteristic polypyrrole peaks can be observed at 1560 cm^{-1} and 1485 cm^{-1} indicative of C=C stretching. Similarly, there is a peak at 1690 cm^{-1} representing C=N and another peak at 1317 cm^{-1} representing C-N bonds. These peaks are particularly evident in the 0 µg/ml PPy-DS sulphate film but also are present in the other films indicating the presence of the fibronectin does not interfere with the ability to form PPy using electrodeposition [330].

Secondly, all bulk solutions of the deposition solutions contained dextran sulphate as a counterion to balance the positive charge of the polypyrrole backbone. Peaks at 1260 cm^{-1} and 830 cm^{-1} indicate the presence of S=O and O-S-O bonds, respectively. The presence of these peaks is indicative of the dextran sulphate successfully acting as a counterion during deposition and remaining present in the films [331].

Finally, there are peaks present in the FTIR spectra which confirm the presence of fibronectin in or on the films. The large peaks present at 1650 cm^{-1} and particularly 1540 cm^{-1} are considered amide I and amide II peaks respectively. These peaks are typical of the polypeptides and indicative of the presence of fibronectin at the film surface. In particular the presence and growth of the amide II peak at 1540 cm^{-1} , while it is a peak indicative of C=C stretching discussed in relation to PPy the growth of the peak in the films deposited using 5, 15, and 20 μg/ml fibronectin indicates that there is u polypeptide presence in the film additional to the PPy [332]. The growth of the peaks suggests that the initial concentration of fibronectin in the bulk deposition solution does affect the quantity of fibronectin found in the FTIR spectra however the levels varied widely and did not represent a reliable or quantifiable doping level of fibronectin in the films. Increasing the concentration of fibronectin in the bulk concentration does increase the level of doping in the deposited film however reproducibility is an issue.

FTIR did not provide further clarification on the positioning of the fibronectin in relation to the film. It was not possible to deduce if the fibronectin is imbedded in the film or adsorbed only to the surface passively in the time following deposition. It is possible for this deposition to occur and withstand the cleaning processes following deposition. The evidence gathered is ultimately inconclusive about a possible mechanism for fibronectin inclusion in the film during electrodeposition.

4.   Conclusions

The work above describes the successful design of a reliable and reusable cell stimulation platform based on bipolar electrochemical process. It allows for the application of an interfacial potential at a bipolar electrode using a **wireless** methodology. It also describes the characterisation of the bipolar electrode surface with respect to presence of key components for the integration of the electrode into a biological system. The presence of fibronectin was successfully shown in the film using immunocytochemical staining for surface fibronectin availability. This was backed up by the results of FTIR spectra of the films which confirmed the presence of fibronectin, which was deposited during the electrodeposition process from the bulk solution. The spectra also suggested the amount of fibronectin present was related to the concentration of the protein in the bulk deposition solution, however reproducibility was not high enough to provide a quantitative relationship between bulk solution

concentration and final fibronectin content of the deposited film. Unfortunately, neither ICC nor FTIR could elucidate the precise distribution characteristics of the fibronectin in the film, with regards to its presence within the film itself or solely at the surface of the film.

The work shows that the cells could successfully be cultured on a wireless bipolar electrode with a stimulation potential of 1 V. According to the calculation for wireless bipolar electrode the interfacial potential likely experienced by the cells was 300 mV. The bipolar electrode with incorporated fibronectin could support both unstimulated and stimulated cell cultures. This indicates the doping method of fibronectin, and the electrodeposition of the PPy-DS-Fibronectin film is suitable for the culture of HL-1 cardiomyocytes. There was no immediate evidence of electroporation at the 300 mV potential, however, extended stimulation times did lead to metal leeching from the driving electrode causing cell death. Further work is required to fully assess the platform with respect to stimulation performance in a variety of experimental conditions and stimulation waveforms.

Chapter 4

Wireless Bipolar Electrostimulation of Cardiomyocytes on variable Fibronectin Doped PPy-DS-Fibronectin bipolar electrodes using biphasic electrostimulation waveforms

1. Introduction

Electrostimulation of cell cultures is an important method for many cell lines in influencing differentiation and phenotypes [333]. Close approximation of *in vivo* conditions allows for *in vitro* models to give a more accurate representation of biological dynamics of a given system. Electrostimulation is particularly important for cardiomyocytes *in vitro* as they are exposed to an activation potential *in vivo* consistently which impacts on the cells genotypic and phenotypic profile [334]. Cells are typically stimulated at a biological relevant frequency (~ 1 Hz) and at the activation potential of the cardiomyocyte (~ 90 mV). This work aims to elucidate how the cardiomyocyte cell cultures respond to various electrical stimulation waveforms and how that impacts the properties of the culture. The work represents the first-time that cardiomyocytes have been stimulated using a *wireless* bipolar electrode. The work also represents the first use of biphasic, or ac, waveforms for wireless bipolar electrostimulation of cells.

It is well understood that cell lines such as neurons and cardiomyocytes require electrical stimulation *in vitro* to reflect *in vivo* condition more accurately [335–337]. Cell culture stimulation *in vitro* is often multi-faceted as an accurate cell culture model requires the use of chemical, mechanical and electrical stimulation. Chemical stimulation is typically achieved through the addition of hormones, such as norepinephrine which is required by the HL-1 cardiomyocytes used in this study. Norepinephrine induces a contraction in cardiomyocytes through a G protein-coupled receptor kinase 2 (GRK2) phosphorylation pathway [338]. It is commonly supplemented into cell culture medias in order to maintain a contractile phenotype in *in vitro* cultured cardiomyocytes for both primary and immortalised cardiomyocyte cell lines. Mechanical stimulation refers to the surface on which the cells are adhered which can tuned for optimised cell growth [339,340]. Mechanical stimulation in traditional 2D cell culture is typically achieved by adding extracellular matrix proteins to the surface on which the cells adhere. For example, fibronectin and gelatin is used to coat polystyrene cell culture flasks in cardiomyocyte cultures [341]. Electrical stimulation involves the culture of cells in an electric field. The electric field seeks to reproduce the action potential experienced by the cells *in vivo*. It has been shown that electrostimulation impacts the cells in a variety of way, e.g., changes in the internal cytoskeletal configuration which helps to maintain a contractile phenotype and improve the contractile strength of cardiomyocytes comparable to those experienced by cells *in vivo*.

The model for cardiac electrostimulation action potentials is a complex waveform with biphasic properties. In this case biphasic refers to both a cathodic and anodic component in the waveform. A cardiac waveform as characterised by an electrocardiogram (ECG) consists of a repeating cycle of P, Q, R, S, and T waves within a cycle [342]. In a murine ECG the electroactivity of the cardiomyocyte has been measured at approximately 1 Vpp (peak-to-peak potential), i.e., with a maximum cathodic potential of 500 mV and a maximum anodic potential of 500 mV [343]. The stimulation waveforms cited in literature in cardiac cell culture stimulation typically quote three parameters when detailing electrostimulation protocols. The first is the electric field strength and indicates the applied potential to the cells. The amplitude of the electric field varies on the application of the stimulation, in galvanotaxis studies, for instance, the electric field strength can be as high as 5 V cm^{-1} [344]. Electrostimulation for the purposes of contraction typically mirror the action potential required of the cell line and can be lower than 1 V*cm^{-1} [345]. Pulse width is the second parameter indicated and refers to the duration of the electric field strength experienced by the cells in culture. Extended periods of time in an electric field, particularly at greater potentials, can cause damage to the cells therefore the pulse width is typically measured on a millisecond time scale [346–348]. Finally, the frequency of the pulses is given in Hz and indicated the pace at which the culture is stimulated and experiences the potential during the stimulation [349]. This is typically done to mimic the contraction frequency of the *in vivo* tissue type. A typical human heart beats at a rate of 60 beats per minute (BPM) which is equivalent to a stimulation frequency of 1 Hz. In comparison a murine heart will can have a resting heart rate of 600 BPM, or 10 Hz. Unfortunately, in electrostimulation protocols these vary wide parameters vary widely even with the same cell line, a table representing this variation can be seen in Chen, Bai, *et al.* [333] . There is no consensus on optimal electric field strength, pulse width, or frequency in the literature when referring to cell origin (primary or immortalised), species origin (human or murine), or cell lineage (induced pluripotent stem cells, or mature cells).

By their nature bipolar electrodes have both cathodic and anodic poles which are reciprocal in polarity to the driving electrode inducing the electric field, i.e., the cathodic driving electrode will induce an anodic pole at the area of driving electrode closest to it and vice versa for the anodic driving electrode [167,350]. Previous work conducted with Wallace and Chen et al. utilised a monophasic pulsed waveform for the electrostimulation of PC12 neuronal cells causing an increase in dendrite formation within the cell population [165]. This work uses a biphasic, along with a monophasic, waveforms to stimulate the HL-1 cardiomyocytes as a typical cardiac waveform has anodic and cathodic potentials. It is important to elucidate how the culture would react

when exposed to cycling anodic and cathodic poles at the bipolar electrode interface. In a monophasic waveform the poles would remain in the same orientation throughout the stimulation period. Given the interfacial potential gradient one half of the bipolar electrode will stimulate with a positive potential and the other will experience only a negative potential. In a biphasic waveform, as the potential alternates at the driving electrodes so too will the potential alternate at the adjacent poles of the bipolar electrode. During a single cycle the cells adhered to the bipolar electrode will experience both positive and negative potentials [351]. As a cardiac waveform is a compound waveform made up of both positive and negative potentials it is important to evaluate how the cells are affected by this alternating potential pattern when cultured on a wireless bipolar electrode.

This work examines the effect of electrical stimuli parameters on cell cultures adhered to the surface of the bipolar or contactless electrode. The cell density and distribution on the bipolar electrode surface was assessed along with their relative distribution across the area of the electrode. In this way the effect of both monophasic and biphasic stimulation on cardiac cell culture was elucidated.

2. Materials and method

2.1. Cell culture

HL-1 murine cardiomyocytes were sourced from Sigma Aldrich. Cells were passaged in a T75 culture flask coated with 0.02% Gelatin Fibronectin using supplemented Claycomb medium purchased from Sigma Aldrich at 37°C with 5% CO_2 as recommended. Claycomb medium was supplemented with 10% HL-1 screened Foetal Bovine Serum (FBS), 100 µg/ml Penicillin/Streptomycin, 0.1 mM Norepinephrine, and 2 mM L-Glutamine. Claycomb media is a formulated cell culture medium developed by Claycomb *et al.* and who originally formed the HL-1 cell line. Foetal bovine serum is included to supply additional nutrients to the cells along with key developmental hormones and stimuli. Penicillin/Streptomycin is included to prevent bacterial contamination during culture. Both Norepinephrine and L-Glutamine are included to encourage and maintain a contractile phenotype during cell culture. Cells were cultured until they reached

confluency then split using Trypsin/EDTA and soybean trypsin inhibitor, spun at 500 g for 5 minutes and seeded 1:3 in a precoated T75 flask.

2.2. Cell stimulation

For culture using the bipolar electrochemical cell, the cells were removed from the T75 culture flask using Trypsin and soybean trypsin inhibitor as before and spun at 500 g for 5 minutes. The cell pellet was resuspended in 2 ml of wash medium (Claycomb medium with 10% FBS) and a 10 µl aliquot was taken to conduct a cell count using 10 µl of Trypan Blue and a haemocytometer. Trypan Blue is an alive/dead stain for viable cell counting, it cannot pass through the cell wall of viable cells and stains dead cells blue. Two bipolar electrodes were chosen based on the results of previous work, these were the 10 µg/ml (~2 x 10^{-8} M) PPy-DS-Fibronectin film, and 0.02% w/v Gelatin (~ 6 x 10^{-7} M) with 5µg/ml Fibronectin (~1 x 10^{-8} M) coated FTO glass. The bipolar electrodes were seeded with 25000 cells/cm^2 in a 24 well plate and allowed to adhere overnight. The following day the bipolar electrodes were transferred from the 24 well plates to the stimulation platform. Cells were stimulated using a Keysight EDU33210 Series Trueform Arbitrary Waveform Generator with dual output channels. Pulse, sine, and cardiac waveforms were used from the pre-programmed waveforms available on the generator. Parameters were altered to customise the stimulation conditions as indicated in *Table 6*. The cells were subjected to electrostimulation conditions for two hours per day for three consecutive days. Cultures were maintained in an incubator at 37 degrees Celsius and 5% CO_2. The medium was exchanged daily in all three wells of each row to ensure there was enough nutrients for the cells to grow.

Table 6 - Waveform parameters for electrostimulation protocols

Waveform	Amplitude (V)	Pulse width (ms)	Frequency (Hz)
Monophasic pulsed	1	500	3
Biphasic pulsed	2 (peak-to-peak)	500	3
Sine	2 (peak-to-peak)	N/A	3
Cardiac	2 (peak-to-peak)	N/A	3

2.3. Immunocytochemistry

Following culture of the cells on the bipolar electrodes, ICC was performed on the cultures using DAPI nuclear stain. Once the experimental conditions had been completed, the cells were prepared for fixing by aspirating the cell culture media followed by washing gently with PBS 3 times with gentle agitation then fixed using 4% paraformaldehyde in PBS for 20 minutes at room temperature. The paraformaldehyde was then aspirated and washed again with PBS three times with gentle agitation. The surfaces were then blocked to prevent non-specific binding of antibodies to the bipolar electrode surface using 500 µl of a blocking buffer of PBS with 5% Bovine Serum Albumin, 0.1% Tween-20, and 0.3 M Glycine for an hour at room temperature. For nuclear visualisation the cells were also stained with DAPI by incubating the electrodes for 15 minutes at room temperature protected from light. Once the DAPI had been removed the electrodes were rinsed a final three times using PBST, they were then inverted onto a microscope slide and mounted using 15 µl of mounting media. Once mounted the microscope slides were stored for at least 3 hours, preferably overnight, at 4°C while protected from light to allow the mounting media to set and fix the electrodes in place on the microscope slide. The slides were then imaged using an Olympus fluorescent microscope.

3. Results and Discussion

The dynamic nature of cells makes the impact of the bipolar electrostimulation challenging to assess. Biological systems inherently have a high degree of variability and are subject to interference from any uncontrolled factors. Cells were used between passage 17 and 22 to keep the cell cultures as reproducible as possible. Experiments where microbial or fungal infection, or contamination, occurred were terminated. Every attempt was made to maintain the reproducibility of these experiments and each parameter was assessed in triplicate.

3.1. Unstimulated cell culture

In order to assess the suitability of the bipolar electrostimulation platform a baseline was established in the absence of stimulation. Cells were cultured for three days total in order

to match the electrostimulation time frame r. Three days was also selected as this is typically represents the duration of time for HL-1 to become confluent in a T75 flask when the supplier (Sigma) protocol is followed. Cells were cultured on the six bipolar electrode substrates described in **Chapter 2 and 3**. Five electrodes consisted of a polypyrrole – dextran sulphate – fibronectin film (PPy-DS-Fib) on a Fluorine doped tin oxide (FTO) substrate, along with a Gelatin/fibronectin coated FTO substrate, further detail can be found in the materials section. The conducting polymer composite films were deposited using cyclic voltammetry. The fibronectin content was varied (0, 5, 10, 15, and 20 µg/ml) in the deposition solution in order to assess the optimal concentration for developing a surface which maximises cell adhesion and the number of adherent cells.

This work not only serves as a baseline for future experiments but is also an assessment of the PPy-DS-Fib films suitability for a biological system. To date, the physical and electrochemical properties have been elucidated, however this work represents the first description of HL-1 cardiomyocytes cultured on a PPy-DS-Fib bipolar electrode. Environmental factors such as surface availability of extracellular proteins and cytotoxic materials play a big role in the success of a cell culture and therefore must be elucidated prior the introduction of additional electrical stimulation so that the effects of the presence of a stimulating potential can be properly extracted.

The number of cells per electrode was assessed by nuclei staining using DAPI and imaged using a fluorescent microscope, the nuclei were then counted using ImageJ software. The results for nuclei counted per electrode with respect to bipolar electrode material can be seen in **Figure 23** below.

Each of the bipolar electrode surfaces successfully supported the culture of viable cells over the three-day time period. It is worth noting that the PPy-DS-Fib film containing 0 µg/ml fibronectin concentration also supported a viable cell culture with comparable cell number to films which also include fibronectin. This indicates that the PPy-DS components of the films provide a surface topography to support the adhesion of HL-1 cardiomyocytes. However, it is known that the presence of fibronectin is important to maintain a contractile phenotype in the cultured cells and is therefore an important component which cannot be excluded from the surface of the bipolar electrode.
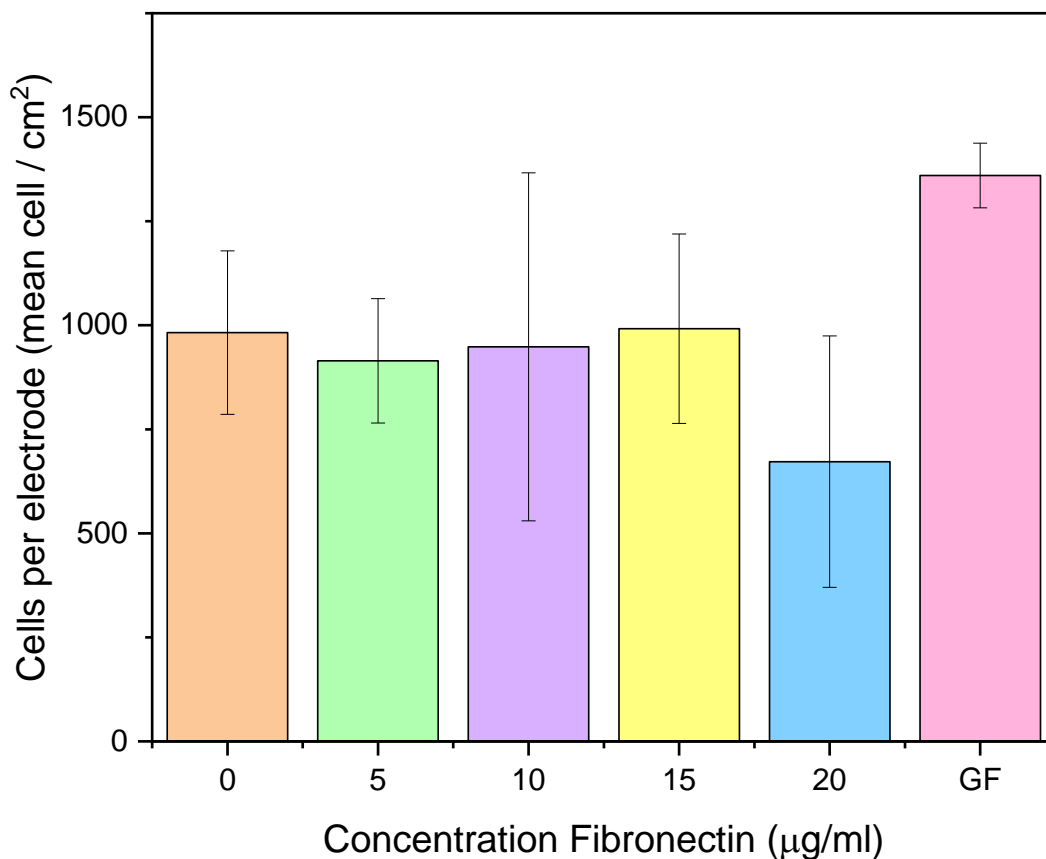
Figure 23. Cell count of nuclei stained using DAPI nuclear stain following three days of culture in on the electrode materials and in the custom cell culture platform without any stimulation applied to the cells. PPy-DS-Fibronectin described in **Chapter 2 and 3** were assessed with the concentration of fibronectin varied. Each condition was performed in a single replicate with four independent electrodes (n=4). Cells were counted by taking 6 images of each electrode in random locations. Total cells in each of the 6 images was summed together and statistics were calculated using total cell count for the 4 independent replicates.

The importance of the fibronectin is observed in the cell count for the Gelatin/ Fibronectin coated electrodes which represented the highest cell count (1350 cells per electrode) and the lowest inter culture variability (± 78). HL-1 cardiomyocytes are typically grown on a gelatin/fibronectin coating when cultured in a polystyrene cultureware such as well plates and culture flasks so it is expected the cells could be well maintained on a similar coating. Previous work shows that the gelatin/fibronectin does not affect the electrochemical properties of the electrode for the purposes of bipolar electrostimulation.

The viable cells present on the films deposited from 5, 10, and 15 µg/ml solutions of PPy-DS-Fib were very similar in terms of viable cells present following three days of

culture, 915 ± 149, 948 ± 418, and 992 ± 228 respectively. These results indicate that there is not a significant increase in viable cells when the concentration of fibronectin is increased in the deposition solution. This is supported by the heterogenous distribution of surface fibronectin observed in **Chapter 3**. This dataset represents the most reproducible conditions of future experiments described in this work. It is worth noting the high degree of relative standard deviation in all bipolar electrode materials. This is representative of cell culture experiments given the inherent variability of cells and their responses to environmental stimuli and conditions [352–354]. The RSD observed are represented in **Table 7**.

Table 7 - Variability of viable cell numbers following three days of culture.

Bipolar electrode material	Mean cells per electrode (cells)	Standard deviation (cells)	RSD (%)
PPy-DS-Fib 0 µg/ml	982	197	20.061
PPy-DS-Fib 5 µg/ml	915	149	16.284
PPy-DS-Fib 10 µg/ml	948	418	44.093
PPy-DS-Fib 15 µg/ml	992	228	22.984
PPY-DS-Fib 20 µg/ml	672	302	44.940
Gelatin/Fibronectin	1360	78	5.735

3.2. Wireless bipolar monophasic pulsed stimulation of HL-1 cardiomyocytes

The cultured HL-1 cardiomyocytes were exposed to monophasic waveforms with an amplitude of 1 V and a pulse width of 500 ms. Given the dimensions of the stimulation platform (channel length = 3cm) an electric field strength of 0.33 V*cm^{-1} can be calculated. In this case, an electrical stimulus was introduced to the cells from the day of transfer into the stimulation platform and the cells were exposed to the stimulus for a total of two hours per day for three consecutive days. This would represent the first wireless bipolar electrostimulation of a cardiac cell line described in the literature.
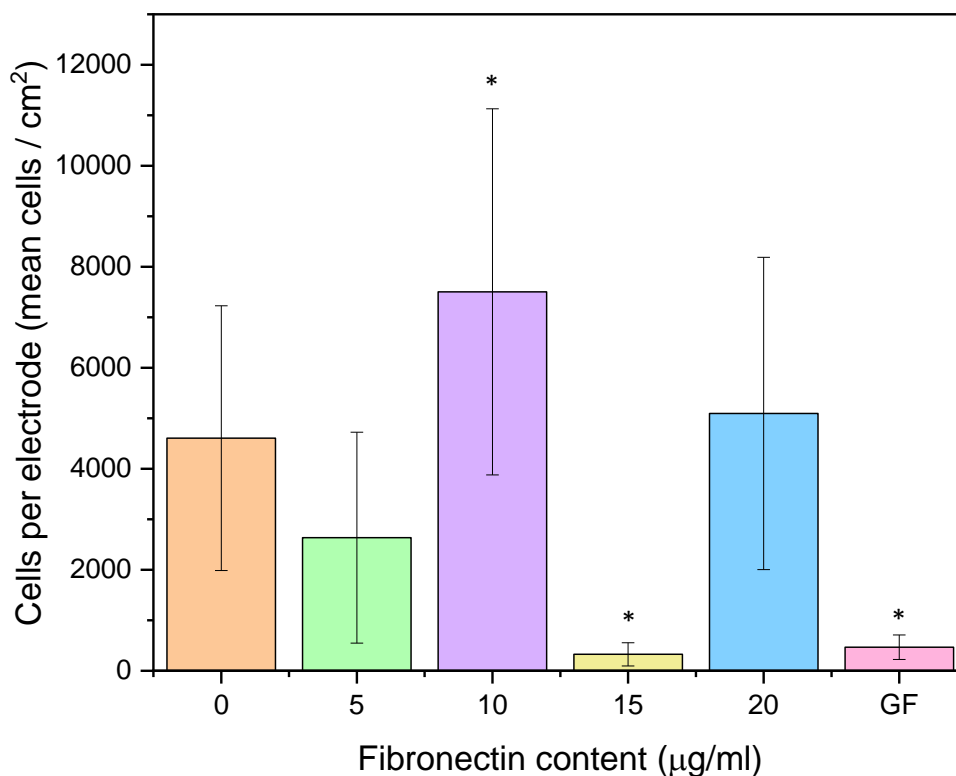
Figure 24. Cell count of nuclei stained using DAPI nuclear stain following three days of culture on the electrode materials and in the custom cell culture platform with monophasic 1 V stimulation applied to the cells. PPy-DS-Fibronectin described in **Chapter 2 and 3** were assessed with the concentration of fibronectin varied. Each condition was performed in a single replicate with four independent electrodes (n=4). Cells were counted by taking 6 images of each electrode in random locations. Total cells in each of the 6 images was summed together and statistics were calculated using total cell count for the 3 independent replicates. One-way ANOVA testing with Tukey ad hoc analysis showed 15 µg/ml and Gelatin/ fibronectin showed a statistically significant variance from the 10 µg/ml film.

Mean viable nuclei per electrode is represented above in **Figure 24**. A one-way ANOVA test with Tukey ad hoc analysis indicated that the low viable cells identified on the 15 µg/ml and gelatin/ fibronectin electrodes was only statistically significant from the 10 µg/ml film. This indicates that the variance observed is not statistically significant and shows no correlation between the fibronectin concentration and the number of viable cells on the electrode surface. These results are typical of cell cultures on modified surfaces as natural variances in growth from one culture to another lead to a high degree of inherent variation in the data. All five of the bipolar electrode material PPy-DS-Fib

films along with the gelatin/ fibronectin coated FTO sustained viable cell cultures for three days of exposure to the electrical stimulation. The data is further represented and analysed in **Table 8**.

Table 8 – Variability of viable cell numbers following three days of culture with monophasic pulsed waveform electrical stimulus.

Bipolar electrode material	Mean cells per electrode (cells)	Standard deviation (cells)	RSD (%)
PPy-DS-Fib 0 µg/ml	4606	2621	57
PPy-DS-Fib 5 µg/ml	2636	2089	79
PPy-DS-Fib 10 µg/ml	7504	3625	48
PPy-DS-Fib 15 µg/ml	326	230.	71
PPy-DS-Fib 20 µg/ml	5095	3092	61
Gelatin/Fibronectin	467	243	52

It is clear from the data represented above that the electrical stimulus is having a measurable effect on the cells during the three days of exposure and this is represented in 2 key areas. Firstly, the relative standard deviation (RSD) also increased across every bipolar electrode material. Secondly, viable cell numbers also increased in all but two bipolar electrode materials (PPy-DS-Fib 15 µg/ml, and gelatin/ fibronectin coated FTO), these two findings are represented in **Table 8** and **Table 9** respectively. This indicates that the cells did experience the electrical stimulus applied to the stimulation platform and that wireless bipolar stimulation is an effective method for introducing an electrical stimulus to a cardiomyocyte culture *in vitro*. The increase in RSD serves to confirm the hypothesis that the cells have reacted to the introduction of an electrical stimulus and confirms that the platform is capable of delivering an experimentally significant electrical stimulus. The increase in RSD also serves to reaffirm that the cell cultures experience a high degree of variability from culture to culture with all but one culture recording an RSD of > 50%. The high RSD is indicative of the inherently noisy signal recorded from in vitro cell culture work.

Table 9 - Comparative analysis of viable cells per electrode with and without exposure to monophasic pulsed waveform electrical stimulus

Bipolar electrode material	Unstimulated (mean cells)	Monophasic stimulation (mean cells)	Cell count change (%)	P value (*= P < 0.05)
PPy-DS-Fib 0 µg/ml	982	4606	369	0.079
PPy-DS-Fib 5 µg/ml	915	2636	188	0.227
PPy-DS-Fib 10 µg/ml	948	7504	691	0.036 (*)
PPy-DS-Fib 15 µg/ml	992	326	-67	0.024 (*)
PPy-DS-Fib 20 µg/ml	672	5095	658	0.069
Gelatin/Fibronectin	1360	467	-66	0.017 (*)

Given the high degree of inter culture variation only PPy-DS-Fib 10 µg/ml bipolar electrode showed a significant increase (p = 0.03582) in viable cell number in comparison to the unstimulated. Both PPy-DS-Fib 15 µg/ml and gelatin/fibronectin coated FTO cultures recorded a significant decrease (p = 0.02354 and p = 0.017, respectively). This can be explained due to the high RSD noted earlier and indicates that the cell cultures are extremely sensitive to small changes in experimental set up, namely exact position of the bipolar electrode in the platforms channel and exact position of the driving electrodes at each end of the channel, which can affect the exact interfacial potential at the surface of the bipolar electrode [351].

3.3. Biphasic electrostimulation of HL-1 cardiomyocyte cultures using pulsed, sine, and cardiac waveforms

In order to assess further the suitability other bipolar electrostimulation platform for the delivery of electrical stimulus to the cell cultures biphasic waveform stimulation was applied to the cells in culture. The application of a biphasic waveform differs from a monophasic waveform in the effect it has on the interfacial potential at the bipolar electrode. In a monophasic stimulation scenario, a single potential is applied in pulses to the driving electrodes, this in turn induces a cathodic and anodic pole at the bipolar electrode. During the pulse the bipolar electrode experiences an interfacial potential and between pulses no interfacial potential is present. This means one pole is intermittently cathodic and the other is anodic.

When biphasic waveforms are used, the potential is alternated from positive to negative according to the waveform (square, sine, etc.). This means when a potential is applied

to the driving electrode a cathodic and anodic pole is induced at the bipolar electrode, as in the case of monophasic stimulation. However, as the potential is inverted i.e., enters the second phase, then so two are cathodic and anodic poles of the bipolar electrode. Each half of the bipolar electrode is alternately polarised and therefore both poles of the electrode experience both cathodic and anodic interfacial potentials in sequence.

Biphasic stimulation is more consistent with the depolarisation of cardiomyocytes *in vivo* and thus is an important parameter to examine how an alternating potential effect the growth of the cells in culture. A pulsed biphasic waveform mimics the pulsed monophasic waveform in that the potential is switched from positive to negative rapidly with minimal ramping time and a sustained pulse with of 500 ms. The sine waveform alternates the positive and negative potential as the biphasic pulsed waveform does however the magnitude is increased more gradually, and the peak potential is not held as it is in the pulsed waveform. The sine waveform aims to mimic the action potential of the QRS complex of a compound cardiac waveform. Finally, a complete cardiac waveform, as measured on an electrocardiogram was used to mimic potential variation experienced by the cardiomyocytes *in vivo*. Average cell count per electrode under each waveform condition is summarised in **Figure 25**. Bipolar electrodes of gelatin/fibronectin coated FTO, and PPy-DS-Fib 10 µg/ml were used to analyse the biphasic waveforms as they provided the highest mean cells per electrode in unstimulated and monophasic stimulation conditions, respectively.
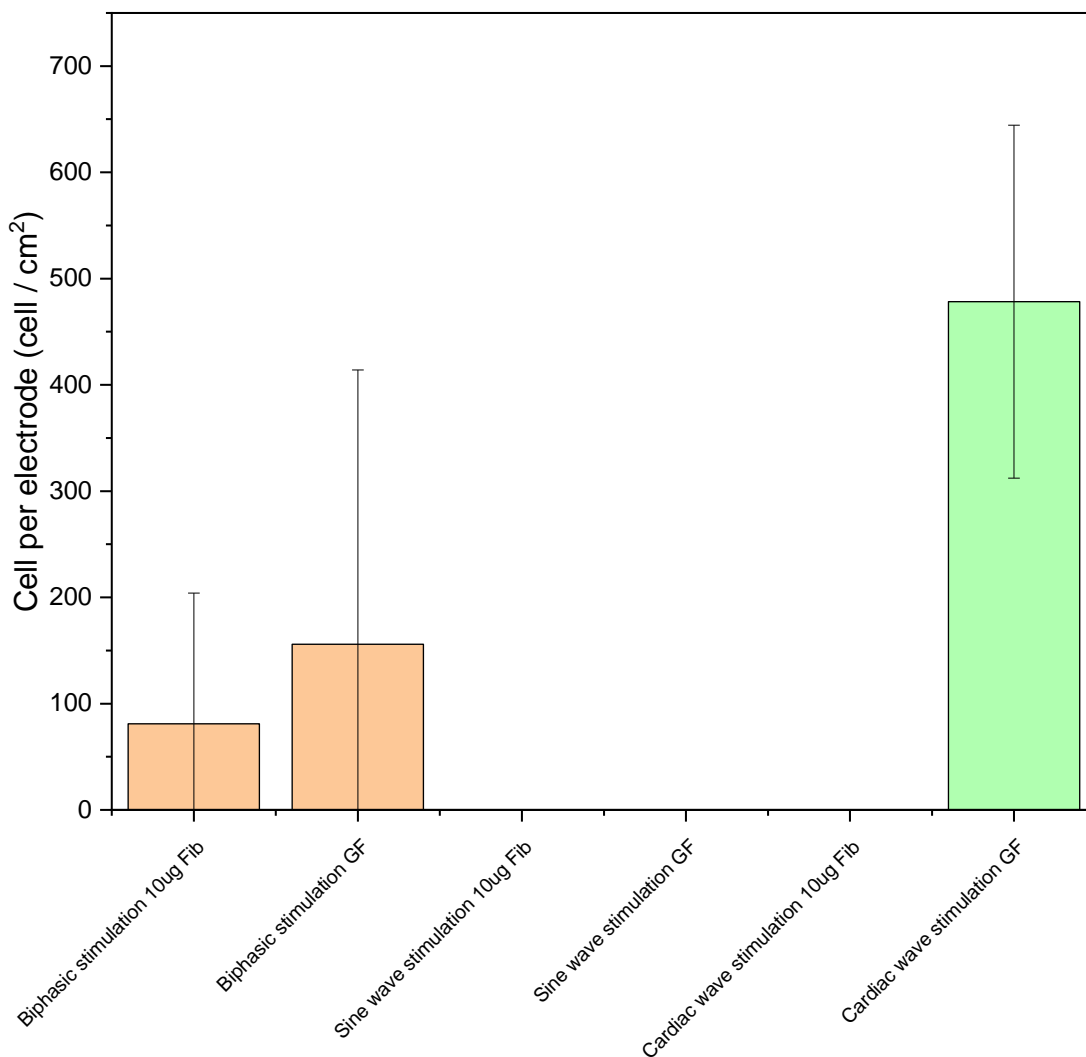
Figure 25. Cell count of nuclei stained using DAPI nuclear stain following three days of culture on 10 µg/ml PPy-DS-Fib and Gelatin/ Fibronectin bipolar electrodes and in the custom cell culture platform with biphasic (2 Vpp), Sine wave (2 Vpp), and Cardiac waveform (2 Vpp) stimulation applied to the cells for 1 hour per day. Each condition was performed in a single replicate with four independent electrodes (n=4). Cells were counted by taking 6 images of each electrode in random locations. Total cells in each of the 6 images was summed together and statistics were calculated using total cell count for the 4 independent replicates.

Once again, the high standard deviation is evident across all cultures with all stimulation waveforms. The presence of the anodic and cathodic poles on both halves of the electrode did impact the cells viability. Pulsed biphasic showed low viable cell count and extremely high std deviation, 81 ± 123 (RSD 152%), and 156 ± 258 (RSD 165%) on PPy-DS-Fib 10 µg/ml and gelatin/fibronectin coated FTO respectively. Sine wave electrical stimulation also did not support any viable cells on the surface of the electrodes following the three-day culture protocol. Only the cardiac waveform stimulation on the cells

cultured on the gelatin/fibronectin coated FTO substrate showed consistent cell growth, despite this the PPy-DS-Fib 10 μg/ml did not provide viable cells. **Figure 26** represents the comparison of both the gelatin/fibronectin coated FTO and PPy-DS-Fib 10 μg/ml across all stimulation conditions used in this work.

It is also evident that the biphasic stimulation does have an overall negative impact on the cells per electrode count. ANOVA two-way testing with ad hoc Tukey analysis did not indicate the presence of any significant differences between the stimulation waveform used and the electrode materials on which the cells were cultured, with the exception of the sine waveform which did not yield viable cells.

One explanation for the increased cell death is that the presence of both positive and negative potentials during the biphasic stimulation is causing an increase cell death. Cells have a natural resting potential, and it is possible that increasing the polarisation has a negative effect on the cell's viability. As the biphasic waveform ensures the entire electrode will experience a cathodic and anodic pole cells distributed across all areas of the bipolar electrode are subjected to this high degree of polarisation. This would be reinforced by the greater number of cells present on the electrode exposed to monophasic stimulus as half of the electrodes surface area will not experience this hyperpolarisation event and instead experiences only the action potential for initiating contractions.
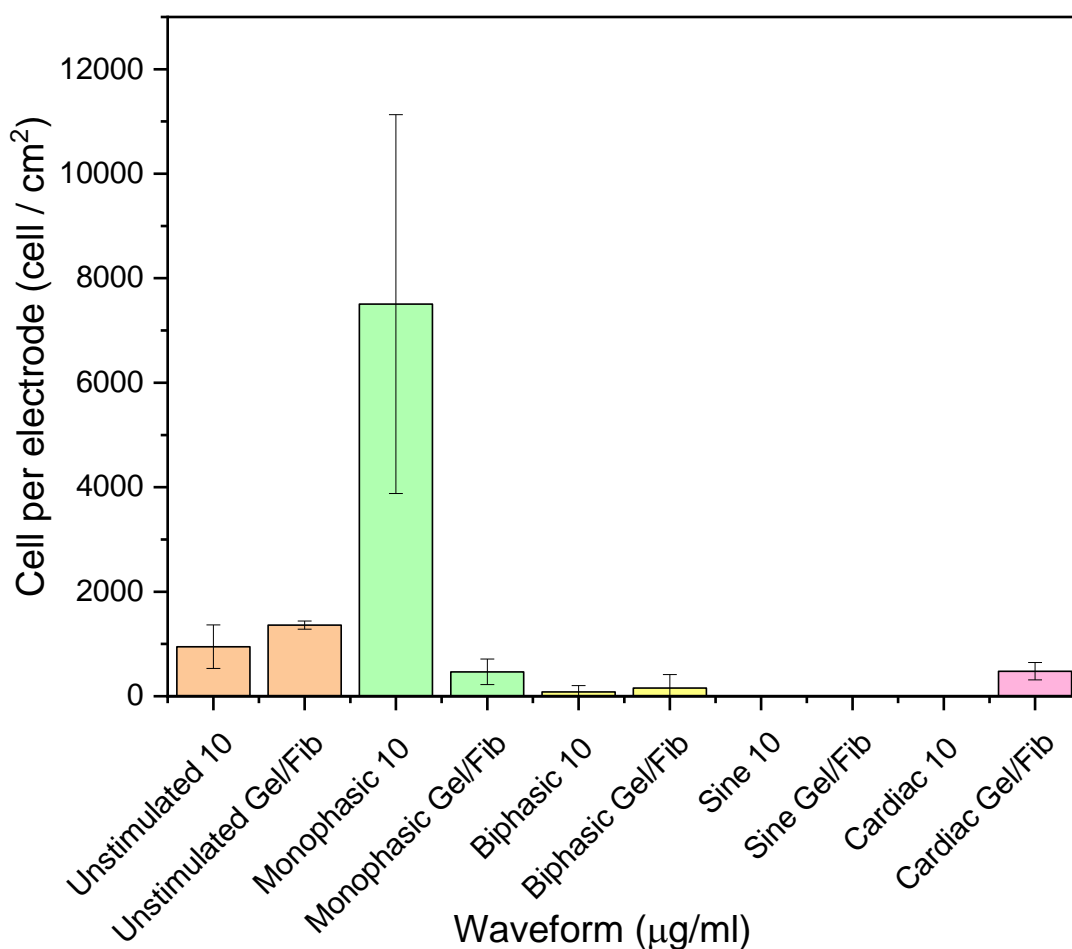
Figure 26. Comparative cell count of 10 µg/ml PPy-DS-Fib and Gelatin/ Fibronectin bipolar electrodes and in the custom cell culture platform across unstimulated and the four stimulation waveforms used (Monophasic, biphasic, sine, and cardiac). Each condition was performed in a single replicate with four independent electrodes (n=4). Cells were counted by taking 6 images of each electrode in random locations. Total cells in each of the 6 images was summed together and statistics were calculated using total cell count for the 4 independent replicates.

4. Conclusion

This work represents the first reported electrostimulation of HL-1 cardiomyocytes using wireless bipolar electrochemistry using a monophasic electrostimulation protocol. Successful viable cell cultures were observed on PPy-DS-Fibronectin cultures of varying concentrations of fibronectin along with gelatin/fibronectin coated conductive FTO electrodes. Furthermore, this work represents the first reported wireless bipolar

electrostimulation of a cell culture using biphasic electrostimulation protocols. While the electrodes did support viable cells in both biphasic pulsed, and cardiac waveform conditions the cell numbers and inter-culture variability were low indicating further refinement of methodology is required to optimise biphasic stimulation conditions for high yield viable cell culture under stimulation conditions. This is an encouraging start point for wireless bipolar biphasic stimulation of cell cultures which can closely recreate the electrical field conditions of in vivo biological conditions. Further work is required to further refine the experimental conditions of the cultures and genetic analysis would further elucidate and differentiate the genotypic effect of the electrostimulation conditions on the cultures.

Chapter 5

Screen-printed Electrode Based Electrochemical Biosensor for Cardiovascular miRNA Detection.

1. Introduction

Biosensors have become an essential tool in diagnostics and disease monitoring at all levels of health care, including research lab cell culture modelling of diseases [355,356], hospital testing for disease markers and infection [357,358], to handheld blood monitoring such as in the case for blood sugar sensors used by diabetes patients [359]. The recent global COVID-19 pandemic has brought an even greater spotlight on the need for rapid testing, which is also simple, reliable, and easily used by untrained operators (namely the public at large). Biosensors cover a wide range of devices and techniques but can be generally defined as "*a device that measures biological or chemical reactions by generating signals proportional to the concentration of an analyte in the reaction.*" [360]. As with all sensors, the key parameters for an effective biosensor are sensitivity and selectivity. They must be sensitive enough to detect the analyte in a relevant biological range and they must also be selective for that analyte in a sample which maybe contain a low concentration of the analyte or have other molecules in the sample which may interfere with the detection of the desired analyte [361].

Biomarkers are defined as "*a defined characteristic that is measured as an indicator of normal biological processes, pathogenic processes or responses to an exposure or intervention.*", however, there can be more refined definitions according to the application of the assay [362]. Typically, when discussing biomarkers in relation to disease pathology and its progression, these biomarkers have been proteins as they are found in most bodily fluids and their regulation with biological systems is best understood at this time [363,364]. Proteins are useful biomarkers as their appearance, disappearance, or relative abundance indicates a change in cells which in turn can be correlated with a disease. Interest in alternative biomarkers is growing and one alternative to proteins are miRNA biomarkers [365,366]. miRNA are sequences of RNA typically 22 base-pairs long which, when associated with RNA Induced Silencing Complexes (RISCs), play a role RNA interference blocking translation of RNA into their respective proteins [92,367]. With recent advances in genome sequencing and large genetic libraries of disease it is possible to generate libraries of miRNAs, either individual or clusters, which have a strong association to disease [368,369].

There is an extremely large number of miRNAs identified which have been observed not only in cells but also in body fluids of all kinds [370,371]. These cell free miRNAs are typically found in liposomes circulating the body and while the exact function of these liposomal miRNAs is not well understood, studies have shown that changes in liposomal

concentrations are directly proportional to cellular concentrations of miRNA changes [372–374]. This makes them legitimate potential biomarkers as they are readily sampled and can be strongly correlated to the state of a disease. It is hoped that monitoring miRNA can lead to early detection and even prevention of disease due to their role in gene regulation within the cell [375,376]. They can also be more readily correlated with diseases as they can affect proteins that are not always excreted by the cell and therefore not available for use as conventional biomarkers. The sequence of each miRNA is highly conserved, they intrinsically hybridise with complementary RNA strands which are attractive traits for emergent biomarkers. One major disadvantage in that the predictive or prognostic value of a single miRNA is often limited, individual miRNA may be dysregulated due to several different diseases, and typically an expression profile is a better correlative indicator towards disease [377,378]. Another area of concern is the susceptibility of miRNA to the RNase family of enzymes. An RNase is an enzyme designed to break down strands of nucleic acids, including miRNA [379,380]. This can be overcome with careful sterilisation of the environment, and careful sample preparation and treatment to reduce miRNA degradation. This has not been a major issue for biosensors which have been developed to date [381,382]. While DNA is typically used as a capture and probe element in these types of nucleic acid sandwich assay, this assay uses RNA capture and probe elements. While it has been highlighted that the instability of RNA in laboratory conditions, at room temperature, and in neutral buffer there is evidence in the literature that RNA-RNA hybrids are more stable than DNA-RNA hybrids. The literature also suggests that these RNA-RNA hybrids are resistance to RNase degradation [383–385].

The surface properties of the electrode selected significantly affects the performance of the electrochemical based biomarker assay, in particular the immobilisation of a bioreceptor on the transducer surface. Many materials with varying functional groups have been developed which facilitate the use of biomolecular capture elements [386,387]. One of the most widely used surfaces is a bare gold electrode as it is a well characterised electrode material and molecules can be covalently immobilised using gold-thiol chemistry [388]. This is a convenient method of electrode surface functionalisation which is simple and quick to perform. The major drawback, particularly when using an electrocatalytic nanoparticle label, is that the gold surface can also reduce hydrogen peroxide thus producing a background signal that disimproves the limit of detection (LOD) as this signal cannot be distinguished from the contribution due to the target analyte mediated capture of nanoparticles [228]. On the other hand carbon electrodes, such as screen-printed carbon electrodes, can generate a low background current for

peroxide reduction making them useful for biosensor development and they are low-cost [389]. Unfortunately, while strategies such as diazonium coupling, exist, biological materials are less easily covalently linked to carbon which is important for the stability of the biosensor [390,391]. This work aims to assess the feasibility of combining the well-established thiol binding affinity of gold with the low background characteristic of screen-printed carbon electrode. This is achieved by using a carbon-based ink that contains gold nanoparticles to produce screen-printed electrodes, SPEs, in which the gold nanoparticles act as anchor points for the miRNA capture strands.This chapter describes the development of a novel miRNA biosensor that uses a screen-printed carbon electrode, containing gold nanoparticles that are functionalised with capture strands that are complementary to the target mir-1-3p (Accession number MIMAT0000416), a miRNA linked to cardiovascular disease. [392,393] .The assay uses capture strands of a thiol terminated RNA complementary to half of the target miRNA strand that are bound to the gold nanoparticles trapped within the SPE. As shown in **Figure 27**, following target hybridisation, a platinum nanoparticle functionalised with probe strands that are complementary to the target strand overhang is hybridised. This electrochemical biosensor utilises the reduction of hydrogen peroxide and the electrons released to quantify the amount of target miRNA present on the transducers surface. The mechanism of hydrogen peroxide degradation at a platinum surface can be described by the following scheme:

$$2Pt + H2O2 \rightarrow 2Pt(OH) \qquad (1)$$

$$2Pt(OH) + 2H^+ + 2e- \rightarrow 2Pt(H2O) \quad (2)$$
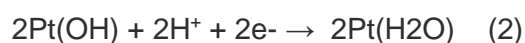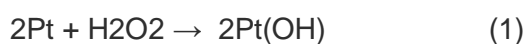
At low potentials, as in this case, the hydrogen peroxide is first disassociated onto two platinum sites on the nanoparticle (Eq 1). This adsorbed OH is not stable on the platinum surface site. The site is regenerated through the electrochemical reduction shown in Eq 2. The platinum site is then freed to adsorb another OH from a dissociated hydrogen peroxide. It should be noted that the hydrogen peroxide itself undergoes a chemical reaction and the current measured is in fact the reduction of the Pt(OH) site. This process is a 2-electron process as described above. Literature suggests that experiments conducted using nucleic acid sequences that the electron transport from the transducer electrode occurs along the length of the nucleic acid backbone to the platinum nanoparticle [394–396].

The development of an accurate and quantitative miRNA assay is an essential tool for the future use of miRNA as a prognostic biomarker in the fight not just against

cardiovascular disease, but many other diseases [376,397,398]. Quantitative detection of miRNA without the need for replication or amplification, as is the case for RT-qPCR techniques, offers advantages as normal levels of circulating biomarkers can differ greatly from person to person and so relative fold increases may not always be sufficient to detect early cellular genetic dysregulation in the course of disease pathology and progression [399,400]. Another advantage is that development of a robust protocol allows for reconfiguration of the assay to detect a wide range miRNA by using custom capture and probe sequences without the need to alter any other materials within the assay [366]. The small size of the sensor platform and disposable nature of the electrode coupled with the aforementioned simplicity with respect to editing the target sequence could allow for single sample multiplex testing using multiple electrodes each detecting a different target.
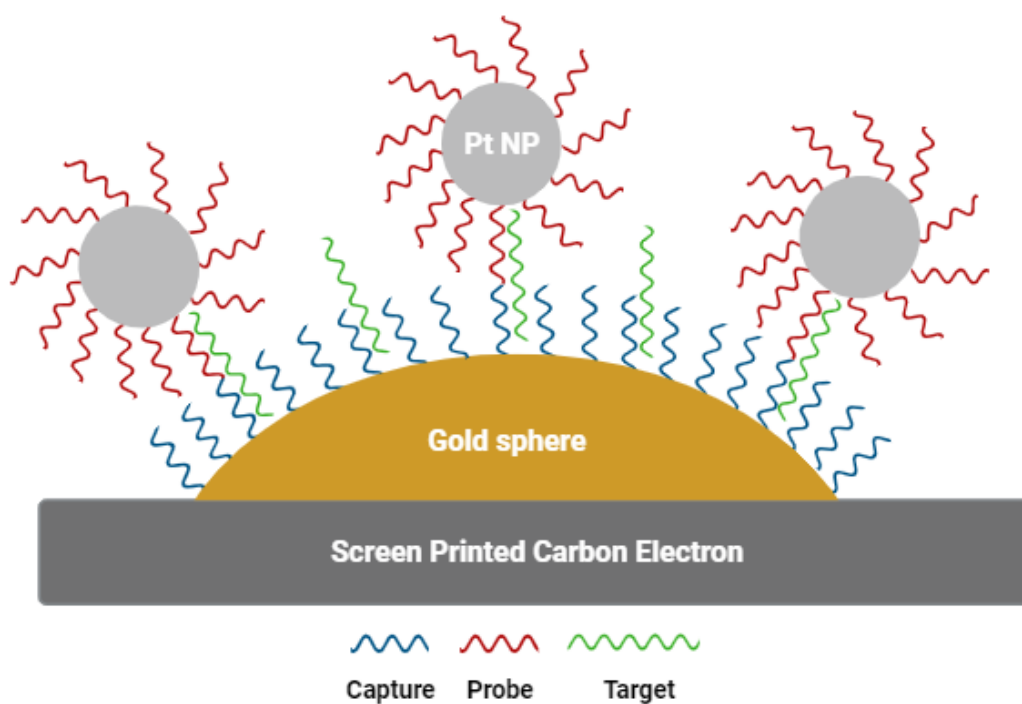
Figure 27. Schematic representation of the miRNA assay described in this work showing the screen-printed carbon electrode material (black) containing with gold nanoparticles (gold). The sandwich assay design comprises a capture strand of RNA (blue) and probe strand of RNA (red) which are complementary to the target miRNA (green). The probe RNA is functionalised with platinum nanoparticles (grey). The scale has been altered to show all components of the assay clearly. It should be noted that a higher degree of surface coverage would be expected on both the gold surface and the PtNPs in experimental conditions. This figure was created using BioRender.

2. **Materials and methods**

2.1. **Gold disc electrode preparation and assay**

Gold disc electrodes (IJ Cambria, England) with a working area diameter of 2 mm, were polished using standard mechanical cleaning methods with alumina powder of fine grades, 0.5 µm, 0.1 µm, and 0.05 µm on a polishing pad (powder and pads supplied by IJ Cambria, England). Electrodes were polished in a figure eight motion for at least 15 minutes to ensure a reproducible roughness factor. The roughness factor was assessed through single atom layer oxidation and reduction of the electrode in a 0.1 M H_2SO_4 electrolyte in a standard three electrode cell with a platinum counter and an 1M KCl Ag/AgCl reference electrode. Additional polishing was done if required to ensure similar roughness factor across all gold disk electrodes.

For the capture strand immobilisation 300 µL of 1 µM capture strand RNA in Denhardt's buffer (pH 8, Sigma Aldrich, Ireland) were incubated with the gold disc electrodes for 3 hours at 37 °C [401]. Capture strand miR-5p were purchased with thiol termination from (Eurogentec, Belgium). Following immobilisation, the electrode was gently rinsed in deionised water three times and dried gently under a stream of nitrogen. Once the electrodes were rinsed, they were incubated with the desired concentration of target miR-5p miRNA, for three hours at 37 °C to allow hybridisation between the capture and target strands of the RNA [402]. A further three step rinse steps were performed before the addition of probe miRNA. The probe miRNA was also purchased with a thiol termination to facilitate binding to 50 nm platinum nanoparticles (NanoComposix, CA, USA). Functionalisation was done by rinsing 1 ml of 3.3 x10^{10} particles/mL stock concentration nanoparticles three times in DI water followed by high speed microcentrifugation after the storage solution was removed. The nanoparticles were then resuspended in 900 µL of 1 µM probe RNA in Denhardt's buffer and placed in the oven at 37 °C for 1 hour to functionalise. The functionalised probe was then allowed to hybridise to the overhang of the miRNA target for 3 hours at 37 °C [403].

The chronoamperometric current vs time curves (i-t curves) were all recorded for 2400 seconds, consisting of a 60 second equalisation period, injection of 200 µM H_2O_2 final concentration, then signal recording for a further 120 seconds. The signal was recorded

at a potential of -0.25 V in a 0.01 M H_2SO_4 electrolyte solution (pH 1.7) with a final cell volume of 8 ml following the addition of H_2O_2.

Electrochemical characterisation such as cyclic voltammetry and chronoamperometry were performed using a CH Instruments (TX, USA) 760 and were recorded in a three-electrode cell using a platinum counter electrode and 1M KCl Ag/AgCl counter electrode. All chemicals and materials were obtained from Sigma Aldrich, Ireland unless otherwise stated.

2.2. Screen-printed gold functionalised carbon electrode preparation and assay

Gold nanoparticle containing carbon screen-printed electrodes were produced by Dr Loanda Cumba (School of Chemical Science, DCU, Ireland). The technique allows the percentage of gold at the surface of the screen-printed electrode by carefully tuning the curing parameters of the ink. The gold surface area is achieved through the addition of the 500 nm gold nanoparticles to the ink mixture prior to the printing process.

For screen-printed electrodes, miR-1 (hsa-miR-1-3p MIMAT0000416) was used and was supplied by Integrated DNA Technologies (Belgium). TE buffer of pH 8 was used in place of Denhardt's buffer in line with suppliers' recommendations. As before, 1 µM capture RNA was used to coat the electrode surface, and 1 µM of probe RNA functionalised 50 nm platinum nanoparticle was used as the label in the sandwich assay.

Table 10 – Sequence information for nucleic acid sandwich assay used in this work.

Strand	Sequence
Capture	5'- Thiol (C6)- AUA CAU ACU UC -3'
hsa-miR-1-3p	5'- UGG AAU GUA AAG AAG UAU GUA U -3'
Probe	5'- UUU ACA UUC CA -Thiol (C6) -3'

The capture layer was immobilised by immersing the screen-printed electrode in the thiolated capture strand solution for one hour. The electrode was then removed and rinsed in RNase free water and incubated with the target miRNA for one hour to allow hybridisation to occur at 37 °C. During this time 300 µl of the platinum nanoparticles were

removed and rinsed in RNase free water using centrifugation to pellet the nanoparticles. Once rinsed, the nanoparticles were added to 900 µl of probe RNA and incubated at 37 °C to allow immobilisation. The resulting probeRNA functionalised platinum nanoparticles are now considered probes. To complete the sandwich the probeRNA functionalised platinum nanoparticle probes are incubated after the capture RNA and miRNA target have been hybridised to allow the final hybridisation step to take place for one hour at 37 °C.

The i-t curves were all recorded for 180 seconds, consisting of a 60 second equalisation period, injection of H_2O_2 to a final concentration of 1.25 mM, then signal recording for a further 120 seconds. The signal was recorded at a potential of -0.4 V in a 0.1 M $LiClO_4$ electrolyte solution (pH 8) with a final cell volume of 8 ml following the addition of H_2O_2. The potential was optimised using cyclic voltammetry to optimise the faradaic current of Pt nanoparticle driven H_2O_2 catalysis. It was necessary to establish a new potential due to the peak shift attributed to the use of a screen-printed carbon counter electrode relative to the platinum coil electrode used with the traditional gold three-electrode cell.

For electrochemical analysis of the screen-printed electrode a Metrohm Autolab potentiostat (Netherlands) was used in conjunction with a three-electrode adapter for the printed electrodes. The three-electrode cell consisted of the gold functionalised carbon screen-printed working electrode, AgCl screen printed reference electrode, and a carbon screen-printed counter electrode, shown in **Figure 28**. The Metrohm Autolab was controlled using NOVA 2.1 software.
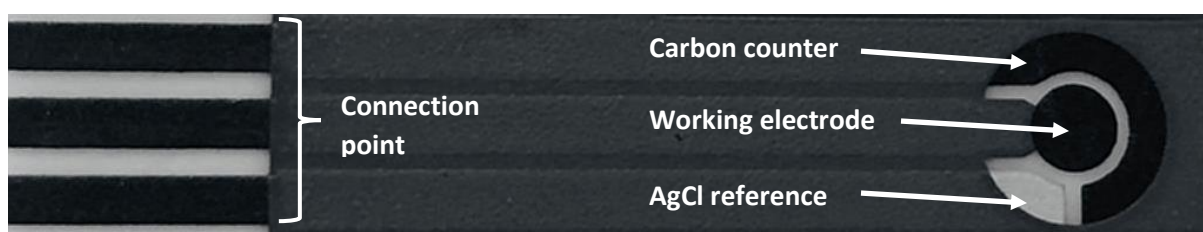
Figure 28. Screen printed electrode configuration featuring working electrode, carbon counter electrode, and AgCl reference electrode. The left side shows the connection point which allows the electrodes to be connected to a traditional potentiostat using an adapter.

3. Results and discussion

3.1. miRNA assay on planar gold electrode

Biosensors have become a growing sector in both academic and industry fields. The thing that both defines and differentiates a biosensor is the use of a biorecognition element. Nucleic acid biosensors are popular platforms due to the hybridisation of single stranded mature target miRNAs with complementary single stranded nucleic acid strands. While the complementary sequences will bind, even a single nucleic acid mismatch affects the hybridisation affinity. The reduction in hybridisation affinity of a single mismatch means even miRNA within the same families can be selected for using nucleic acid capture elements, which gives the assay is specificity [404,405]. The ability to quantify the level of target in a sample, regardless of whether the matrix is buffer or bodily fluids, relies on the efficiency and stability of the capture – target – probe binding event. When designing an assay, the higher the capture and probe binding affinity for the target, the greater the LOD of the assay. The LOD of an assay can therefore be improved by increasing the binding events per unit area or the ability to detect a low number of binding events, i.e., create more binding events or detect binding events more effectively. To create more binding events, the area of the electrode can be increased thus allowing a higher number of binding sites. Alternatively, the surface coverage of the capture units can be optimised in order induce a signal for each individual binding events by removing probe steric hinderance which might lead to target hybridisation with capture without a further probe hybridisation step. This assay uses an RNA polymer chain of 11 bases as the capture unit, given the short base length of the target miRNA sequence and the low Gibbs free energy attributed to short complementary nucleic acid sequences a 50-50 split of the sequence was chosen for the capture and probe lengths. Furthermore, as the goal of the assay was to create an ultrasensitive miRNA assay neither the capture nor probe hybridisation could be prioritised and therefore there was no advantage to increase the length of the capture or the probe. These capture RNA are designed to be complementary to half the length of the miR-1-3p miRNA target strand. A probe strand of RNA, which is complementary to the second half of the target sequence. To generate a current signal in this assay, design a platinum nanoparticle is used and it is functionalised using thiol chemistry with these probe RNA strands.

Nucleic acid sequences, both DNA and RNA based, are commonly used for the detection of nucleic acid biomarkers [406–409]. They provide a valuable capture and probe element due to their predisposition for hybridisation to complementary sequences. This is especially useful when target molecules are also single stranded nucleic acid sequences, such as in the case of miRNA. Literature reports a typical surface coverage

of probe nucleic acid strands to be ~ 3 – 5 pmol cm^{-2}. This is equivalent to $1.8 – 3 \times 10^{12}$ nucleic acid copies per cm^2.

Using a typical gold disc electrode, a high-density capture monolayer approach was taken with the goal of designing a sensitive miRNA assay. 5' modified capture RNA strands (captureRNA) featuring a thiol – C6 terminal were immobilised to the gold surface of the electrode using thiol chemistry allowing for direct immobilisation of RNA strands to the electrode surface [410,411]. The monolayer was allowed to form overnight on the gold disc electrode surface to maximise the monolayer coverage using 1 µM concentration of capture RNA stands and removing any limitations from the time needed for capture strands to diffuse to the electrode surface and bind. Using cyclic voltammetry, the properties of the immobilised capture monolayer were examined, the results of which are represented in **Figure 29**. In the presence of a H_2SO_4 electrolyte a gold oxide is formed when a potential greater than 1 V is applied. This gold oxide is then reduced back to gold when a potential of 800 mV is subsequently applied. Using a scan rate of 100 mV s^{-1} it is possible to generate a monolayer of gold oxide which represents the surface area of available gold, thus the resulting reduction peak at 800 mV can be used to quantify the available gold on the electrode surface which is expected to decrease as the capture strands bind [412]. By comparing the charge passed during the reduction of the gold oxide on the bare gold electrode versus the charge passed in the presence of the captureRNA immobilised on the surface it is possible to estimate the degree of surface coverage. To compare to a highly compact and ordered monolayer, 11-Mercaptoundecanoic acid (MUA) was used as a control monolayer. Replication of capture RNA immobilisation (N = 6) shows reasonable reproducibility of the monolayer with an average charge passed of 1.596×10^{-5} C ($\pm 9.8 \times 10^{-7}$) giving a relative standard deviation of 6.3%and suggests reasonably good reproducibility. However, analysis of the comparative reduction peaks of bare, capture RNA and MUA SAM shows that in comparison to the MUA SAM the capture RNA covers only 31.6% of the available gold surface. Therefore, captureRNA alone is not sufficient to effectively block the electrode surface under these conditions with up to 70% of the gold surface remaining exposed. It is possible that some of the increased current seen in the miRNA capture immobilised electrode is from the oxidative desorption of the monolayer during cycling. This is evidenced by the presence of an oxidation peak in the CV of the capture RNA immobilised gold electrode. While oxidative absorption is more common, it is possible that the oxidation of the crystalline gold lead to the desorption of the capture RNA from the surface of the gold electrode. This same oxidation peak is not present in the MUA SAM immobilised gold electrode cyclic voltammogram.
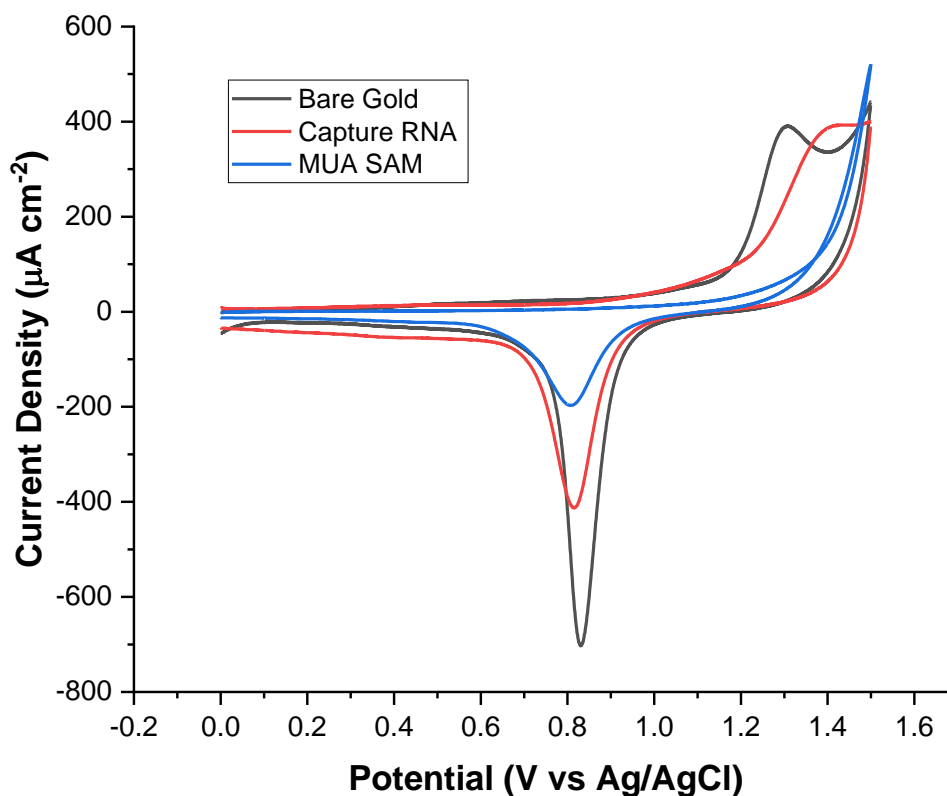
Figure 29. Cyclic voltammogram demonstrating the change in charge passed during the reduction of gold oxide using a bare gold electrode (black) and in the presence of capture RNA (red) established overnight and mercaptoundecanoic acid SAM (blue) established for 2 hours. The cyclic voltammograms were recorded in 0.1 M H_2SO_4 using an 1M KCl Ag/AgCl reference electrode and platinum wire coil as a counter. All CVs were recorded at a scan rate of 100 mV s^{-1}. CVs were recorded in fully independent triplicates.

The effect of the low surface coverage presented by the captureRNA on the assay was investigated by recording a chronoamperometric curve (i-t curve) of the current released by the degradation of hydrogen peroxide by the platinum nanoparticles, which when coated with probe RNA strands (probeRNA) acts as the probe. The probe RNA-functionalised platinum nanoparticles will henceforth be referred to as the "probe" with the nucleic acid sequences being denoted as probeRNA and the nanoparticles as PtNPs when referred to as unique reagents. The capture RNA layer was assembled on the bare gold electrode surface as before. Three bracketing concentrations of target miRNA-1-3p (1 µM, 1 nM, and 1 pM) were used in the assay to elucidate the effect of target concentration on the current response. It was expected, if the coverage of captureRNA was sufficient, then an appreciable difference in current could be observed given the

large difference, six orders of magnitude, in target concentration. The experimental protocol was based off a similar methodology on the electrochemical detection of miRNA using a variety of metallic nanoparticles [413,414]. A final concentration of 200 µM of hydrogen peroxide was used to reduce the likelihood of surface bubbles of oxygen forming on the electrode due to the degradation of hydrogen peroxide. Bubbles can block the probes and thus reduce the current response during the assay. Secondarily, the bubble may also affect the stability of the captureRNA on the gold surface, causing desorption [415,416].

The probe was assembled using 1 ml of 50 nm diameter PtNPs with a stock concentration of 3.3×10^{10} particles mL^{1}. The particles were functionalised using 900 µL of 1 µM probeRNA strands, which equates to a total of 5.42×10^{14} probeRNA strands. The final probes (PtNP functionalised with probeRNA strands) were aliquoted to 300 µl for use in the assay. This provides a final probe count of 1.1×10^{10} particles available for hybridisation with the target miRNA during the assay. Given a circular area of 3.14×10^{12} nm^2 and 1963.5 nm^2 respectively for the gold electrode and the 2D area of the nanoparticles, this puts the probes in a 7-fold excess to the physical capacity of the working electrode assay area, assuming enough hybridisation events occur. A high surface coverage is preferable to maximise the number of hybridisation events. This is especially important when a low concentration of target is expected, to maximise the current generated. The curvature of the nanoparticle allows for a high degree of surface coverage on the nanoparticle as it mitigates steric and electrostatic issues due to the negatively charged nucleic backbone arising between probeRNA strands [417–419]. A high surface coverage can also lead to less favourable properties, in particular when the surface coverage is so dense so as to create a blocking effect at the nanoparticle surface it may inhibit the catalytic effect of the nanoparticles on the hydrogen peroxide [420]. Reducing the degree of hydrogen peroxide degradation in turn reduces the current generated per probe which affects the low-end sensitivity as smaller currents may not be detectable through any noise which might be present in the assay. In this case the most likely source of noise would come from the carbon/gold electrode surface itself reducing the hydrogen peroxide and consequently generating a current [421–423].

To assess the optimal potential at which to record the i-t cures at the faradaic current attributed to peroxide degradation at the PtNPs was assessed using the screen-printed electrode cell. The potential of -0.4 V was chosen to maximise the faradaic current relative to the capacitive and cathodic current of the nanoparticles without the presence of the hydrogen peroxide. It should be noted that although the -0.4 V potential in relation to the screen-printed electrode cell the negativity can be attributed to the potential shift

of the pseudo-reference AgCl electrode used relative to the Ag/AgCl reference. That shift is between -300 and -400 mV and hence the i-t curve potential is approximately -0.1 V vs 1M KCl Ag/AgCl which mitigates possible hydrogen evolution during the assay.

The expected outcome of a stepwise increase in faradaic current, proportional to the increase in target miRNA concentration, was not observed, as shown in **Figure 30**. All three target concentrations displayed broadly similar current responses upon addition of hydrogen peroxide and no steady-state current was observed over the 2400 second assay duration. This current appears to be independent of target concentration. The most likely explanation for this independent current is background signal being generated by the system which can be seen in the black like shown in **Figure 30** . The origin of the background signal is the large (70%) unblocked gold surface area observed in **Figure 29**. This is due to golds catalytic effect on hydrogen peroxide generating current [424,425]. The independent current coupled with a relatively large, exposed gold area therefore explains the large and similar currents observed at all three target concentrations.
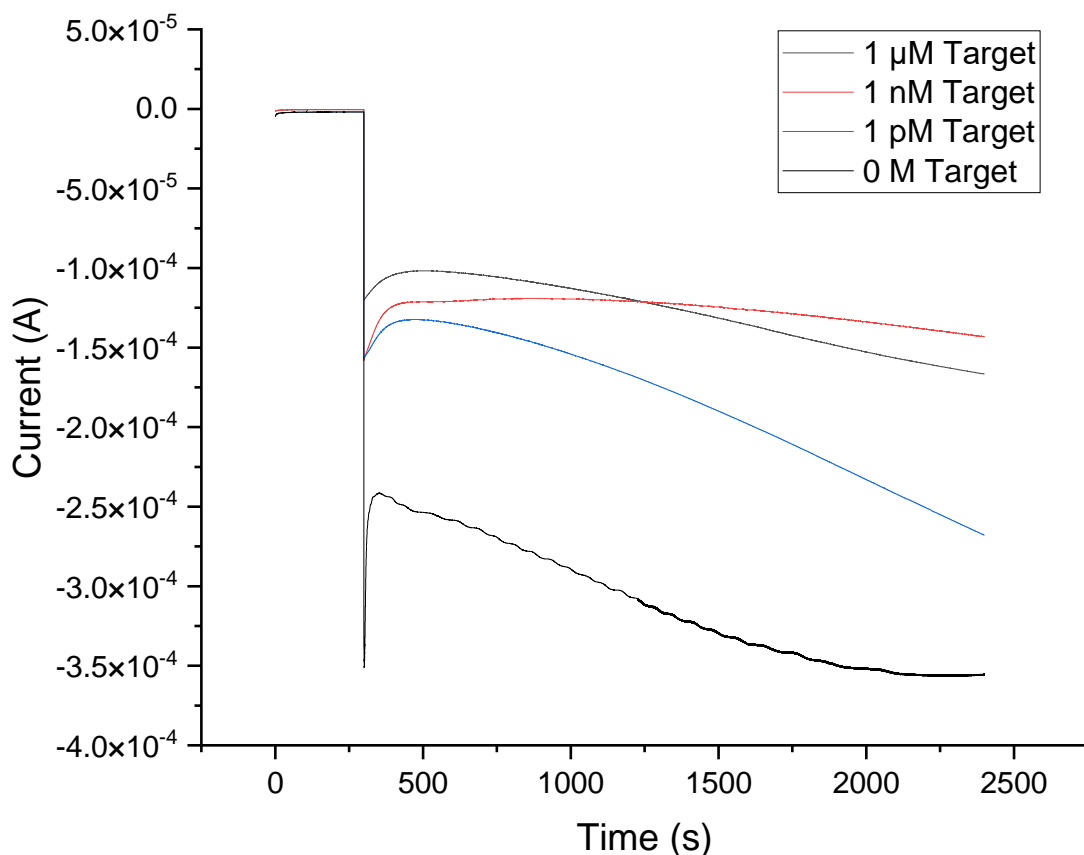
Figure 30. Chronoamperometric curve (i-t curve) of captureRNA monolayer established using a 1 μM bulk solution. Target miRNA concentrations of 1 μM, 1 nM, 1 pM, and 0 M concentrations of target miRNA with 50 nm platinum nanoparticle functionalised with 1 μM probe RNA concentration. i-t curves were recorded in 0.1 M H_2SO_4 with a working concentration of 200 μM H_2O_2. Chronoamperometry was recorded at a scan rate of 100 mV s^{-1}. Chronoamperometry was recorded in fully independent triplicates.

The results of the experiments conducted on a bare gold electrode indicated that a large available surface area of gold at the electrode substrate was contributing to a high background signal [426]. This signal was caused by nonspecific degradation of the hydrogen peroxide which was independent of the miRNA target concentration and was attributed to the catalytic effect of gold on hydrogen peroxide degradation. One common method for reducing this signal attributed to gold disc electrode substrate in other assays is to use a blocking species to reduce the available gold surface. This is most often achieved using an alkanethiol chain of appropriate length. The length is typically dictated

by the length of the spacer used for the capture element of the assay, for example a 6-Mercapto-1-hexanol (MCH) given the C6 spacer used on the captureRNA in this work, however alkane chain spacer lengths are not standardised and may be longer or shorter according to the desired application [427,428]. Alternative strategies also include using proteins such as bovine serum albumin (BSA) which performs a similar function of blocking available gold surface following deposition of the capture elements on the gold substrate [429,430], and developing alternative surfaces in order to avoid the use of metallic substrates which can degrade the hydrogen peroxide in a similar manner [431,432].

3.2. miRNA assay on Au-SPE electrode

To improve sensitivity of the assay a gold containing screen-printed carbon electrode (Au-SPE) substrate was used to reduce the surface area of gold at the electrode surface. 500 nm gold nanoparticles were added to carbon ink for screen-printing electrodes prior the printing process. Using proprietary techniques, the level of gold nanoparticles which are exposed at the surface of the electrode can be tuned and controlled during the curing process. Two factors make the Au-SPE an attractive alternative to a planar gold electrode substrate. The first is that the carbon ink of the screen-printed electrode does not contribute to the catalysis of the hydrogen peroxide. Although unblocked gold can still generate a background signal the rest of the unblocked surface, the carbon ink, will not contribute to this background current associated with reduction of peroxide. This however also means that while the electrocatalytic area, the Au, is small, there is a large area, Au and C, of the working electrode contributing to the capacitive current of the system. This capacitive current may contribute to the noise of the system and make it come difficult to distinguish faradaic currents attributed to the probes. The second benefit is that the spherical nature of the nanoparticles could allow for a closer packing of the captureRNA strands on the gold surface. This curvature can mitigate the steric hindrance between charged captureRNA strand to allow for a higher degree of surface blocking [420]. The orientation of the capture strands immobilised on a curved surface can also allow for improved hybridisation with target and probeRNA strands by exposing the nucleic acid sequences while remaining closely packed at the surface through the C6 spacers [433]. This effect also aids in the reduction of exposed gold at the surface of the electrode without the need to immobilise blockers on the surface.

Upon introduction of the Au-SPE substrate the potential applied during the i-t was optimised. Due to this optimisation process the potential at which the i-t curve was decreased (more negative) in an attempt to select for the current contribution of the

probe over any nonspecific (background) signal. Recent work by Chang *et al.* shows that hydrogen peroxide disproportionation (simultaneous oxidation and reduction) generates a measurable faradaic current between -0.4 and -0.5 V using platinum microelectrodes [434]. Hence, in order to optimise the faradaic current due to the hydrogen peroxide degradation at the probes (Pt nanoparticles functionalised with probeRNA) a potential of -0.4 V was selected for chronoamperometric measurements using Au-SPE electrodes.

Alongside the alternative electrode substrate some other parameters of the assay were optimised to further improve the signal to noise ratio. Despite the reduced gold surface area, the same bulk concentration of captureRNA was used. This ensures a high degree of surface coverage on the gold nanoparticles at the surface of the electrode substrate. The aim of the high surface coverage is to ensure the maximum degree of surface blocking. Surface blocking is needed to reduce the current attributed to the nonspecific degradation of hydrogen peroxide (degradation not catalysed by the probe). Furthermore, in order to generate a higher current, the concentration of hydrogen peroxide used in the assay was increased from 200 µM final concentration to a final concentration of 1.25 mM. The higher concentration of the hydrogen peroxide should increase the current recorded during the assay across all target concentrations [435,436]. Experimental evidence showed that the bare Au-SPE generated a peak current of approximately 2 µA, **Figure 31**. This can be considered the maximum current of the assay as this would also represent the maximum area of probe assuming saturation of the probe and semi-infinite linear diffusion dynamics between the probes being dominant. Thus, a higher concentration of hydrogen peroxide provides a more desirable current range in which to conduct the assay. Finally, the time was reduced from 2400 seconds to 180 seconds for the recording time of the assay as the time was initially selected to allow a steady current to be formed following the addition of hydrogen peroxide however following analysis of the preliminary experiments it was determined that 180 seconds was considered adequate to record a suitable current signal.
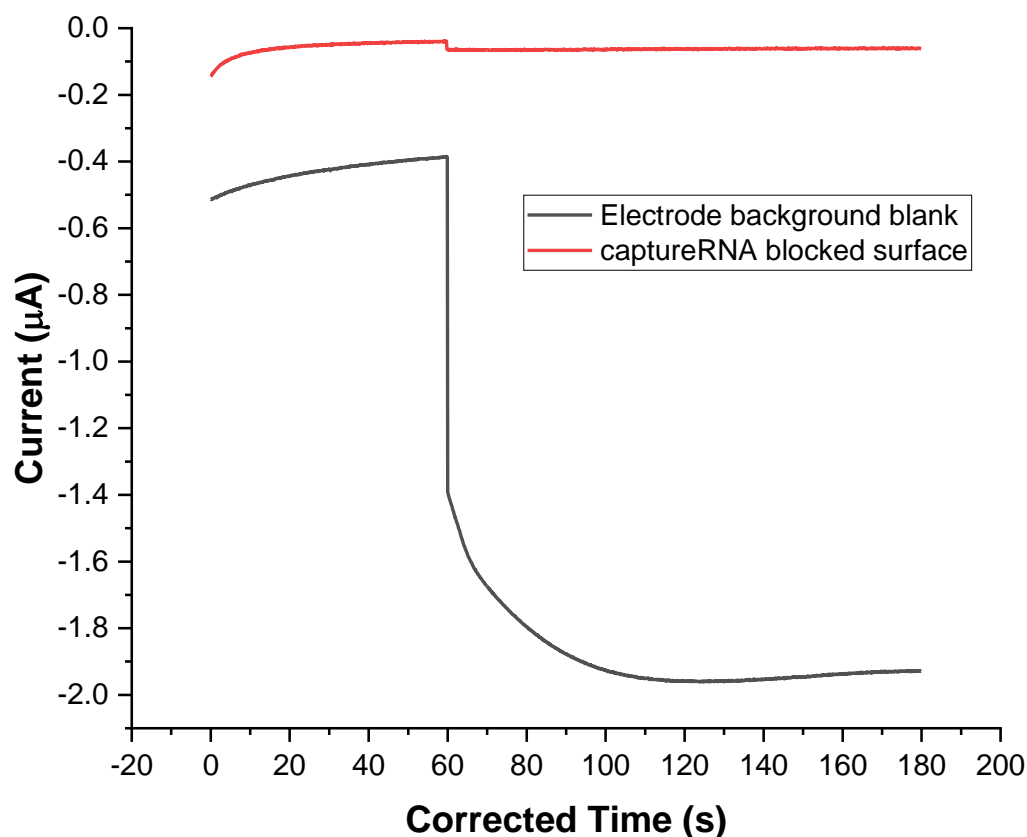
Figure 31. i-t curve showing the current response of the bare Au-SPE electrode substrate (black) and with captureRNA immobilised on the surface in the presence of 1.25 mM H_2O_2. Current was recorded at -0.4 V and H_2O_2 was injected after 60 seconds. Chronoamperometry recorded in fully independent triplicates.

Figure 31 demonstrates the change in current observed between the bare Au-SPE electrode and when the surface is blocked using the captureRNA strands [437,438]. The 2 µA current observed for the bare electrode demonstrates the catalytic effect of the gold nanoparticles present in the SPE substrate. It is greatly reduced when compared to the response seen in a bare gold disc electrode despite a higher concentration of H_2O_2 being used. Thus, showing the Au-SPE has gold present at the surface of the electrode to catalyse the hydrogen peroxide and that the total gold area is significantly less than the planar gold disc electrode, as expected. A significant drop in current of 1.8 µA is observed upon addition of the same concentration of hydrogen peroxide when the captureRNA layer is present. This shows the captureRNA strands alone do provide a significant blocking effect on the active gold area at the surface of the Au-SPE. The lower current indicates the packing density of the captureRNA on the available gold is sufficient

to reduce the catalysis of the hydrogen peroxide. It was also observed that similar blocking effects could be achieved with a reduced incubation time of just one hour when compared to a three-hour incubation. A comparison between the three-hour and one-hour is demonstrated in **Figure 33**. The lower reproducibility may be attributed to batch to batch variation of the Au-SPE as surface morphology is known to effect the stability of nucleic acid monolayer at high and low concentrations [439]. This variation was quantified using cyclic voltammetry in 0.1 M H_2SO_4 at a scan rate of 100 mV s^{-1} (**Figure 32**), the result of which indicates that there can be as much as an 18% variation in available surface gold between AuC-SPEs, data is tabulated in **Table 11**. The same method for surface area gold availability was used as described in **Figure 29**, it should be noted that the gold oxide reduction peak is shifted from 0.8 V to 0.45 V which can be attributed to the use of the screen-printed AgCl pseudo-reference in comparison to the Ag/AgCl reference electrode. The shift is confirmed using ferrocene methanol redox probe showing a redox peak shift of approximately 300 mV, which is in agreement with the observed shift in gold oxide reduction peak. This reinforces the importance of captureRNA bulk concentration to available gold surface. It is also likely that the curvature of the particles allows for a denser packing due to the mitigation of steric hinderance and electrostatic repulsion between the charged captureRNA strands [420,433].
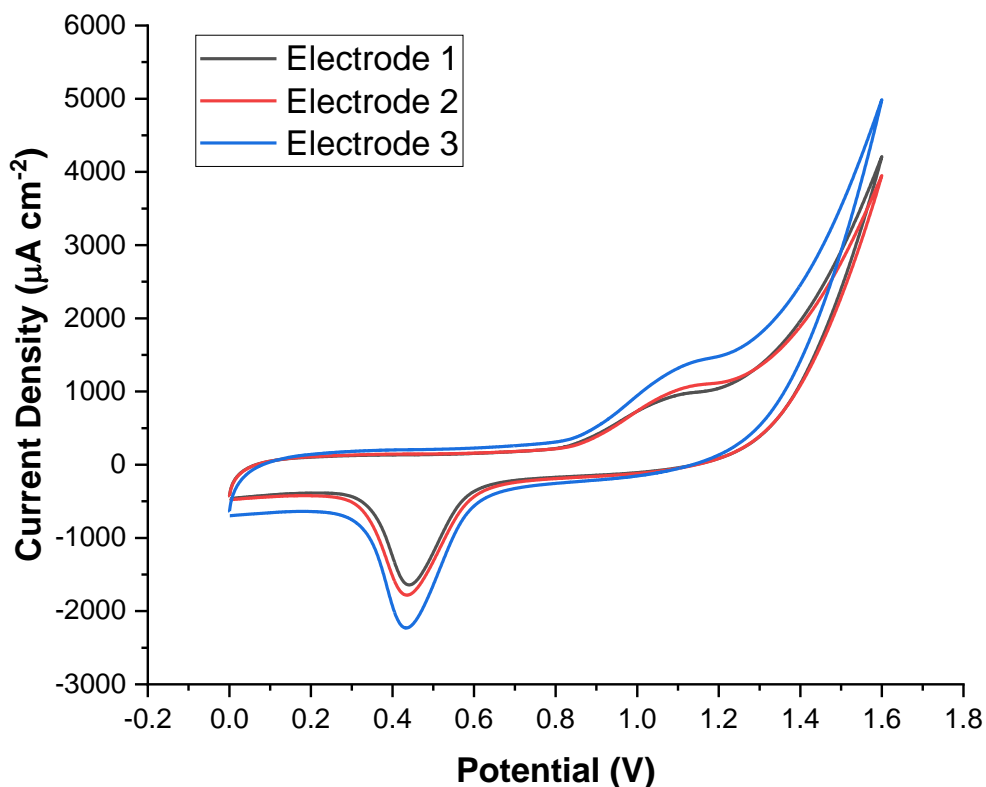
Figure 32. Cyclic voltammogram of three independent AuC-SPEs demonstrating the intra-batch variation in exposed gold. The cyclic voltammograms were recorded in 0.1 M H_2SO_4 with a scan rate of 100 mV s^{-1}. The available gold area was calculated using the reductive charge passed at 0.4 V. The peak shift for the gold oxide reduction can be attributed to the use of the screen-printed AgCl pseudo-reference electrode when compared to the traditional 1M KCl Ag/AgCl reference used for the gold disc electrode described previously. The CVs were recorded in fully independent triplicates.

Table 11 - Tabulated data for the intra-batch variation in available gold surface in the AuC-SPE

	Electrode 1	Electrode 2	Electrode 3	Std Dev (C)	Mean (C)	RSD
Charge (C)	6.40 x10^{-5}	7.62 x10^{-5}	9.15 x10^{-5}	1.38 x10^{-5}	7.72 x10^{-5}	18 %
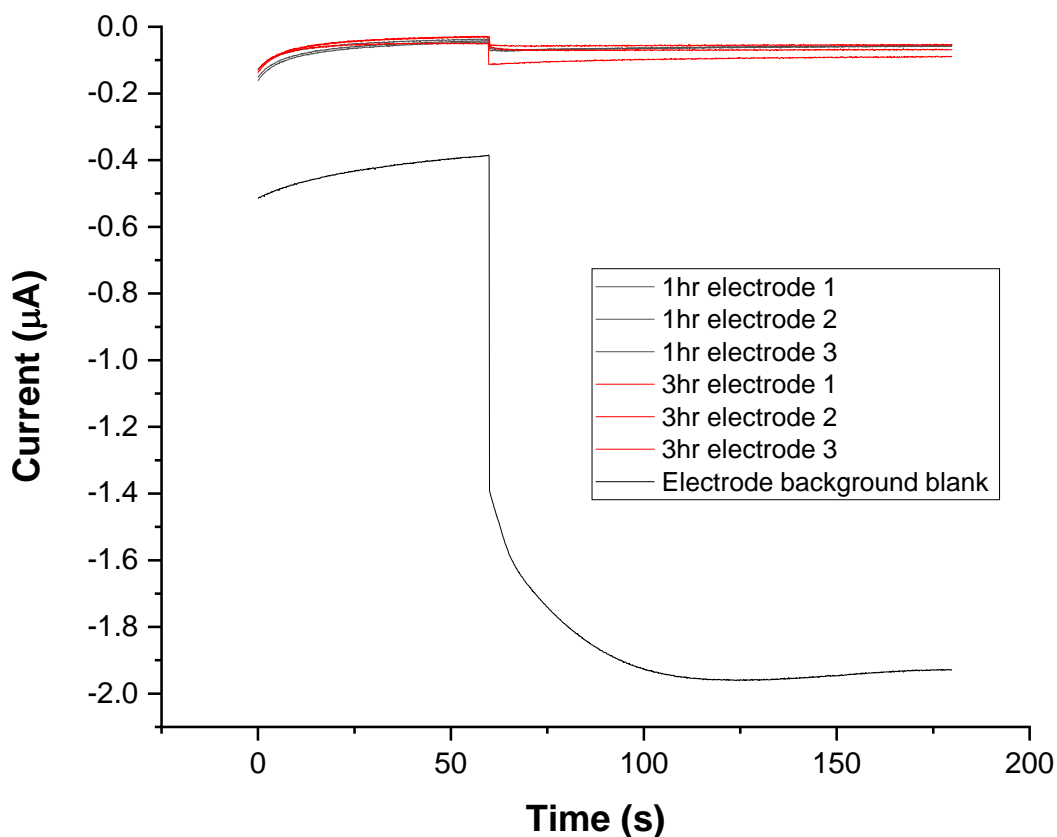
Figure 33. Comparative i-t curves of capture RNA deposition varying immobilisation time at 1 hour (black) and 3 hours (red). All it curves were recorded using 1.25 mM of H_2O_2 in 0.1 M $LiClO_4$ with a final cell volume of 8 ml at a potential of -0.4 V. The reference was screen printed AgCl electrode and the counter was a screen-printed carbon electrode. Chronoamperometry was recorded in fully independent triplicates.

Table 12 – Tabulated data for **Figure 33** for unmodified electrode surface and the electrode surface modified with captureRNA for one hour and three hours. Currents recorded at 180 seconds (N=2)

Electrode Modification	Current at 180 seconds (µA)
1-hour incubation of captureRNA	-0.057 (± 0.001)
3-hour incubation of captureRNA	-0.072 (± 0.018)
Unmodified electrode surface	-1.929

The change in current between the bare and covered surface indicates that the Au-SPE does offer a current range which is acceptable for a biosensor. The limited surface area of the gold will limit the maximum limit of detection however the low background current does suggest that surface modification with captureRNA strands alone at the electrode surface could detect ultrasensitive, low concentrations of free miRNA targets. While the evidence suggests that the packing density of the captureRNA on the Au-SPE is suitable for reducing the nonspecific signal of golds catalysis of without the need for additional surface blocking steps, such as protein or alkane-thiol deposition, further elucidation is required to examine the effect of the higher surface packing on the hybridisation of target. A high surface density of captureRNA strands may impede the hybridisation of target and probe in the assay, despite the curvature mitigation of the gold nanoparticle [440].
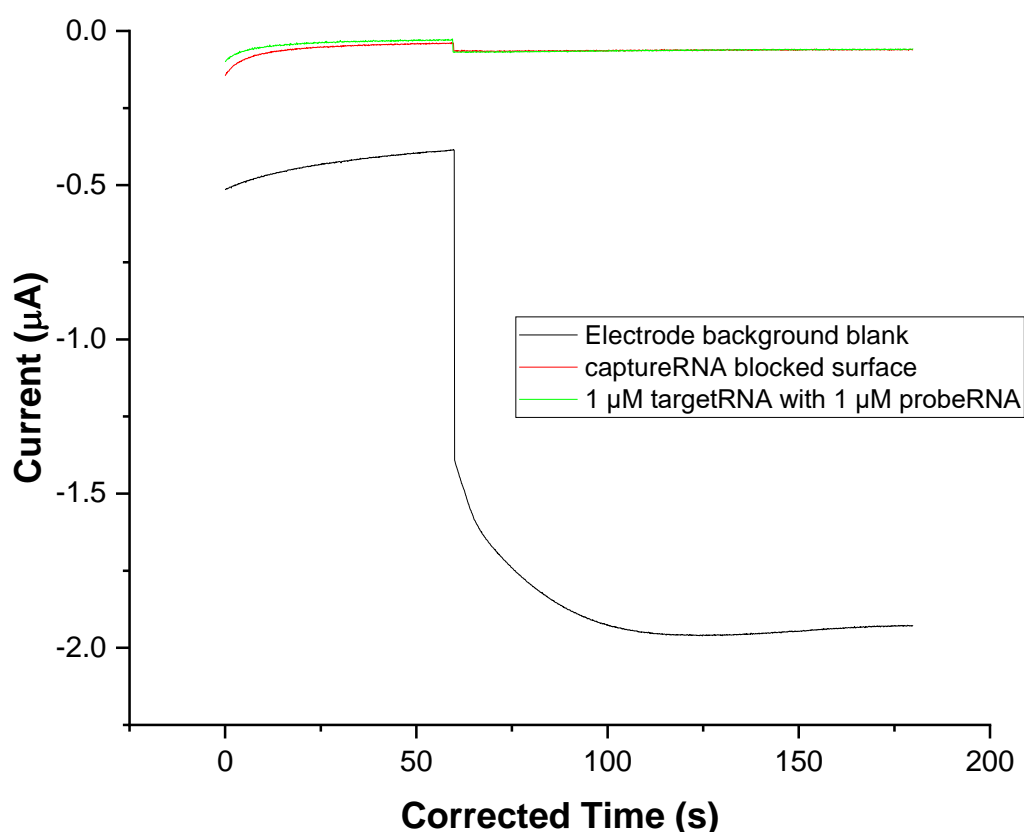
Figure 34. Comparison of current response upon introduction of hydrogen peroxide of the bare electrode surface, the surface with the captureRNA in place, and an assembled assay with captureRNA in place with 1 µM target with 1µM functionalised probe. The i-t curves were all recorded for 180 seconds, consisting of a 60 second equalisation period, injection of 1.25 mM H_2O_2, then signal recording for a further 120 seconds. The signal was recorded at a potential of

-0.4 V in a 0.1 M LiClO$_4$ electrolyte solution with a final cell volume of 8 ml following the addition of H$_2$O$_2$ (final concentration 1.25 mM). The reference was screen printed AgCl electrode and the counter was a screen-printed carbon electrode. The gold functionalised screen-printed carbon electrode is represented by the black line and represents the unblocked background signal of the assay. The red line represents the gold functionalised screen-printed carbon electrode following the immobilisation of the capture RNA. The green represents the full RNA sandwich assay using 1 µM concentration of target miR-1 miRNA with platinum nanoparticles functionalised using 1 µM of probe RNA. Chronoamperometry was recorded in fully independent triplicates.

To assess the impact of using an AuC-SPE substrate for the detection of the miRNA target, the assay was assembled, and i-t curves were recorded with captureRNA in place. Initial experiments were recorded using 1 uM of miR-1-3p to ensure a high probe concentration if the target hybridises. A high probe concentration was used to maximise the current output and assess the sensitivity of the assay when the captureRNA is at a high surface coverage. However, there was no significant change in the current observed when the capture, target, probe was present compared to the capture layer alone, **Figure 34**. The lack of an observed increased current was likely by one of two possible scenarios. The first was that due to the high density of the captureRNA, the hybridisation of the target was inhibited, and the NP labelled with probe strands could not be hybridised. Thus, the absence of probe led to the absence of a recordable current as the due to the absence of the reduction of 2Pt(OH) sites required. An alternative scenario is that the peroxide cannot access the surface of the platinum due to a close packed monolayer of probe on their surface. Thus, if the curvature of the nanoparticles was contributing to a higher surface density of probeRNA strands on the platinum nanoparticle surface this effect could contribute to the absence of signal through two possible mechanisms [433,441]. The surface density of the probeRNA was inhibiting hybridisation to the target thus leading to the absence of signal despite the presence of target miRNA. Alternatively, the dense coverage of probeRNA on the nanoparticle is causing a similar blocking effect at the nanoparticles surface. This blocking would prevent the diffusion of the hydrogen peroxide to the nanoparticles surface thus preventing the catalysis and production of current [442–444]. In the latter scenario hybridisation is occurring between the capture target and probe RNA strands however no current is being generated.

The issue with current generation may also be linked to the surface of the screen-printed electrode. Gold disc electrodes are cleaned mechanically prior to immobilisation of the capture strands to the surface. In the case of the screen-printed electrodes this is not possible. Physically polishing of the screen-printed electrodes is not possible prior to

immobilisation as there is a risk of damaging the printed electrode. Also, the thiol binds to the gold surface of the AuNPs within the ink thus polishing the printed electrodes may remove some of these sites for RNA immobilisation. Therefore, there is a risk that the surface of the screen-printed electrode could be contaminated. This contamination can be with organic molecules, blocking the immobilisation of RNA, or it can mean the presence of RNA on the surface of the electrode. Single stranded RNA is not stable and easily degraded by RNase in the environment which would lead to the degradation of the RNA sequence on the surface of the electrode either during or immediately after immobilisation. Ultimately, this would leave the immobilised thiol sequences on the surface of the gold which would contribute to the diminished current observed over the blank electrode surface but make hybridisation with either the target miRNA or probe strand of RNA impossible leading to the absence of the expected current upon addition of miRNA target. It is also possible the addition of a self-assembled monolayer following the immobilisation of capture RNA may help to improve the stability of the capture layer. The SAM is typically added to disperser the thiolated nucleic acid chains more evenly across the gold surface. It can also increase the blocking effect on the gold surface. Using C6 spacers on the capture strands of RNA means a SAM using 5- or 6-mercapto alcohol would be appropriate to block the surface and not interfere with the capture strand's ability to hybridise with the target. In this case a blocking SAM was not used as the gold surface is more limited than that of a gold disc electrode, meaning the blocking was not such a high priority. Also, some assays in the literature which use similar electrochemical principles do not use blocking of the electrode surface. Ultimately it was determined that the issue leading to the absence of expected current was more likely to be contributing from a source other than surface blocking and therefore future experiments were continued without the addition of a SAM.

3.3.   probeRNA density impact on current generation of Probe

Elucidating which of the three mechanisms (capture density inhibited hybridisation, probeRNA density inhibited hybridisation, or nanoparticle surface blocking) was an important next step in order to determine the viability of the assay using the Au-SPE substrate. Assuming the surface blocking mechanism inhibited the catalytic decomposition of the hydrogen peroxide by the platinum nanoparticle, a lower surface concentration of probeRNA strands on the platinum nanoparticles should expose a greater surface area of nanoparticles and thus lead to an increase in observed current upon addition of hydrogen peroxide to the system. To assess the effect of surface loading of probeRNA on the blocking of the nanoparticle surface the bulk concentration of probeRNA in the deposition solution was systematically reduced. The concentration

of platinum nanoparticles during functionalisation remained the same in all cases. The duration of incubation was maintained at one hour. Reducing the incubation time while maintaining a bulk concentration of 1 µM probeRNA could also be used to reduce the surface coverage but would have required very short incubation periods which could have introduced more variability. The level of excess probeRNA strands to platinum nanoparticle area was calculated for the original 1 µM deposition solution. This was done assuming a high packing density which is facilitated by both the high curvature of the 50 nm platinum nanoparticles (relative to a 100 nm nanoparticle or a planar surface) and the salt concentration of the TE buffer in which the immobilisation occurred (10 mM Tris, 1 mM EDTA). Literature suggests that include a salt to screen the negative charge of the RNA backbone combined with a highly curved surface can generate close to theoretically maximal surface concentration of RNA strands [420,433]. Given a sufficient curvature and salt concentration the limiting factor for RNA surface concentration is the footprint of the RNA strands in comparison to the surface area of the platinum nanoparticle. The literature does not offer an exact diameter of single RNA strand however estimates suggest a diameter of approximately 26 Å, equivalent to 2.6 nm or a radius of 1.3 nm. Hence, the footprint of the probeRNA stands is taken to be 5.31 nm^2 [445,446]. The diameter of the platinum nanoparticle is 50 nm, giving an available surface area of 7853.98 nm^2. As described in Materials and Methods 900 µL of 3.3 x10^{10} particles mL^{-1} platinum nanoparticle stock was washed thoroughly and then resuspended in 900 µL of TE buffer containing the appropriate concentration of probeRNA. By converting the concentration of the probeRNA to copy number in the bulk solution it is possible therefore to calculate the ratio of excess to which the probeRNA is present. This information is displayed in **Table 13** and **Figure 35** below.

Table 13 - Calculations of the determination of the ratio of excess of the probeRNA total area in comparison to the platinum nanoparticle total area when using 900 µL of stock for both.

Stock probeRNA Concentration (nM)	Mole of probeRNA in bulk solution	Strands of probeRNA in bulk solution	Total footprint of probe RNA (cm2)	Total platinum surface area (cm2)	Ratio (total probe area: total np area)
1000	9×10^{-10}	5.418×10^{14}	28.766	2.333	12.33
500	4.5×10^{-10}	2.709×10^{14}	14.383	2.333	6.17
100	$9 \times 10^{10-11}$	5.418×10^{13}	2.877	2.333	1.23
50	4.5×10^{-11}	2.709×10^{13}	1.438	2.333	0.62
25	2.25×10^{-11}	1.355×10^{13}	0.719	2.333	0.31
10	9×10^{-12}	5.418×10^{12}	0.288	2.333	0.12
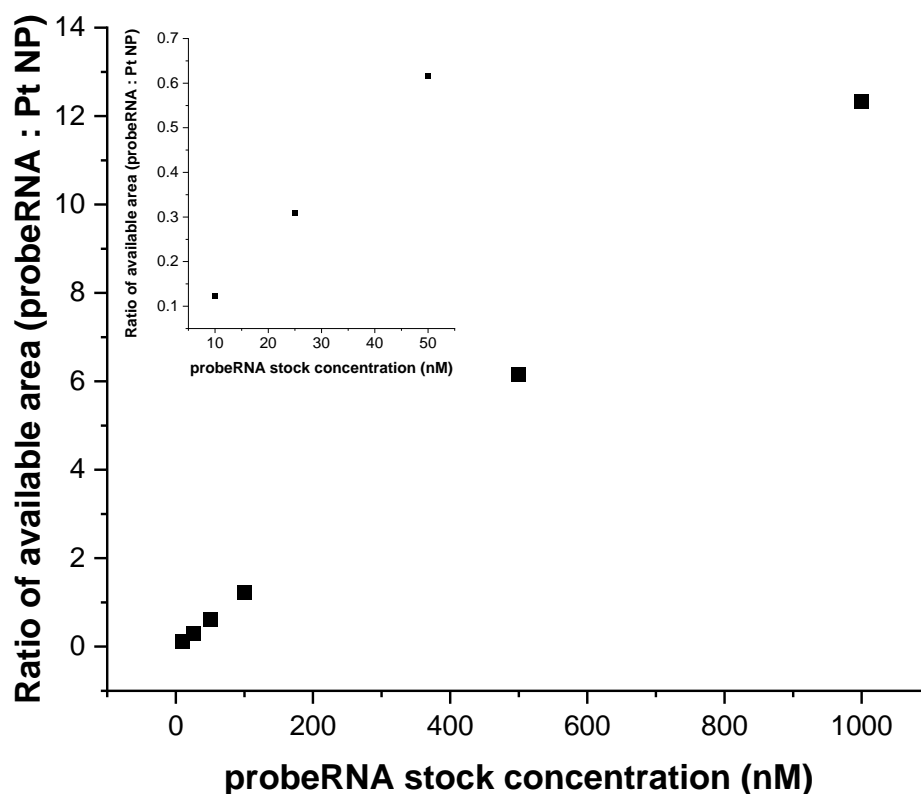
Figure 35. Ratio of available area of probeRNA footprint relative to the available surface area of PtNP. Inset: expanded view of 10 nM to 50 nM stock probeRNA concentration.

Table 13 demonstrates that at a concentration of 1 µM of probeRNA (1000 nM) the total sum of the probeRNA footprint, in other words the total surface area which the probeRNA when close packed, is in a twelve-fold excess to the available. This suggests that the packing density given this concentration of probeRNA, the salt concentration of the buffer, and the high curvature of the nanoparticles should block a significant area of each platinum nanoparticle, with an approximate surface coverage of 1400 probeRNA strands per nanoparticle. This surface coverage would equate to an approximate coverage of ~2 x10^{13} strands cm^{-2}, this fits well with reported densities on similar size nanoparticles and is greater that the reported density for planar gold [433,447]. Both **Table 13** and **Figure 35** indicate that a much lower degree of surface coverage is likely when the ratio of available probeRNA compared with the available nanoparticle surface area is lower and the literature also supports the conclusion that bulk concentration affects the surface coverage [448]. At a concentration of 25 nM the expected coverage of an individual nanoparticle surface area is a maximum of approximately 30%, which is equivalent to 450 strands per nanoparticle or ~6 x10^{12} strands cm^{-2}. At a stock concentration of 10 nM the coverage is approximately 10% of the available surface area of the nanoparticles, giving surface coverages of 180 strands per nanoparticle which equates to ~2 x10^{12} strands cm^{-2}.
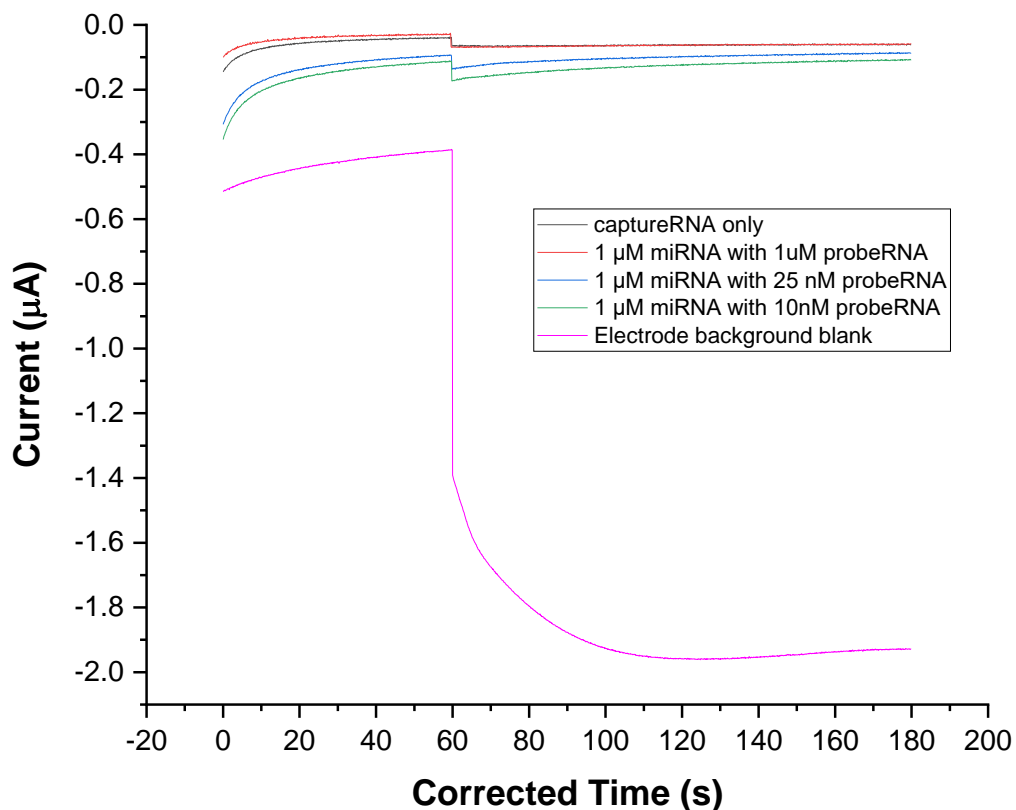
Figure 36. i-t curve of complete RNA sandwich assay showing an increase in current observed in the presence of 1 μM miR-1 target miRNA and 50 nm platinum nanoparticle functionalised probe. The 50 nm Pt probes were functionalised using 1 μM (red), 25 nM (blue) and 10 nM (green) of probe RNA prior to addition to the capture and target complex of the assy. All i-t curves were recorded using final concentration of 1.25 mM of H_2O_2 and a 0.1 M $LiClO_4$ electrolyte at a potential of -0.4 V. The reference was a screen printed AgCl electrode and the counter was a screen-printed carbon electrode. Chronoamperometry was recorded in fully independent triplicates.

Table 14 – Tabulated data of **Figure 10** showing relative currents of each modification recorded at 180 seconds.

Electrode background blank	captureRNA blocked surface	1 µM miRNA with 1uM probeRNA	1 µM miRNA with 25 nM probeRNA	1 µM miRNA with 10nM probeRNA
-1.929 µA	-0.061 µA	-0.059 µA	-0.087 µA	-0.108 µA

To assess the effect of increasing the active surface area of the nanoparticle on the current observed during the i-t curve the experiment was repeated using probes which had been functionalised using a 25 nM and 10 nM stock solution, respectively. These concentrations were chosen as the calculations show a greater than 50% platinum surface area per nanoparticle. Choosing a concentration much lower than the theoretical maximum also ensures good available platinum surface area in the case of heterogeneous distribution of surface coverage attributed to aggregation of probeRNA strands or platinum nanoparticles. The catalytic reduction of hydrogen peroxide at the platinum surface requires two free platinum sites to be available. The immobilisation of a probeRNA to the surface of the platinum nanoparticle decreases the free surface are for hydrogen peroxide reduction. Thus, a high surface density of immobilised probeRNA on the surface of the platinum nanoparticle reduces the surface area. This corresponds to a reduction in peak current. By reducing the probeRNA solution surface saturation of probe RNA on the platinum nanoparticles is avoided and free site of platinum are maintained for hydrogen peroxide catalysis. The resulting i-t curves are shown in **Figure 36**. As the concentration of probeRNA used to functionalise the NPs is decreased, and thus reduce the final surface coverage of the probe on the nanoparticle, an increase in current is observed. The captureRNA layer, shown in black, illustrates the low background signal as described in **Figure 31** and **Figure 33**. The red line is the same data which is described in **Figure 34** and shows the lack of signal, above the background, when the 1 μM stock concentration of probeRNA is used in generating the probes. The blue and green line indicate the observed signal from probes which have been functionalised using 25 nM and 10 nM stock concentration of probeRNA, respectively. The signal increase between the 1 uM and 25 nM functionalised probes is approximately 0.28 μA. A further current increase of 0.21 μA is observed between 25 nM and 10 nM stock concentrations. This limited dataset shows an exponential relationship between the stock concentration of probe RNA used in probe functionalisation and the absolute current observed, shown in the inset of **Figure 37**. Absolute current is shown here for clarity and ease of comprehension. Although it is a limited sample size, it is possible to extrapolate the theoretical peak current when an optimal probeRNA surface coverage is used to functionalise the nanoparticles. Logically, the maximum current will be generated by the nanoparticle with the maximum available surface area. As hybridisation is still essential to correlate the current to the target miRNA concentration through the formation of a sandwich configuration, a minimum of one probeRNA strand is necessary on each nanoparticle. Thus, the optimal ratio when considering only maximum current is a stock probeRNA which gives a single strand per

nanoparticle. Using **Table 13** that can be calculated to be a stock concentration of 0.055 nM (55 pM).
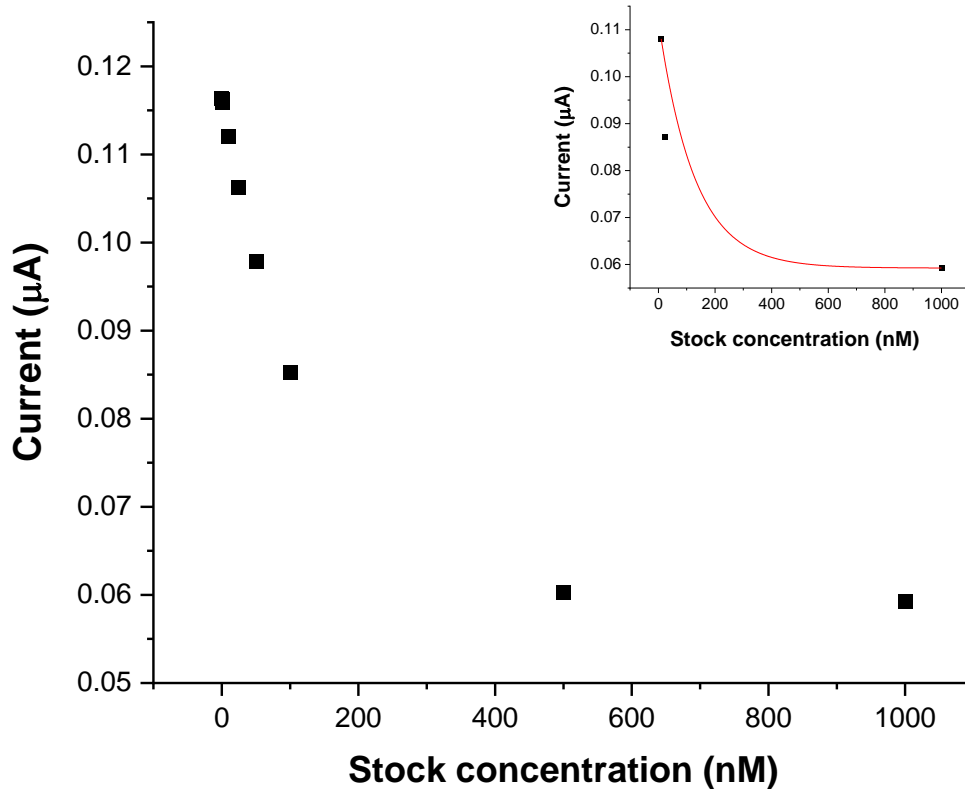
Figure 37. Extrapolated curve demonstrating the exponential growth relationship between stock concentration of probeRNA used during functionalisation. Current is plotted in absolute value for presentation purposes. Inset: original data points recorded at 180 seconds showing the fitting curve used to extrapolate the major plot.

Figure 37 demonstrates the theoretical absolute current at different stock concentrations of probeRNA. An exponential growth relationship was established from the experimental data, and this was extrapolated to determine the maximum current achievable using the established 55 pM optimal concentration. The plot determines the peak current to be 0.116 µA when a target concentration of 1 µM miRNA is used and all other parameters are maintained. The fitting determined that this is likely the maximum achievable current when the assay is maintained in its current format as similar peak currents were seen for 500 pM, 250 pM, and 100 pM stock concentrations also. This implies the current generated by the probe drops dramatically when the available surface area is reduced below 99%. It must be noted that these calculations are designed to optimise current generation and do not consider the impact of surface coverage on the target miRNA to

probeRNA hybridisation events. Fewer probeRNA present create limitations related to orientation which maybe become a limiting factor for assay performance. However, these results do show the impact available surface area has on the ability for the assay to generate a signal and that surface coverage can be an extremely limiting factor in this regard.

3.4. Effect of captureRNA density on hybridisation

Although experimental data and subsequent calculations suggest a strong correlation between the lack of observed current seen in **Figure 34** and the probeRNA coverage of the nanoparticles during probe functionalisation, other processes, such as low hybridisation efficiency, may also contribute. Short RNA sequences as well as the established dense surface packing may impact the hybridisation of both the electrode immobilised captureRNA and the platinum nanoparticle immobilised probeRNA with the miRNA target. Improvements in hybridisation efficiency can be achieved by conducting the experiments approximately 5 °C below the melting temperature of the double stranded recognition element – miRNA sandwich which makes double stranded nucleic acids energetically preferential hence, this method is frequently used to improve primer dynamics in PCR methods. The melting temperature is the temperature in which half of double stranded nucleic acid will dissociate into single stranded nucleic acid strands and indicates the stability of the RNA sandwich of the assay [449–452]. Staying below the melting temperature is preferential for ensuring the stability of double stranded RNA formation due to capture – target – probe hybridisation. Establishing the presence of successful hybridisation and subsequent double stranded RNA sandwich is a difficult one, particularly on a surface bound assay such as the one described in this work. One possible method for this would be to use a double stranded RNA intercalating dye to visually confirm the presence of double stranded RNA on the surface of the electrode. However, the issue with this method is that most intercalating dye for double stranded nucleic acid sequences also show some affinity for single stranded nucleic acid sequences, which would impede the effectiveness of this method in establishing exclusively establishing the presence in this application. Typically, a dye is conjugated to the probeRNA strand however, the visualisation of the dye would also be problematic given the opaque nature of the electrode material meaning specialised fluorescence imaging, such as STED microscopy, would be required to visualise and analyse the results.

The possible impact of hybridisation efficiency should be considered when optimising nucleic acid-based electrodes. Hybridisation is an important parameter which may also impact the ability of the sensor to generate a current at a broad range of target concentrations. The energy required for a strand of ssRNA to hybridise with a complementary strand, such as in this assay, is quantified by the Gibbs free energy. The Gibbs free energy can be computed from the sequence of the target strand and there are numerous open-source tools which perform this calculation as it is particularly important when designing primers for PCR. The Gibbs free energy can be related to the equilibrium constant between the single stranded RNA sequences by the following equation [453]:

$$\Delta G° = -RTln(K_{eq}) \qquad (4)$$

Short oligonucleotides can be modelled by the simplified 2 state process where in the reactant ssRNA and the product dsRNA complex are the only two states which exist in the process of hybridising, that is to say that no intermediate states are formed [454,455]. Thus, it is possible to determine the number of binding events for a given concentration of capture, target, and probe concentration using the equation:

$$K_{eq} = \frac{[CTP]}{[C][T][P]} \qquad (5)$$

Where C represents captureRNA strands, T represents target miRNA sequences, and P represents probeRNA strands. CTP indicates the hybridised complex of capture, target, and probe strands. Using the aforementioned calculation tools, the K_{eq} was for the target miRNA strands with the complementary captureRNA and probeRNA sequences as 7.29×10^{-17}. Hence, the following model can be established using Equation 5:
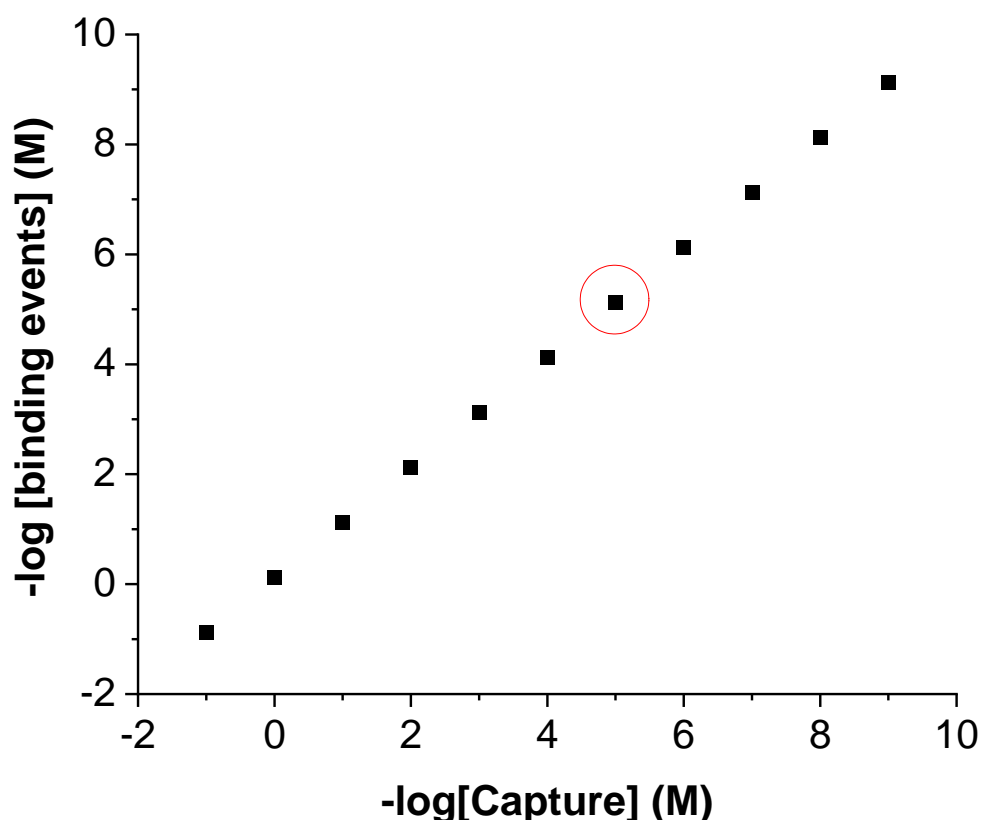
Figure 38. Modelling of binding events were the concentration of the target was maintained at 1 μM and the concentration of the probe was maintained at 55.8 pM and 37°C as per the parameters of the experimental data collected. The graph represents how the concentration of binding events changes as the capture concentration is varied. The red circle denotes the point at which 1 μM has occurred.

The model shows the ratio of the concentration of double stranded RNA relative to the concentration of the captureRNA, target miRNA, and probeRNA. The concentration of 1 μM binding events was chosen as it represents the hybridisation of 1 μM target miRNA in the assay. To date the highest concentration used in the development of this assay has been 1 μM, and hence this concentration was used to calculate the captureRNA concentration required. Using the established parameters of the assay (1 μM target miRNA, 55.8 pM, and with the reaction conducted at 37°C) a captureRNA concentration of 2.19 μM is required. The short nature of miRNA leads to a low K_{eq} for the hybridisation reaction. Due to this low K_{eq}, the capture strands must be in a two-fold excess to the target miRNA concentration to facilitate complete hybridisation. The captureRNA concentration required could be lowered if the probe concentration is raised.

3.5. Impact of probe distribution on peak current

From the understanding gained from the experiments carried out on the Au-SPE demonstrate the importance of electrode materials and probe functionalisation on the expected current which is generated during the assay. One further parameter which can be optimised in order to increase the sensitivity of the electrode is the probe distribution upon successful hybridisation. Spacing of the nanoparticles can have an impact on expected currents by dictating the diffusion mechanism which dominates the hydrogen peroxide degradation. The dominant mechanism of diffusion affects the current profile of the probes. In the assay described above both radial diffusion and semi-infinite linear diffusion may occur. Radial diffusion of H_2O_2 to the probe will occur when the interparticle distance (r_{pp}) is greater than the radius of the of the nanoparticle used as the probe. Radial diffusion will continue to occur until such time as the independent diffusion layers of the probes overlap, at which point the primary mechanism of diffusion is semi-infinite linear diffusion [456]. The point at which radial diffusion becomes semi-infinite linear diffusion occurs when the radial diffusion layers of independent probes overlap and can be described be the following two equations:

$$r_p \ll \sqrt{Dt} \ll r_{pp} \qquad \textbf{(6)}$$

$$\sqrt{Dt} \gg r_{pp} \qquad \textbf{(7)}$$

Equation 6 represents when radial diffusion is the dominant and **Equation 7** represents when semi-infinite linear diffusion occurs.

In the case of this assay, it is preferable for radial diffusion to be dominant as the steady-state current observed is dependent on the radius of the nanoparticle and the number of nanoparticles. Hence, the current observed is proportional to the number of probes (PtNP functionalised with probeRNA strands) present and therefore also the number of hybridised miRNA target sequences. Semi-infinite linear diffusion occurs once the individual depletion zones have coalesced is independent of the number of probes and instead is limited by the geometric area of the Au-C SPE electrode which has been modified by the probes. As such, once linear diffusion has become dominant the current observed will be independent of the target miRNA concentration.

Radial diffusion has been established as the preferred mechanism of diffusion for a probe dependent current response which is correlated to the target miRNA concentration

[457,458]. It is then possible to model the time scale within which the current must be measured such that radial diffusion is dominant using **Equation 6**. This equation dictates that in order to measure the peak steady-state current over a longer time scale then the distance between the probes must be increased to maintain radial diffusion. The relationship between the timescale of the steady-state current and the interparticle distance has been visualised in **Figure 39** below.
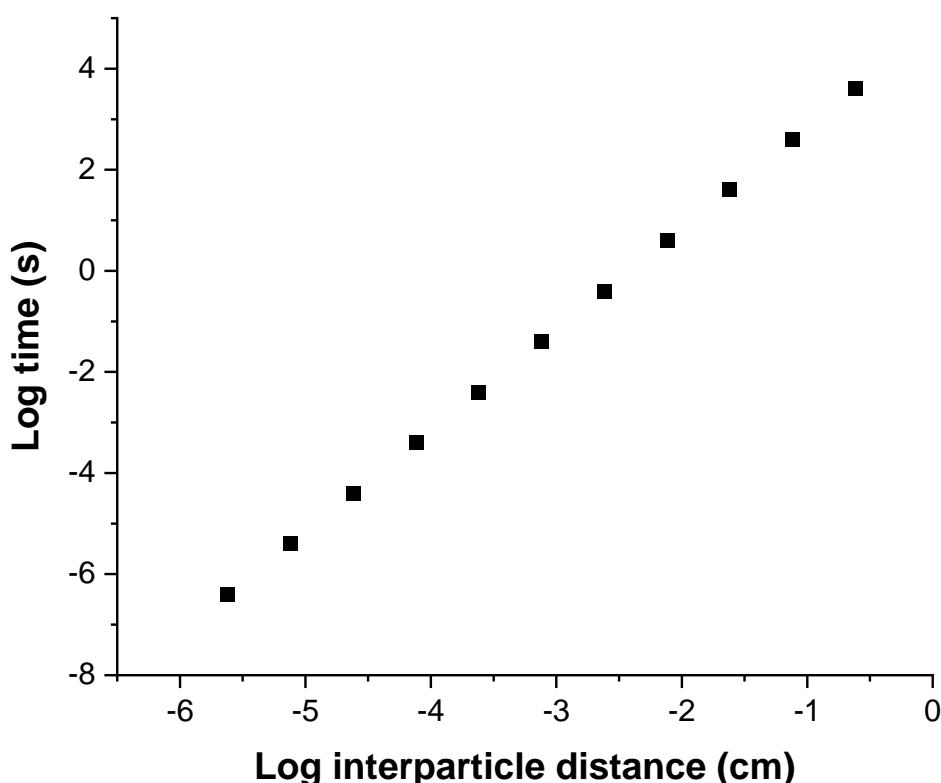
Figure 39. Maximum time vs interparticle distance where radial diffusion is occurring. The axes have been converted to log in order to linearise the plot.

This plot demonstrates that in order to measure steady-state current occurring from radial diffusion with a densely populated probe area (r_{pp} < 100 nm) then current must be measured less than a 10 µs time frame. Additionally, to maintain and record a steady-state current on a second timescale an interparticle distance on the 100 nm scale is required. The lower limit of timescale is dictated by the radius of the probe nanoparticle, as denoted by $r_p \ll \sqrt{Dt}$, in **Equation 6**. However, the maximum timescale is dependent on the interparticle distance and independent of the particle radius.

156

Both the empirical evidence and modelled data show the difficulty of developing a chronoamperometric assay for nucleic acids. Key parameters such as the substrate material, nucleic acid sequence's physical interactions with solid surfaces during immobilisation, and nucleic acid thermodynamic properties must all be carefully considered when optimising the assay for peak current at low target concentrations. It is also possible that at the low potential -0.4 V that there could be a contribution of oxygen reduction within the system contributing to the overall current within this assay configuration. The oxygen reduction could occur at either an exposed site on the AuNPs within the electrode surface, caused by an incomplete monolayer or by RNase degradation of the capture RNA, or from the PtNPs when the sandwich assay is complete. There is likely to be a significant amount of oxygen within the system through the disassociation of the hydrogen peroxide and from the aqueous electrolyte. While the potential used is not particularly low it is plausible that there may be some current contribution through these mechanisms. This could be tested by perform cyclic voltammetry on the final assay where successful capture RNA immobilisation has occurred, capture: target miRNA hybridisation has happened at a high target concentration, and probe has been successfully hybridised to the target miRNA overhang. At that point cyclic voltammetry could determine the oxygen reduction peak potential and determine if the assembled assay is likely to experience a current contribution from oxygen reduction.

Unfortunately, there is not enough published literature to determine what a required analytical sensitivity range might be. This is predominantly because the gold standard RT-qPCR method is more suitable from providing relative fold change in concentration than in actual concentration. However, it is likely that given the small gold surface area of the screen-printed electrode and relatively large size of the PtNPs to the electrode area it is likely that in surface saturated conditions there will be an impact on analytical sensitivity drive by the physical limit of PtNPs relative to the concentrations of target miRNA bound to the assay surface.

4.   Conclusion

The increasing integration of technology into the field of healthcare is opening the door for advances in biosensors. The ability to detect biomarkers rapidly and accurately without the need for excessive processing or amplification is and will continue to be at

the forefront of personal medicine. Using nucleic acids, in particular miRNA, as biomarkers can provide sensitive detection of disease states and be readily tuned targets, as required. Coupling the growing understanding of miRNAs role in pathology in disease with sensitive and rapid chronoamperometric assay designs promises to be a fruitful area of research at present and into the future. However, this work has elucidated through the use of experimental data and calculations, the potential limiting factors which can impact such assays. Biological samples can test even the most assays and so a deep understanding of the underlying mechanisms of nucleic acid biosensors will aid in the design of impactful point-of-care biosensors. This work describes the impact of the electrode material of the level of background current is observed. Furthermore, material surface chemistry and topography can play a significant impact on the signal generation of the assay. This impacts both the capture and probe density and distribution which can greatly impact noise and signal respectively. The short nature of the miRNA target means special attention must be paid to optimising the current response for individual target strands. Poor K_{eq} associated with capture-target-probe hybridisation mean the generation of an appreciable current per binding event is a priority as the number of binding events should be expected to be low. Finally, the distribution of the probes, and hence the captureRNA on the electrode surface is crucial for determining the timescales and expected peak current of any nanoparticle-based chronoamperometric biosensor.

It is hoped that this work can contribute to the development of an ultrasensitive miRNA biosensor for use in a point-of-care device. By elucidating some of the mechanisms behind the key parameters required to further the understanding and ensure a more effective assay which may one day be used for an improved outcome for patients through the early detection of critical disease biomarkers.

Chapter 6

Future Work

1.   Introduction

The work presented in this thesis opens interesting avenues for further investigation which can drive relevant research into cardiovascular disease. Both cell stimulation and miRNA detection are at the forefront of current research aimed at improving our understanding of underlying pathways of the disease and possible avenues for treatment. Improvements must be made to combat the epidemic of cardiovascular disease and the toll it takes on the global health care system. This work lays the groundwork for overlapping projects which can further improve our understanding of cellular responses to electrical stimulation, applicability of electrical stimulation with respect to *in vivo* conditions, screen-printed substrates for sensitive testing, and multiplexed assays to allow a high-level view of the miRNA landscape in relation to both heart disease and the effect of electrical stimulation.

2.   Implications

Cyclic voltammetry of PPy-DS-Fib films demonstrated that there is a sufficient potential window at positive potentials for use in the electrochemical stimulation using the interfacial potential of the wireless bipolar electrode. This conclusion has important implications for the electrical stimulation of all cell types. The wider applicability of the films could be used in the electrical stimulation of both primary and immortalised cell lines. It could also be used for the differentiation and maturation of stem cell lines. The work demonstrated the ability to include available surface extracellular matrix proteins into the electrochemically deposited films. Hence, it is possible then to modify the co-doped extracellular matrix protein to be optimised for the cell line which will be used. As electrochemical deposition of PPy is the most commonly used methodology for deposition of PPy films onto conducting substrates it therefore represents a readily modifiable and optimisable surface for the stimulation of any cell lines which require both environmental proteins for stable culture and an electrical stimulus for differentiation or maturation.

The introduction in this work of a cell line-specific modified wireless bipolar electrostimulation platform could impact the use of electrical stimulation in cell culture. Currently it is an under-utilised tool which can have significant impacts on the robustness and quality of protocols over a wide range of applications. The ability to use a reusable stimulation platform could increase uptake of electrical stimuli in cell culture protocols leading to improvements in in vitro cell culture modelling of disease. Improvements in in

vitro modelling have knock-on benefits to the research of diseases and the development of future treatment both directly in the study of drug treatments and indirectly in the understanding of the mechanisms of disease. The ability to modify the surface of the bipolar electrode for the specific cell line used also increases the applicability of wireless bipolar electrostimulation and thus its convenience for integration in many protocols regardless of cell type or the disease of interest.

The cell culture response demonstrate also that the system is well suited to bot mono-phasic and biphasic stimulation of cells demonstrates a useful dynamic range of stimulation parameters which increase the applicability of the system. A dynamic and applicable system influence its use in the development of future conductive films for the purposes of cell stimulation. Having a methodology for the application of an interfacial potential to cells in culture using novel polymers could open the door to the development of robust polymers for in vivo stimulation of cells. This is important for the development of electrodes which are suitable for in vivo biological environments which have applicability in electroceuticals such as deep-brain stimulation for Parkinson's disease or in rejuvenation of nerves cells following traumatic spinal cord injuries.

The issues seen in the electrochemical detection of miRNAs using screen-printed electrodes demonstrate drawbacks for a promising electrochemical application of screen-printed electrodes. Their lack of robustness in comparison to traditional disk electrodes makes them unsuitable for mechanical preparation of the electrode surface. This increases the risk of surface contamination which in turn could lead to an accelerated degradation of RNA through environmental RNA. The work performed here also demonstrates a limitation with electrochemical detection of miRNA using nanoparticles. The peak current is achieved when the nanoparticles are spaced out in such a way where radial diffusion dominates, maximising the surface area of the particles. There is a concern that during surface saturated conditions the peak current is limited to semi-infinite linear diffusion, thus limiting the assays peak current generating and limiting analytical sensitivity.

3.   3D cell stimulation

The work in this thesis describes the successful electrical stimulation of a 2D culture of cardiomyocytes on a wireless bipolar electrode. The bipolar electrochemical approach has proved effective for cell stimulation purposes. However, in the bioengineering space the applicability of 2D stimulations is being debated. 3D cell cultures such as organoids and spheroids have been growing in popularity due to their inclusion of more representative cell to cell connections and the presence of stimuli from all directions.

However, current 3D cell culture protocols make traditional cell culture techniques for electrical stimulation difficult. Wireless bipolar electrical stimulation is uniquely suited to fill the niche requirements for 3D cell stimulation. Work in the electrochemistry space has already shown that 3D electrodes can be applied to bipolar electrochemical cells. The interfacial potential caused by placing a conductor in an electrical field is equal across the surface of the electrode at a given distance in the channel. This aspect of bipolar electrochemistry means that 3D structures of cells can be homogenously stimulated wirelessly using an appropriate conductive scaffold to act as the bipolar electrode in a bipolar electrochemical cell. Further research into these conductive 3D scaffolds, and even emerging technologies such as graphene doped hydrogels will only serve to improve the possibly of applying bipolar electrochemical techniques to 3D cell cultures. The ability to stimulate 3D cultures opens interesting avenues into the development and maintenance of cardiomyocyte which are more applicable towards *in vivo* conditions. Wireless bipolar electrical stimulation could be further applied to the development of electroceuticals. Electroceuticals are medical devices which use electrical potential with therapeutic effects. The currently include devices such pacemakers and deep-brain stimulation for epilepsy. These devices use electrodes placed in the body to provide appropriate electrical stimulation in a specific area. The downfall of these devices currently is the use of wired electrical connection to the control unit from the electrode. Effective electrical stimulation through the wireless bipolar electrode method could provide wireless alternative to these wired devices. A wireless setup which can effectively replace the required stimulation potential magnitudes can greatly improve patient comfort. The lack of a wired connection can also improve applicability of electroceuticals and potentially open up new applications such as electrically stimulated bone healing and nerve regeneration.

4.   Genomic analysis of electrostimulated cells

The work presented here describes wireless bipolar stimulation of cardiomyocytes on PPy-DS-Fib using a custom stimulation platform. Future work in the ae of wireless bipolar electrode stimulation must push to quantify the effect of electrical stimulation of cardiomyocytes. This work focused on the stimulation of HL-1 cardiomyocytes however future work could focus on the use of electrical stimulation of other cardiomyocyte cell lines, particularly stem cell differentiation using the wireless bipolar stimulation. In order to fully elucidate the effect of the stimulation using the bipolar electrode genomic screening of cells which have experienced will be the most valuable tool for this. The

transcriptome in particular will show the detail required of the intracellular response to the electrical stimulation. The transcriptome refers to the nucleic acid sequences which are transcribed from the genetic DNA. Changes in the transcriptome illustrate key differences in the cells in response to stimuli which will serve to illustrate the effect of electrical stimulation alongside the physical characterisation which has been begun in this work. Of particular interest will be the miRNA levels in response to the electrical stimulation. Comparison between the transcriptome and the miRNA can help to elucidate key genetic pathways which are key in both stem cell differentiation of immature cells and development of primary cells *in vitro*. Understanding the key genotypic responses of cells to the electrical stimulation will be essential in developing effective stimulation methodologies. These methodologies must endeavour to develop a deeper understanding of the genetic consequences of electrical stimulation on all lineages of cardiomyocytes. The miRNA sequences are instrumental in RNA interference and as such can supply valuable insight into the genomic response to electrical stimulation. The miRNA assay work described in this thesis will be essential in the quantification of miRNA levels of cardiomyocytes. Amplification free electrochemical detection of cardiac miRNA is important for accurate quantification of miRNA expression. Sensitive detection allows for the quantification of not only intracellular miRNA levels and also extracellular miRNA. Extracellular miRNAs are an interesting aspect of miRNA expression which has not yet been fully characterised or understood in the literature. They may be bioactive, intercellular signalling, or incidental inclusion in extracellular vesicles. Whatever the role, the ability to detect low concentrations in cell lysate or cellular media will provide valuable insight into the genetic response within the cell, furthering the understanding of the overall role of miRNA in response to electrical stimulation.

5.   Improved screen-printed electrode surfaces.

This work illustrates the promising future of screen-printed electrodes for use in sensitive biosensors. However, it is clear that screen-printed electrode-based systems do require refinement in order to truly drive the lower limit of detection of these assays. Gold surfaces have very attractive qualities when it comes to conductivity and surface modifications. Specifically, thiol-gold chemistry is often used in biosensors as the provide a facile way to add biorecognition elements to a substrate surface. This usefulness is improved given the relative abundance of sulphurs which naturally occur in proteins such as immunoglobulins due to their presence in the amino acids, methionine, and cysteine. They can also be readily added to nucleic acid sequences of both DNA and RNA which

allows them to be deposited on a surface in an orientated fashion. However, gold is also electroactive which can cause issues with signal to noise ratios, particularly those sensors which focus on ultrasensitive detection. Carbon is an essential screen-printing material with respect to electrodes. It allows for dynamic designs, cheaper mass manufacturing, and opens the possibility of eco-friendly design by allowing recycling to be done post use. However, carbon is far less readily modified than gold which can cause a problem for the effective immobilisation of biorecognition elements within the assay system. The work described in this thesis has begun to amalgamate the desirable properties of both materials to assist in the ultrasensitive detection of miRNAs however, an issue persists with screen-printing reproducibility. As the gold surface area is an essential metric for comparison between assay a consistent surface area is required for a functional assay which could be employed in a clinical setting. Maintaining a consistent gold working surface will be key in driving the relative standard deviation of points on standard curve based on these electrode substrates low enough to develop ultrasensitive detection platforms with strong correlations and a high signal to noise ratio.

6.   Multiplexed assay

Drawing on the flexibility with respect to assay design and mass production of screen-printing, the future of this work should focus on driving multiplexing of electrochemical miRNA biosensors. Individual electrodes testing the same sample matrix or segregated signal generating molecules can be used to add a multiplexing capability to the work described in this thesis. It has been established through the literature that the highest correlation of miRNA as a biomarker towards a specific disease state is most likely to be a panel-based approach. As such it is imperative that any assay focused on the detection of miRNAs should endeavour to develop platforms which are inherently or readily adapted to a multiplexed configuration. Using ultrasensitive miRNA detection on a screen-printed carbon electrode containing gold nanoparticles offers an attractive configuration for multiplexing based off the electrochemical nature of the assay. Using multiple signals generating molecules whose potential at which they generate a signal current is one possible method of adapting a multiplex approach. Two driving potentials can be applied sequentially in order to determine the concentration of two or more targets whose signal corresponds to the respective potential. Alternatively, alternative electrochemical techniques such as electrochemiluminescence can be used in order to generate a multiplexed assay. In this method the use of light producing redox probes can be used as the signal generators. By knowing the redox potential of each probe and

using a light detecting system, such as a photomultiplier tube it is possible to quantify and differentiate multiple targets on the same assay. Finally, one relatively simple method for multiplexing is to take advantage of the tuneable surface area and design of the electrode afforded by the screen-printing process. Printing a design with effectively places more than one working electrode is such a way that a single sample could be added to each one simultaneously. Therefore, the signal at each electrode could effectively quantify an individual target independently of the other working electrodes. In this design it would also be possible to use the same counter and reference electrode. As with all scree-printed electrodes it could then be disposed of removing the need to be cleaned or polished ahead of the next sample.

7.   Conclusion

This work has provided a platform for improvement in both the cell culture and bioengineering space, and in the biosensors space. The improvement to *in vitro* cell culture will be an essential tool in the future in the battle against cardiovascular disease. Not only can the future work based on this thesis improve laboratory techniques which can be reproducibly and easily shared among research labs globally, it will also provide an improved platform for essential research into cardiomyocytes. The work on electrochemical miRNA biosensors works in parallel to this objective by providing a platform on which to grow our global understanding of a novel biomarker. miRNA's role in gene expression also provides us with a valuable insight in the genomic responses of cells to environmental stimuli. The biosensors may also serve to further elucidate the role of extracellular miRNAs and their impact on neighbouring cells and cells of different types.

Bibliography

(1)   WHO. *Cardiovascular diseases*. https://www.who.int/health-
        topics/cardiovascular-diseases#tab=tab_1 (accessed 2022-09-27).

(2)   WHO. *Cardiovascular diseases (CVDs)*. https://www.who.int/en/news-room/fact-
        sheets/detail/cardiovascular-diseases-(cvds) (accessed 2022-09-27).

(3)   Gaziano, T.; Reddy, K. S.; Paccaud, F.; Horton, S.; Chaturvedi, V.
        Cardiovascular Disease. *Dis. Control Priorities Dev. Ctries.* **2006**.

(4)   Xing, C.; Arai, K.; Lo, E. H.; Hommel, M. Pathophysiologic Cascades in Ischemic
        Stroke. *International Journal of Stroke*. 2012, pp 378–385.
        https://doi.org/10.1111/j.1747-4949.2012.00839.x.

(5)   Kunst, M. M.; Schaefer, P. W. Ischemic Stroke. *Radiologic Clinics of North
        America*. Elsevier January 1, 2011, pp 1–26.
        https://doi.org/10.1016/j.rcl.2010.07.010.

(6)   Grysiewicz, R. A.; Thomas, K.; Pandey, D. K. Epidemiology of Ischemic and
        Hemorrhagic Stroke: Incidence, Prevalence, Mortality, and Risk Factors.
        Neurologic Clinics. 2008, pp 871–895. https://doi.org/10.1016/j.ncl.2008.07.003.

(7)   Gere, J.; Minier, D.; Osseby, G. V.; Couvreur, G.; Moreau, T.; Ricolfi, F.; Giroud,
        M. Épidémiologie Des Accidents Hémorragiques Cérébraux. In *Journal of
        Neuroradiology*; 2003; Vol. 30, pp 291–297.

(8)   Saand, A. R.; Yu, F.; Chen, J.; Chou, S. H. Y. Systemic Inflammation in
        Hemorrhagic Strokes – A Novel Neurological Sign and Therapeutic Target?
        Journal of Cerebral Blood Flow and Metabolism. SAGE Publications Ltd June 1,
        2019, pp 959–988. https://doi.org/10.1177/0271678X19841443.

(9)   Aamodt, E. B.; Lydersen, S.; Alnæs, D.; Schellhorn, T.; Saltvedt, I.; Beyer, M. K.;
        Håberg, A. Longitudinal Brain Changes After Stroke and the Association With
        Cognitive Decline. *Front. Neurol.* **2022**, *13* (June), 1–13.
        https://doi.org/10.3389/fneur.2022.856919.

(10)   Moskowitz, M. A.; Lo, E. H.; Iadecola, C. The Science of Stroke: Mechanisms in
        Search of Treatments. *Neuron*. NIH Public Access July 7, 2010, pp 181–198.
        https://doi.org/10.1016/j.neuron.2010.07.002.

(11)   Brown, R. D. The Clinical Neuropsychiatry of Stroke: Cognitive, Behavioral, and
        Emotional Disorders Following Vascular Brain Injury. *Neurosurgery* **1999**, *44* (6),

1359–1360. https://doi.org/10.1227/00006123-199906000-00130.

(12)   Antman, E.; Bassand, J. P.; Klein, W.; Ohman, M.; Lopez Sendon, J. L.; Rydén,
L.; Simoons, M.; Tendera, M.; Chaitman, B. R.; Clemmensen, P.; Falk, E.;
Fishbein, M. C.; Galvani, M.; Garson A., J.; Grines, C.; Hamm, C.; Hoppe, U.;
Jaffe, A.; Katus, H.; Kjekshus, J.; Klein, W.; Klootwijk, P.; Lenfant, C.; Levy, D.;
Levy, R. I.; Luepker, R.; Marcus, F.; Naslund, U.; Ohman, M.; Pahlm, O.; Poole-
Wilson, P.; Popp, R.; Pyorala, K.; Ravkilde, J.; Rehnquist, N.; Roberts, W.;
Roberts, R.; Roelandt, J.; Ryden, L.; Sans, S.; Simoons, M. L.; Thygesen, K.;
Tunstall-Pedoe, H.; Underwood, R.; Uretsky, B. F.; Van de Werf, F.; Voipio-
Pulkki, L. M.; Wagner, G.; Wallentin, L.; Wijns, W.; Wood, D. Myocardial
Infarction Redefined - A Consensus Document of The Joint European Society of
Cardiology/American College of Cardiology Committee f or the Redefinition of
Myocardial Infarction. *J. Am. Coll. Cardiol.* **2000**, *36* (3), 959–969.
https://doi.org/10.1016/S0735-1097(00)00804-4.

(13)   Boersma, E.; Mercado, N.; Poldermans, D.; Gardien, M.; Vos, J.; Simoons, M. L.
Acute Myocardial Infarction. In *Lancet*; Elsevier B.V., 2003; Vol. 361, pp 847–
858. https://doi.org/10.1016/S0140-6736(03)12712-2.

(14)   Timmis, A.; Vardas, P.; Townsend, N.; Torbica, A.; Katus, H.; De Smedt, D.;
Gale, C. P.; Maggioni, A. P.; Petersen, S. E.; Huculeci, R.; Kazakiewicz, D.; de
Benito Rubio, V.; Ignatiuk, B.; Raisi-Estabragh, Z.; Pawlak, A.; Karagiannidis, E.;
Treskes, R.; Gaita, D.; Beltrame, J. F.; McConnachie, A.; Bardinet, I.; Graham,
I.; Flather, M.; Elliott, P.; Mossialos, E. A.; Weidinger, F.; Achenbach, S.
European Society of Cardiology: Cardiovascular Disease Statistics 2021. *Eur.
Heart J.* **2022**, *43* (8), 716–799. https://doi.org/10.1093/eurheartj/ehab892.

(15)   Harper, S.; Riddell, C. A.; King, N. B. Declining Life Expectancy in the United
States: Missing the Trees for the Forest. In *Annual Review of Public Health*;
2020; Vol. 42, pp 381–403. https://doi.org/10.1146/annurev-publhealth-082619-
104231.

(16)   Mensah, G. A.; Roth, G. A.; Fuster, V. The Global Burden of Cardiovascular
Diseases and Risk Factors: 2020 and Beyond. *Journal of the American College
of Cardiology*. Elsevier USA November 19, 2019, pp 2529–2532.
https://doi.org/10.1016/j.jacc.2019.10.009.

(17)   Mayou, R.; Bryant, B. Quality of Life in Cardiovascular Disease. *British Heart
Journal*. BMJ Publishing Group 1993, pp 460–466.

https://doi.org/10.1136/hrt.69.5.460.

(18)   Dhakal, B. P.; Sweitzer, N. K.; Indik, J. H.; Acharya, D.; William, P. SARS-CoV-2 Infection and Cardiovascular Disease: COVID-19 Heart. *Heart Lung and Circulation.* Elsevier July 1, 2020, pp 973–987. https://doi.org/10.1016/j.hlc.2020.05.101.

(19)   Lippi, G.; Plebani, M. Laboratory Abnormalities in Patients with COVID-2019 Infection. *Clinical Chemistry and Laboratory Medicine.* De Gruyter June 25, 2020, pp 1131–1134. https://doi.org/10.1515/cclm-2020-0198.

(20)   Bansal, M. Cardiovascular Disease and COVID-19. *Diabetes Metab. Syndr. Clin. Res. Rev.* **2020**, *14* (3), 247–250. https://doi.org/10.1016/j.dsx.2020.03.013.

(21)   Lippi, G.; Lavie, C. J.; Sanchis-Gomar, F. Cardiac Troponin I in Patients with Coronavirus Disease 2019 (COVID-19): Evidence from a Meta-Analysis. *Progress in Cardiovascular Diseases.* 2020, pp 390–391. https://doi.org/10.1016/j.pcad.2020.03.001.

(22)   Du, X.; Su, X.; Zhang, W.; Yi, S.; Zhang, G.; Jiang, S.; Li, H.; Li, S.; Xia, F. Progress, Opportunities, and Challenges of Troponin Analysis in the Early Diagnosis of Cardiovascular Diseases. *Analytical Chemistry.* 2022, pp 442–463. https://doi.org/10.1021/acs.analchem.1c04476.

(23)   Gaze, D. C.; Collinson, P. O. Multiple Molecular Forms of Circulating Cardiac Troponin: Analytical and Clinical Significance. *Annals of Clinical Biochemistry.* 2008, pp 349–355. https://doi.org/10.1258/acb.2007.007229.

(24)   Nishiga, M.; Wang, D. W.; Han, Y.; Lewis, D. B.; Wu, J. C. COVID-19 and Cardiovascular Disease: From Basic Mechanisms to Clinical Perspectives. *Nature Reviews Cardiology.* 2020, pp 543–558. https://doi.org/10.1038/s41569-020-0413-9.

(25)   Buddeke, J.; Bots, M. L.; Van Dis, I.; Visseren, F. L. J.; Hollander, M.; Schellevis, F. G.; Vaartjes, I. Comorbidity in Patients with Cardiovascular Disease in Primary Care: A Cohort Study with Routine Healthcare Data. *Br. J. Gen. Pract.* **2019**, *69* (683), E398–E406. https://doi.org/10.3399/bjgp19X702725.

(26)   Zhou, M.; Zhao, G.; Zeng, Y.; Zhu, J.; Cheng, F.; Liang, W. Aging and Cardiovascular Disease: Current Status and Challenges. *Reviews in*

Cardiovascular Medicine. IMR Press Limited April 8, 2022, p 135. https://doi.org/10.31083/j.rcm2304135.

(27)   Harrington, W. N.; Kackos, C. M.; Webby, R. J. The Evolution and Future of Influenza Pandemic Preparedness. *Experimental and Molecular Medicine*. 2021, pp 737–749. https://doi.org/10.1038/s12276-021-00603-0.

(28)   Behl, A.; Nair, A.; Mohagaonkar, S.; Yadav, P.; Gambhir, K.; Tyagi, N.; Sharma, R. K.; Butola, B. S.; Sharma, N. Threat, Challenges, and Preparedness for Future Pandemics: A Descriptive Review of Phylogenetic Analysis Based Predictions. *Infection, Genetics and Evolution*. Elsevier B.V. March 1, 2022. https://doi.org/10.1016/j.meegid.2022.105217.

(29)   Bell, R. M.; Yellon, D. M. Conditioning the Whole Heart-Not Just the Cardiomyocyte. *Journal of Molecular and Cellular Cardiology*. July 2012, pp 24–32. https://doi.org/10.1016/j.yjmcc.2012.04.001.

(30)   Tran, D. B.; Mahabadi, N. *Anatomy, Thorax, Heart Muscles*; StatPearls Publishing, 2019.

(31)   The Texas Heart Institute. *Heart Information Center: Heart Anatomy | Texas Heart Institute*. https://www.texasheart.org/heart-health/heart-information-center/topics/heart-anatomy/ (accessed 2022-10-01).

(32)   Weinhaus, A. J. Anatomy of the Human Heart. In *Handbook of Cardiac Anatomy, Physiology, and Devices, Third Edition*; Springer International Publishing, 2015; pp 61–88. https://doi.org/10.1007/978-3-319-19464-6_5.

(33)   Funakoshi, S.; Fernandes, I.; Mastikhina, O.; Wilkinson, D.; Tran, T.; Dhahri, W.; Mazine, A.; Yang, D.; Burnett, B.; Lee, J.; Protze, S.; Bader, G. D.; Nunes, S. S.; Laflamme, M.; Keller, G. Generation of Mature Compact Ventricular Cardiomyocytes from Human Pluripotent Stem Cells. *Nat. Commun.* **2021**, *12* (1). https://doi.org/10.1038/s41467-021-23329-z.

(34)   Bishop, S. P.; Zhou, Y.; Nakada, Y.; Zhang, J. Changes in Cardiomyocyte Cell Cycle and Hypertrophic Growth during Fetal to Adult in Mammals. *J. Am. Heart Assoc.* **2021**, *10* (2), 1–12. https://doi.org/10.1161/JAHA.120.017839.

(35)   Hirt, M. N.; Boeddinghaus, J.; Mitchell, A.; Schaaf, S.; Börnchen, C.; Müller, C.; Schulz, H.; Hubner, N.; Stenzig, J.; Stoehr, A.; Neuber, C.; Eder, A.; Luther, P. K.; Hansen, A.; Eschenhagen, T. Functional Improvement and Maturation of Rat and Human Engineered Heart Tissue by Chronic Electrical Stimulation. *J. Mol.*

Cell. Cardiol. **2014**, *74*, 151–161. https://doi.org/10.1016/j.yjmcc.2014.05.009.

(36) Jacot, J. G.; Martin, J. C.; Hunt, D. L. Mechanobiology of Cardiomyocyte Development. *J. Biomech.* **2010**, *43* (1), 93–98. https://doi.org/10.1016/j.jbiomech.2009.09.014.

(37) Baumgartner, S.; Halbach, M.; Krausgrill, B.; Maass, M.; Srinivasan, S. P.; Sahito, R. G. A.; Peinkofer, G.; Nguemo, F.; Müller-Ehmsen, J.; Hescheler, J. Electrophysiological and Morphological Maturation of Murine Fetal Cardiomyocytes during Electrical Stimulation in Vitro. *J. Cardiovasc. Pharmacol. Ther.* **2015**, *20* (1), 104–112. https://doi.org/10.1177/1074248414536273.

(38) Karbassi, E.; Fenix, A.; Marchiano, S.; Muraoka, N.; Nakamura, K.; Yang, X.; Murry, C. E. Cardiomyocyte Maturation: Advances in Knowledge and Implications for Regenerative Medicine. *Nature Reviews Cardiology*. 2020, pp 341–359. https://doi.org/10.1038/s41569-019-0331-x.

(39) Liao, H.; Qi, Y.; Ye, Y.; Yue, P.; Zhang, D.; Li, Y. Mechanotranduction Pathways in the Regulation of Mitochondrial Homeostasis in Cardiomyocytes. *Frontiers in Cell and Developmental Biology*. Frontiers Media S.A. January 21, 2021, p 1602. https://doi.org/10.3389/fcell.2020.625089.

(40) Derks, W.; Bergmann, O. Polyploidy in Cardiomyocytes: Roadblock to Heart Regeneration? *Circulation Research*. 2020, pp 552–565. https://doi.org/10.1161/CIRCRESAHA.119.315408.

(41) Velayutham, N.; Alfieri, C. M.; Agnew, E. J.; Riggs, K. W.; Baker, R. S.; Ponny, S. R.; Zafar, F.; Yutzey, K. E. Cardiomyocyte Cell Cycling, Maturation, and Growth by Multinucleation in Postnatal Swine. *J. Mol. Cell. Cardiol.* **2020**, *146*, 95–108. https://doi.org/10.1016/j.yjmcc.2020.07.004.

(42) Fang, J.; Van Der Geest, J.; Yao, B.; Yang, Q.; Chirico, N.; Brans, M.; Roefs, M.; Vader, P.; De Jager, S.; De Bruin, A.; Vink, A.; Van Mil, A.; Schiffelers, R.; Lei, Z.; Sluijter, J. E2F7/8 Is Involved in Cardiomyocyte Polyploidy but Does Not Affect Myocardial Reperfusion Injury Recovery. *Cardiovasc. Res.* **2022**, *118* (Supplement_1). https://doi.org/10.1093/cvr/cvac066.061.

(43) Kirillova, A.; Han, L.; Liu, H.; Kühn, B. Polyploid Cardiomyocytes: Implications for Heart Regeneration. *Dev.* **2021**, *148* (14). https://doi.org/10.1242/DEV.199401.

(44) Milani-Nejad, N.; Janssen, P. M. L. Small and Large Animal Models in Cardiac

Contraction Research: Advantages and Disadvantages. *Pharmacology and Therapeutics*. 2014, pp 235–249. https://doi.org/10.1016/j.pharmthera.2013.10.007.

(45)   Krishnan, A.; Samtani, R.; Dhanantwari, P.; Lee, E.; Yamada, S.; Shiota, K.; Donofrio, M. T.; Leatherbury, L.; Lo, C. W. A Detailed Comparison of Mouse and Human Cardiac Development. *Pediatr. Res.* **2014**, *76* (6), 500–507. https://doi.org/10.1038/pr.2014.128.

(46)   Woodcock, E. A.; Matkovich, S. J. Cardiomyocytes Structure, Function and Associated Pathologies. *International Journal of Biochemistry and Cell Biology*. 2005, pp 1746–1751. https://doi.org/10.1016/j.biocel.2005.04.011.

(47)   Ribeiro, A. J. S.; Ang, Y. S.; Fu, J. D.; Rivas, R. N.; Mohamed, T. M. A.; Higgs, G. C.; Srivastava, D.; Pruitt, B. L. Contractility of Single Cardiomyocytes Differentiated from Pluripotent Stem Cells Depends on Physiological Shape and Substrate Stiffness. *Proc. Natl. Acad. Sci. U. S. A.* **2015**, *112* (41), 12705–12710. https://doi.org/10.1073/pnas.1508073112.

(48)   Isenberg, G.; Kondratev, D.; Dyachenko, V.; Kazanski, V.; Gallitelli, M. F. *Isolated Cardiomyocytes: Mechanosensitivity of Action Potential, Membrane Current and Ion Concentration*; Academia, 2005.

(49)   Belardinelli, L.; Shryock, J. C.; Song, Y.; Wang, D.; Srinivas, M. Ionic Basis of the Electrophysiological Actions of Adenosine on Cardiomyocytes. *FASEB J.* **1995**, *9* (5), 359–365. https://doi.org/10.1096/fasebj.9.5.7896004.

(50)   Calkins, H. Principles of Electrophysiology. In *Goldman's Cecil Medicine: Twenty Fourth Edition*; 2012; Vol. 1, pp 334–337. https://doi.org/10.1016/B978-1-4377-1604-7.00061-0.

(51)   He, J. Q.; Ma, Y.; Lee, Y.; Thomson, J. A.; Kamp, T. J. Human Embryonic Stem Cells Develop into Multiple Types of Cardiac Myocytes: Action Potential Characterization. *Circ. Res.* **2003**, *93* (1), 32–39. https://doi.org/10.1161/01.RES.0000080317.92718.99.

(52)   Wei, X.; Yohannan, S.; Richards, J. R. *Physiology, Cardiac Repolarization Dispersion and Reserve*; StatPearls Publishing, 2020.

(53)   Difrancesco, D. The Role of the Funny Current in Pacemaker Activity. *Circulation Research*. February 2010, pp 434–446. https://doi.org/10.1161/CIRCRESAHA.109.208041.

(54) Smit, N. W.; Coronel, R. Stem Cells Can Form Gap Junctions with Cardiac Myocytes and Exert Pro-Arrhythmic Effects. *Front. Physiol.* **2014**, *5* (OCT). https://doi.org/10.3389/fphys.2014.00419.

(55) Haraguchi, Y.; Shimizu, T.; Yamato, M.; Kikuchi, A.; Okano, T. Electrical Coupling of Cardiomyocyte Sheets Occurs Rapidly via Functional Gap Junction Formation. *Biomaterials* **2006**, *27* (27), 4765–4774. https://doi.org/10.1016/j.biomaterials.2006.04.034.

(56) CLAPHAM, D. E.; KEATING, M. T. Cardiac Excitability and Heritable Arrhythmias. In *Nadas' Pediatric Cardiology*; W.B. Saunders, 2006; pp 891–906. https://doi.org/10.1016/b978-1-4160-2390-6.50066-0.

(57) Grant, A. O. Cardiac Ion Channels. *Circulation: Arrhythmia and Electrophysiology*. 2009, pp 185–194. https://doi.org/10.1161/CIRCEP.108.789081.

(58) B., B.; P., B. Patient Specific Long QT Syndrome Type 3 Cardiomyocytes Can Be Used for Clinical Drug Safety Assessments. *Acta Cardiol.* **2019**, *74* (May 2018), 56.

(59) Lakatta, E. G. Functional Implications of Spontaneous Sarcoplasmic Reticulum Ca2+ Release in the Heart. *Cardiovascular Research*. 1992, pp 193–214. https://doi.org/10.1093/cvr/26.3.193.

(60) De Meis, L. Fast Efflux of Ca2+ Mediated by the Sarcoplasmic Reticulum Ca2+-ATPase. *J. Biol. Chem.* **1991**, *266* (9), 5736–5742. https://doi.org/10.1016/s0021-9258(19)67657-x.

(61) Smith, D. A.; Geeves, M. A. Cooperative Regulation of Myosin-Actin Interactions by a Continuous Flexible Chain II: Actin-Tropomyosin-Troponin and Regulation by Calcium. *Biophys. J.* **2003**, *84* (5), 3168–3180. https://doi.org/10.1016/S0006-3495(03)70041-1.

(62) POTTER, J. D. Reprint of: The Content of Troponin, Tropomyosin, Actin, and Myosin in Rabbit Skeletal Muscle Myofibrils. *Arch. Biochem. Biophys.* **2022**, *726*, 436–441. https://doi.org/10.1016/j.abb.2022.109241.

(63) Gregorio, C. C.; Antin, P. B. To the Heart of Myofibril Assembly. In *Trends in Cell Biology*; Elsevier Current Trends, 2000; Vol. 10, pp 355–362. https://doi.org/10.1016/S0962-8924(00)01793-1.

(64) Hwang, P. M.; Sykes, B. D. Targeting the Sarcomere to Correct Muscle Function. *Nature Reviews Drug Discovery*. Nature Publishing Group April 17, 2015, pp 313–328. https://doi.org/10.1038/nrd4554.

(65) Parmacek, M. S.; Solaro, R. J. Biology of the Troponin Complex in Cardiac Myocytes. *Prog. Cardiovasc. Dis.* **2004**, *47* (3), 159–176. https://doi.org/10.1016/j.pcad.2004.07.003.

(66) Katrukha, I. A. Human Cardiac Troponin Complex. Structure and Functions. *Biochemistry (Moscow)*. 2013, pp 1447–1465. https://doi.org/10.1134/S0006297913130063.

(67) Farah, C. S.; Reinach, F. C. The Troponin Complex and Regulation of Muscle Contraction. *FASEB J.* **1995**, *9* (9), 755–767. https://doi.org/10.1096/fasebj.9.9.7601340.

(68) Mornet, D.; Bertrand, R.; Pantel, P.; Audemard, E.; Kassab, R. Structure of the Actin-Myosin Interface. *Nature* **1981**, *292* (5821), 301–306. https://doi.org/10.1038/292301a0.

(69) Cooke, R.; White, H.; Pate, E. A Model of the Release of Myosin Heads from Actin in Rapidly Contracting Muscle Fibers. *Biophys. J.* **1994**, *66* (3), 778–788. https://doi.org/10.1016/S0006-3495(94)80854-9.

(70) Spyracopoulos, L.; Li, M. X.; Sia, S. K.; Gagné, S. M.; Chandra, M.; Solaro, R. J.; Sykes, B. D. Calcium-Induced Structural Transition in the Regulatory Domain of Human Cardiac Troponin C. *Biochemistry* **1997**, *36* (40), 12138–12146. https://doi.org/10.1021/bi971223d.

(71) Li, M. X.; Spyracopoulos, L.; Sykes, B. D. Binding of Cardiac Troponin-I147-163 Induces a Structural Opening in Human Cardiac Troponin-C. *Biochemistry* **1999**, *38* (26), 8289–8298. https://doi.org/10.1021/bi9901679.

(72) Livshitz, L. M.; Rudy, Y. Regulation of Ca2+ and Electrical Alternans in Cardiac Myocytes: Role of CAMKII and Repolarizing Currents. *Am. J. Physiol. - Hear. Circ. Physiol.* **2007**, *292* (6), 2854–2866. https://doi.org/10.1152/ajpheart.01347.2006.

(73) Sah, R.; Ramirez, R. J.; Backx, P. H. Modulation of Ca2+ Release in Cardiac Myocytes by Changes in Repolarization Rate: Role of Phase-1 Action Potential Repolarization in Excitation-Contraction Coupling. *Circ. Res.* **2002**, *90* (2), 165–173. https://doi.org/10.1161/hh0202.103315.

(74) Park, K. C.; Gaze, D. C.; Collinson, P. O.; Marber, M. S. Cardiac Troponins: From Myocardial Infarction to Chronic Disease. *Cardiovascular Research*. Oxford Academic December 1, 2017, pp 1708–1718. https://doi.org/10.1093/cvr/cvx183.

(75) Fathil, M. F. M.; Md Arshad, M. K.; Gopinath, S. C. B.; Hashim, U.; Adzhri, R.; Ayub, R. M.; Ruslinda, A. R.; Nuzaihan, M.; Azman, A. H.; Zaki, M.; Tang, T. H. Diagnostics on Acute Myocardial Infarction: Cardiac Troponin Biomarkers. *Biosensors and Bioelectronics*. 2015, pp 209–220. https://doi.org/10.1016/j.bios.2015.03.037.

(76) Reichlin, T.; Hochholzer, W.; Bassetti, S.; Steuer, S.; Stelzig, C.; Hartwiger, S.; Biedert, S.; Schaub, N.; Buerge, C.; Potocki, M.; Noveanu, M.; Breidthardt, T.; Twerenbold, R.; Winkler, K.; Bingisser, R.; Mueller, C. Early Diagnosis of Myocardial Infarction with Sensitive Cardiac Troponin Assays. *N. Engl. J. Med.* **2009**, *361* (9), 858–867. https://doi.org/10.1056/nejmoa0900428.

(77) Ghantous, C. M.; Kamareddine, L.; Farhat, R.; Zouein, F. A.; Mondello, S.; Kobeissy, F.; Zeidan, A. Advances in Cardiovascular Biomarker Discovery. *Biomedicines*. 2020, pp 1–19. https://doi.org/10.3390/biomedicines8120552.

(78) Libby, P.; Ridker, P. M. Inflammation and Atherosclerosis: Role of C-Reactive Protein in Risk Assessment. In *American Journal of Medicine*; 2004; Vol. 116, pp 9–16. https://doi.org/10.1016/j.amjmed.2004.02.006.

(79) Singh, S. K.; Suresh, M. V; Voleti, B.; Agrawal, A. The Connection between C-Reactive Protein and Atherosclerosis. *Annals of Medicine*. 2008, pp 110–120. https://doi.org/10.1080/07853890701749225.

(80) Alizadeh Dehnavi, R.; de Roos, A.; Rabelink, T. J.; van Pelt, J.; Wensink, M. J.; Romijn, J. A.; Tamsma, J. T. Elevated CRP Levels Are Associated with Increased Carotid Atherosclerosis Independent of Visceral Obesity. *Atherosclerosis* **2008**, *200* (2), 417–423. https://doi.org/10.1016/j.atherosclerosis.2007.12.050.

(81) Arici, M.; Walls, J. End-Stage Renal Disease, Atherosclerosis, and Cardiovascular Mortality: Is C-Reactive Protein the Missing Link? *Kidney Int.* **2001**, *59* (2), 407–414. https://doi.org/10.1046/j.1523-1755.2001.059002407.x.

(82) Anand, I. S.; Latini, R.; Florea, V. G.; Kuskowski, M. A.; Rector, T.; Masson, S.; Signorini, S.; Mocarelli, P.; Hester, A.; Glazer, R.; Cohn, J. N. C-Reactive

Protein in Heart Failure: Prognostic Value and the Effect of Valsartan. *Circulation* **2005**, *112* (10), 1428–1434. https://doi.org/10.1161/CIRCULATIONAHA.104.508465.

(83)   Yin, W. H.; Chen, J. W.; Jen, H. L.; Chiang, M. C.; Huang, W. P.; Feng, A. N.; Young, M. S.; Lin, S. J. Independent Prognostic Value of Elevated High-Sensitivity C-Reactive Protein in Chronic Heart Failure. *Am. Heart J.* **2004**, *147* (5), 931–938. https://doi.org/10.1016/j.ahj.2003.11.021.

(84)   Doust, J.; Lehman, R.; Glasziou, P. The Role of BNP Testing in Heart Failure. *American Family Physician*. 2006, pp 1893–1898. www.aafp.org/afp. (accessed 2022-10-23).

(85)   Park, Y. H.; Park, H. J.; Kim, B. S.; Ha, E.; Jung, K. H.; Yoon, S. H.; Yim, S. V.; Chung, J. H. BNP as a Marker of the Heart Failure in the Treatment of Imatinib Mesylate. *Cancer Lett.* **2006**, *243* (1), 16–22. https://doi.org/10.1016/j.canlet.2005.11.014.

(86)   Oremus, M.; McKelvie, R.; Don-Wauchope, A.; Santaguida, P. L.; Ali, U.; Balion, C.; Hill, S.; Booth, R.; Brown, J. A.; Bustamam, A.; Sohel, N.; Raina, P. A Systematic Review of BNP and NT-ProBNP in the Management of Heart Failure: Overview and Methods. *Heart Failure Reviews*. 2014, pp 413–419. https://doi.org/10.1007/s10741-014-9440-0.

(87)   Lowe, G. D. O. Fibrin D-Dimer and Cardiovascular Risk. *Seminars in Vascular Medicine*. 2005, pp 387–398. https://doi.org/10.1055/s-2005-922485.

(88)   Akgul, O.; Uyarel, H.; Pusuroglu, H.; Gul, M.; Isiksacan, N.; Turen, S.; Erturk, M.; Surgit, O.; Cetin, M.; Bulut, U.; Baycan, O. F.; Uslu, N. Predictive Value of Elevated D-Dimer in Patients Undergoing Primary Angioplasty for ST Elevation Myocardial Infarction. *Blood Coagul. Fibrinolysis* **2013**, *24* (7), 704–710. https://doi.org/10.1097/MBC.0b013e3283610396.

(89)   Zorlu, A.; Yilmaz, M. B.; Yucel, H.; Bektasoglu, G.; Ege, M. R.; Tandogan, I. Increased D-Dimer Levels Predict Cardiovascular Mortality in Patients with Systolic Heart Failure. *J. Thromb. Thrombolysis* **2012**, *33* (4), 322–328. https://doi.org/10.1007/s11239-011-0635-0.

(90)   Jiang, Y.; Wang, H. Y.; Cao, H. M.; Wang, C. Y.; Zhang, L.; Wang, H.; Liu, L.; Li, Y.; Cai, J. H. Peripheral Blood MiRNAs as a Biomarker for Chronic Cardiovascular Diseases. *Sci. Rep.* **2014**, *4*. https://doi.org/10.1038/srep05026.

(91)   Cai, Y.; Yu, X.; Hu, S.; Yu, J. A Brief Review on the Mechanisms of MiRNA Regulation. *Genomics, Proteomics and Bioinformatics*. December 2009, pp 147–154. https://doi.org/10.1016/S1672-0229(08)60044-3.

(92)   Tijsterman, M.; Plasterk, R. H. A. Dicers at RISC: The Mechanism of RNAi. *Cell*. Elsevier B.V. April 2, 2004, pp 1–3. https://doi.org/10.1016/S0092-8674(04)00293-4.

(93)   Murchison, E. P.; Hannon, G. J. MiRNAs on the Move: MiRNA Biogenesis and the RNAi Machinery. *Current Opinion in Cell Biology*. June 2004, pp 223–229. https://doi.org/10.1016/j.ceb.2004.04.003.

(94)   Kosaka, N.; Iguchi, H.; Ochiya, T. Circulating MicroRNA in Body Fluid: A New Potential Biomarker for Cancer Diagnosis and Prognosis. *Cancer Science*. Blackwell Publishing Ltd 2010, pp 2087–2092. https://doi.org/10.1111/j.1349-7006.2010.01650.x.

(95)   Katoh, M. Cardio-MiRNAs and Onco-MiRNAs: Circulating MiRNA-Based Diagnostics for Non-Cancerous and Cancerous Diseases. *Front. Cell Dev. Biol.* **2014**, *2*. https://doi.org/10.3389/fcell.2014.00061.

(96)   Turchinovich, A.; Samatov, T. R.; Tonevitsky, A. G.; Burwinkel, B. Circulating MiRNAs: Cell-Cell Communication Function? *Frontiers in Genetics*. 2013. https://doi.org/10.3389/fgene.2013.00119.

(97)   Peters, L. J. F.; Biessen, E. A. L.; Hohl, M.; Weber, C.; van der Vorst, E. P. C.; Santovito, D. Small Things Matter: Relevance of MicroRNAs in Cardiovascular Disease. *Frontiers in Physiology*. 2020. https://doi.org/10.3389/fphys.2020.00793.

(98)   Colpaert, R. M. W.; Calore, M. MicroRNAs in Cardiac Diseases. *Cells*. 2019. https://doi.org/10.3390/cells8070737.

(99)   Mir, R.; Elfaki, I.; Khullar, N.; Waza, A. A.; Jha, C.; Mir, M. M.; Nisa, S.; Mohammad, B.; Mir, T. A.; Maqbool, M.; Barnawi, J.; Albalawi, S. O.; Abu-Duhier, F. M. Role of Selected MiRNAs as Diagnostic and Prognostic Biomarkers in Cardiovascular Diseases, Including Coronary Artery Disease, Myocardial Infarction and Atherosclerosis. *Journal of Cardiovascular Development and Disease*. 2021, pp 1–17. https://doi.org/10.3390/jcdd8020022.

(100) Schulte, C.; Karakas, M.; Zeller, T. MicroRNAs in Cardiovascular Disease - Clinical Application. *Clinical Chemistry and Laboratory Medicine*. Walter de

Gruyter GmbH May 1, 2017, pp 687–704. https://doi.org/10.1515/cclm-2016-0576.

(101) Olson, E. N. MicroRNAs as Therapeutic Targets and Biomarkers of Cardiovascular Disease. *Science Translational Medicine.* 2014. https://doi.org/10.1126/scitranslmed.3009008.

(102) Zhang, X.; Cai, H.; Zhu, M.; Qian, Y.; Lin, S.; Li, X. Circulating MicroRNAs as Biomarkers for Severe Coronary Artery Disease. *Medicine (Baltimore).* **2020**, *99* (17), e19971. https://doi.org/10.1097/MD.0000000000019971.

(103) Matin, F.; Jeet, V.; Moya, L.; Selth, L. A.; Chambers, S.; Clements, J. A.; Batra, J.; Yeadon, T.; Saunders, P.; Eckert, A.; Heathcote, P.; Wood, G.; Malone, G.; Samaratunga, H.; Collins, A.; Turner, M.; Kerr, K. A Plasma Biomarker Panel of Four MicroRNAs for the Diagnosis of Prostate Cancer. *Sci. Rep.* **2018**, *8* (1). https://doi.org/10.1038/s41598-018-24424-w.

(104) Su, Y. J.; Lin, I. C.; Wang, L.; Lu, C. H.; Huang, Y. L.; Kuo, H. C. Next Generation Sequencing Identifies MiRNA-Based Biomarker Panel for Lupus Nephritis. *Oncotarget* **2018**, *9* (46), 27911–27919. https://doi.org/10.18632/oncotarget.25575.

(105) Crouser, E. D.; Julian, M. W.; Bicer, S.; Ghai, V.; Kim, T. K.; Maier, L. A.; Gillespie, M.; Hamzeh, N. Y.; Wang, K. Circulating Exosomal MicroRNA Expression Patterns Distinguish Cardiac Sarcoidosis from Myocardial Ischemia. *PLoS One* **2021**, *16* (1 January), e0246083. https://doi.org/10.1371/journal.pone.0246083.

(106) Kanuri, S. H.; Ipe, J.; Kassab, K.; Gao, H.; Liu, Y.; Skaar, T. C.; Kreutz, R. P. Next Generation MicroRNA Sequencing to Identify Coronary Artery Disease Patients at Risk of Recurrent Myocardial Infarction. *Atherosclerosis* **2018**, *278*, 232–239. https://doi.org/10.1016/j.atherosclerosis.2018.09.021.

(107) Yan, L.; Li, J.; Wu, Q.; Chen, L. Specific MiRNA Expression Profile in the Blood Serum of Cardiac Myxoma Patients. *Oncol. Lett.* **2018**, *16* (4), 4235–4242. https://doi.org/10.3892/ol.2018.9209.

(108) Boštjančič, E.; Zidar, N.; Glavač, D. MicroRNA Microarray Expression Profiling in Human Myocardial Infarction. *Dis. Markers* **2009**, *27* (6), 255–268. https://doi.org/10.3233/DMA-2009-0671.

(109) Kuwabara, Y.; Ono, K.; Horie, T.; Nishi, H.; Nagao, K.; Kinoshita, M.; Watanabe,

S.; Baba, O.; Kojima, Y.; Shizuta, S.; Imai, M.; Tamura, T.; Kita, T.; Kimura, T. Increased MicroRNA-1 and MicroRNA-133a Levels in Serum of Patients with Cardiovascular Disease Indicate Myocardial Damage. *Circ. Cardiovasc. Genet.* **2011**, *4* (4), 446–454. https://doi.org/10.1161/CIRCGENETICS.110.958975.

(110) Kondkar, A. A.; Abu-Amero, K. K. Utility of Circulating MicroRNAs as Clinical Biomarkers for Cardiovascular Diseases. *BioMed Research International*. Hindawi Publishing Corporation 2015. https://doi.org/10.1155/2015/821823.

(111) Belevych, A. E.; Sansom, S. E.; Terentyeva, R.; Ho, H. T.; Nishijima, Y.; Martin, M. M.; Jindal, H. K.; Rochira, J. A.; Kunitomo, Y.; Abdellatif, M.; Carnes, C. A.; Elton, T. S.; Györke, S.; Terentyev, D. MicroRNA-1 and -133 Increase Arrhythmogenesis in Heart Failure by Dissociating Phosphatase Activity from RyR2 Complex. *PLoS One* **2011**, *6* (12), 28324. https://doi.org/10.1371/journal.pone.0028324.

(112) Kaur, A.; Mackin, S. T.; Schlosser, K.; Wong, F. L.; Elharram, M.; Delles, C.; Stewart, D. J.; Dayan, N.; Landry, T.; Pilote, L. Systematic Review of MicroRNA Biomarkers in Acute Coronary Syndrome and Stable Coronary Artery Disease. *Cardiovascular Research*. 2021, pp 1113–1124. https://doi.org/10.1093/CVR/CVZ302.

(113) Zhou, S. S.; Jin, J. P.; Wang, J. Q.; Zhang, Z. G.; Freedman, J. H.; Zheng, Y.; Cai, L. MiRNAS in Cardiovascular Diseases: Potential Biomarkers, Therapeutic Targets and Challenges Review-Article. *Acta Pharmacologica Sinica*. 2018, pp 1073–1084. https://doi.org/10.1038/aps.2018.30.

(114) Thorp, H. H. The Importance of Being r: Greater Oxidative Stability of RNA Compared with DNA. *Chemistry and Biology*. 2000. https://doi.org/10.1016/S1074-5521(00)00080-6.

(115) Hackl, M.; Semmelrock, E.; Grillari, J. Analytical Challenges in MicroRNA Biomarker Development: Best Practices for Analyzing MicroRNAs in Cell-Free Biofluids. In *Epigenetics in Cardiovascular Disease*; Academic Press, 2021; pp 415–430. https://doi.org/10.1016/B978-0-12-822258-4.00004-3.

(116) Bernhardt, H. S.; Tate, W. P. Primordial Soup or Vinaigrette: Did the RNA World Evolve at Acidic PH? *Biol. Direct* **2012**, *7*, 4. https://doi.org/10.1186/1745-6150-7-4.

(117) Makarova, J. A.; Shkurnikov, M. U.; Wicklein, D.; Lange, T.; Samatov, T. R.;

Turchinovich, A. A.; Tonevitsky, A. G. Intracellular and Extracellular MicroRNA: An Update on Localization and Biological Role. *Progress in Histochemistry and Cytochemistry*. Elsevier GmbH November 1, 2016, pp 33–49. https://doi.org/10.1016/j.proghi.2016.06.001.

(118) Makarova, J.; Turchinovich, A.; Shkurnikov, M.; Tonevitsky, A. Extracellular MiRNAs and Cell–Cell Communication: Problems and Prospects. *Trends in Biochemical Sciences*. 2021, pp 640–651. https://doi.org/10.1016/j.tibs.2021.01.007.

(119) Chakraborty, C.; Sharma, A. R.; Sharma, G.; Lee, S. S. Therapeutic Advances of MiRNAs: A Preclinical and Clinical Update. *Journal of Advanced Research*. Elsevier B.V. February 1, 2021, pp 127–138. https://doi.org/10.1016/j.jare.2020.08.012.

(120) Mellis, D.; Caporali, A. MicroRNA-Based Therapeutics in Cardiovascular Disease: Screening and Delivery to the Target. *Biochemical Society Transactions*. Portland Press February 19, 2018, pp 11–21. https://doi.org/10.1042/BST20170037.

(121) Arabian, M.; Azad, F. M.; Maleki, M.; Malakootian, M. Insights into Role of MicroRNAs in Cardiac Development, Cardiac Diseases, and Developing Novel Therapies. *Iran. J. Basic Med. Sci.* **2020**, *23* (8), 961–969. https://doi.org/10.22038/IJBMS.2020.40974.10015.

(122) Jongsma, H. J.; Wilders, R. Gap Junctions in Cardiovascular Disease. *Circulation Research*. Lippincott Williams & Wilkins June 23, 2000, pp 1193–1197. https://doi.org/10.1161/01.RES.86.12.1193.

(123) Davis, R. P.; van den Berg, C. W.; Casini, S.; Braam, S. R.; Mummery, C. L. Pluripotent Stem Cell Models of Cardiac Disease and Their Implication for Drug Discovery and Development. *Trends in Molecular Medicine*. 2011, pp 475–484. https://doi.org/10.1016/j.molmed.2011.05.001.

(124) Nikolic, M.; Sustersic, T.; Filipovic, N. In Vitro Models and On-Chip Systems: Biomaterial Interaction Studies with Tissues Generated Using Lung Epithelial and Liver Metabolic Cell Lines. *Frontiers in Bioengineering and Biotechnology*. 2018, p 120. https://doi.org/10.3389/fbioe.2018.00120.

(125) Egido, J.; Zaragoza, C.; Gomez-Guerrero, C.; Martin-Ventura, J. L.; Blanco-Colio, L.; Lavin, B.; Mallavia, B.; Tarin, C.; Mas, S.; Ortiz, A. Animal Models of

Cardiovascular Diseases. *Journal of Biomedicine and Biotechnology*. Hindawi Publishing Corporation 2011, p 13. https://doi.org/10.1155/2011/497841.

(126) Hasenfuss, G. Animal Models of Human Cardiovascular Disease, Heart Failure and Hypertrophy. *Cardiovascular Research*. 1998, pp 60–76. https://doi.org/10.1016/S0008-6363(98)00110-2.

(127) Musunuru, K.; Sheikh, F.; Gupta, R. M.; Houser, S. R.; Maher, K. O.; Milan, D. J.; Terzic, A.; Wu, J. C. Induced Pluripotent Stem Cells for Cardiovascular Disease Modeling and Precision Medicine: A Scientific Statement from the American Heart Association. *Circulation: Genomic and Precision Medicine*. Lippincott Williams & Wilkins Hagerstown, MD January 1, 2018, p E000043. https://doi.org/10.1161/HCG.0000000000000043.

(128) Savoji, H.; Mohammadi, M. H.; Rafatian, N.; Toroghi, M. K.; Wang, E. Y.; Zhao, Y.; Korolj, A.; Ahadian, S.; Radisic, M. Cardiovascular Disease Models: A Game Changing Paradigm in Drug Discovery and Screening. *Biomaterials* **2019**, *198*, 3–26. https://doi.org/10.1016/j.biomaterials.2018.09.036.

(129) Harlaar, N.; Pijnappels, D. A.; de Vries, A. A. F. Conditional Immortalization of Human Cardiomyocytes for Translational in Vitro Modelling of Cardiovascular Disease. *Cardiovasc. Res.* **2022**. https://doi.org/10.1093/cvr/cvac078.

(130) Richter, M.; Piwocka, O.; Musielak, M.; Piotrowski, I.; Suchorska, W. M.; Trzeciak, T. From Donor to the Lab: A Fascinating Journey of Primary Cell Lines. *Front. Cell Dev. Biol.* **2021**, *9* (July), 1–11. https://doi.org/10.3389/fcell.2021.711381.

(131) White, S. M.; Constantin, P. E.; Claycomb, W. C. Cardiac Physiology at the Cellular Level: Use of Cultured HL-1 Cardiomyocytes for Studies of Cardiac Muscle Cell Structure and Function. *American Journal of Physiology - Heart and Circulatory Physiology*. American Physiological Society 2004. https://doi.org/10.1152/ajpheart.00986.2003.

(132) *Guide to Research Techniques in Neuroscience*; 2022. https://doi.org/10.1016/c2018-0-04205-x.

(133) Hoes, M. F.; Bomer, N.; van der Meer, P. Concise Review: The Current State of Human In Vitro Cardiac Disease Modeling: A Focus on Gene Editing and Tissue Engineering. *Stem Cells Translational Medicine*. Oxford Academic January 1, 2019, pp 66–74. https://doi.org/10.1002/sctm.18-0052.

(134) Musunuru, K.; Domian, I. J.; Chien, K. R. Stem Cell Models of Cardiac Development and Disease. *Annual Review of Cell and Developmental Biology*. 2010, pp 667–687. https://doi.org/10.1146/annurev-cellbio-100109-103948.

(135) Pomeroy, V. M.; King, L. M.; Pollock, A.; Baily-Hallam, A.; Langhorne, P. Electrostimulation for Promoting Recovery of Movement or Functional Ability after Stroke. *Cochrane Database Syst. Rev.* **2006**. https://doi.org/10.1002/14651858.cd003241.pub2.

(136) Rojahn, R. Transcutaneous Electrostimulation for Osteoarthritis of the Knee. *J. Pain Manag.* **2011**, *4* (4), 447–449. https://doi.org/10.5867/medwave.2013.08.5789.

(137) Long, Y.; Li, J.; Yang, F.; Wang, J.; Wang, X. Wearable and Implantable Electroceuticals for Therapeutic Electrostimulations. *Advanced Science*. John Wiley & Sons, Ltd April 1, 2021, p 2004023. https://doi.org/10.1002/advs.202004023.

(138) Scott, L.; Elídóttir, K.; Jeevaratnam, K.; Jurewicz, I.; Lewis, R. Electrical Stimulation through Conductive Scaffolds for Cardiomyocyte Tissue Engineering: Systematic Review and Narrative Synthesis. *Annals of the New York Academy of Sciences*. NLM (Medline) September 1, 2022, pp 105–119. https://doi.org/10.1111/nyas.14812.

(139) Nunes, S. S.; Miklas, J. W.; Liu, J.; Aschar-Sobbi, R.; Xiao, Y.; Zhang, B.; Jiang, J.; Massé, S.; Gagliardi, M.; Hsieh, A.; Thavandiran, N.; Laflamme, M. A.; Nanthakumar, K.; Gross, G. J.; Backx, P. H.; Keller, G.; Radisic, M. Biowire: A Platform for Maturation of Human Pluripotent Stem Cell-Derived Cardiomyocytes. *Nat. Methods* **2013**, *10* (8), 781–787. https://doi.org/10.1038/nmeth.2524.

(140) Camci-Unal, G.; Annabi, N.; Dokmeci, M. R.; Liao, R.; Khademhosseini, A. Hydrogels for Cardiac Tissue Engineering. *NPG Asia Materials*. 2014. https://doi.org/10.1038/am.2014.19.

(141) Guo, Y.; Bae, J.; Fang, Z.; Li, P.; Zhao, F.; Yu, G. Hydrogels and Hydrogel-Derived Materials for Energy and Water Sustainability. *Chemical Reviews*. American Chemical Society August 12, 2020, pp 7642–7707. https://doi.org/10.1021/acs.chemrev.0c00345.

(142) Kim, J.; Koo, B. K.; Knoblich, J. A. Human Organoids: Model Systems for

Human Biology and Medicine. *Nature Reviews Molecular Cell Biology*. Nature Publishing Group July 7, 2020, pp 571–584. https://doi.org/10.1038/s41580-020-0259-3.

(143) Li, X. P.; Qu, K. Y.; Zhou, B.; Zhang, F.; Wang, Y. Y.; Abodunrin, O. D.; Zhu, Z.; Huang, N. P. Electrical Stimulation of Neonatal Rat Cardiomyocytes Using Conductive Polydopamine-Reduced Graphene Oxide-Hybrid Hydrogels for Constructing Cardiac Microtissues. *Colloids Surfaces B Biointerfaces* **2021**, *205*. https://doi.org/10.1016/j.colsurfb.2021.111844.

(144) Zhang, F.; Qu, K.; Li, X.; Liu, C.; Ortiz, L. S.; Wu, K.; Wang, X.; Huang, N. Gelatin-Based Hydrogels Combined with Electrical Stimulation to Modulate Neonatal Rat Cardiomyocyte Beating and Promote Maturation. *Bio-Design Manuf.* **2021**, *4* (1), 100–110. https://doi.org/10.1007/s42242-020-00100-9.

(145) Zhang, F.; Qu, K. Y.; Zhou, B.; Luo, Y.; Zhu, Z.; Pan, D. J.; Cui, C.; Zhu, Y.; Chen, M. L.; Huang, N. P. Design and Fabrication of an Integrated Heart-on-a-Chip Platform for Construction of Cardiac Tissue from Human IPSC-Derived Cardiomyocytes and in Situ Evaluation of Physiological Function. *Biosens. Bioelectron.* **2021**, *179*, 113080. https://doi.org/10.1016/j.bios.2021.113080.

(146) Scott, L.; Elídóttir, K.; Jeevaratnam, K.; Jurewicz, I.; Lewis, R. Electrical Stimulation through Conductive Scaffolds for Cardiomyocyte Tissue Engineering: Systematic Review and Narrative Synthesis. *Annals of the New York Academy of Sciences*. John Wiley & Sons, Ltd September 1, 2022, pp 105–119. https://doi.org/10.1111/nyas.14812.

(147) Thrivikraman, G.; Boda, S. K.; Basu, B. Unraveling the Mechanistic Effects of Electric Field Stimulation towards Directing Stem Cell Fate and Function: A Tissue Engineering Perspective. *Biomaterials*. Elsevier Ltd January 1, 2018, pp 60–86. https://doi.org/10.1016/j.biomaterials.2017.10.003.

(148) Chen, C.; Bai, X.; Ding, Y.; Lee, I. S. Electrical Stimulation as a Novel Tool for Regulating Cell Behavior in Tissue Engineering. *Biomaterials Research*. BioMed Central Ltd. December 5, 2019. https://doi.org/10.1186/s40824-019-0176-8.

(149) Balint, R.; Cassidy, N. J.; Cartmell, S. H. Electrical Stimulation: A Novel Tool for Tissue Engineering. *Tissue Engineering - Part B: Reviews*. February 1, 2013, pp 48–57. https://doi.org/10.1089/ten.teb.2012.0183.

(150) Nazari, H.; Kehtari, M.; Rad, I.; Ashtari, B.; Joghataei, M. T. Electrical

Stimulation Induces Differentiation of Human Cardiosphere-Derived Cells (HCDCs) to Committed Cardiomyocyte. *Mol. Cell. Biochem.* **2020**, *470* (1–2), 29–39. https://doi.org/10.1007/s11010-020-03742-6.

(151) Taghadosi, H.; Ghomsheh, F. T.; Farajidavar, A. Simulation of A Gastric Smooth Muscle Cell Model Utilizing the Electrophysiological Parameters of Colon Cell. *Front. Biomed. Technol.* **2023**, *10* (3), 237–247. https://doi.org/10.18502/FBT.V10I3.13148.

(152) Proskocil, B. J.; Calco, G. N.; Nie, Z. Insulin Acutely Increases Agonist-Induced Airway Smooth Muscle Contraction in Humans and Rats. *Am. J. Physiol. - Lung Cell. Mol. Physiol.* **2021**, *320* (4), L545–L556. https://doi.org/10.1152/ajplung.00232.2020.

(153) Zhang, J.; Zhang, X.; Wang, C.; Li, F.; Qiao, Z.; Zeng, L.; Wang, Z.; Liu, H.; Ding, J.; Yang, H. Conductive Composite Fiber with Optimized Alignment Guides Neural Regeneration under Electrical Stimulation. *Adv. Healthc. Mater.* **2021**, *10* (3). https://doi.org/10.1002/adhm.202000604.

(154) Zhu, R.; Sun, Z.; Li, C.; Ramakrishna, S.; Chiu, K.; He, L. Electrical Stimulation Affects Neural Stem Cell Fate and Function in Vitro. *Experimental Neurology*. 2019. https://doi.org/10.1016/j.expneurol.2019.112963.

(155) Lou, L.; Rubfiaro, A. S.; He, J.; Agarwal, A. Effect of Electrical Stimulation on Spontaneously Beating Dynamics of Cardiac Tissues: An Analysis Using Digital Image Correlation. *Adv. Mater. Technol.* **2021**, *6* (12). https://doi.org/10.1002/admt.202100669.

(156) Pretorius, D.; Kahn-Krell, A. M.; LaBarge, W. C.; Lou, X.; Zhang, J. Engineering of Thick Human Functional Myocardium via Static Stretching and Electrical Stimulation. *iScience* **2022**, *25* (3), 103824. https://doi.org/10.1016/j.isci.2022.103824.

(157) LaBarge, W.; Mattappally, S.; Kannappan, R.; Fast, V. G.; Pretorius, D.; Berry, J. L.; Zhang, J. Maturation of Three-Dimensional, HiPSC-Derived Cardiomyocyte Spheroids Utilizing Cyclic, Uniaxial Stretch and Electrical Stimulation. *PLoS One* **2019**, *14* (7). https://doi.org/10.1371/journal.pone.0219442.

(158) Li, J.; Feng, X.; Wei, X. Modeling Hypertrophic Cardiomyopathy with Human Cardiomyocytes Derived from Induced Pluripotent Stem Cells. *Stem Cell*

Research and Therapy. BioMed Central June 3, 2022, pp 1–20. https://doi.org/10.1186/s13287-022-02905-0.

(159) Alave Reyes-Furrer, A.; De Andrade, S.; Bachmann, D.; Jeker, H.; Steinmann, M.; Accart, N.; Dunbar, A.; Rausch, M.; Bono, E.; Rimann, M.; Keller, H. Matrigel 3D Bioprinting of Contractile Human Skeletal Muscle Models Recapitulating Exercise and Pharmacological Responses. *Commun. Biol.* **2021**, *4* (1), 1183. https://doi.org/10.1038/s42003-021-02691-0.

(160) Khodabukus, A.; Madden, L.; Prabhu, N. K.; Koves, T. R.; Jackman, C. P.; Muoio, D. M.; Bursac, N. Electrical Stimulation Increases Hypertrophy and Metabolic Flux in Tissue-Engineered Human Skeletal Muscle. *Biomaterials* **2019**, *198*, 259–269. https://doi.org/10.1016/j.biomaterials.2018.08.058.

(161) Lichtenstein, M. P.; Suñol, C.; Casañ-Pastor, N. Short-Term Electrostimulation Enhancing Neural Repair in Vitro Using Large Charge Capacity Nanostructured Electrodes. *Appl. Mater. Today* **2017**, *6*, 29–43. https://doi.org/10.1016/j.apmt.2016.12.002.

(162) Bertucci, C.; Koppes, R.; Dumont, C.; Koppes, A. Neural Responses to Electrical Stimulation in 2D and 3D in Vitro Environments. *Brain Research Bulletin*. Elsevier October 1, 2019, pp 265–284. https://doi.org/10.1016/j.brainresbull.2019.07.016.

(163) Loget, G.; Zigah, D.; Bouffier, L.; Sojic, N.; Kuhn, A. Bipolar Electrochemistry: From Materials Science to Motion and Beyond. **2013**, *5*. https://doi.org/10.1021/ar400039k.

(164) Fosdick, S. E.; Knust, K. N.; Scida, K.; Crooks, R. M. Bipolar Electrochemistry. *Angewandte Chemie - International Edition*. September 27, 2013, pp 10438–10456. https://doi.org/10.1002/anie.201300947.

(165) Qin, C.; Yue, Z.; Chao, Y.; Forster, R. J.; Maolmhuaidh, F.; Huang, X. F.; Beirne, S.; Wallace, G. G.; Chen, J. Bipolar Electroactive Conducting Polymers for Wireless Cell Stimulation. *Appl. Mater. Today* **2020**, *21*, 100804. https://doi.org/10.1016/j.apmt.2020.100804.

(166) Hu, S.; Gao, J. Materials and Physics of Light-Emitting Electrochemical Cells (LECs). In *Handbook of Organic Materials for Electronic and Photonic Devices*; Woodhead Publishing, 2019; pp 727–757. https://doi.org/10.1016/b978-0-08-102284-9.00022-x.

(167) Crooks, R. M. Principles of Bipolar Electrochemistry. *ChemElectroChem* **2016**, *3* (3), 357–359. https://doi.org/10.1002/celc.201500549.

(168) Duval, J. F. L.; Huijs, G. K.; Threels, W. F.; Lyklema, J.; Van Leeuwen, H. P. Faradaic Depolarization in the Electrokinetics of the Metal-Electrolyte Solution Interface. *J. Colloid Interface Sci.* **2003**, *260* (1), 95–106. https://doi.org/10.1016/S0021-9797(02)00134-0.

(169) Mavré, F.; Anand, R. K.; Laws, D. R.; Chow, K. F.; Chang, B. Y.; Crooks, J. A.; Crooks, R. M. Bipolar Electrodes: A Useful Tool for Concentration, Separation, and Detection of Analytes in Microelectrochemical Systems. *Anal. Chem.* **2010**, *82* (21), 8766–8774. https://doi.org/10.1021/ac101262v.

(170) Chen, C.; Bai, X.; Ding, Y.; Lee, I. S. Electrical Stimulation as a Novel Tool for Regulating Cell Behavior in Tissue Engineering. *Biomaterials Research*. BioMed Central December 5, 2019, pp 1–12. https://doi.org/10.1186/s40824-019-0176-8.

(171) Chan, Y. C.; Ting, S.; Lee, Y. K.; Ng, K. M.; Zhang, J.; Chen, Z.; Siu, C. W.; Oh, S. K. W.; Tse, H. F. Electrical Stimulation Promotes Maturation of Cardiomyocytes Derived from Human Embryonic Stem Cells. *J. Cardiovasc. Transl. Res.* **2013**, *6* (6), 989–999. https://doi.org/10.1007/s12265-013-9510-z.

(172) Matsa, E.; Sallam, K.; Wu, J. C. Cardiac Stem Cell Biology: Glimpse of the Past, Present, and Future. *Circ. Res.* **2014**, *114* (1), 21–27. https://doi.org/10.1161/CIRCRESAHA.113.302895.

(173) Bearzi, C.; Rota, M.; Hosoda, T.; Tillmanns, J.; Nascimbene, A.; De Angelis, A.; Yasuzawa-Amano, S.; Trofimova, I.; Siggins, R. W.; LeCapitaine, N.; Cascapera, S.; Beltrami, A. P.; D'Alessandro, D. A.; Zias, E.; Quaini, F.; Urbanek, K.; Michler, R. E.; Bolli, R.; Kajstura, J.; Leri, A.; Anversa, P. Human Cardiac Stem Cells. *Proc. Natl. Acad. Sci. U. S. A.* **2007**, *104* (35), 14068–14073. https://doi.org/10.1073/pnas.0706760104.

(174) Hou, J.; Wang, L.; Jiang, J.; Zhou, C.; Guo, T.; Zheng, S.; Wang, T. Cardiac Stem Cells and Their Roles in Myocardial Infarction. *Stem Cell Reviews and Reports*. Springer December 13, 2013, pp 326–338. https://doi.org/10.1007/s12015-012-9421-4.

(175) Radisic, M.; Park, H.; Shing, H.; Consi, T.; Schoen, F. J.; Langer, R.; Freed, L. E.; Vunjak-Novakovic, G. Functional Assembly of Engineered Myocardium by

Electrical Stimulation of Cardiac Myocytes Cultured on Scaffolds. *Proc. Natl. Acad. Sci. U. S. A.* **2004**, *101* (52), 18129–18134. https://doi.org/10.1073/pnas.0407817101.

(176) Xia, Y.; McMillin, J. B.; Lewis, A.; Moore, M.; Zhu, W. G.; Williams, R. S.; Kellems, R. E. Electrical Stimulation of Neonatal Cardiac Myocytes Activates the NFAT3 and GATA4 Pathways and Up-Regulates the Adenylosuccinate Synthetase 1 Gene. *J. Biol. Chem.* **2000**, *275* (3), 1855–1863. https://doi.org/10.1074/jbc.275.3.1855.

(177) Pedrotty, D. M.; Klinger, R. Y.; Kirkton, R. D.; Bursac, N. Cardiac Fibroblast Paracrine Factors Alter Impulse Conduction and Ion Channel Expression of Neonatal Rat Cardiomyocytes. *Cardiovasc. Res.* **2009**, *83* (4), 688–697. https://doi.org/10.1093/cvr/cvp164.

(178) Seki, S.; Nagashima, M.; Yamada, Y.; Tsutsuura, M.; Kobayashi, T.; Namiki, A.; Tohse, N. Fetal and Postnatal Development of Ca2+ Transients and Ca2+ Sparks in Rat Cardiomyocytes. *Cardiovasc. Res.* **2003**, *58* (3), 535–548. https://doi.org/10.1016/S0008-6363(03)00255-4.

(179) Mohamed, M. A.; Islas, J. F.; Schwartz, R. J.; Birla, R. K. Electrical Stimulation of Artificial Heart Muscle: A Look into the Electrophysiologic and Genetic Implications. *ASAIO J.* **2017**, *63* (3), 333–341. https://doi.org/10.1097/MAT.0000000000000486.

(180) Xia, Y.; Buja, L. M.; Scarpulla, R. C.; Mcmillin, J. B. Electrical Stimulation of Neonatal Cardiomyocytes Results in the Sequential Activation of Nuclear Genes Governing Mitochondrial Proliferation and Differentiation. *Proc. Natl. Acad. Sci. U. S. A.* **1997**, *94* (21), 11399–11404. https://doi.org/10.1073/pnas.94.21.11399.

(181) Hoebart, C.; Rojas-Galvan, N. S.; Ciotu, C. I.; Aykac, I.; Reissig, L. F.; Weninger, W. J.; Kiss, A.; Podesser, B. K.; Fischer, M. J. M.; Heber, S. No Functional TRPA1 in Cardiomyocytes. *Acta Physiol.* **2021**, *232* (4). https://doi.org/10.1111/apha.13659.

(182) Zhou, B.; Shi, X.; Tang, X.; Zhao, Q.; Wang, L.; Yao, F.; Hou, Y.; Wang, X.; Feng, W.; Wang, L.; Sun, X.; Wang, L.; Hu, S. Functional Isolation, Culture and Cryopreservation of Adult Human Primary Cardiomyocytes. *Signal Transduct. Target. Ther.* **2022**, *7* (1). https://doi.org/10.1038/s41392-022-01044-5.

(183) Onódi, Z.; Visnovitz, T.; Kiss, B.; Hambalkó, S.; Koncz, A.; Ágg, B.; Váradi, B.;

Tóth, V.; Nagy, R. N.; Gergely, T. G.; Gergő, D.; Makkos, A.; Pelyhe, C.; Varga, N.; Reé, D.; Apáti, Á.; Leszek, P.; Kovács, T.; Nagy, N.; Ferdinandy, P.; Buzás, E. I.; Görbe, A.; Giricz, Z.; Varga, Z. V. Systematic Transcriptomic and Phenotypic Characterization of Human and Murine Cardiac Myocyte Cell Lines and Primary Cardiomyocytes Reveals Serious Limitations and Low Resemblances to Adult Cardiac Phenotype. *J. Mol. Cell. Cardiol.* **2022**, *165*, 19–30. https://doi.org/10.1016/j.yjmcc.2021.12.007.

(184) Nguyen, B.; Fong, C.; Luthra, A.; Smith, S. A.; DiNatale, R. G.; Nandakumar, S.; Walch, H.; Chatila, W. K.; Madupuri, R.; Kundra, R.; Bielski, C. M.; Mastrogiacomo, B.; Donoghue, M. T. A.; Boire, A.; Chandarlapaty, S.; Ganesh, K.; Harding, J. J.; Iacobuzio-Donahue, C. A.; Razavi, P.; Reznik, E.; Rudin, C. M.; Zamarin, D.; Abida, W.; Abou-Alfa, G. K.; Aghajanian, C.; Cercek, A.; Chi, P.; Feldman, D.; Ho, A. L.; Iyer, G.; Janjigian, Y. Y.; Morris, M.; Motzer, R. J.; O'Reilly, E. M.; Postow, M. A.; Raj, N. P.; Riely, G. J.; Robson, M. E.; Rosenberg, J. E.; Safonov, A.; Shoushtari, A. N.; Tap, W.; Teo, M. Y.; Varghese, A. M.; Voss, M.; Yaeger, R.; Zauderer, M. G.; Abu-Rustum, N.; Garcia-Aguilar, J.; Bochner, B.; Hakimi, A.; Jarnagin, W. R.; Jones, D. R.; Molena, D.; Morris, L.; Rios-Doria, E.; Russo, P.; Singer, S.; Strong, V. E.; Chakravarty, D.; Ellenson, L. H.; Gopalan, A.; Reis-Filho, J. S.; Weigelt, B.; Ladanyi, M.; Gonen, M.; Shah, S. P.; Massague, J.; Gao, J.; Zehir, A.; Berger, M. F.; Solit, D. B.; Bakhoum, S. F.; Sanchez-Vega, F.; Schultz, N. Genomic Characterization of Metastatic Patterns from Prospective Clinical Sequencing of 25,000 Patients. *Cell* **2022**, *185* (3), 563-575.e11. https://doi.org/10.1016/j.cell.2022.01.003.

(185) Godoy, P. M.; Barczak, A. J.; DeHoff, P.; Srinivasan, S.; Etheridge, A.; Galas, D.; Das, S.; Erle, D. J.; Laurent, L. C. Comparison of Reproducibility, Accuracy, Sensitivity, and Specificity of MiRNA Quantification Platforms. *Cell Rep.* **2019**, *29* (12), 4212-4222.e5. https://doi.org/10.1016/j.celrep.2019.11.078.

(186) Shen, M.; Zhou, Y.; Ye, J.; Abdullah AL-maskri, A. A.; Kang, Y.; Zeng, S.; Cai, S. Recent Advances and Perspectives of Nucleic Acid Detection for Coronavirus. *Journal of Pharmaceutical Analysis*. Xi'an Jiaotong University April 1, 2020, pp 97–101. https://doi.org/10.1016/j.jpha.2020.02.010.

(187) Kang, K.; Peng, X.; Luo, J.; Gou, D. Identification of Circulating MiRNA Biomarkers Based on Global Quantitative Real-Time PCR Profiling. *Journal of Animal Science and Biotechnology*. BioMed Central February 28, 2012, pp 1–9. https://doi.org/10.1186/2049-1891-3-4.

(188) Schmittgen, T. D.; Lee, E. J.; Jiang, J.; Sarkar, A.; Yang, L.; Elton, T. S.; Chen, C. Real-Time PCR Quantification of Precursor and Mature MicroRNA. *Methods* **2008**, *44* (1), 31–38. https://doi.org/10.1016/j.ymeth.2007.09.006.

(189) Dellett, M.; Simpson, D. A. Considerations for Optimization of MicroRNA PCR Assays for Molecular Diagnosis. *Expert Rev. Mol. Diagn.* **2016**, *16* (4), 407–414. https://doi.org/10.1586/14737159.2016.1152184.

(190) Mathur, P.; Rani, V. Investigating MicroRNAs in Diabetic Cardiomyopathy as Tools for Early Detection and Therapeutics. *Mol. Cell. Biochem.* **2022**, *1*, 3. https://doi.org/10.1007/s11010-022-04473-6.

(191) Kramer, M. F. Stem-Loop RT-QPCR for MiRNAs. *Curr. Protoc. Mol. Biol.* **2011**, No. SUPPL. 95. https://doi.org/10.1002/0471142727.mb1510s95.

(192) Chen, C.; Ridzon, D. A.; Broomer, A. J.; Zhou, Z.; Lee, D. H.; Nguyen, J. T.; Barbisin, M.; Xu, N. L.; Mahuvakar, V. R.; Andersen, M. R.; Lao, K. Q.; Livak, K. J.; Guegler, K. J. Real-Time Quantification of MicroRNAs by Stem-Loop RT-PCR. *Nucleic Acids Res.* **2005**, *33* (20). https://doi.org/10.1093/nar/gni178.

(193) Redshaw, N.; Wilkes, T.; Whale, A.; Cowen, S.; Huggett, J.; Foy, C. A. A Comparison of MiRNA Isolation and RT-QPCR Technologies and Their Effects on Quantification Accuracy and Repeatability. *Biotechniques* **2013**, *54* (3), 155–164. https://doi.org/10.2144/000114002.

(194) Siddika, T.; Heinemann, I. U. Bringing MicroRNAs to Light: Methods for MicroRNA Quantification and Visualization in Live Cells. *Frontiers in Bioengineering and Biotechnology*. 2021, p 619583. https://doi.org/10.3389/fbioe.2020.619583.

(195) Chugh, P.; Dittmer, D. P. Potential Pitfalls in MicroRNA Profiling. *Wiley Interdisciplinary Reviews: RNA*. 2012, pp 601–616. https://doi.org/10.1002/wrna.1120.

(196) Kramer, M. F. Stem-Loop RT-QPCR for MiRNAs. *Curr. Protoc. Mol. Biol.* **2011**, *95* (SUPPL. 95), 15.10.1-15.10.15. https://doi.org/10.1002/0471142727.mb1510s95.

(197) Hu, K.; Lan, D.; Li, X.; Zhang, S. Electrochemical DNA Biosensor Based on Nanoporous Gold Electrode and Multifunctional Encoded DNA-Au Bio Bar Codes. *Anal. Chem.* **2008**, *80* (23), 9124–9130. https://doi.org/10.1021/ac8017197.

(198) Ren, Y.; Deng, H.; Shen, W.; Gao, Z. A Highly Sensitive and Selective Electrochemical Biosensor for Direct Detection of MicroRNAs in Serum. *Anal. Chem.* **2013**, *85* (9), 4784–4789. https://doi.org/10.1021/ac400583e.

(199) Tran, H. V.; Piro, B.; Reisberg, S.; Huy Nguyen, L.; Dung Nguyen, T.; Duc, H. T.; Pham, M. C. An Electrochemical ELISA-like Immunosensor for MiRNAs Detection Based on Screen-Printed Gold Electrodes Modified with Reduced Graphene Oxide and Carbon Nanotubes. *Biosens. Bioelectron.* **2014**, *62*, 25–30. https://doi.org/10.1016/j.bios.2014.06.014.

(200) Subhasis Mahari; Akanksha Roberts; Deepshikha Shahdeo; Sonu Gandhi. ECovSens-Ultrasensitive Novel In-House Built Printed Circuit Board Based Electrochemical Device for Rapid Detection of NCovid-19 Antigen, a Spike Protein Domain 1 of SARS-CoV-2. *Biorxiv* **2020**. https://doi.org/10.1101/2020.04.24.059204.

(201) Thapa, K.; Liu, W.; Wang, R. Nucleic Acid-Based Electrochemical Biosensor: Recent Advances in Probe Immobilization and Signal Amplification Strategies. *Wiley Interdisciplinary Reviews: Nanomedicine and Nanobiotechnology.* John Wiley and Sons Inc January 1, 2022. https://doi.org/10.1002/wnan.1765.

(202) Meng, F.; Jiang, Z.; Li, Y.; Zhang, P.; Liu, H.; Sun, Y.; Wang, X. An Enzyme-Free and Label-Free Electrochemical Biosensor for Polynucleotide Kinase. *Talanta* **2023**, *253*. https://doi.org/10.1016/j.talanta.2022.124004.

(203) Cagnani, G. R.; Ibáñez-Redín, G.; Tirich, B.; Gonçalves, D.; Balogh, D. T.; Oliveira, O. N. Fully-Printed Electrochemical Sensors Made with Flexible Screen-Printed Electrodes Modified by Roll-to-Roll Slot-Die Coating. *Biosens. Bioelectron.* **2020**, *165*. https://doi.org/10.1016/j.bios.2020.112428.

(204) Li, Q.; Zhang, J.; Li, Q.; Li, G.; Tian, X.; Luo, Z.; Qiao, F.; Wu, X.; Zhang, J. Review of Printed Electrodes for Flexible Devices. *Frontiers in Materials.* 2019. https://doi.org/10.3389/fmats.2018.00077.

(205) Inam, A. K. M. S.; Costa Angeli, M. A.; Shkodra, B.; Douaki, A.; Avancini, E.; Magagnin, L.; Petti, L.; Lugli, P. Flexible Screen-Printed Electrochemical Sensors Functionalized with Electrodeposited Copper for Nitrate Detection in Water. *ACS Omega* **2021**, *6* (49), 33523–33532. https://doi.org/10.1021/acsomega.1c04296.

(206) Ye, Q.; Zhang, Z.; Liu, J.; Wang, X. Screen-Printed Electrode-Based Biosensors

Modified with Functional Nucleic Acid Probes and Their Applications in This Pandemic Age: A Review. *Analytical Methods.* 2022, pp 2961–2975. https://doi.org/10.1039/d2ay00666a.

(207) Shabaninejad, Z.; Yousefi, F.; Movahedpour, A.; Ghasemi, Y.; Dokanehiifard, S.; Rezaei, S.; Aryan, R.; Savardashtaki, A.; Mirzaei, H. Electrochemical-Based Biosensors for MicroRNA Detection: Nanotechnology Comes into View. *Analytical Biochemistry.* 2019. https://doi.org/10.1016/j.ab.2019.113349.

(208) Low, S. S.; Ji, D.; Chai, W. S.; Liu, J.; Khoo, K. S.; Salmanpour, S.; Karimi, F.; Deepanraj, B.; Show, P. L. Recent Progress in Nanomaterials Modified Electrochemical Biosensors for the Detection of MicroRNA. *Micromachines.* 2021. https://doi.org/10.3390/mi12111409.

(209) Johnson, B. N.; Mutharasan, R. Biosensor-Based MicroRNA Detection: Techniques, Design, Performance, and Challenges. *Analyst* **2014**, *139* (7), 1576–1588. https://doi.org/10.1039/c3an01677c.

(210) Campuzano, S.; Barderas, R.; Pedrero, M.; Yáñez-Sedeño, P.; Pingarrón, J. M. Electrochemical Biosensing to Move Forward in Cancer Epigenetics and Metastasis: A Review. *Analytica Chimica Acta.* Elsevier B.V. May 1, 2020, pp 169–190. https://doi.org/10.1016/j.aca.2020.01.047.

(211) Hai, X.; Li, Y.; Zhu, C.; Song, W.; Cao, J.; Bi, S. DNA-Based Label-Free Electrochemical Biosensors: From Principles to Applications. *TrAC - Trends in Analytical Chemistry.* Elsevier B.V. December 1, 2020. https://doi.org/10.1016/j.trac.2020.116098.

(212) Mujica, M. L.; Gallay, P. A.; Perrachione, F.; Montemerlo, A. E.; Tamborelli, L. A.; Vaschetti, V. M.; Reartes, D. F.; Bollo, S.; Rodríguez, M. C.; Dalmasso, P. R.; Rubianes, M. D.; Rivas, G. A. New Trends in the Development of Electrochemical Biosensors for the Quantification of MicroRNAs. *Journal of Pharmaceutical and Biomedical Analysis.* Elsevier B.V. September 10, 2020. https://doi.org/10.1016/j.jpba.2020.113478.

(213) Krepelkova, I.; Mrackova, T.; Izakova, J.; Dvorakova, B.; Chalupova, L.; Mikulik, R.; Slaby, O.; Bartos, M.; Ruzicka, V. Evaluation of MiRNA Detection Methods for the Analytical Characteristics Necessary for Clinical Utilization. *Biotechniques* **2019**, *66* (6), 277–284. https://doi.org/10.2144/btn-2019-0021.

(214) De Ronde, M. W. J.; Ruijter, J. M.; Moerland, P. D.; Creemers, E. E.; Pinto-

Sietsma, S. J. Study Design and QPCR Data Analysis Guidelines for Reliable Circulating MiRNA Biomarker Experiments: A Review. *Clinical Chemistry*. 2018, pp 1308–1318. https://doi.org/10.1373/clinchem.2017.285288.

(215) Taleat, Z.; Khoshroo, A.; Mazloum-Ardakani, M. Screen-Printed Electrodes for Biosensing: A Review (2008-2013). *Microchimica Acta*. 2014, pp 865–891. https://doi.org/10.1007/s00604-014-1181-1.

(216) Suresh, R. R.; Lakshmanakumar, M.; Arockia Jayalatha, J. B. B.; Rajan, K. S.; Sethuraman, S.; Krishnan, U. M.; Rayappan, J. B. B. Fabrication of Screen-Printed Electrodes: Opportunities and Challenges. *Journal of Materials Science*. 2021, pp 8951–9006. https://doi.org/10.1007/s10853-020-05499-1.

(217) Kuntamung, K.; Jakmunee, J.; Ounnunkad, K. A Label-Free Multiplex Electrochemical Biosensor for the Detection of Three Breast Cancer Biomarker Proteins Employing Dye/Metal Ion-Loaded and Antibody-Conjugated Polyethyleneimine-Gold Nanoparticles. *J. Mater. Chem. B* **2021**, *9* (33), 6576–6585. https://doi.org/10.1039/d1tb00940k.

(218) García-González, R.; Costa-García, A.; Fernández-Abedul, M. T. Dual Screen-Printed Electrodes with Elliptic Working Electrodes Arranged in Parallel or Perpendicular to the Strip. *Sensors Actuators, B Chem.* **2014**, *198*, 302–308. https://doi.org/10.1016/j.snb.2014.03.036.

(219) García-Miranda Ferrari, A.; Rowley-Neale, S. J.; Banks, C. E. Screen-Printed Electrodes: Transitioning the Laboratory in-to-the Field. *Talanta Open*. Elsevier August 1, 2021, p 100032. https://doi.org/10.1016/j.talo.2021.100032.

(220) Morrin, A.; Killard, A. J.; Smyth, M. R. Electrochemical Characterization of Commercial and Home-Made Screen-Printed Carbon Electrodes. *Anal. Lett.* **2003**, *36* (9), 2021–2039. https://doi.org/10.1081/AL-120023627.

(221) Wang, J.; Tian, B.; Nascimento, V. B.; Angnes, L. Performance of Screen-Printed Carbon Electrodes Fabricated from Different Carbon Inks. *Electrochim. Acta* **1998**, *43* (23), 3459–3465. https://doi.org/10.1016/S0013-4686(98)00092-9.

(222) Wahyuni, W. T.; Putra, B. R.; Fauzi, A.; Ramadhanti, D.; Rohaeti, E.; Heryanto, R. A Brief Review on Fabrication of Screen-Printed Carbon Electrode: Materials and Techniques. *Indo. J Chem. Res.* **2021**, *8* (3), 210–218. https://doi.org/10.30598//ijcr.2021.7-wul.

(223) Musa, A. M.; Kiely, J.; Luxton, R.; Honeychurch, K. C. Recent Progress in Screen-Printed Electrochemical Sensors and Biosensors for the Detection of Estrogens. *TrAC - Trends in Analytical Chemistry*. 2021. https://doi.org/10.1016/j.trac.2021.116254.

(224) Jaiswal, N.; Tiwari, I. Recent Build Outs in Electroanalytical Biosensors Based on Carbon-Nanomaterial Modified Screen Printed Electrode Platforms. *Analytical Methods*. 2017, pp 3895–3907. https://doi.org/10.1039/c7ay01276d.

(225) Smith, D. A.; Simpson, K.; Lo Cicero, M.; Newbury, L. J.; Nicholas, P.; Fraser, D. J.; Caiger, N.; Redman, J. E.; Bowen, T. Detection of Urinary MicroRNA Biomarkers Using Diazo Sulfonamide-Modified Screen Printed Carbon Electrodes. *RSC Adv.* **2021**, *11* (31), 18832–18839. https://doi.org/10.1039/d0ra09874d.

(226) Congur, G.; Erdem, A. PAMAM Dendrimer Modified Screen Printed Electrodes for Impedimetric Detection of MiRNA-34a. *Microchem. J.* **2019**, *148*, 748–758. https://doi.org/10.1016/j.microc.2019.05.040.

(227) Pothipor, C.; Jakmunee, J.; Bamrungsap, S.; Ounnunkad, K. An Electrochemical Biosensor for Simultaneous Detection of Breast Cancer Clinically Related MicroRNAs Based on a Gold Nanoparticles/Graphene Quantum Dots/Graphene Oxide Film. *Analyst* **2021**, *146* (12), 4000–4009. https://doi.org/10.1039/d1an00436k.

(228) Cardoso, A. R.; Moreira, F. T. C.; Fernandes, R.; Sales, M. G. F. Novel and Simple Electrochemical Biosensor Monitoring Attomolar Levels of MiRNA-155 in Breast Cancer. *Biosens. Bioelectron.* **2016**, *80*, 621–630. https://doi.org/10.1016/j.bios.2016.02.035.

(229) Cimmino, W.; Migliorelli, D.; Singh, S.; Miglione, A.; Generelli, S.; Cinti, S. Design of a Printed Electrochemical Strip towards MiRNA-21 Detection in Urine Samples: Optimization of the Experimental Procedures for Real Sample Application. *Anal. Bioanal. Chem.* **2023**, *415*, 4511–4520. https://doi.org/10.1007/s00216-023-04659-x.

(230) Erdem, A.; Congur, G.; Eksin, E. Multi Channel Screen Printed Array of Electrodes for Enzyme-Linked Voltammetric Detection of MicroRNAs. *Sensors Actuators, B Chem.* **2013**, *188*, 1089–1095. https://doi.org/10.1016/j.snb.2013.07.114.

(231) Congur, G.; Erdem, A. PAMAM Dendrimer Modified Screen Printed Electrodes for Impedimetric Detection of MiRNA-34a. *Microchem. J.* **2019**, *148*, 748–758. https://doi.org/10.1016/j.microc.2019.05.040.

(232) Horn, C. C.; Ardell, J. L.; Fisher, L. E. Electroceutical Targeting of the Autonomic Nervous System. *Physiology*. 2019, pp 150–162. https://doi.org/10.1152/physiol.00030.2018.

(233) Mishra, S. Electroceuticals in Medicine – The Brave New Future. *Indian Heart J.* **2017**, *69* (5), 685–686. https://doi.org/10.1016/j.ihj.2017.10.001.

(234) Kavehei, O.; Hamilton, T. J.; Truong, N. D.; Nikpour, A. Opportunities for Electroceuticals in Epilepsy. *Trends in Pharmacological Sciences*. Elsevier Ltd October 1, 2019, pp 735–746. https://doi.org/10.1016/j.tips.2019.08.001.

(235) Horn, C. C.; Ardell, J. L.; Fisher, L. E. Electroceutical Targeting of the Autonomic Nervous System. *Physiology*. American Physiological Society Bethesda, MD March 1, 2019, pp 150–162. https://doi.org/10.1152/physiol.00030.2018.

(236) Bourdillon, P.; Hermann, B.; Sitt, J. D.; Naccache, L. Electromagnetic Brain Stimulation in Patients With Disorders of Consciousness. *Frontiers in Neuroscience*. Frontiers March 18, 2019, p 223. https://doi.org/10.3389/fnins.2019.00223.

(237) Monti, G.; De Giovanni, G. R.; De Liso, M.; Pascali, M.; Tarricone, L. Wireless Power Transfer Strategies for Medical Implants: Focus on Robustness and EM Compatibility. *IEEE Microw. Mag.* **2021**, *22* (9), 28–41. https://doi.org/10.1109/mmm.2021.3086315.

(238) Buffet, J. Technological Progress in Pacemaker Design: Hermetic Sealing. *Med. Prog. Technol.* **1975**, *3* (3), 133–142.

(239) Long, Y.; Li, J.; Yang, F.; Wang, J.; Wang, X. Wearable and Implantable Electroceuticals for Therapeutic Electrostimulations. *Advanced Science*. John Wiley & Sons, Ltd April 1, 2021, p 2004023. https://doi.org/10.1002/advs.202004023.

(240) Antzelevitch, C.; Burashnikov, A. Overview of Basic Mechanisms of Cardiac Arrhythmia. *Cardiac Electrophysiology Clinics*. Elsevier March 1, 2011, pp 23–45. https://doi.org/10.1016/j.ccep.2010.10.012.

(241) Famm, K.; Litt, B.; Tracey, K. J.; Boyden, E. S.; Slaoui, M. Drug Discovery: A

Jump-Start for Electroceuticals. *Nature*. Nature Publishing Group April 10, 2013, pp 159–161. https://doi.org/10.1038/496159a.

(242) Eshraghi, A. A.; Nazarian, R.; Telischi, F. F.; Rajguru, S. M.; Truy, E.; Gupta, C. The Cochlear Implant: Historical Aspects and Future Prospects. *Anat. Rec.* **2012**, *295* (11), 1967–1980. https://doi.org/10.1002/ar.22580.

(243) Zeng, F. G.; Rebscher, S.; Harrison, W.; Sun, X.; Feng, H. Cochlear Implants: System Design, Integration, and Evaluation. *IEEE Rev. Biomed. Eng.* **2008**, *1*, 115–142. https://doi.org/10.1109/RBME.2008.2008250.

(244) Tenreiro, M. F.; Louro, A. F.; Alves, P. M.; Serra, M. Next Generation of Heart Regenerative Therapies: Progress and Promise of Cardiac Tissue Engineering. *npj Regenerative Medicine*. Nature Publishing Group June 1, 2021, pp 1–17. https://doi.org/10.1038/s41536-021-00140-4.

(245) Love, M. R.; Palee, S.; Chattipakorn, S. C.; Chattipakorn, N. Effects of Electrical Stimulation on Cell Proliferation and Apoptosis. *Journal of Cellular Physiology*. John Wiley & Sons, Ltd March 1, 2018, pp 1860–1876. https://doi.org/10.1002/jcp.25975.

(246) Ghasemi-Mobarakeh, L.; Prabhakaran, M. P.; Morshed, M.; Nasr-Esfahani, M. H.; Baharvand, H.; Kiani, S.; Al-Deyab, S. S.; Ramakrishna, S. Application of Conductive Polymers, Scaffolds and Electrical Stimulation for Nerve Tissue Engineering. *Journal of Tissue Engineering and Regenerative Medicine*. John Wiley & Sons, Ltd April 1, 2011, pp e17–e35. https://doi.org/10.1002/term.383.

(247) Backhurst, J. R.; Coulson, J. M.; Goodridge, F.; Plimley, R. E.; Fleischmann, M. A Preliminary Investigation of Fluidized Bed Electrodes. *J. Electrochem. Soc.* **1969**, *116* (11), 1600. https://doi.org/10.1149/1.2411628.

(248) Fleischmann, M.; Oldfield, J. W. Fluidised Bed Electrodes. Part I. Polarisation Predicted by Simplified Models. *J. Electroanal. Chem.* **1971**, *29* (2), 211–230. https://doi.org/10.1016/S0022-0728(71)80084-0.

(249) Tandon, N.; Cannizzaro, C.; Chao, P. H. G.; Maidhof, R.; Marsano, A.; Au, H. T. H.; Radisic, M.; Vunjak-Novakovic, G. Electrical Stimulation Systems for Cardiac Tissue Engineering. *Nat. Protoc.* **2009**, *4* (2), 155–173. https://doi.org/10.1038/nprot.2008.183.

(250) Sathaye, A.; Bursac, N.; Sheehy, S.; Tung, L. Electrical Pacing Counteracts Intrinsic Shortening of Action Potential Duration of Neonatal Rat Ventricular

Cells in Culture. *J. Mol. Cell. Cardiol.* **2006**, *41* (4), 633–641. https://doi.org/10.1016/j.yjmcc.2006.06.076.

(251) Zare, E. N.; Agarwal, T.; Zarepour, A.; Pinelli, F.; Zarrabi, A.; Rossi, F.; Ashrafizadeh, M.; Maleki, A.; Shahbazi, M. A.; Maiti, T. K.; Varma, R. S.; Tay, F. R.; Hamblin, M. R.; Mattoli, V.; Makvandi, P. Electroconductive Multi-Functional Polypyrrole Composites for Biomedical Applications. *Applied Materials Today*. Elsevier September 1, 2021, p 101117. https://doi.org/10.1016/j.apmt.2021.101117.

(252) Huang, W.; Leng, T.; Gao, M.; Hu, Q.; Liu, L.; Dou, H. Scalable Dextran-Polypyrrole Nano-Assemblies with Photothermal/Photoacoustic Dual Capabilities and Enhanced Biocompatibility. *Carbohydr. Polym.* **2020**, *241*, 116224. https://doi.org/10.1016/j.carbpol.2020.116224.

(253) Gelmi, A.; Higgins, M. J.; Wallace, G. G. Physical Surface and Electromechanical Properties of Doped Polypyrrole Biomaterials. *Biomaterials* **2010**, *31* (8), 1974–1983. https://doi.org/10.1016/j.biomaterials.2009.11.040.

(254) Molino, P. J.; Innis, P. C.; Higgins, M. J.; Kapsa, R. M. I.; Wallace, G. G. Influence of Biopolymer Loading on the Physiochemical and Electrochemical Properties of Inherently Conducting Polymer Biomaterials. *Synth. Met.* **2015**, *200*, 40–47. https://doi.org/10.1016/j.synthmet.2014.12.018.

(255) Kim, S.; Jang, Y.; Jang, M.; Lim, A.; Hardy, J. G.; Park, H. S.; Lee, J. Y. Versatile Biomimetic Conductive Polypyrrole Films Doped with Hyaluronic Acid of Different Molecular Weights. *Acta Biomater.* **2018**, *80*, 258–268. https://doi.org/10.1016/j.actbio.2018.09.035.

(256) Huang, J.; Hu, X.; Lu, L.; Ye, Z.; Zhang, Q.; Luo, Z. Electrical Regulation of Schwann Cells Using Conductive Polypyrrole/Chitosan Polymers. *J. Biomed. Mater. Res. - Part A* **2010**, *93* (1), 164–174. https://doi.org/10.1002/jbm.a.32511.

(257) Thompson, B. C.; Moulton, S. E.; Richardson, R. T.; Wallace, G. G. Effect of the Dopant Anion in Polypyrrole on Nerve Growth and Release of a Neurotrophic Protein. *Biomaterials* **2011**, *32* (15), 3822–3831. https://doi.org/10.1016/j.biomaterials.2011.01.053.

(258) Yuan, Y. J.; Adeloju, S. B.; Wallace, G. G. In-Situ Electrochemical Studies on the Redox Properties of Polypyrrole in Aqueous Solutions. *Eur. Polym. J.* **1999**, *35* (10), 1761–1772. https://doi.org/10.1016/S0014-3057(98)00268-7.

(259) Kaynak, A. Effect of Synthesis Parameters on the Surface Morphology of Conducting Polypyrrole Films. *Mater. Res. Bull.* **1997**, *32* (3), 271–285. https://doi.org/10.1016/S0025-5408(96)00200-0.

(260) Su, D.; Zhou, J.; Ahmed, K. S.; Ma, Q.; Lv, G.; Chen, J. Fabrication and Characterization of Collagen-Heparin-Polypyrrole Composite Conductive Film for Neural Scaffold. *Int. J. Biol. Macromol.* **2019**, *129*, 895–903. https://doi.org/10.1016/j.ijbiomac.2019.02.087.

(261) Hodgson, A. J.; John, M. J.; Campbell, T.; Georgevich, A.; Woodhouse, S.; Aoki, T.; Ogata, N.; Wallace, G. G. Integration of Biocomponents with Synthetic Structures: Use of Conducting Polymer Polyelectrolyte Composites. In *Smart Structures and Materials 1996: Smart Materials Technologies and Biomimetics*; International Society for Optics and Photonics, 1996; Vol. 2716, p 164. https://doi.org/10.1117/12.232137.

(262) Hallab, N. J.; Bundy, K. J.; O'Connor, K.; Moses, R. L.; Jacobs, J. J. Evaluation of Metallic and Polymeric Biomaterial Surface Energy and Surface Roughness Characteristics for Directed Cell Adhesion. *Tissue Eng.* **2001**, *7* (1), 55–70. https://doi.org/10.1089/107632700300003297.

(263) Fonner, J. M.; Forciniti, L.; Nguyen, H.; Byrne, J. D.; Kou, Y. F.; Syeda-Nawaz, J.; Schmidt, C. E. Biocompatibility Implications of Polypyrrole Synthesis Techniques. *Biomed. Mater.* **2008**, *3* (3). https://doi.org/10.1088/1748-6041/3/3/034124.

(264) Yamaura, M.; Sato, K.; Hagiwara, T. Effect of Counter-Anion Exchange on Electrical Conductivity of Polypyrrole Films. *Synth. Met.* **1991**, *41* (1–2), 439–442. https://doi.org/10.1016/0379-6779(91)91102-G.

(265) Barisci, J. N.; Hughes, D.; Minett, A.; Wallace, G. G. Characterisation and Analytical Use of a Polypyrrole Electrode Containing Anti-Human Serum Albumin. *Anal. Chim. Acta* **1998**, *371* (1), 39–48. https://doi.org/10.1016/S0003-2670(98)00277-3.

(266) Kumar, D.; Sharma, R. C. Advances in Conductive Polymers. *European Polymer Journal*. Elsevier Ltd August 1, 1998, pp 1053–1060. https://doi.org/10.1016/S0014-3057(97)00204-8.

(267) Bhattacharya, A.; De, A. *CONDUCTING COMPOSITES OF POLYPYRROLE AND POLYANILINE A REVIEW*; 1996; Vol. 24.

(268) Sadki, S.; Schottland, P.; Brodie, N.; Sabouraud, G. The Mechanisms of Pyrrole Electropolymerization. *Chem. Soc. Rev.* **2000**, *29* (5), 283–293. https://doi.org/10.1039/a807124a.

(269) Li, Y.; Qian, R. Effect of Anion and Solution PH on the Electrochemical Behavior of Polypyrrole in Aqueous Solution. *Synth. Met.* **1989**, *28* (1–2), 127–132. https://doi.org/10.1016/0379-6779(89)90509-2.

(270) Kent, C. A.; Concepcion, J. J.; Dares, C. J.; Torelli, D. A.; Rieth, A. J.; Miller, A. S.; Hoertz, P. G.; Meyer, T. J. Water Oxidation and Oxygen Monitoring by Cobalt-Modified Fluorine-Doped Tin Oxide Electrodes. *J. Am. Chem. Soc.* **2013**, *135* (23), 8432–8435. https://doi.org/10.1021/ja400616a.

(271) Sougueh, C. M.; Lakard, S.; Husson, J.; Contal, E.; Monney, S.; Moutarlier, V.; Magnenet, C.; Lakard, B. Influence of Pre-Grafted Pyrrole-Based Silane on the Electrodeposition and Chemical Properties of Polypyrrole Films. *Synth. Met.* **2018**, *246*, 220–229. https://doi.org/10.1016/j.synthmet.2018.10.017.

(272) Grzeszczuk, M.; Ozsakarya, R. *Surface Morphology and Corresponding Electrochemistry of Polypyrrole Films Electrodeposited Using Water Miscible Ionic Liquid*. www.rsc.org/advances (accessed 2019-10-21).

(273) Garfias-García, E.; Romero-Romo, M.; Ramírez-Silva, M. T.; Morales, J.; Palomar-Pardavé, M. *Eletrochemical Nucleation of Polypyrrole onto Different Substrates*; 2010; Vol. 5. www.electrochemsci.org (accessed 2019-10-21).

(274) Snook, G. A.; Chen, G. Z.; Fray, D. J.; Hughes, M.; Shaffer, M. Studies of Deposition of and Charge Storage in Polypyrrole-Chloride and Polypyrrole-Carbon Nanotube Composites with an Electrochemical Quartz Crystal Microbalance. *J. Electroanal. Chem.* **2004**, *568* (1–2), 135–142. https://doi.org/10.1016/j.jelechem.2004.01.013.

(275) Asavapiriyanont, S.; Chandler, G. K.; Gunawardena, G. A.; Pletcher, D. The Electrodeposition of Polypyrrole Films from Aqueous Solutions. *J. Electroanal. Chem.* **1984**, *177* (1–2), 229–244. https://doi.org/10.1016/0022-0728(84)80225-9.

(276) Serra Moreno, J.; Panero, S.; Artico, M.; Filippini, P. Synthesis and Characterization of New Electroactive Polypyrrole-Chondroitin Sulphate A Substrates. *Bioelectrochemistry* **2008**, *72* (1), 3–9. https://doi.org/10.1016/j.bioelechem.2007.11.002.

(277) Collier, J. H.; Camp, J. P.; Hudson, T. W.; Schmidt, C. E. Synthesis and Characterization of Polypyrrole-Hyaluronic Acid Composite Biomaterials for Tissue Engineering Applications. *J. Biomed. Mater. Res.* **2000**, *50* (4), 574–584. https://doi.org/10.1002/(SICI)1097-4636(20000615)50:4<574::AID-JBM13>3.0.CO;2-I.

(278) Ren, X.; Pickup, P. G. Ion Transport in Polypyrrole and a Polypyrrole/Polyanion Composite. *J. Phys. Chem.* **1993**, *97* (20), 5356–5362. https://doi.org/10.1021/j100122a029.

(279) Wang, J.; Wu, C.; Wu, P.; Li, X.; Zhang, M.; Zhu, J. Polypyrrole Capacitance Characteristics with Different Doping Ions and Thicknesses. *Phys. Chem. Chem. Phys.* **2017**, *19* (31), 21165–21173. https://doi.org/10.1039/c7cp02707a.

(280) Ateh, D. D.; Navsaria, H. A.; Vadgama, P. Polypyrrole-Based Conducting Polymers and Interactions with Biological Tissues. *Journal of the Royal Society Interface*. 2006, pp 741–752. https://doi.org/10.1098/rsif.2006.0141.

(281) Yang, Z.; Shen, W.; Rottman, J. N.; Wikswo, J. P.; Murray, K. T. Rapid Stimulation Causes Electrical Remodeling in Cultured Atrial Myocytes. *J. Mol. Cell. Cardiol.* **2005**, *38* (2), 299–308. https://doi.org/10.1016/j.yjmcc.2004.11.015.

(282) White, S. M.; Constantin, P. E.; Claycomb, W. C. Cardiac Physiology at the Cellular Level: Use of Cultured HL-1 Cardiomyocytes for Studies of Cardiac Muscle Cell Structure and Function. *American Journal of Physiology - Heart and Circulatory Physiology*. 2004. https://doi.org/10.1152/ajpheart.00986.2003.

(283) Sartiani, L.; Bochet, P.; Cerbai, E.; Mugelli, A.; Fischmeister, R. Functional Expression of the Hyperpolarization-Activated Non-Selective Cation Current/f in Immortalized HL-1 Cardiomyocytes. *Journal of Physiology*. November 15, 2002, pp 81–92. https://doi.org/10.1113/jphysiol.2002.021535.

(284) Webb, K.; Hlady, V.; Tresco, P. A. Relative Importance of Surface Wettability and Charged Functional Groups on NIH 3T3 Fibroblast Attachment, Spreading, and Cytoskeletal Organization. *J. Biomed. Mater. Res.* **1998**, *41* (3), 422–430. https://doi.org/10.1002/(SICI)1097-4636(19980905)41:3<422::AID-JBM12>3.0.CO;2-K.

(285) Bacakova, L.; Filova, E.; Parizek, M.; Ruml, T.; Svorcik, V. Modulation of Cell Adhesion, Proliferation and Differentiation on Materials Designed for Body

Implants. *Biotechnology Advances*. November 2011, pp 739–767.
https://doi.org/10.1016/j.biotechadv.2011.06.004.

(286) Altankov, G.; Grinnell, F.; Groth, T. Studies on the Biocompatibility of Materials: Fibroblast Reorganization of Substratum-Bound Fibronectin on Surfaces Varying in Wettability. *J. Biomed. Mater. Res.* **1996**, *30* (3), 385–391. https://doi.org/10.1002/(SICI)1097-4636(199603)30:3<385::AID-JBM13>3.0.CO;2-J.

(287) Ponsonnet, L.; Reybier, K.; Jaffrezic, N.; Comte, V.; Lagneau, C.; Lissac, M.; Martelet, C. Relationship between Surface Properties (Roughness, Wettability) of Titanium and Titanium Alloys and Cell Behaviour. *Mater. Sci. Eng. C* **2003**, *23* (4), 551–560. https://doi.org/10.1016/S0928-4931(03)00033-X.

(288) Mize, R. R. Quantitative Image Analysis for Immunocytochemistry and in Situ Hybridization. *J. Neurosci. Methods* **1994**, *54* (2), 219–237. https://doi.org/10.1016/0165-0270(94)90195-3.

(289) Gould, V. E.; Wiedenmann, B.; Lee, I.; Schwechheimer, K.; Dockhorn-Dworniczak, B.; Radosevich, J. A.; Moll, R.; Franke, W. W. Synaptophysin Expression in Neuroendocrine Neoplasms as Determined by Immunocytochemistry. *Am. J. Pathol.* **1987**, *126* (2), 243–257.

(290) Cao, N.; Liao, J.; Liu, Z.; Zhu, W.; Wang, J.; Liu, L.; Yu, L.; Xu, P.; Cui, C.; Xiao, L.; Yang, H. T. In Vitro Differentiation of Rat Embryonic Stem Cells into Functional Cardiomyocytes. *Cell Res.* **2011**, *21* (9), 1316–1331. https://doi.org/10.1038/cr.2011.48.

(291) Nam, Y. J.; Song, K.; Luo, X.; Daniel, E.; Lambeth, K.; West, K.; Hill, J. A.; Di Maio, J. M.; Baker, L. A.; Bassel-Duby, R.; Olson, E. N. Reprogramming of Human Fibroblasts toward a Cardiac Fate. *Proc. Natl. Acad. Sci. U. S. A.* **2013**, *110* (14), 5588–5593. https://doi.org/10.1073/pnas.1301019110.

(292) Moreira, F. T. C.; Truta, L. A. A. N. A.; Sales, M. G. F. Biomimetic Materials Assembled on a Photovoltaic Cell as a Novel Biosensing Approach to Cancer Biomarker Detection. *Sci. Rep.* **2018**, *8* (1). https://doi.org/10.1038/s41598-018-27884-2.

(293) Sonavane, A. C.; Inamdar, A. I.; Dalavi, D. S.; Deshmukh, H. P.; Patil, P. S. Simple and Rapid Synthesis of NiO/PPy Thin Films with Improved Electrochromic Performance. *Electrochim. Acta* **2010**, *55* (7), 2344–2351.

https://doi.org/10.1016/j.electacta.2009.11.087.

(294) Mather, J. P. Concise Review: Cancer Stem Cells: In Vitro Models. *Stem Cells*. John Wiley & Sons, Ltd February 1, 2012, pp 95–99. https://doi.org/10.1002/stem.774.

(295) Vailhé, B.; Vittet, D.; Feige, J. J. In Vitro Models of Vasculogenesis and Angiogenesis. *Laboratory Investigation*. 2001, pp 439–452. https://doi.org/10.1038/labinvest.3780252.

(296) Rubin, L. L.; Hall, D. E.; Porter, S.; Barbu, K.; Cannon, C.; Horner, H. C.; Janatpour, M.; Liaw, C. W.; Manning, K.; Morales, J.; Tanner, L. I.; Tomaselli, K. J.; Bard, F. A Cell Culture Model of the Blood-Brain Barrier. *J. Cell Biol.* **1991**, *115* (6), 1725–1735. https://doi.org/10.1083/jcb.115.6.1725.

(297) Graudejus, O.; Ponce Wong, R.; Varghese, N.; Wagner, S.; Morrison, B. Bridging the Gap between in Vivo and in Vitro Research: Reproducing in Vitro the Mechanical and Electrical Environment of Cells in Vivo. *Front. Cell. Neurosci.* **2018**, *12*. https://doi.org/10.3389/conf.fncel.2018.38.00069.

(298) Committee on Methods of Producing Monoclonal Antibodies; Institute for Laboratory Animal Research; Council, N. R. Summary of Advantages and Disadvantages of In Vitro and In Vivo Methods - Monoclonal Antibody Produc. *Monoclon. Antib. Prod.* **1999**, 0–3.

(299) Inamdar, N. K.; Borenstein, J. T. Microfluidic Cell Culture Models for Tissue Engineering. *Current Opinion in Biotechnology*. October 2011, pp 681–689. https://doi.org/10.1016/j.copbio.2011.05.512.

(300) Katt, M. E.; Placone, A. L.; Wong, A. D.; Xu, Z. S.; Searson, P. C. In Vitro Tumor Models: Advantages, Disadvantages, Variables, and Selecting the Right Platform. *Frontiers in Bioengineering and Biotechnology*. Frontiers Media S.A. February 12, 2016. https://doi.org/10.3389/fbioe.2016.00012.

(301) Kenny, H. A.; Lal-Nag, M.; White, E. A.; Shen, M.; Chiang, C. Y.; Mitra, A. K.; Zhang, Y.; Curtis, M.; Schryver, E. M.; Bettis, S.; Jadhav, A.; Boxer, M. B.; Li, Z.; Ferrer, M.; Lengyel, E. Quantitative High Throughput Screening Using a Primary Human Three-Dimensional Organotypic Culture Predicts in Vivo Efficacy. *Nat. Commun.* **2015**, *6*. https://doi.org/10.1038/ncomms7220.

(302) Huch, M.; Koo, B. K. Modeling Mouse and Human Development Using Organoid Cultures. *Development (Cambridge)*. Company of Biologists Ltd September 23,

2015, pp 3113–3125. https://doi.org/10.1242/dev.118570.

(303) Rubin, L. L.; Hall, D. E.; Porter, S.; Barbu, K.; Cannon, C.; Homer, H. C.; Janatpour, M.; Liaw, C. W.; Manning, K.; Morales, J.; Tanner, L. 1; Tbmaselli, K. J.; Bard, F. A Cell Culture Model of the Blood-Brain Barrier. https://doi.org/10.1083/jcb.115.6.1725.

(304) Bandyopadhyay, B.; Li, G.; Yin, H.; Kuret, J. Tau Aggregation and Toxicity in a Cell Culture Model of Tauopathy *. **2007**. https://doi.org/10.1074/jbc.M700192200.

(305) Duval, K.; Grover, H.; Han, L. H.; Mou, Y.; Pegoraro, A. F.; Fredberg, J.; Chen, Z. Modeling Physiological Events in 2D vs. 3D Cell Culture. *Physiology*. American Physiological Society June 14, 2017, pp 266–277. https://doi.org/10.1152/physiol.00036.2016.

(306) Kapałczyńska, M.; Kolenda, T.; Przybyła, W.; Zajączkowska, M.; Teresiak, A.; Filas, V.; Ibbs, M.; Bliźniak, R.; Łuczewski, Ł.; Lamperska, K. 2D and 3D Cell Cultures – a Comparison of Different Types of Cancer Cell Cultures. *Arch. Med. Sci.* **2018**, *14* (4), 910–919. https://doi.org/10.5114/aoms.2016.63743.

(307) Brodersen, P.; Sakvarelidze-Achard, L.; Bruun-Rasmussen, M.; Dunoyer, P.; Yamamoto, Y. Y.; Sieburth, L.; Voinnet, O. Widespread Translational Inhibition by Plant MiRNAs and SiRNAs. *Science (80-.).* **2008**, *320* (5880), 1185–1190. https://doi.org/10.1126/science.1159151.

(308) Pampaloni, F.; Reynaud, E. G.; Stelzer, E. H. K. The Third Dimension Bridges the Gap between Cell Culture and Live Tissue. *Nature Reviews Molecular Cell Biology*. October 2007, pp 839–845. https://doi.org/10.1038/nrm2236.

(309) Jaffe, L. F.; Poo, M. -M. Neurites Grow Faster towards the Cathode than the Anode in a Steady Field. *J. Exp. Zool.* **1979**, *209* (1), 115–127. https://doi.org/10.1002/jez.1402090114.

(310) Patel, N.; Poo, M. M. Orientation of Neurite Growth by Extracellular Electric Fields. *J. Neurosci.* **1982**, *2* (4), 483–496. https://doi.org/10.1523/jneurosci.02-04-00483.1982.

(311) Yu, L. M. Y.; Leipzig, N. D.; Shoichet, M. S. Promoting Neuron Adhesion and Growth. *Materials Today*. May 2008, pp 36–43. https://doi.org/10.1016/S1369-7021(08)70088-9.

(312) Xia, Y.; Buja, L. M.; Scarpulla, R. C.; Mcmillin, J. B. Electrical Stimulation of Neonatal Cardiomyocytes Results in the Sequential Activation of Nuclear Genes Governing Mitochondrial Proliferation and Differentiation. *Proc. Natl. Acad. Sci. U. S. A.* **1997**, *94* (21), 11399–11404. https://doi.org/10.1073/pnas.94.21.11399.

(313) Hirt, M. N.; Boeddinghaus, J.; Mitchell, A.; Schaaf, S.; Börnchen, C.; Müller, C.; Schulz, H.; Hubner, N.; Stenzig, J.; Stoehr, A.; Neuber, C.; Eder, A.; Luther, P. K.; Hansen, A.; Eschenhagen, T. Functional Improvement and Maturation of Rat and Human Engineered Heart Tissue by Chronic Electrical Stimulation. *J. Mol. Cell. Cardiol.* **2014**, *74*, 151–161. https://doi.org/10.1016/j.yjmcc.2014.05.009.

(314) Langelaan, M. L. P.; Boonen, K. J. M.; Rosaria-Chak, K. Y.; van der Schaft, D. W. J.; Post, M. J.; Baaijens, F. P. T. Advanced Maturation by Electrical Stimulation: Differences in Response between C2C12 and Primary Muscle Progenitor Cells. *J. Tissue Eng. Regen. Med.* **2011**, *5* (7), 529–539. https://doi.org/10.1002/term.345.

(315) Jacot, J. G.; Martin, J. C.; Hunt, D. L. Mechanobiology of Cardiomyocyte Development. *J. Biomech.* **2010**, *43* (1), 93–98. https://doi.org/10.1016/j.jbiomech.2009.09.014.

(316) Baumgartner, S.; Halbach, M.; Krausgrill, B.; Maass, M.; Srinivasan, S. P.; Sahito, R. G. A.; Peinkofer, G.; Nguemo, F.; Müller-Ehmsen, J.; Hescheler, J. Electrophysiological and Morphological Maturation of Murine Fetal Cardiomyocytes during Electrical Stimulation in Vitro. *J. Cardiovasc. Pharmacol. Ther.* **2015**, *20* (1), 104–112. https://doi.org/10.1177/1074248414536273.

(317) Holt, E.; Lunde, P. K.; Sejersted, O. M.; Christensen, G. Electrical Stimulation of Adult Rat Cardiomyocytes in Culture Improves Contractile Properties and Is Associated with Altered Calcium Handling. *Basic Res. Cardiol.* **1997**, *92* (5), 289–298. https://doi.org/10.1007/BF00788941.

(318) Tandon, N.; Cannizzaro, C.; Chao, P. H. G.; Maidhof, R.; Marsano, A.; Au, H. T. H.; Radisic, M.; Vunjak-Novakovic, G. Electrical Stimulation Systems for Cardiac Tissue Engineering. *Nat. Protoc.* **2009**, *4* (2), 155–173. https://doi.org/10.1038/nprot.2008.183.

(319) Schmidt, C. E.; Shastri, V. R.; Vacanti, J. P.; Langer, R. *Stimulation of Neurite Outgrowth Using an Electrically Conducting Polymer (Conductive Polymeroxidized Polypyrrolenerve RegenerationPC-12 Cellselectrical Stimulationneuronal Stimulation)*; 1997; Vol. 94. www.pnas.org. (accessed

2019-10-24).

(320) Veerman, C. C.; Kosmidis, G.; Mummery, C. L.; Casini, S.; Verkerk, A. O.; Bellin, M. Immaturity of Human Stem-Cell-Derived Cardiomyocytes in Culture: Fatal Flaw or Soluble Problem? *Stem Cells and Development*. Mary Ann Liebert, Inc. 140 Huguenot Street, 3rd Floor New Rochelle, NY 10801 USA January 12, 2015, pp 1035–1052. https://doi.org/10.1089/scd.2014.0533.

(321) Nagashima, T.; Hadiwidjaja, S.; Ohsumi, S.; Murata, A.; Hisada, T.; Kato, R.; Okada, Y.; Honda, H.; Shimizu, K. In Vitro Model of Human Skeletal Muscle Tissues with Contractility Fabricated by Immortalized Human Myogenic Cells. *Adv. Biosyst.* **2020**, *4* (11), 2000121. https://doi.org/10.1002/adbi.202000121.

(322) Chan, Y. C.; Ting, S.; Lee, Y. K.; Ng, K. M.; Zhang, J.; Chen, Z.; Siu, C. W.; Oh, S. K. W.; Tse, H. F. Electrical Stimulation Promotes Maturation of Cardiomyocytes Derived from Human Embryonic Stem Cells. *J. Cardiovasc. Transl. Res.* **2013**, *6* (6), 989–999. https://doi.org/10.1007/s12265-013-9510-z.

(323) Fang, J.; Wei, X.; Li, H.; Hu, N.; Liu, X.; Xu, D.; Zhang, T.; Wan, H.; Wang, P.; Xie, X. Cardiomyocyte Electrical-Mechanical Synchronized Model for High-Content, Dose-Quantitative and Time-Dependent Drug Assessment. *Microsystems Nanoeng.* **2021**, *7* (1), 1–12. https://doi.org/10.1038/s41378-021-00247-0.

(324) Zhang, F.; Qu, K. Y.; Zhou, B.; Luo, Y.; Zhu, Z.; Pan, D. J.; Cui, C.; Zhu, Y.; Chen, M. L.; Huang, N. P. Design and Fabrication of an Integrated Heart-on-a-Chip Platform for Construction of Cardiac Tissue from Human IPSC-Derived Cardiomyocytes and in Situ Evaluation of Physiological Function. *Biosens. Bioelectron.* **2021**, *179*, 113080. https://doi.org/10.1016/j.bios.2021.113080.

(325) Stejskal, J.; Trchová, M.; Kučka, J.; Capáková, Z.; Humpolíček, P.; Prokeš, J. Effect of Sterilization Techniques on the Conductivity of Polyaniline and Polypyrrole. *Synth. Met.* **2021**, *282*. https://doi.org/10.1016/j.synthmet.2021.116937.

(326) Grasman, J. M.; O'Brien, M. P.; Ackerman, K.; Gagnon, K. A.; Wong, G. M.; Pins, G. D. The Effect of Sterilization Methods on the Structural and Chemical Properties of Fibrin Microthread Scaffolds. *Macromol. Biosci.* **2016**, 836–846. https://doi.org/10.1002/mabi.201500410.

(327) Mascharak, S.; Benitez, P. L.; Proctor, A. C.; Madl, C. M.; Hu, K. H.; Dewi, R. E.;

Butte, M. J.; Heilshorn, S. C. YAP-Dependent Mechanotransduction Is Required for Proliferation and Migration on Native-like Substrate Topography. *Biomaterials* **2017**, *115*, 155–166. https://doi.org/10.1016/j.biomaterials.2016.11.019.

(328) Richardson, S. A.; Rawlings, T. M.; Muter, J.; Walker, M.; Brosens, J. J.; Cameron, N. R.; Eissa, A. M. Covalent Attachment of Fibronectin onto Emulsion-Templated Porous Polymer Scaffolds Enhances Human Endometrial Stromal Cell Adhesion, Infiltration, and Function. *Macromol. Biosci.* **2019**, *19* (2). https://doi.org/10.1002/mabi.201800351.

(329) Douman, S. F.; Collins, D.; Cumba, L. R.; Beirne, S.; Wallace, G. G.; Yue, Z.; Iwuoha, E. I.; Melinato, F.; Pellegrin, Y.; Forster, R. J. Wireless Electrochemiluminescence at Functionalised Gold Microparticles Using 3D Titanium Electrode Arrays. *Chem. Commun.* **2021**, *57* (38), 4642–4645. https://doi.org/10.1039/d1cc01010g.

(330) Chougule, M. A.; Pawar, S. G.; Godse, P. R.; Mulik, R. N.; Sen, S.; Patil, V. B. Synthesis and Characterization of Polypyrrole (PPy) Thin Films. *Soft Nanosci. Lett.* **2011**, *01* (01), 6–10. https://doi.org/10.4236/snl.2011.11002.

(331) Cakić, M.; Glišić, S.; Nikolić, G.; Nikolić, G. M.; Cakić, K.; Cvetinov, M. Synthesis, Characterization and Antimicrobial Activity of Dextran Sulphate Stabilized Silver Nanoparticles. *J. Mol. Struct.* **2016**, *1110*, 156–161. https://doi.org/10.1016/j.molstruc.2016.01.040.

(332) Akkouch, A.; Shi, G.; Zhang, Z.; Rouabhia, M. Bioactivating Electrically Conducting Polypyrrole with Fibronectin and Bovine Serum Albumin. *J. Biomed. Mater. Res. - Part A* **2010**, *92* (1), 221–231. https://doi.org/10.1002/jbm.a.32357.

(333) Chen, C.; Bai, X.; Ding, Y.; Lee, I. S. Electrical Stimulation as a Novel Tool for Regulating Cell Behavior in Tissue Engineering. *Biomaterials Research*. BioMed Central December 5, 2019, pp 1–12. https://doi.org/10.1186/s40824-019-0176-8.

(334) Chan, Y. C.; Ting, S.; Lee, Y. K.; Ng, K. M.; Zhang, J.; Chen, Z.; Siu, C. W.; Oh, S. K. W.; Tse, H. F. Electrical Stimulation Promotes Maturation of Cardiomyocytes Derived from Human Embryonic Stem Cells. *J. Cardiovasc. Transl. Res.* **2013**, *6* (6), 989–999. https://doi.org/10.1007/s12265-013-9510-z.

(335) Ahadian, S.; Ostrovidov, S.; Hosseini, V.; Kaji, H.; Ramalingam, M.; Bae, H.;

Khademhosseini, A. Electrical Stimulation as a Biomimicry Tool for Regulating Muscle Cell Behavior. *Organogenesis*. Taylor & Francis April 2013, pp 87–92. https://doi.org/10.4161/org.25121.

(336) Zhu, R.; Sun, Z.; Li, C.; Ramakrishna, S.; Chiu, K.; He, L. Electrical Stimulation Affects Neural Stem Cell Fate and Function in Vitro. *Experimental Neurology*. Academic Press September 1, 2019, p 112963. https://doi.org/10.1016/j.expneurol.2019.112963.

(337) Jin, G.; Yang, G. H.; Kim, G. Tissue Engineering Bioreactor Systems for Applying Physical and Electrical Stimulations to Cells. *Journal of Biomedical Materials Research - Part B Applied Biomaterials*. John Wiley & Sons, Ltd May 1, 2015, pp 935–948. https://doi.org/10.1002/jbm.b.33268.

(338) Wang, Y.; De Arcangelis, V.; Gao, X.; Ramani, B.; Jung, Y. S.; Xiang, Y. Norepinephrine- and Epinephrine-Induced Distinct B2- Adrenoceptor Signaling Is Dictated by GRK2 Phosphorylation in Cardiomyocytes. *J. Biol. Chem.* **2008**, *283* (4), 1799–1807. https://doi.org/10.1074/jbc.M705747200.

(339) Geuss, L. R.; Suggs, L. J. Making Cardiomyocytes: How Mechanical Stimulation Can Influence Differentiation of Pluripotent Stem Cells. *Biotechnol. Prog.* **2013**, *29* (5), 1089–1096. https://doi.org/10.1002/btpr.1794.

(340) Chen, Y.; Ouyang, X.; Wu, Y.; Guo, S.; Xie, Y.; Wang, G. Co-Culture and Mechanical Stimulation on Mesenchymal Stem Cells and Chondrocytes for Cartilage Tissue Engineering. *Curr. Stem Cell Res. Ther.* **2019**, *15* (1), 54–60. https://doi.org/10.2174/1574888x14666191029104249.

(341) MacKenna, D.; Summerour, S. R.; Villarreal, F. J. Role of Mechanical Factors in Modulating Cardiac Fibroblast Function and Extracellular Matrix Synthesis. *Cardiovascular Research*. Oxford Academic May 1, 2000, pp 257–263. https://doi.org/10.1016/S0008-6363(00)00030-4.

(342) Ho, D.; Zhao, X.; Gao, S.; Hong, C.; Vatner, D. E.; Vatner, S. F. Heart Rate and Electrocardiography Monitoring in Mice. *Curr. Protoc. Mouse Biol.* **2011**, *1* (1), 123–139. https://doi.org/10.1002/9780470942390.mo100159.

(343) Sudhir, R.; Du, Q.; Sukhodub, A.; Jovanović, S.; Jovanović, A. Improved Adaptation to Physical Stress in Mice Overexpressing SUR2A Is Associated with Changes in the Pattern of Q-T Interval. *Pflugers Arch. Eur. J. Physiol.* **2020**, *472* (6), 683–691. https://doi.org/10.1007/s00424-020-02401-5.

(344) Babona-Pilipos, R.; Pritchard-Oh, A.; Popovic, M. R.; Morshead, C. M. Biphasic Monopolar Electrical Stimulation Induces Rapid and Directed Galvanotaxis in Adult Subependymal Neural Precursors. *Stem Cell Res. Ther.* **2015**, *6* (1), 1–13. https://doi.org/10.1186/s13287-015-0049-6.

(345) Ryan, C. N. M.; Doulgkeroglou, M. N.; Zeugolis, D. I. Electric Field Stimulation for Tissue Engineering Applications. *BMC Biomed. Eng.* **2021**, *3* (1), 1–9. https://doi.org/10.1186/s42490-020-00046-0.

(346) UEMURA, M.; SUGIMOTO, M.; YOSHIKAWA, Y.; HIRAMATSU, T.; INOUE, T. Monophasic Pulsed Current Stimulation of Duty Cycle 10% Promotes Differentiation of Human Dermal Fibroblasts into Myofibroblasts. *Phys. Ther. Res.* **2021**, *24* (2), 145–152. https://doi.org/10.1298/ptr.e10064.

(347) Meng, S.; Rouabhia, M.; Zhang, Z. Electrical Stimulation and Cellular Behaviors in Electric Field in Biomedical Research. *Materials*. Multidisciplinary Digital Publishing Institute December 27, 2022, p 165. https://doi.org/10.3390/ma15010165.

(348) Pettersen, E.; Shah, F. A.; Ortiz-Catalan, M. Enhancing Osteoblast Survival through Pulsed Electrical Stimulation and Implications for Osseointegration. *Sci. Rep.* **2021**, *11* (1), 1–8. https://doi.org/10.1038/s41598-021-01901-3.

(349) Luiken, J. J. F. P.; Willems, J.; Van Der Vusse, G. J.; Glatz, J. F. C. Electrostimulation Enhances FAT/CD36-Mediated Long-Chain Fatty Acid Uptake by Isolated Rat Cardiac Myocytes. *Am. J. Physiol. - Endocrinol. Metab.* **2001**, *281* (4 44-4), 704–712. https://doi.org/10.1152/ajpendo.2001.281.4.e704.

(350) Ois Mavré, F.; Anand, R. K.; Laws, D. R.; Chow, K.-F.; Chang, B.-Y.; Crooks, J. A.; Crooks, R. M. Bipolar Electrodes: A Useful Tool for Concentration, Separation, and Detection of Analytes in Microelectrochemical Systems. https://doi.org/10.1021/ac101262v.

(351) Takeuchi, R.; Asoh, H. Effects of Size and Position of an Unconnected Aluminum Electrode on Bipolar Anodization in an AC Electric Field. *Sci. Rep.* **2021**, *11* (1), 1–7. https://doi.org/10.1038/s41598-021-01633-4.

(352) Niederstaetter, L.; Neuditschko, B.; Brunmair, J.; Janker, L.; Bileck, A.; Favero, G. Del; Gerner, C. Eicosanoid Content in Fetal Calf Serum Accounts for Reproducibility Challenges in Cell Culture. *Biomol. 2021, Vol. 11, Page 113* **2021**, *11* (1), 113. https://doi.org/10.3390/BIOM11010113.

(353) Hirsch, C.; Schildknecht, S. In Vitro Research Reproducibility: Keeping up High Standards. *Front. Pharmacol.* **2019**, *10*, 1484. https://doi.org/10.3389/FPHAR.2019.01484/BIBTEX.

(354) Reddin, I. G.; Fenton, T.; Wass, M. N.; Michaelis, M. Data Variability in Standardised Cell Culture Experiments. *bioRxiv* **2021**, 2021.02.27.433153. https://doi.org/10.1101/2021.02.27.433153.

(355) Bakhtiari, H.; Palizban, A.; Khanahmad, H.; Mofid, M. Aptamer-Based Approaches for in Vitro Molecular Detection of Cancer. *Research in Pharmaceutical Sciences*. Medknow Publications and Media Pvt. Ltd. April 1, 2020, pp 107–122. https://doi.org/10.4103/1735-5362.283811.

(356) Maduraiveeran, G.; Sasidharan, M.; Ganesan, V. Electrochemical Sensor and Biosensor Platforms Based on Advanced Nanomaterials for Biological and Biomedical Applications. *Biosensors and Bioelectronics*. Elsevier April 30, 2018, pp 113–129. https://doi.org/10.1016/j.bios.2017.12.031.

(357) Patel, S.; Nanda, R.; Sahoo, S.; Mohapatra, E. Biosensors in Health Care: The Milestones Achieved in Their Development towards Lab-on-Chip-Analysis. *Biochemistry Research International*. Hindawi Limited 2016. https://doi.org/10.1155/2016/3130469.

(358) Haleem, A.; Javaid, M.; Singh, R. P.; Suman, R.; Rab, S. Biosensors Applications in Medical Field: A Brief Review. *Sensors Int.* **2021**, *2*, 100100. https://doi.org/10.1016/j.sintl.2021.100100.

(359) Yoo, E. H.; Lee, S. Y. Glucose Biosensors: An Overview of Use in Clinical Practice. *Sensors*. Multidisciplinary Digital Publishing Institute (MDPI) May 2010, pp 4558–4576. https://doi.org/10.3390/s100504558.

(360) Bhalla, N.; Jolly, P.; Formisano, N.; Estrela, P. Introduction to Biosensors. *Essays Biochem.* **2016**, *60* (1), 1–8. https://doi.org/10.1042/EBC20150001.

(361) Batool, R.; Rhouati, A.; Nawaz, M. H.; Hayat, A.; Marty, J. L. A Review of the Construction of Nano-Hybrids for Electrochemical Biosensing of Glucose. *Biosensors*. Multidisciplinary Digital Publishing Institute March 25, 2019, p 46. https://doi.org/10.3390/bios9010046.

(362) Califf, R. M. Biomarker Definitions and Their Applications. *Exp. Biol. Med.* **2018**, *243* (3), 213–221. https://doi.org/10.1177/1535370217750088.

(363) Lyngbakken, M. N.; Myhre, P. L.; Røsjø, H.; Omland, T. Novel Biomarkers of Cardiovascular Disease: Applications in Clinical Practice. *Critical Reviews in Clinical Laboratory Sciences.* Taylor & Francis January 2, 2019, pp 33–60. https://doi.org/10.1080/10408363.2018.1525335.

(364) Wong, Y.-K.; Tse, H.-F. Circulating Biomarkers for Cardiovascular Disease Risk Prediction in Patients With Cardiovascular Disease. *Front. Cardiovasc. Med.* **2021**, *8*, 1255. https://doi.org/10.3389/fcvm.2021.713191.

(365) Ghantous, C. M.; Kamareddine, L.; Farhat, R.; Zouein, F. A.; Mondello, S.; Kobeissy, F.; Zeidan, A. Advances in Cardiovascular Biomarker Discovery. *Biomedicines.* MDPI AG December 1, 2020, pp 1–19. https://doi.org/10.3390/biomedicines8120552.

(366) Mir, R.; Elfaki, I.; Khullar, N.; Waza, A. A.; Jha, C.; Mir, M. M.; Nisa, S.; Mohammad, B.; Mir, T. A.; Maqbool, M.; Barnawi, J.; Albalawi, S. O.; Abu-Duhier, F. M. Role of Selected MiRNAs as Diagnostic and Prognostic Biomarkers in Cardiovascular Diseases, Including Coronary Artery Disease, Myocardial Infarction and Atherosclerosis. *Journal of Cardiovascular Development and Disease.* Multidisciplinary Digital Publishing Institute February 19, 2021, pp 1–17. https://doi.org/10.3390/jcdd8020022.

(367) Gregory, R. I.; Chendrimada, T. P.; Cooch, N.; Shiekhattar, R. Human RISC Couples MicroRNA Biogenesis and Posttranscriptional Gene Silencing. *Cell* **2005**, *123* (4), 631–640. https://doi.org/10.1016/j.cell.2005.10.022.

(368) Kim, J. Identification of Micrornas as Diagnostic Biomarkers for Breast Cancer Based on the Cancer Genome Atlas. *Diagnostics* **2021**, *11* (1), 107. https://doi.org/10.3390/diagnostics11010107.

(369) Sarkar, J. P.; Saha, I.; Lancucki, A.; Ghosh, N.; Wlasnowolski, M.; Bokota, G.; Dey, A.; Lipinski, P.; Plewczynski, D. Identification of MiRNA Biomarkers for Diverse Cancer Types Using Statistical Learning Methods at the Whole-Genome Scale. *Front. Genet.* **2020**, *11*, 982. https://doi.org/10.3389/fgene.2020.00982.

(370) Bryzgunova, O.; Konoshenko, M.; Zaporozhchenko, I.; Yakovlev, A.; Laktionov, P. Isolation of Cell-Free Mirna from Biological Fluids: Influencing Factors and Methods. *Diagnostics.* Multidisciplinary Digital Publishing Institute May 11, 2021, p 865. https://doi.org/10.3390/diagnostics11050865.

(371) Mo, M. H.; Chen, L.; Fu, Y.; Wang, W.; Fu, S. W. Cell-Free Circulating MiRNA

Biomarkers in Cancer. *J. Cancer* **2012**, *3* (1), 432–448. https://doi.org/10.7150/jca.4919.

(372) Condrat, C. E.; Thompson, D. C.; Barbu, M. G.; Bugnar, O. L.; Boboc, A.; Cretoiu, D.; Suciu, N.; Cretoiu, S. M.; Voinea, S. C. MiRNAs as Biomarkers in Disease: Latest Findings Regarding Their Role in Diagnosis and Prognosis. *Cells*. Multidisciplinary Digital Publishing Institute January 23, 2020, p 276. https://doi.org/10.3390/cells9020276.

(373) Bryzgunova, O.; Konoshenko, M.; Zaporozhchenko, I.; Yakovlev, A.; Laktionov, P. Isolation of Cell-Free Mirna from Biological Fluids: Influencing Factors and Methods. *Diagnostics*. Multidisciplinary Digital Publishing Institute May 11, 2021, p 865. https://doi.org/10.3390/diagnostics11050865.

(374) Ren, Y.; Deng, H.; Shen, W.; Gao, Z. A Highly Sensitive and Selective Electrochemical Biosensor for Direct Detection of MicroRNAs in Serum. *Anal. Chem.* **2013**, *85* (9), 4784–4789. https://doi.org/10.1021/ac400583e.

(375) Yan, B.; Wang, H.; Tan, Y.; Fu, W. MicroRNAs in Cardiovascular Disease: Small Molecules but Big Roles. *Curr. Top. Med. Chem.* **2019**, *19* (21), 1918–1947. https://doi.org/10.2174/1568026619666190808160241.

(376) Zhou, S. S.; Jin, J. P.; Wang, J. Q.; Zhang, Z. G.; Freedman, J. H.; Zheng, Y.; Cai, L. MiRNAS in Cardiovascular Diseases: Potential Biomarkers, Therapeutic Targets and Challenges Review-Article. *Acta Pharmacologica Sinica*. Nature Publishing Group June 7, 2018, pp 1073–1084. https://doi.org/10.1038/aps.2018.30.

(377) Wang, H.; Peng, R.; Wang, J.; Qin, Z.; Xue, L. Circulating MicroRNAs as Potential Cancer Biomarkers: The Advantage and Disadvantage. *Clinical Epigenetics*. BioMed Central Ltd. April 23, 2018, pp 1–10. https://doi.org/10.1186/s13148-018-0492-1.

(378) Cui, M.; Wang, H.; Yao, X.; Zhang, D.; Xie, Y.; Cui, R.; Zhang, X. Circulating MicroRNAs in Cancer: Potential and Challenge. *Front. Genet.* **2019**, *10*, 626. https://doi.org/10.3389/fgene.2019.00626.

(379) Mraz, M.; Malinova, K.; Mayer, J.; Pospisilova, S. MicroRNA Isolation and Stability in Stored RNA Samples. *Biochemical and Biophysical Research Communications*. December 4, 2009, pp 1–4. https://doi.org/10.1016/j.bbrc.2009.09.061.

(380) Zampetaki, A.; Mayr, M. Analytical Challenges and Technical Limitations in Assessing Circulating MiRNAs. *Thrombosis and Haemostasis*. Schattauer GmbH September 2012, pp 592–598. https://doi.org/10.1160/TH12-02-0097.

(381) Blumberg, D. D. Creating a Ribonuclease-Free Environment. *Methods Enzymol.* **1987**, *152* (C), 20–24. https://doi.org/10.1016/0076-6879(87)52005-5.

(382) Kramer, M. F.; Coen, D. M. Enzymatic Amplification of DNA by PCR: Standard Procedures and Optimization. *Current protocols in immunology / edited by John E. Coligan ... [et al.]*. John Wiley & Sons, Ltd October 1, 2001, pp 15.1.1-15.1.14. https://doi.org/10.1002/0471142727.mb1501s56.

(383) Bhattacharya, A.; Chaturvedi, G.; Singhal, K.; Pandey, R. Experimental Toolkit to Study RNA Level Regulation. In *RNA-Based Regulation in Human Health and Disease*; Academic Press, 2020; pp 371–396. https://doi.org/10.1016/B978-0-12-817193-6.00016-9.

(384) Cheatham, T. E.; Kollman, P. A. Molecular Dynamics Simulations Highlight the Structural Differences among DNA:DNA, RNA:RNA, and DNA:RNA Hybrid Duplexes. *J. Am. Chem. Soc.* **1997**, *119* (21), 4805–4825. https://doi.org/10.1021/ja963641w.

(385) Broitman-Maduro, G.; Maduro, M. F. In Situ Hybridization of Embryos with Antisense RNA Probes. In *Methods in Cell Biology*; Academic Press, 2011; Vol. 106, pp 253–270. https://doi.org/10.1016/B978-0-12-544172-8.00009-8.

(386) Zhang, C.; Miao, P.; Sun, M.; Yan, M.; Liu, H. Progress in MiRNA Detection Using Graphene Material–Based Biosensors. *Small*. John Wiley & Sons, Ltd September 1, 2019, p 1901867. https://doi.org/10.1002/smll.201901867.

(387) Masud, M. K.; Na, J.; Lin, T. E.; Malgras, V.; Preet, A.; Ibn Sina, A. A.; Wood, K.; Billah, M.; Kim, J.; You, J.; Kani, K.; Whitten, A. E.; Salomon, C.; Nguyen, N. T.; Shiddiky, M. J. A.; Trau, M.; Hossain, M. S. A.; Yamauchi, Y. Nanostructured Mesoporous Gold Biosensor for MicroRNA Detection at Attomolar Level. *Biosens. Bioelectron.* **2020**, *168*, 112429. https://doi.org/10.1016/j.bios.2020.112429.

(388) Ferapontova, E. E. DNA Electrochemistry and Electrochemical Sensors for Nucleic Acids. *Annual Review of Analytical Chemistry*. Annual Reviews June 12, 2018, pp 197–218. https://doi.org/10.1146/annurev-anchem-061417-125811.

(389) Antuña-Jiménez, D.; González-García, M. B.; Hernández-Santos, D.; Fanjul-

Bolado, P. Screen-Printed Electrodes Modified with Metal Nanoparticles for Small Molecule Sensing. *Biosensors*. Multidisciplinary Digital Publishing Institute February 1, 2020, p 9. https://doi.org/10.3390/bios10020009.

(390) Pilan, L. Tailoring the Performance of Electrochemical Biosensors Based on Carbon Nanomaterials via Aryldiazonium Electrografting. *Bioelectrochemistry*. 2021. https://doi.org/10.1016/j.bioelechem.2020.107697.

(391) Gillan, L.; Teerinen, T.; Johansson, L. S.; Smolander, M. Controlled Diazonium Electrodeposition towards a Biosensor for C-Reactive Protein. *Sensors Int.* **2021**, *2*, 100060. https://doi.org/10.1016/j.sintl.2020.100060.

(392) Badacz, R.; Kleczyński, P.; Legutko, J.; Żmudka, K.; Gacoń, J.; Przewłocki, T.; Kabłak-Ziembicka, A. Expression of Mir-1-3p, Mir-16-5p and Mir-122-5p as Possible Risk Factors of Secondary Cardiovascular Events. *Biomedicines* **2021**, *9* (8). https://doi.org/10.3390/biomedicines9081055.

(393) Kura, B.; Kalocayova, B.; Devaux, Y.; Bartekova, M. Potential Clinical Implications of Mir-1 and Mir-21 in Heart Disease and Cardioprotection. *International Journal of Molecular Sciences*. 2020. https://doi.org/10.3390/ijms21030700.

(394) Maie, K.; Miyagi, K.; Takada, T.; Nakamura, M.; Yamana, K. RNA-Mediated Electron Transfer: Double Exponential Distance Dependence. *J. Am. Chem. Soc.* **2009**, *131* (37), 13188–13189. https://doi.org/10.1021/ja902647j.

(395) Takada, T.; Otsuka, Y.; Nakamura, M.; Yamana, K. Electron Transfer through RNA: Chemical Probing of Dual Distance Dependence. In *Bioorganic and Medicinal Chemistry*; Pergamon, 2011; Vol. 19, pp 6881–6884. https://doi.org/10.1016/j.bmc.2011.09.027.

(396) Ferapontova, E. E. Electron Transfer in DNA at Electrified Interfaces. *Chemistry - An Asian Journal*. John Wiley & Sons, Ltd November 4, 2019, pp 3773–3781. https://doi.org/10.1002/asia.201901024.

(397) Wang, L.; Zhang, L. Circulating Exosomal MiRNA as Diagnostic Biomarkers of Neurodegenerative Diseases. *Frontiers in Molecular Neuroscience*. Frontiers Media S.A. April 15, 2020, p 53. https://doi.org/10.3389/fnmol.2020.00053.

(398) Swarbrick, S.; Wragg, N.; Ghosh, S.; Stolzing, A. Systematic Review of MiRNA as Biomarkers in Alzheimer's Disease. *Molecular Neurobiology*. 2019, pp 6156–6167. https://doi.org/10.1007/s12035-019-1500-y.

(399) Spain, E.; McArdle, H.; Keyes, T. E.; Forster, R. J. Detection of Sub-Femtomolar DNA Based on Double Potential Electrodeposition of Electrocatalytic Platinum Nanoparticles. *Analyst* **2013**, *138* (15), 4340–4344. https://doi.org/10.1039/c3an00500c.

(400) Ye, J.; Xu, M.; Tian, X.; Cai, S.; Zeng, S. Research Advances in the Detection of MiRNA. *Journal of Pharmaceutical Analysis.* Elsevier August 1, 2019, pp 217–226. https://doi.org/10.1016/j.jpha.2019.05.004.

(401) Steel, A. B.; Levicky, R. L.; Herne, T. M.; Tarlov, M. J. Immobilization of Nucleic Acids at Solid Surfaces: Effect of Oligonucleotide Length on Layer Assembly. *Biophys. J.* **2000**, *79* (2), 975–981. https://doi.org/10.1016/S0006-3495(00)76351-X.

(402) Spain, E.; Kojima, R.; Kaner, R. B.; Wallace, G. G.; O'Grady, J.; Lacey, K.; Barry, T.; Keyes, T. E.; Forster, R. J. High Sensitivity DNA Detection Using Gold Nanoparticle Functionalised Polyaniline Nanofibres. *Biosens. Bioelectron.* **2011**, *26* (5), 2613–2618. https://doi.org/10.1016/j.bios.2010.11.017.

(403) Spain, E.; Jimenez-Mateos, E. M.; Raoof, R.; ElNaggar, H.; Delanty, N.; Forster, R. J.; Henshall, D. C. Direct, Non-Amplified Detection of MicroRNA-134 in Plasma from Epilepsy Patients. *RSC Adv.* **2015**, *5* (109), 90071–90078. https://doi.org/10.1039/c5ra16352h.

(404) Spain, E.; Keyes, T. E.; Forster, R. J. Polypyrrole-Gold Nanoparticle Composites for Highly Sensitive DNA Detection. *Electrochim. Acta* **2013**, *109,* 102–109. https://doi.org/10.1016/j.electacta.2013.07.018.

(405) Ren, Y.; Deng, H.; Shen, W.; Gao, Z. A Highly Sensitive and Selective Electrochemical Biosensor for Direct Detection of MicroRNAs in Serum. *Anal. Chem.* **2013**, *85* (9), 4784–4789. https://doi.org/10.1021/ac400583e.

(406) Zouari, M.; Campuzano, S.; Pingarrón, J. M.; Raouafi, N. Femtomolar Direct Voltammetric Determination of Circulating MiRNAs in Sera of Cancer Patients Using an Enzymeless Biosensor. *Anal. Chim. Acta* **2020**, *1104,* 188–198. https://doi.org/10.1016/j.aca.2020.01.016.

(407) Kasturi, S.; Eom, Y.; Torati, S. R.; Kim, C. G. Highly Sensitive Electrochemical Biosensor Based on Naturally Reduced RGO/Au Nanocomposite for the Detection of MiRNA-122 Biomarker. *J. Ind. Eng. Chem.* **2021**, *93,* 186–195. https://doi.org/10.1016/j.jiec.2020.09.022.

(408) Meng, T.; Shang, N.; Nsabimana, A.; Ye, H.; Wang, H.; Wang, C.; Zhang, Y. An Enzyme-Free Electrochemical Biosensor Based on Target-Catalytic Hairpin Assembly and Pd@UiO-66 for the Ultrasensitive Detection of MicroRNA-21. *Anal. Chim. Acta* **2020**, *1138*, 59–68. https://doi.org/10.1016/j.aca.2020.09.022.

(409) Pothipor, C.; Jakmunee, J.; Bamrungsap, S.; Ounnunkad, K. An Electrochemical Biosensor for Simultaneous Detection of Breast Cancer Clinically Related MicroRNAs Based on a Gold Nanoparticles/Graphene Quantum Dots/Graphene Oxide Film. *Analyst* **2021**, *146* (12), 4000–4009. https://doi.org/10.1039/d1an00436k.

(410) Steel, A. B.; Herne, T. M.; Tarlov, M. J. Electrochemical Quantitation of DNA Immobilized on Gold. *Anal. Chem.* **1998**, *70* (22), 4670–4677. https://doi.org/10.1021/ac980037q.

(411) Herne, T. M.; Tarlov, M. J. Characterization of DNA Probes Immobilized on Gold Surfaces. *J. Am. Chem. Soc.* **1997**, *119* (38), 8916–8920. https://doi.org/10.1021/ja9719586.

(412) Juodkazis, K.; Juodkazyt, J.; Šebeka, B.; Lukinskas, A. Cyclic Voltammetric Studies on the Reduction of a Gold Oxide Surface Layer. *Electrochem. commun.* **1999**, *1* (8), 315–318. https://doi.org/10.1016/S1388-2481(99)00062-4.

(413) Spain, E.; McArdle, H.; Keyes, T. E.; Forster, R. J. Detection of Sub-Femtomolar DNA Based on Double Potential Electrodeposition of Electrocatalytic Platinum Nanoparticles. *Analyst* **2013**. https://doi.org/10.1039/c3an00500c.

(414) Spain, E.; Jimenez-Mateos, E. M.; Raoof, R.; ElNaggar, H.; Delanty, N.; Forster, R. J.; Henshall, D. C. Direct, Non-Amplified Detection of MicroRNA-134 in Plasma from Epilepsy Patients. *RSC Adv.* **2015**, *5* (109), 90071–90078. https://doi.org/10.1039/c5ra16352h.

(415) Ahn, S. H.; Choi, I.; Park, H. Y.; Hwang, S. J.; Yoo, S. J.; Cho, E.; Kim, H. J.; Henkensmeier, D.; Nam, S. W.; Kim, S. K.; Jang, J. H. Effect of Morphology of Electrodeposited Ni Catalysts on the Behavior of Bubbles Generated during the Oxygen Evolution Reaction in Alkaline Water Electrolysis. *Chem. Commun.* **2013**, *49* (81), 9323–9325. https://doi.org/10.1039/c3cc44891f.

(416) Lv, P.; Le The, H.; Eijkel, J.; Van Den Berg, A.; Zhang, X.; Lohse, D. Growth and Detachment of Oxygen Bubbles Induced by Gold-Catalyzed Decomposition of Hydrogen Peroxide. *J. Phys. Chem. C* **2017**, *121* (38), 20769–20776.

https://doi.org/10.1021/acs.jpcc.7b04994.

(417)   Kleinjung, F.; Klussmann, S.; Erdmann, V. A.; Scheller, F. W.; Fürste, J. P.; Bier, F. F. High-Affinity RNA as a Recognition Element in a Biosensor. *Anal. Chem.* **1998**, *70* (2), 328–331. https://doi.org/10.1021/ac9706483.

(418)   Chu, V. B.; Bai, Y.; Lipfert, J.; Herschlag, D.; Doniach, S. A Repulsive Field: Advances in the Electrostatics of the Ion Atmosphere. *Current Opinion in Chemical Biology.* 2008, pp 619–625. https://doi.org/10.1016/j.cbpa.2008.10.010.

(419)   Xu, F.; Pellino, A. M.; Knoll, W. Electrostatic Repulsion and Steric Hindrance Effects of Surface Probe Density on Deoxyribonucleic Acid (DNA)/Peptide Nucleic Acid (PNA) Hybridization. *Thin Solid Films* **2008**, *516* (23), 8634–8639. https://doi.org/10.1016/j.tsf.2008.06.067.

(420)   Cederquist, K. B.; Keating, C. D. Curvature Effects in DNA:Au Nanoparticle Conjugates. *ACS Nano* **2009**, *3* (2), 256–260. https://doi.org/10.1021/nn9000726.

(421)   Damjanovic, A.; Genshaw, M. A.; Bockris, J. O. M. Hydrogen Peroxide Formation in Oxygen Reduction at Gold Electrodes. II. Alkaline Solution. *J. Electroanal. Chem.* **1967**, *15* (C), 173–180. https://doi.org/10.1016/0022-0728(67)85021-6.

(422)   Zeis, R.; Lei, T.; Sieradzki, K.; Snyder, J.; Erlebacher, J. Catalytic Reduction of Oxygen and Hydrogen Peroxide by Nanoporous Gold. *J. Catal.* **2008**, *253* (1), 132–138. https://doi.org/10.1016/j.jcat.2007.10.017.

(423)   Genshaw, M. A.; Damjanovic, A.; Bockris, J. O. M. Hydrogen Peroxide Formation in Oxygen Reduction at Gold Electrodes. I. Acid Solution. *J. Electroanal. Chem.* **1967**, *15* (C), 163–172. https://doi.org/10.1016/0022-0728(67)85020-4.

(424)   He, W.; Zhou, Y. T.; Wamer, W. G.; Hu, X.; Wu, X.; Zheng, Z.; Boudreau, M. D.; Yin, J. J. Intrinsic Catalytic Activity of Au Nanoparticles with Respect to Hydrogen Peroxide Decomposition and Superoxide Scavenging. *Biomaterials* **2013**, *34* (3), 765–773. https://doi.org/10.1016/j.biomaterials.2012.10.010.

(425)   Golchin, K.; Golchin, J.; Ghaderi, S.; Alidadiani, N.; Eslamkhah, S.; Eslamkah, M.; Davaran, S.; Akbarzadeh, A. Gold Nanoparticles Applications: From Artificial Enzyme till Drug Delivery. *Artificial Cells, Nanomedicine and Biotechnology.*

Taylor & Francis February 17, 2018, pp 250–254.
https://doi.org/10.1080/21691401.2017.1305393.

(426) Jirkovský, J. S.; Halasa, M.; Schiffrin, D. J. Kinetics of Electrocatalytic Reduction
of Oxygen and Hydrogen Peroxide on Dispersed Gold Nanoparticles. *Phys.*
Chem. Chem. Phys. **2010**, *12* (28), 8042–8052.
https://doi.org/10.1039/c002416c.

(427) Benvidi, A.; Firouzabadi, A. D.; Moshtaghiun, S. M.; Mazloum-Ardakani, M.;
Tezerjani, M. D. Ultrasensitive DNA Sensor Based on Gold
Nanoparticles/Reduced Graphene Oxide/Glassy Carbon Electrode. *Anal.*
Biochem. **2015**, *484*, 24–30. https://doi.org/10.1016/j.ab.2015.05.009.

(428) Chen, J.; Zhang, J.; Guo, Y.; Li, J.; Fu, F.; Yang, H. H.; Chen, G. An
Ultrasensitive Electrochemical Biosensor for Detection of DNA Species Related
to Oral Cancer Based on Nuclease-Assisted Target Recycling and Amplification
of DNAzyme. *Chem. Commun.* **2011**, *47* (28), 8004–8006.
https://doi.org/10.1039/c1cc11929j.

(429) Liu, Y. H.; Li, H. N.; Chen, W.; Liu, A. L.; Lin, X. H.; Chen, Y. Z. Bovine Serum
Albumin-Based Probe Carrier Platform for Electrochemical DNA Biosensing.
Anal. Chem. **2013**, *85* (1), 273–277. https://doi.org/10.1021/ac303397f.

(430) Mao, X.; Yang, L.; Su, X. L.; Li, Y. A Nanoparticle Amplification Based Quartz
Crystal Microbalance DNA Sensor for Detection of Escherichia Coli O157:H7.
Biosens. Bioelectron. **2006**, *21* (7), 1178–1185.
https://doi.org/10.1016/j.bios.2005.04.021.

(431) Chen, M.; Wu, D.; Tu, S.; Yang, C.; Chen, D. J.; Xu, Y. A Novel Biosensor for
the Ultrasensitive Detection of the LncRNA Biomarker MALAT1 in Non-Small
Cell Lung Cancer. *Sci. Rep.* **2021**, *11* (1), 1–11. https://doi.org/10.1038/s41598-
021-83244-7.

(432) Zhang, Y.; Li, N.; Ma, W.; Yang, M.; Hou, C.; Luo, X.; Huo, D. Ultrasensitive
Detection of MicroRNA-21 by Using Specific Interaction of Antimonene with
RNA as Electrochemical Biosensor. *Bioelectrochemistry* **2021**, *142*.
https://doi.org/10.1016/j.bioelechem.2021.107890.

(433) Hurst, S. J.; Lytton-Jean, A. K. R.; Mirkin, C. A. Maximizing DNA Loading on a
Range of Gold Nanoparticle Sizes. *Anal. Chem.* **2006**, *78* (24), 8313–8318.
https://doi.org/10.1021/ac0613582.

(434) Chang, X.; Batchelor-McAuley, C.; Compton, R. G. Hydrogen Peroxide Reduction on Single Platinum Nanoparticles. *Chem. Sci.* **2020**, *11* (17), 4416–4421. https://doi.org/10.1039/d0sc00379d.

(435) Zhao, J.; Yan, Y.; Zhu, L.; Li, X.; Li, G. An Amperometric Biosensor for the Detection of Hydrogen Peroxide Released from Human Breast Cancer Cells. *Biosens. Bioelectron.* **2013**, *41* (1), 815–819. https://doi.org/10.1016/j.bios.2012.10.019.

(436) Qian, L.; Yang, X. Composite Film of Carbon Nanotubes and Chitosan for Preparation of Amperometric Hydrogen Peroxide Biosensor. *Talanta* **2006**, *68* (3), 721–727. https://doi.org/10.1016/j.talanta.2005.05.030.

(437) Li, C. Z.; Liu, Y.; Luong, J. H. T. Impedance Sensing of DNA Binding Drugs Using Gold Substrates Modified with Gold Nanoparticles. *Anal. Chem.* **2005**, *77* (2), 478–485. https://doi.org/10.1021/ac048672l.

(438) Saeed, A. A.; Sánchez, J. L. A.; O'Sullivan, C. K.; Abbas, M. N. DNA Biosensors Based on Gold Nanoparticles-Modified Graphene Oxide for the Detection of Breast Cancer Biomarkers for Early Diagnosis. *Bioelectrochemistry* **2017**, *118*, 91–99. https://doi.org/10.1016/j.bioelechem.2017.07.002.

(439) Ma, T.; Martens, I.; Bizzotto, D. Thermal Stability of Thiolated DNA SAMs in Buffer: Revealing the Influence of Surface Crystallography and DNA Coverage via in Situ Combinatorial Surface Analysis. *Langmuir* **2020**, *36* (48), 14495–14506. https://doi.org/10.1021/acs.langmuir.0c01828.

(440) Gu, Q.; Josephs, E. A.; Ye, T. Hybridization and Self-assembly Behaviors of Surface-immobilized DNA in Close Proximity: A Single-molecule Perspective. *Aggregate* **2022**. https://doi.org/10.1002/agt2.186.

(441) Xu, J.; Craig, S. L. Influence of the Extent of Hybridization on the Hydrodynamic Radius of DNA-Functionalized Gold Nanoparticles. *Langmuir* **2007**, *23* (4), 2015–2020. https://doi.org/10.1021/LA0622830/ASSET/IMAGES/MEDIUM/LA0622830N00001.GIF.

(442) Laroussi, A.; Raouafi, N.; Mirsky, V. M. Electrocatalytic Sensor for Hydrogen Peroxide Based on Immobilized Benzoquinone. *Electroanalysis* **2021**, *33* (9), 2062–2070. https://doi.org/10.1002/elan.202100113.

(443) Schmidt, A. R.; Nguyen, N. D. T.; Leopold, M. C. Nanoparticle Film Assemblies

as Platforms for Electrochemical Biosensing - Factors Affecting the Amperometric Signal Enhancement of Hydrogen Peroxide. *Langmuir* **2013**, *29* (14), 4574–4583. https://doi.org/10.1021/la400359x.

(444) Horrocks, B. R.; Schmidtke, D.; Heller, A.; Bard, A. J. Scanning Electrochemical Microscopy. 24. Enzyme Ultramicroelectrodes for the Measurement of Hydrogen Peroxide at Surfaces. *Anal. Chem.* **1993**, *65* (24), 3605–3614. https://doi.org/10.1021/ac00072a013.

(445) Kasianowicz, J. J.; Brandin, E.; Branton, D.; Deamer, D. W. Characterization of Individual Polynucleotide Molecules Using a Membrane Channel. In *Proceedings of the National Academy of Sciences of the United States of America*; The National Academy of Sciences of the USA, 1996; Vol. 93, pp 13770–13773. https://doi.org/10.1073/pnas.93.24.13770.

(446) Varshavsky, A. Discovering the RNA Double Helix and Hybridization. *Cell*. Elsevier B.V. December 29, 2006, pp 1295–1297. https://doi.org/10.1016/j.cell.2006.12.008.

(447) Rao, A. N.; Grainger, D. W. Biophysical Properties of Nucleic Acids at Surfaces Relevant to Microarray Performance. *Biomaterials Science*. NIH Public Access April 4, 2014, pp 436–471. https://doi.org/10.1039/c3bm60181a.

(448) Zhang, X.; Servos, M. R.; Liu, J. Surface Science of DNA Adsorption onto Citrate-Capped Gold Nanoparticles. *Langmuir* **2012**, *28* (8), 3896–3902. https://doi.org/10.1021/la205036p.

(449) Meunier-Prest, R.; Raveau, S.; Finot, E.; Legay, G.; Cherkaoui-Malki, M.; Latruffe, N. Direct Measurement of the Melting Temperature of Supported DNA by Electrochemical Method. *Nucleic Acids Res.* **2003**, *31* (23), e150–e150. https://doi.org/10.1093/nar/gng150.

(450) Wetmur, J. G. Hybridization and Renaturation Kinetics of Nucleic Acids. *Annual review of biophysics and bioengineering*. 1976, pp 337–361. https://doi.org/10.1146/annurev.bb.05.060176.002005.

(451) Dimitrov, R. A.; Zuker, M. Prediction of Hybridization and Melting for Double-Stranded Nucleic Acids. *Biophys. J.* **2004**, *87* (1), 215–226. https://doi.org/10.1529/biophysj.103.020743.

(452) Xu, J.; Craig, S. L. Thermodynamics of DNA Hybridization on Gold Nanoparticles. *J. Am. Chem. Soc.* **2005**, *127* (38), 13227–13231.

https://doi.org/10.1021/ja052352h.

(453) MacQueen, J. T. Some Observations Concerning the van't Hoff Equation. *J. Chem. Educ.* **1967**, *44* (12), 755–756. https://doi.org/10.1021/ed044p755.

(454) Sambriski, E. J.; Schwartz, D. C.; De Pablo, J. J. Uncovering Pathways in DNA Oligonucleotide Hybridization via Transition State Analysis. *Proc. Natl. Acad. Sci. U. S. A.* **2009**, *106* (43), 18125–18130. https://doi.org/10.1073/pnas.0904721106.

(455) Bielec, K.; Sozanski, K.; Seynen, M.; Dziekan, Z.; Ten Wolde, P. R.; Holyst, R. Kinetics and Equilibrium Constants of Oligonucleotides at Low Concentrations. Hybridization and Melting Study. *Phys. Chem. Chem. Phys.* **2019**, *21* (20), 10798–10807. https://doi.org/10.1039/c9cp01295h.

(456) Lin, C.; Compton, R. G. Understanding Mass Transport Influenced Electrocatalysis at the Nanoscale via Numerical Simulation. *Current Opinion in Electrochemistry.* Elsevier April 1, 2019, pp 186–199. https://doi.org/10.1016/j.coelec.2018.08.001.

(457) Min, J.; Baeumner, A. J. Characterization and Optimization of Interdigitated Ultramicroelectrode Arrays as Electrochemical Biosensor Transducers. *Electroanalysis* **2004**, *16* (9), 724–729. https://doi.org/10.1002/elan.200302872.

(458) Wei, D.; Bailey, M. J. A.; Andrew, P.; Ryhänen, T. Electrochemical Biosensors at the Nanoscale. *Lab on a Chip.* The Royal Society of Chemistry August 7, 2009, pp 2123–2131. https://doi.org/10.1039/b903118a.